

AD-A047 376

PHOTOMETRICS INC LEXINGTON MASS

F/G 4/1

DATA REDUCTION AND AURORAL CHARACTERIZATIONS FOR ICECAP III. HA--ETC(U)

JAN 77 I L KOFSKY, D P VILLANUCCI, R B SLUDER DNA001-76-C-0161

UNCLASSIFIED

PHM-02-77

DNA-4220F

NL

1 OF 3

ADA047 376



AD A047376

12
b.s.

AD-E300 009

DNA 4220F

DATA REDUCTION AND AURORAL CHARACTERIZATIONS FOR ICECAP III

HAES Report No. 59

PhotoMetrics, Inc.
442 Marrett Road
Lexington, Massachusetts 02173

31 January 1977

Final Report for Period 1 December 1975—31 December 1976

CONTRACT No. DNA 001-76-C-0161

APPROVED FOR PUBLIC RELEASE;
DISTRIBUTION UNLIMITED.

THIS WORK SPONSORED BY THE DEFENSE NUCLEAR AGENCY
UNDER RDT&E RMSS CODE B322076462 L25AAXYX96630 H2590D.

AD No. —
DDC FILE COPY:

Prepared for
Director
DEFENSE NUCLEAR AGENCY
Washington, D. C. 20305

DDC
RECEIVED
DEC 9 1977
B

UNCLASSIFIED

SECURITY CLASSIFICATION OF THIS PAGE (When Data Entered)

REPORT DOCUMENTATION PAGE		READ INSTRUCTIONS BEFORE COMPLETING FORM
1. REPORT NUMBER DNA 4220F	2. GOVT ACCESSION NO.	3. RECIPIENT'S CATALOG NUMBER (9)
4. TITLE (and Subtitle) DATA REDUCTION AND AURORAL CHARACTERIZATIONS FOR ICECAP III, HAES Report No. 59.	5. TYPE OF REPORT & PERIOD COVERED Final Report, for Period 1 Dec 75—31 Dec 76.	6. PERFORMING ORG. REPORT NUMBER PhM-02-77
7. AUTHOR(S) I. L. Kofsky, D. P. Villanucci R. B. Sluder	8. CONTRACT OR GRANT NUMBER(S) DNA 001-76-C-0161	9. PROGRAM ELEMENT PROJECT, TASK AREA & WORK UNIT NUMBERS NWET Subtask L25AAXYX966-30
10. PERFORMING ORGANIZATION NAME AND ADDRESS PhotoMetrics, Inc. ✓ 442 Marrett Road Lexington, Massachusetts 02173	11. CONTROLLING OFFICE NAME AND ADDRESS Director Defense Nuclear Agency Washington, D.C. 20305	12. REPORT DATE 31 January 1977
13. MONITORING AGENCY NAME & ADDRESS (if different from Controlling Office) (12) 204p.	14. SECURITY CLASS (of this report) UNCLASSIFIED	15. DECLASSIFICATION DOWNGRADING SCHEDULE
16. DISTRIBUTION STATEMENT (of this Report) Approved for public release; distribution unlimited.		17. DISTRIBUTION STATEMENT (of the abstract entered in Block 20, if different from Report)
18. SUPPLEMENTARY NOTES This work sponsored by the Defense Nuclear Agency under RDT&E RMSS Code B322076462 L25AAXYX96630 H2500D.		
19. KEY WORDS (Continue on reverse side if necessary and identify by block number) Sky Backgrounds Airglow Nuclear Simulation Radiation Transport Infrared Measurements Photometry and Radiometry Aurora		
20. ABSTRACT (Continue on reverse side if necessary and identify by block number) Results of infrared radiometry of auroral particle-excited air from two ICECAP multi-instrumented rocket probes and a zenith-viewing aircraft; characterizations of the ionosphere for other simulation tests; an outline of ICECAP's 1976 program of coordinated NKC-135 aircraft and groundbased measurements; and a review of methods for assessing auroral energy inputs, are reported. Effective efficiencies for emission of what we interpret as NO vibrational fundamental and overtone radiation are derived from rockets A18.205-1 (1973) and A18.219-1 (1974), and aircraft several rocket probes.		

DD FORM 1 JAN 73 1473

EDITION OF 1 NOV 65 IS OBSOLETE

UNCLASSIFIED

SECURITY CLASSIFICATION OF THIS PAGE (When Data Entered)

388596

10

UNCLASSIFIED

SECURITY CLASSIFICATION OF THIS PAGE(When Data Entered)

20. ABSTRACT (Continued)

missions ^{micrometer} 75-4. These are consistent among themselves and with A10.117-3 (1973), within the expected precision and resolution of the measurements. The visible-fluorescent and ~~NO~~-infrared radiances of relatively stable forms appears spatially and temporally correlated, within the accuracy of present analyses of the scanning radiometer data. Some indication of a prompt component of 4.25 \pm 0.05 μ m auroral radiation is observed. The spectroscopic and Thomson-scatter radar methods for determining column ionization rates and altitude profiles are reviewed, with a comparison of meridian-plane data from ICECAP 75; it is found that the optical method is effective for aircraft investigations, and that scattering in the lower atmosphere strongly influences results of photometry from ground stations. Systematic All-sky photographic sequences of the aurora probed by recent ICECAP-HAES rockets are presented.

ACCESSION for	
NTIS	White Section <input checked="" type="checkbox"/>
DDC	Grey Section <input type="checkbox"/>
UNANNOUNCED	<input type="checkbox"/>
JUSTIFICATION	
BY	
DISTRIBUTION/AVAILABILITY CODES	
Dist. <input type="checkbox"/> <input type="checkbox"/> <input type="checkbox"/> or SPECIAL	
A	

UNCLASSIFIED

SECURITY CLASSIFICATION OF THIS PAGE(When Data Entered)

PREFACE

The High Altitude Effects Simulation (HAES) Program sponsored by the Defense Nuclear Agency since the early 1970 time period, comprises several groupings of separate, but interrelated technical activities, e.g., ICECAP (Infrared Chemistry Experiments - Coordinated Auroral Program). Each of the latter have the common objective of providing information ascertained as essential for the development and validation of predictive computer codes designed for use with high priority DoD radar, communications, and optical defensive systems.

Since the inception of the HAES Program, significant achievements and results have been described in reports published by DNA, participating service laboratories, and supportive organizations. In order to provide greater visibility for such information and enhance its timely applications, significant reports published since early calendar 1974 shall be identified with an assigned HAES serial number and the appropriate activity acronym (e.g., ICECAP) as part of the report title. A complete and current bibliography of all HAES reports issued prior to and subsequent to HAES Report No. 1, dated 5 February 1974 entitled, "Rocket Launch of an SWIR Spectrometer into an Aurora (ICECAP 72)," AFCRL Environmental Research Paper No. 466, is maintained and available on request from DASIAC, DoD Nuclear Information and Analysis Center, 816 State Street, Santa Barbara, California 93102, Telephone (805) 965-0551.

This report, which is the final report on Contract DNA001-76-C-0161 and No. 59 in the HAES series, covers PhotoMetrics' technical activities between 01 Dec 75 and 31 Dec 76. It presents reduced and analyzed rocket and aircraft data on short wavelength-infrared emission from air excited by energetic charged particles, and background material for interpreting results of simulations tests. Reference is made to our earlier reports HAES No. 4 (DNA 3511F, 10 Apr 75, 333 pp) and No. 27 (DNA 3789F, 25 Oct 75, 135 pp), Ref's 1 and 2, in

which previous results and our procedures for accessing and analyzing ICECAP data are described.

Sections I and II analyze results of sidelooking radiometry of isolated arcs from multi-instrumented rockets A18.205-1 (1973) and A18.219-1 (1974) to derive effective efficiencies for exciting nitric oxide vibrational fundamental and overtone radiation, and Section IV determines the NO overtone's chemiluminous efficiency from calibrated auroral-ionosphere radiance data taken from a KC-135 aircraft. Procedures applied in these field investigations and consistency of the data returned are reviewed critically. Auroral development and the radiance distribution probed by six recent ICECAP rockets is shown in montages of selected All-sky photographic images in Section III. Section V interprets auroral power input measurements for reference to infrared emission intensities, and Section VI is a record of the ICECAP 76 aircraft flights. Appendix I reprints our operating plan for the aircraft and its coordination with the DNA Project 617 (Chatanika) radar, Appendix II discusses procedures for measuring auroral-deposition altitude profiles for aircraft support, and Appendix III reviews present knowledge about fluctuations in the natural infrared hydroxyl airglow background.

This work was done under the direction of I. L. Kofsky, to whom questions about it should be addressed. Carlton S. Miller made major contributions to the design and assembly of the photographic montages in Section III, and Daniel A. Gentile to the photoreproduction and artwork. Supporting information was provided by many of the staff of the OPR branch of the Air Force Geophysics Laboratory, Utah State University's laboratories, and Stanford Research Institute's DNA 617 radar group. Computer listings and plots of the auroral radiances measured from ICECAP rockets were made available by P. Doyle of AFGL-OPR. Input data elements were kindly provided by D. Archer of Mission Research Corp., R. Olson of (U.S. Army) Atmospheric

Sciences Laboratory, R. Huppi of Stewart Laboratories, T. Degges and W. Grieder of Visidyne, Inc., and R. Sears of Lockheed Missiles and Space Corp. The support and encouragement of H.C. Fitz, Jr., and C.A. Blank of the Defense Nuclear Agency, and A.T. Stair, Jr., and J.C. Ulwick of AFGL are gratefully acknowledged.

TABLE OF CONTENTS

SECTION		PAGE
	PREFACE	1
I	REDUCTION OF PHOTOMETER AND RADIO- METER DATA FROM MULTI-EXPERIMENT ROCKET A18.205-1	15
	INTRODUCTION	15
	ARC GEOMETRY	16
	DATA - ENERGY INPUT ALONG RADIO- METERS' LINE OF SIGHT.....	20
	NI PRECURSOR FORBIDDEN LINES	31
	VISIBLE AURORA ON DOWNLEG.....	38
	5.3 μ m NO FUNDAMENTAL -- BACKGROUND CONSIDERATIONS	42
	5.3 μ m ARC-ASSOCIATED EMISSION	50
	2.7 μ m NO OVERTONE	63
	COMMENTS ON ARC-ASSOCIATED EMISSION AT 5.3 AND 2.7 μ m	72
II	PARTIAL REDUCTION OF PHOTOMETER AND RADIOMETER DATA FROM MULTI-EXPERIMENT ROCKET A18.219-1	74
	INTRODUCTION.....	74
	INSTRUMENT ELEVATION AND AZIMUTH.....	79
	UPLEG DATA - ENERGY INPUT FROM λ 3914 and λ 5577	79
	UPLEG - NI FORBIDDEN LINES.....	83
	UPLEG -- 4.3 μ m and 2.7 μ m RADIOMETER DATA	88
	DOWNLEG -- CORRELATION OF 2.7 μ m EMISSION WITH AIR FLUORESCENCE.....	89
	RADIATION AT 4.3 μ m -- PRELIMINARY REDUCTION	102
III	ALL-SKY PHOTOGRAPHIC RECORDS OF AURORAS PROBED FROM ICECAP ROCKETS	107
IV	ANALYSIS OF ICECAP's 10 MAR 75 AIRCRAFT MEASUREMENTS OF AURORA-ASSOCIATED RADIATION NEAR 2.8 μ m	115
	INTRODUCTION	115
	DATA REDUCTION	118
	SELF-CONSISTENCY OF THE DATA	118
	TEMPERATURE EFFECTS ON INFRARED SKY RADIANCE	122
	CHEMILUMINESCENCE EFFICIENCY, COMMENTS	126

TABLE OF CONTENTS (continued)

SECTION	PAGE
V ENERGY INPUT IN AURORAL SIMULATIONS	131
INTRODUCTION	131
PHOTOMETRY AND INCOHERENT RADAR BACKSCATTER MEASUREMENTS.....	132
SCATTERING AND BUILDUP IN THE LOWER ATMOSPHERE	135
A COMPARISON OF SPATIAL SCANS	141
RATIOS OF IONIZATION TO N ₂ FLUOR- ESCENCE TO NOCHEMILUMINESCENCE.....	150
VI ICECAP 76 AIRCRAFT MEASUREMENT PROGRAM AND AURORAL RADIANCES DATA	154
INTRODUCTION	153
INSTRUMENTS	156
DNA 617 RADAR COORDINATION, OPERATION	158
PHOTOMETER MEASUREMENTS	164
REFERENCES	167
APPENDIXES I-III - TABLE OF CONTENTS	170
ABSTRACTS AND EXPLANATORY NOTES	170

LIST OF ILLUSTRATIONS

<u>Figure</u>		<u>Page</u>
1	27 Mar 73 arc "centers" determined from intercepts of lines from co-meridian photometer stations at zenith angle of maximum surface brightness, with trajectory of A18.205-1	19
2	Three elevation-azimuth spin cycles on upleg of A18.205-1 showing the changing $\lambda 5577$ and $\lambda 3914$ angular distributions with rocket altitude	21
3	Altitude profiles of azimuths of $\lambda 5577$ and $\lambda 3914$ east and west peak intensities, A18.205-1 upleg	22
	Altitude profiles of the $\lambda 3914$ east and west peak intensities with backgrounds included, A18.205-1 upleg	23
5	Altitude profiles of $\lambda 5577$ and $\lambda 3914$ east and west limb halfwidths with mean baseline backgrounds in Fig 2 subtracted, A18.205-1 upleg	25
6	Altitude profiles of $\lambda 5577$ and $\lambda 3914$ east (a) and west (b) peak limb intensities with backgrounds included, A18.205-1 upleg.....	26
7	Intercept altitude profile of $\lambda 5577$ meridian brightness, A18.205-1 upleg	27
8	Altitude profiles of $\lambda 5577/\lambda 3914$ intensity ratios in both peaks, with background included (a) and radiance toward the S subtracted (b), A18.205-1 upleg	29
9	Altitude profiles of the $\lambda 3800$ east and west peak intensities, intensity ratios $\lambda 3800/\lambda 5577$, and $\lambda 3800$ and $\lambda 5577$ azimuths of peak intensities, with backgrounds included, A18.205-1 upleg.....	30
10	Three elevation-azimuth spin cycles on upleg of A18.205-1 showing the changing $\lambda 5199$ and $\lambda 3466$ angular distributions with altitude, A18.205-1	32
11	Altitude profiles of the $\lambda 5199$ east and west peak intensities and azimuth angles of peaks, A18.205 - 1 upleg	33

LIST OF ILLUSTRATIONS (continued)

<u>Figure</u>		<u>Page</u>
12	Altitude profiles of the $\lambda 3466$ east peak, and azimuth angles of the $\lambda 3466$, $\lambda 5577$, and $\lambda 5199$ east peaks, A18.205-1 upleg.....	34
13	Altitude profiles of $\lambda 5199/\lambda 5577$ and $\lambda 3466/\lambda 5577$ intensity ratios, A18.205-1 upleg	36
14	Altitude profiles of west peak $\lambda 5199/\lambda 3914$ intensity ratios, A18.205-1 upleg	37
15	Four representative $\lambda 5577$ spin cycles on downleg of A18.205-1	39
16	Altitude profiles of $\lambda 5577$ and $\lambda 3914$ peak intensities with backgrounds included, A18.205-1 downleg.....	40
17	Altitude profiles of $\lambda 5199$ and $\lambda 3466$ peak intensities with backgrounds included, and ratios of peak intensities $\lambda 5199/\lambda 5577$ and $\lambda 3466/\lambda 5577$, A18.205-1 downleg	41
18	5.3 μ m elevation-azimuth spin cycle from A18.205-1 upleg showing the various noise backgrounds plus aurora-associated modulation near 70° E of geomagnetic N	43
19	Altitude profiles of intensity of the 5.3 μ m "spike," azimuth angle of its center, and number of degrees of azimuth (per spin) off-scale, A18.205-1 upleg.....	44
20	Polar diagrams of the angular sensitivity of A18.205-1's sidelooking dual channel radiometer	45
21	Apparent 5.3 μ m radiance plotted against cosec of 5.3 μ m radiometer axis' elevation angle at a high (176 km) and a low (75 km) rocket altitude, A18.205-1 upleg	47
22	Altitude profiles of 5.3 μ m cyclic-background intensity at minimum (7°) and maximum (13°) radiometer elevation angle, A18.205-1 upleg and downleg	48

LIST OF ILLUSTRATIONS (continued)

<u>Figure</u>		<u>Page</u>
23	5.3 μ m radiometer elevation-azimuth spin cycle at high altitude of A18.205-1 upleg, showing the remaining cyclical background signal	49
24a-l	Twelve elevation-azimuth spin cycles of 5.3 μ m and λ 3914 radiance distributions from A18.205-1 upleg, indicating correlation of the two features at low rocket altitude and further illustrating the various backgrounds	52-57
25	Scatter plot of excess 5.3 μ m and λ 3914 intensities from A18.205-1 upleg traces in Fig 24, with supporting information on range to and intercept altitude on the arc	60
26	Synthetic spectra of NO $\Delta v = 1$ sequences, NO (1,0) band, and 5.3 μ m (NR-3B-7) radiometer response, A18.205-1	62
27	2.7 μ m elevation-azimuth spin cycles from two altitudes of A18.205-1 upleg, showing the various noise backgrounds including large spikes believed to be caused by a thermally-emitting object in the field of view	64
28	Altitude profiles of intensity of the 2.7 μ m "spike" and its center geomagnetic azimuth, A18.205-1 upleg	65
29a-e	Five elevation-azimuth spin cycles of 2.7 μ m and λ 3914 radiance distributions from A18.205-1 upleg, indicating the correlation of the two features at low rocket altitude	67-69
30	Comparison of 2.7 μ m side-looking radiometer scans from multi rockets A18.205-1 and A18.219-1 near 95 km on upleg, showing the higher mean radiance levels in the 1973 data	70
31	Two 2.7 μ m elevation-azimuth spin cycles from A18.205-1 downleg, showing the numerous noise spikes near 145 km rocket altitude and random pulses below 133 km	71

LIST OF ILLUSTRATIONS (continued)

<u>Figure</u>		<u>Page</u>
32	Trajectory of A18.219-1, with location of arc "centers" and maximum $\lambda 5577$ radiances seen from PKR. Centers are 100-km altitude intercepts along the zenith angle at which meridian-plane radiance was maximum	76
33	Elevation vs. azimuth of the side-looking photometers and radiometers after A18.219-1 stabilized	77
34	Representative elevation-azimuth scan from A18.219-1 showing the location of geomagnetic N	78
35	Three elevation-azimuth spin cycles on upleg of A18.219-1 showing the changing $\lambda 5577$ and $\lambda 3914$ angular distributions with rocket altitude	80
36	Altitude profiles of the $\lambda 5577$ and $\lambda 3914$ peak intensities with backgrounds included, A18.219-1 upleg.....	81
37	Altitude profiles of azimuths of $\lambda 5577$ and $\lambda 3914$ peak intensities, and $\lambda 5577/\lambda 3914$ intensity ratios with backgrounds included, A18.219-1 upleg.....	82
38	Three elevation-azimuth spin cycles on upleg of A18.219-1 showing the changing $\lambda 3466$ angular distributions with rocket altitude	84
39	Altitude profiles of azimuth angles of $\lambda 3466$ east and west limb enhancements, A18.219-1	85
40	Altitude profiles of the $\lambda 3466$ east and west peak intensities, with mean baseline backgrounds in Fig 38 subtracted, A18.219-1 upleg	86
41	Altitude profiles of the $\lambda 5199$ meridian intensities measured by the wide- and narrow-band filter photometers, without correction for backgrounds, A18.219-1 upleg	87

LIST OF ILLUSTRATIONS (continued)

<u>Figure</u>		<u>Page</u>
42	$\lambda 5577$ meridian photometer scans from PKR showing the complex auroral structure during downleg of A18.219-1	90
43	Elevation-azimuth spin cycle 721 on downleg of A18.219-1 comparing $\lambda 3914$, $\lambda 5577$, $2.7\mu\text{m}$ and $4.3\mu\text{m}$ radiance distributions near 102 km rocket altitude	91
44	Polar plot of Fig 43's four radiance distributions near 102 km, A18.219-1 downleg	92
45	Azimuth profile of $2.7\mu\text{m}/\lambda 3914$ intensity ratios with backgrounds included for spins 721 and 722, A18.219-1 downleg.....	94
46	Altitude profiles of the $2.7\mu\text{m}$ and $\lambda 3914$ spikes near 70°W , A18.219-1 downleg	95
47	Altitude profiles of the $2.7\mu\text{m}$ and $\lambda 3914$ westward spike intensities and $2.7\mu\text{m}/\lambda 3914$ ratios, A18.219-1 downleg.	96
48	Altitude profiles of $\lambda 5577$ peak intensity and $\lambda 5577/\lambda 3914$ ratio in the spike near 70°W , with background included, A18.219-1 downleg.	97
49	Elevation-azimuth spin cycles on downleg of A18.219-1 showing (among other features) the decreased correlation of $2.7\mu\text{m}$ radiance with $\lambda 3914$ between $91\frac{1}{2}$ and $84\frac{1}{2}$ km and the increased $2.7\mu\text{m}$ intensity toward the southwest.....	99
50	Altitude profiles of meridian intensities for (a) $\lambda 3914$, $\lambda 5577$ and (b) $2.7\mu\text{m}$, and (c) $2.7\mu\text{m}/\lambda 3914$ intensity ratios, with backgrounds included	100
51	Scatter plot of $2.7\mu\text{m}$ and $\lambda 3914$ intensities with backgrounds included, A18.219-1 downleg	101
52	Calculated spectra of NO^+ vibrational fundamental with $v = 0 - 10$ equally populated and $\text{NO}^+ (1,0)$ band only (from Ref 5), and relative response of A18.219-1's $4.3\mu\text{m}$ radiometer	104

LIST OF ILLUSTRATIONS (continued)

<u>Figure</u>		<u>Page</u>
53	Altitude profile of the $4.3\mu\text{m}$ radiances measured at the fixed radiometer elevation angle $\sim 8^\circ$, geo-magnetic azimuth 210° , A18.219-1	105
54	Visible-auroral distribution for ICECAP rocket A18.116-1, HIRIS I, launched 0916:30 21 Feb 74	109
55	Visible-auroral distribution for ICECAP rocket A18.219-1, '74 Multi, launched 0738:30 25 Feb 74	110
56	Visible-auroral distribution for ICECAP rocket NJ-74-1, Quiet CVF, Launched 0801:00 11 Apr 74	111
57	Visible-auroral distribution for ICECAP rocket IC 519.07-1B, '75 Multi, launched 0748:10 12 Mar 75.	112
58	Visible-auroral distribution for ICECAP rocket IC 630.02-1A, HIRIS II, launched 0805:20 01 Apr 76	113
59	Visible-auroral distribution for ICECAP rocket WS 610.27-1, RF/Langmuir Probe, launched 0928:20 01 Apr 76	114
60a,b	ICECAP-4's zenith radiance data with 0.05 Hz bandwidth (half-power) low-pass filtering (a) and 0.0125 Hz filtering (b).	116-117
61a,b	Scatter plots of ICECAP -4's zenith radiance data before (a) and after (b) correction for OH airglow	120-121
62	Scatter plot of five-point averages of $2.8\mu\text{m}$ radiance and outside air temperature at the aircraft, ICECAP-4	123
63	Scatter plot of outside air temperature and latitude of ICECAP-4	125
64	Zenith radiances during ICECAP-4's breakup normalized to the peak at $0957\frac{1}{2}$	127
65	Aircraft location on the DMSP record of optical-NIR aurora in the Alaska sector for 0856-0858 10 Mar 75, with aircraft All-sky photograph for 0858:09 (conclusion of turn to N).	129

LIST OF ILLUSTRATIONS (continued)

<u>Figure</u>		<u>Page</u>
66	Schematic diagram of photon scattering and buildup in the atmosphere between auroral form and sensor	137
67a, b	Meridian photometer scans with (a) and without (b) strong isolated arc forms, from PKR 21 Feb 76	138-139
68	All-sky views of the isolated arc over PKR and the arc N of FYU, 12 Mar 75	142
69	Contours of meridian-plane electron density on 12 Mar 75 at Chatanika, AK with column integrals converted to $\lambda 4278$ radiance at FYU and PKR	143
70a, b	Comparison of measured $\lambda 4278$ meridian radiance distribution at FYU (a) and PKR (b) with calculation from Chatanika radar's electron density profiles, 0840 12 Mar 75	144-145
71	Meridian scans in $\lambda 4278$ from Fort Yukon 12 Mar 75	147
72	Column integral of volume energy deposition rate for two primary electron energy spectra	152
73	Zenith angles of DNA617 radar beam and projection from radar of intercept of aircraft radiometer fields with 110 km altitude plane	159
74	Plan view of radar and aircraft field intercepts at 110 km altitude, ICECAP 76	162
75	Operating cycle for aircraft-radar coordination, ICECAP 76	163
76	Example of zenith radiance recordings from the 12-channel aircraft photometer, ICECAP 76	166
77	Example of a zenith radiance plot from one photometer channel, ICECAP 76	167

LIST OF TABLES

<u>Table</u>		<u>Page</u>
1	A18.205-1 Multi-Experiment Rocket Data Reduced/Analyzed (as of Fall 1976)	17
2	Times of Best Overlap of 5.3 μ m and λ 3914 Enhancements - A18.205-1	51
3	Azimuth Angles and Intensities of λ 3914 and 5.3 μ m Excess Radiances, A18.205-1 Upleg	59
4	RAOB Temperatures Over Poker Flat Research Range, ICECAP 75	124
5	Characteristics of Ground-Based Measurements of Auroral Particle Energy Input	133
6	Log of Flights NKC-135 53120, ICECAP 76	155
7	1-VN Camera Operation Times for IC 11 and 15	157
8	Missions Supported by DNA 617 Radar (Preliminary Data)	161
9	Status of ICECAP 76's Aircraft Photometer Data ...	165

SECTION I

REDUCTION OF PHOTOMETER AND RADIOMETER DATA FROM MULTI-EXPERIMENT ROCKET A18.205-1

INTRODUCTION

Presented here are reduced and partially analyzed data from the seven coaligned side-looking photometers and radiometers pointing 80° from the long axis of Black Brant rocket A18.205-1, which was launched on 27 Mar 73 at 0937:45 (about 1/2 hr before local midnight). This was the second in the ICECAP series of multi-instrumented experiments for determining the processes leading to short wavelength infrared chemiluminescence in air bombarded by energetic particles. Reference is made to PhotoMetrics' similar reduction of data from the first "multi" rocket A17.110-3 launched (on 16 Mar 72) in the direction of an isolated auroral arc, Section I of Ref 1. This earlier report describes the procedures we developed for accessing the data from the raw elevation-azimuth angle scans, and provides information on photometer sensitivity and potential sources of error. The radiometric instruments were designed to measure the $N_2^+(0,0)$ First Negative band with head at 3914.4 \AA , which gives a quantitative measure of the column ionization rate in the field of view (Section V); OI forbidden atomic line at 5577.3 \AA ; N_2 Second Positive $(0,2)$ band with head at 3804.9 \AA ; $N^2D - ^4S$ precursor doublet $5198.7\text{-}5200.5 \text{ \AA}$; $N^2P - ^4S$ forbidden line at 3466.4 \AA , also a potential precursor of the emissions from NO molecules; and in the infrared, a section of the NO vibrational fundamental band sequence above $5.3 \mu\text{m}$ and of the NO overtone above $2.7 \mu\text{m}$.

A description of the complete rocket instrument package, which contains information on the radiometer's wavelength sensitivity, fields of view, and calibration is provided in Ref 3. Much of the data from the onboard remote sensing and in situ measuring instruments, and from ground support instruments that provide information on the

auroral ionosphere in which the arc is embedded (including those that measured wind profiles from the transport of AlO molecules produced as a result of a TMA release from supporting rocket A10.216-3) have been reduced and in part analyzed. The information at present readily available is listed in Table 1.

Table 7 of Ref 2 lists the altitude profiles of maximum and geomagnetic-meridian radiances, azimuth angles of these maxima, ratios of peak radiances of important features, halfwidths of their radiance distributions, and related re-plottings of the data on arc emissions presented in this Section. The visible radiations are intended as usual to be largely diagnostic for the infrared radiations excited in the aurora. Spin rate of A18.205-1 was $\sim \frac{2}{3}$ revolutions/sec, which results in about 1 azimuth scan/km when the rocket was near 100 km altitude. In some cases we have subtracted backgrounds observed over azimuths where there was little or no optical aurora to emphasize and clarify relations among the emissions; the procedures we applied will be explained in the text. In addition we have differentiated where practical between the rocket's altitude and altitude(s) at which its sidelooking instrument fields intercept the visible arc.

ARC GEOMETRY

Ground photometry data locating the isolated, stable IBC II-III arc penetrated by A18.205-1 are given in Ref 1. The rocket's trajectory (Fig 1), reproduced from Section II of Ref 1, was such that it crossed the region of arc in which the volume emission rate was equal to about 1/2 its maximum value, at an altitude of ~ 105 km. Before it reached 80 km the rocket was still strongly precessing, so that the instrument elevations for a given azimuth direction varied from spin to spin. Above this altitude it stabilized with axis tilted at $\sim 3^\circ$ zenith angle and azimuth 25° east of geomagnetic south. Thus maximum instrument elevation was nominally 13° at 25° west of geomagnetic north, and minimum was 7° in the southeast (see Fig 23 of Ref 2). Destabilization on downleg began at about 365 sec, 80 km altitude.

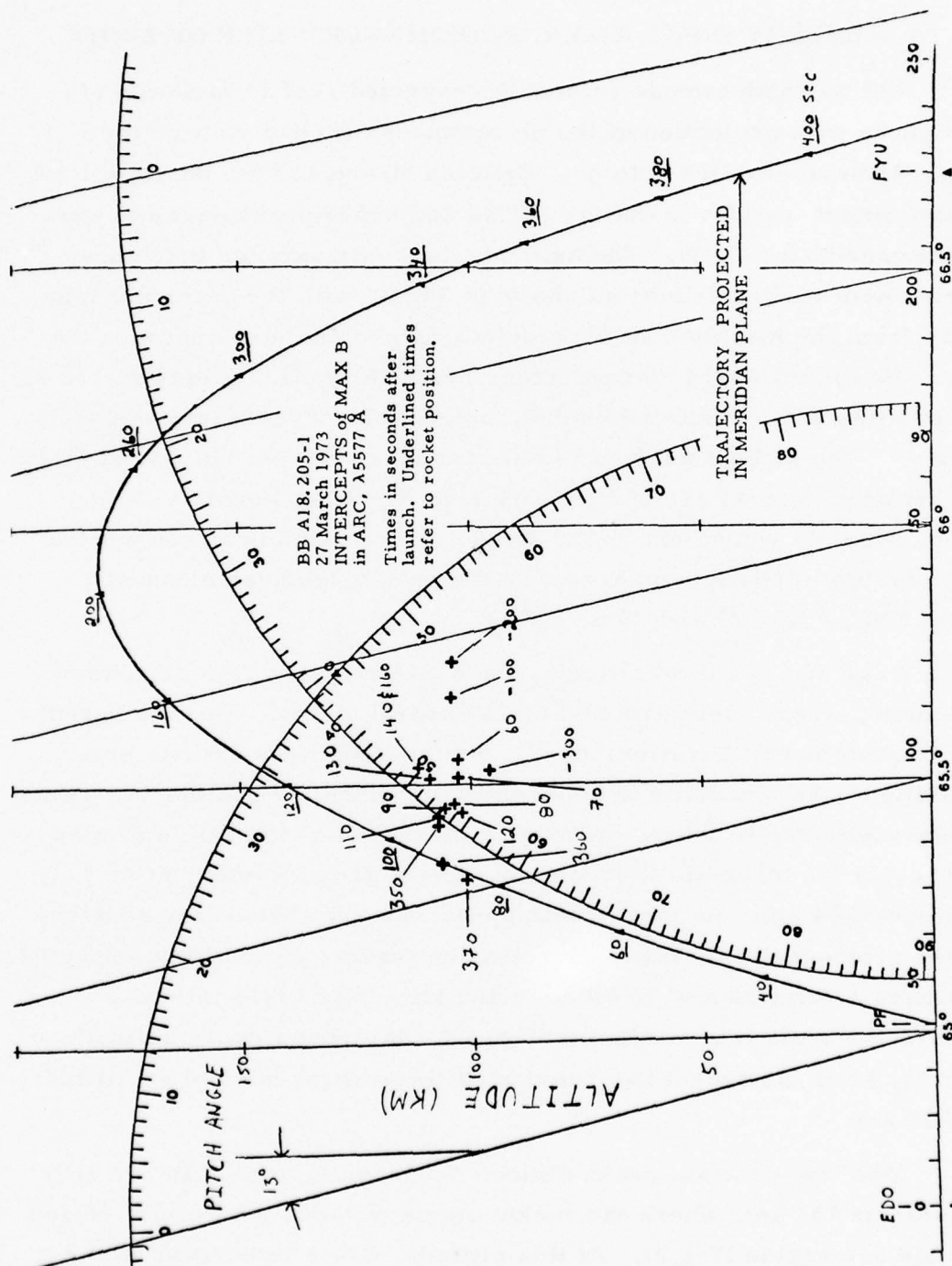
Table 3-1 Multi-Experiment Rocket Data Reduced/
 ized (As of Fall 1976).

<u>Rocket Configuration</u>		
	HAES 3:	Detailed review of instrumentation with some calibration data
<u>Ground Data</u>		
Meridian Photometers	HAES 4:	Lists of reduced records (not printed), Table 3 Altitude and horizontal range of maximum arc emission, Fig's 27 & 28 Maximum arc brightness, Fig. 29 Rocket intercepts on arc from Fig's 27 & 33
Fixed Photometers	HAES 5:	Energy deposition Fig's 1c & 3a
	HAES 5:	Wind drifts in D region, Fig. 8
All Sky Cameras	HAES 4:	Detailed montages from -12 min, Fig's 43 & 44
	HAES 15:	From Chatanika during rocket flight, Fig 64
Magnetometers,	HAES 15:	Plots from instruments at College (FYU data in TR-75-0040)
Radar, Chatanika & Homer	HAES 15:	Chapter 8 gives E- and F-region electron densities, electric fields and temperatures, other parameters derivable from Thomson scatter data
	HAES 5:	Energy deposition, Table 4
Geophysical Background	DNA 3293F:	Energy deposition, Fig. 6
	AFCRL-TR-75-0040 (U of Alaska)	Rocket trajectory, meteorological conditions at all Alaska network stations, solar depression and azimuth, magnetic data including K and D_{ST} indices, ionosonde records. Also sample All-Sky and meridian photometer data.
<u>A10.216-3 Data</u>		
	HAES 17:	Wind profile from photographic images of TMA trail
<u>Rocket Data</u>		
4.3 μ m	HAES 19:	Detailed analysis in terms of CO ₂ - N ₂ ⁺ vibrational luminescence, Section 3.4
Upward spectro-radiometers, particle counters → 5.3 & 2.7 μ m	HAES 6: and HAES 24:	Detailed analysis of data that were available in 1974-75, applying the ARCTIC code for energy deposition and excitation of chemiluminescence and fluorescence
Sidelooking photometers	HAES 6: and HAES 24: HAES 27: HAES 59:	Model applied against very preliminary data points List of data reduced, Table 7 <u>This report:</u> Data are presented, partially analyzed

All-sky photographs of the event (Section II of Ref 1 and also as indicated in Table 1), along with our equibrightness contour plot (Fig 30 of Ref 1) provide a measure of the surface brightness uniformity along the arc as viewed from the ground stations, prior to and during the data taking sequence. The change in the arc's maximum brightness as measured by ground meridian scanning photometers is shown in Fig 29 of Ref 1, and the (small) N-S and vertical movement of its "center" before and during flight is indicated in Figure 28.

Since the rocket approaches and then penetrates the arc on upleg, we have concentrated on this portion of the flight. Indeed, on downleg no arc-associated enhancements of the infrared radiances were detectable.

We would of course expect to see marked changes in the azimuthal dependence of the radiances as the sidelooking instruments enter the heavily dosed region. When the rocket passes through the visible arc, in situ measurements by the various particle counting instruments can be directly coordinated with the radiometry and photometry data, thus providing an "input-output" experiment with extensive plasma diagnostics. Such analyses have previously been done using the data from the zenith-pointing radiometers, in Ref's 4 and 5; the information contributed by the sidelooking instruments, however, has not been quantitatively applied. A major conclusion in Ref 5's analysis of the data from the upward looking radiometer is, that the primary sources of the observed $5.3\mu\text{m}$ radiation intensity are the atom interchange reaction $\text{NO} + \text{O}' \rightarrow \text{NO}' + \text{O}$ and earthshine scattering from ambient NO molecules. (We pointed out the importance of these processes in relatively "quiet" auroral conditions in Section II of Ref 2.) The contribution of the chemiluminescent $\text{N} + \text{O}_2$ reactions, on the other hand, appeared to be small. As we will see, $5.3\mu\text{m}$ horizontal radiances associated with the visible arc provide further information, and even a different viewpoint, about this matter.



DATA - ENERGY INPUT ALONG RADIOMETERS' LINE OF SIGHT

The azimuth sweeps showed the expected (Ref 1) variation of radiances with projection of the photometers' fields of view on the E-W aligned aurora-excited volume. Between 80 and 135 km on upleg, limb enhancement results in defined $\lambda 3914$ and $\lambda 5577$ peaks east and west of the meridian (Fig 2). The azimuth angle of maximum brightness varies with rocket altitude as shown in Fig 3, with the peaks shifting away from the meridian as the sidelooking photometers approach the arc. Maximum $\lambda 3914$ column intensities after stabilization are 190 kR (west limb) and 198 kR (east limb), before the rocket enters the arc (Fig 4). The highest surface radiance measured from the rocket S of the isolated auroral arc of 1972 was 7 kR N_2^+ First Negative (1, 2) band, which is equivalent to 157 kR (0, 0). Thus the two arcs were of comparable intensity (compare also the peak brightness measured from FYU, Fig's 25 and 29 of Ref 1).

Near 80 km rocket altitude, the $\lambda 3914$ radiance is 6 kR toward the south, where there are no visible auroral forms. This background (at 7° photometer elevation) may be due to some weak drizzle precipitation. The intensity is about the same when the photometer points geomagnetic north, where the axis of its (13° elevation) field of view intercepts the magnetic field line through the arc's "center" at an altitude of 84 km. As the rocket approaches arc altitude the radiance in the geomagnetic meridian direction increases, as would be expected, reaching a maximum of 75 kR near 100 km. The $\lambda 3914$ intensity toward the south is a maximum of 20 kR, flat over a broad azimuth region, after the rocket has penetrated the auroral form at an altitude of 103 km.

Two low-contrast peaks almost 90° from the meridian can still be seen at 133 km, where the rocket starts to leave the heavily dosed visible-arc region (Fig 2). At this altitude, $\lambda 3914$ intensities to the north and south are again each ~ 6 kR. The radiances continue to

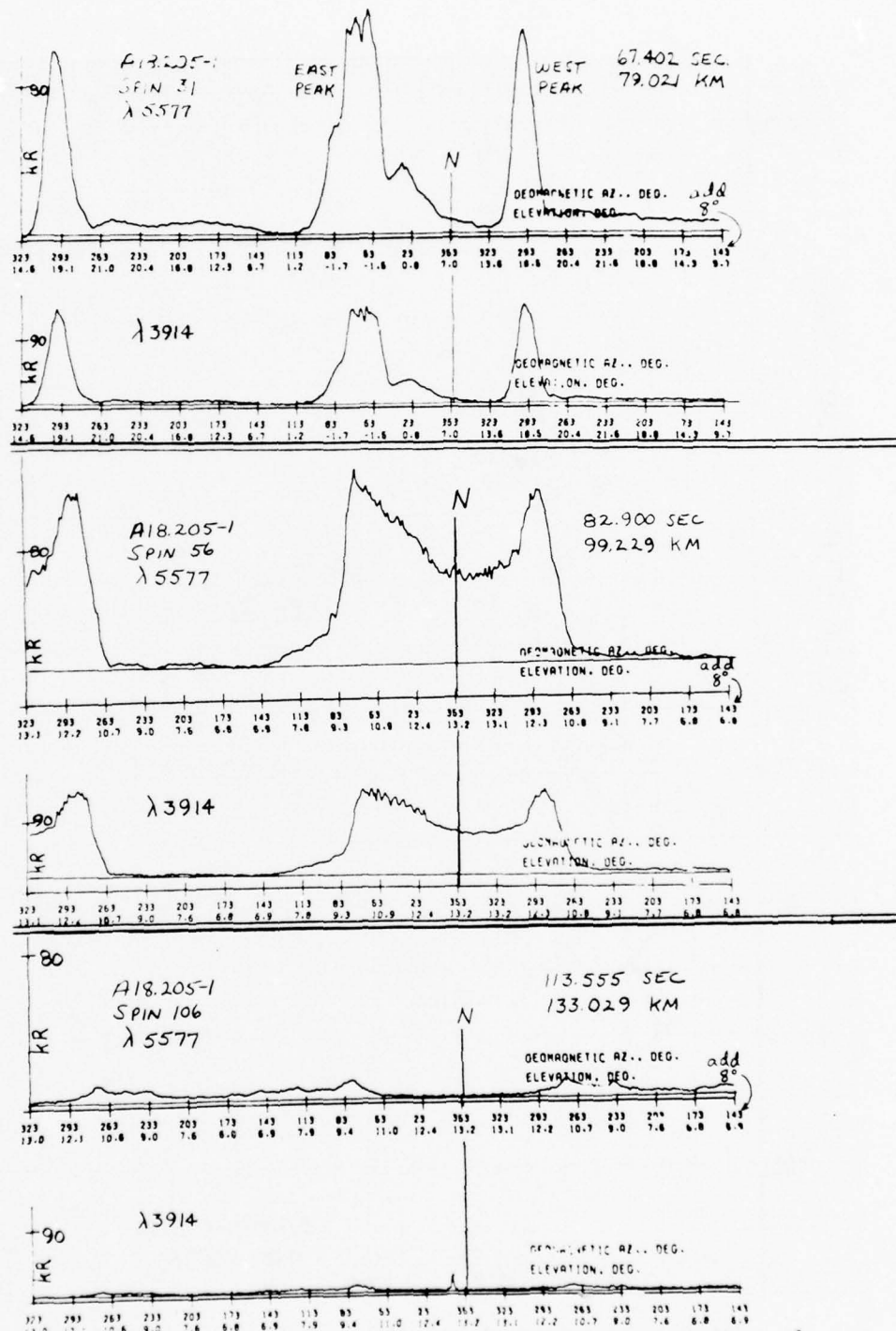


Figure 2. Three elevation-azimuth spin cycles on upleg of A18.205-1 showing the changing $\lambda 5577$ and $\lambda 3914$ angular distributions with rocket altitude. Compare Fig 35.

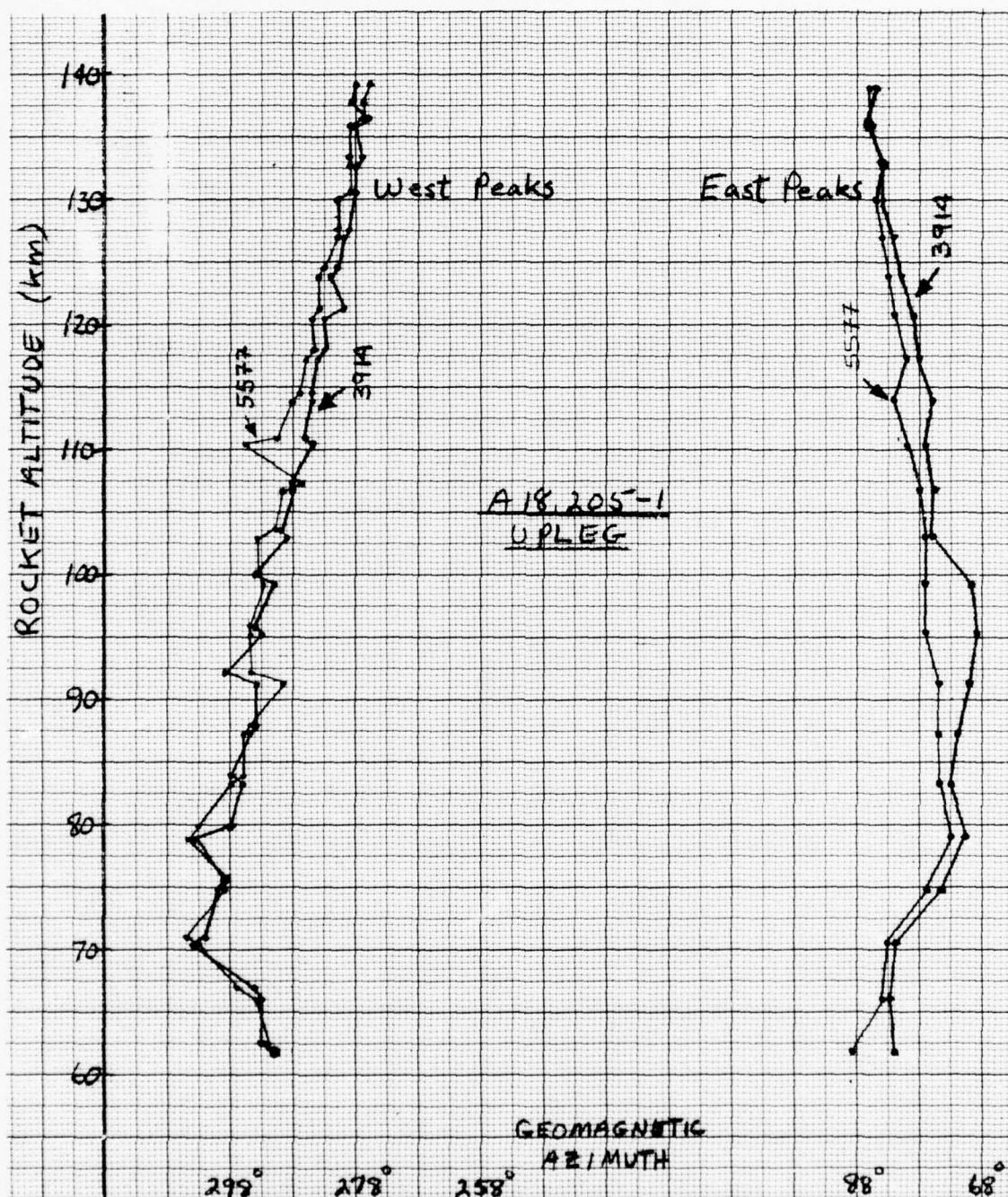


Figure 3. Altitude profiles of azimuths of $\lambda 5577$ and $\lambda 3914$ east and west peak intensities, A18.205-1 upleg.

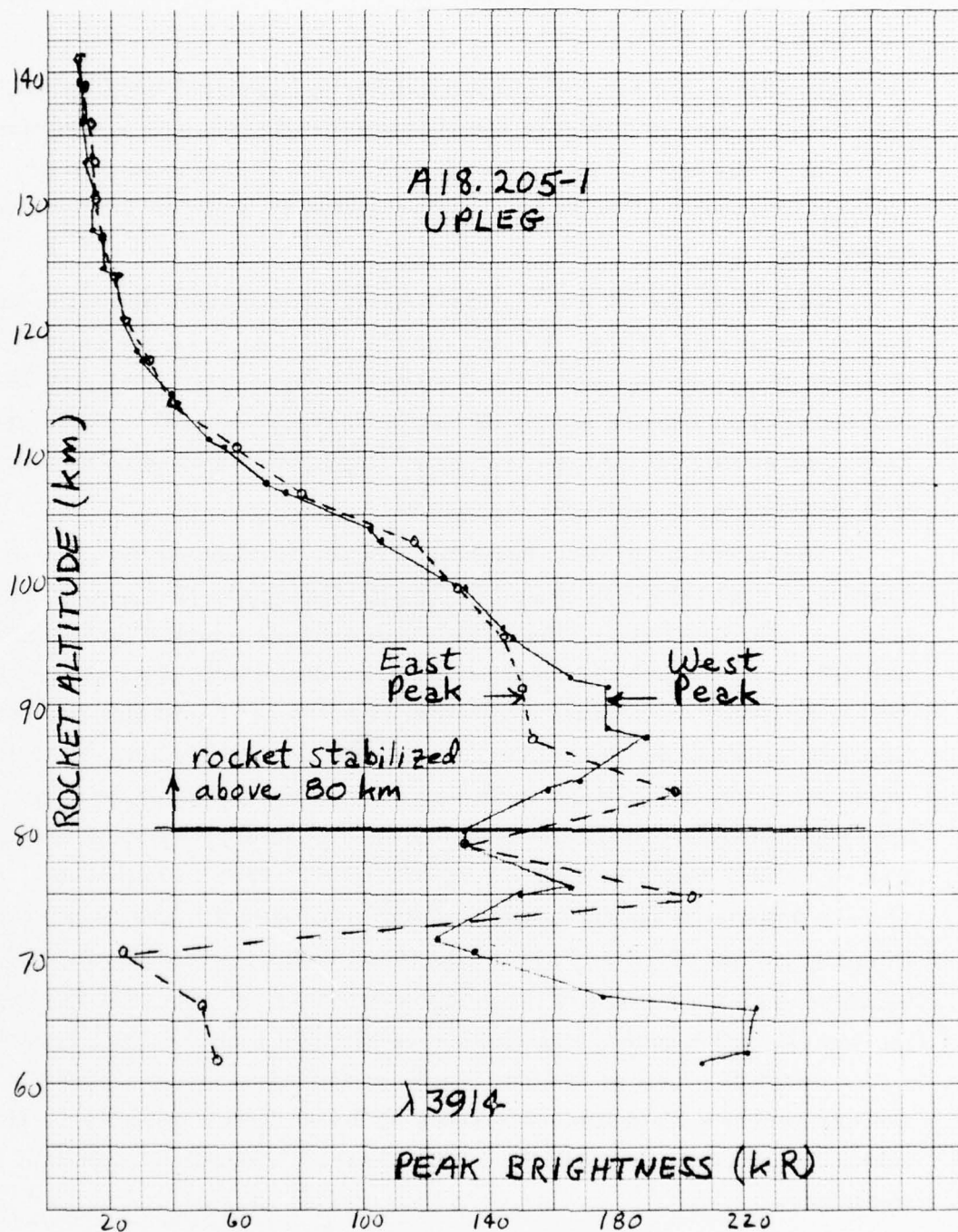


Figure 4. Altitude profiles of the $\lambda 3914$ east and west peak intensities with backgrounds included, A18.205-1 upleg.

decrease above 133 km, at 153 km becoming a general broad glow, 5 kR toward the south (where the photometer elevation is a minimum) and 3 kR to the north. At apogee (182 km) the radiance is nearly uniform at about 3 kR with no clearly detectable azimuth or elevation variation.

Data from the OI $\lambda 5577$ side-looking photometer follow the same general trends as $\lambda 3914$. We have made no effort here to compare in detail these two auroral features for the purpose of clarifying $\lambda 5577$ excitation-deexcitation mechanisms, but have presented altitude profiles and some surface brightness ratios to improve diagnosis of the aurora that is exciting the infrared radiation.

The azimuths of peak brightness of the two emissions correlate closely, with $\lambda 3914$ showing some small tendency to lie farther east (Fig 3). Angular half widths of the limb enhancements (Fig 5) indicate only small differences in surface radiance distributions as viewed from rocket altitude. Maximum half-width is 50° (east limb) and 70° (west limb) at ~ 100 km, as the rocket nears the main arc region. Peak limb intensities (Fig 6) of OI green line are less than $N_2^+(0,0)$, with no apparent difference in altitude at which these radiance maxima occur. The two $\lambda 5577$ peaks are similar to the $\lambda 3914$ peaks in that they remain detectable on the azimuth plots up to ~ 135 km and have mean intensity ratios close to 0.96 (background to the S subtracted). $\lambda 5577$ brightness in the direction of the geomagnetic meridian (Fig 7) also increases as the rocket approaches co-altitude with the arc, reaching a maximum of 63 kR at 104 km intercept altitude. Above 130 km, the arc center's field lines are south of the rocket; measured meridian intensity then drops rapidly to 3 kR, where it holds about constant to apogee.

The ratio of OI green line/ N_2^+ First Negative (0,0) band was calculated for both maxima (Fig 8a), neglecting the small offsets in azimuth indicated in Fig 3 and making no correction for background.

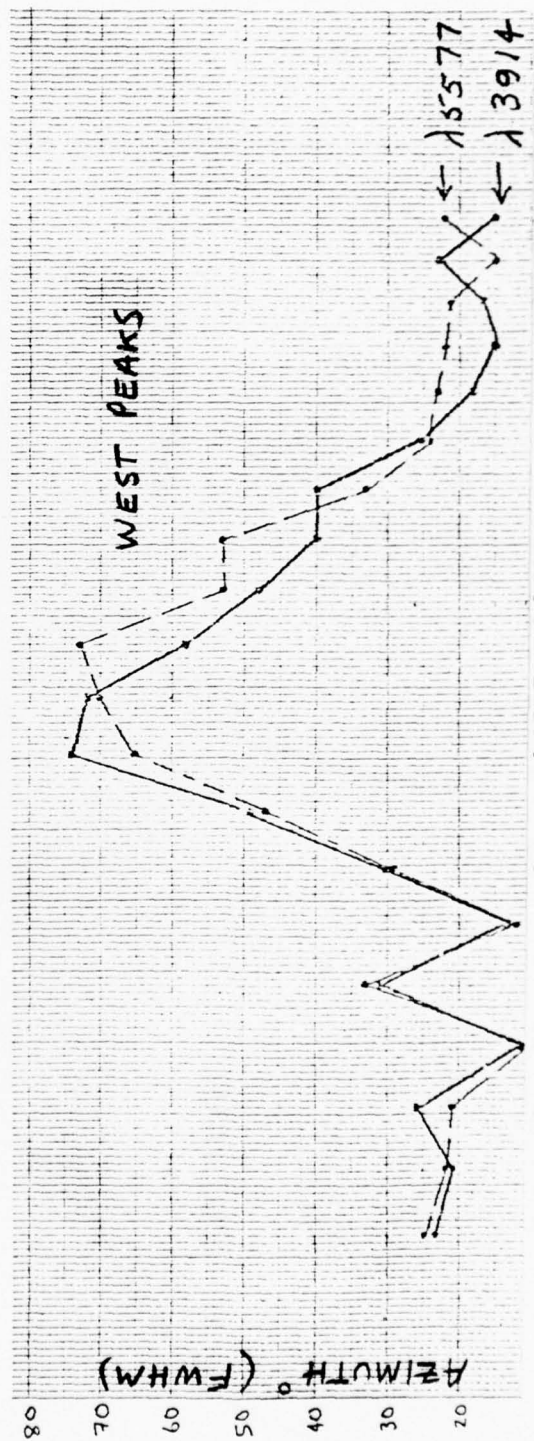
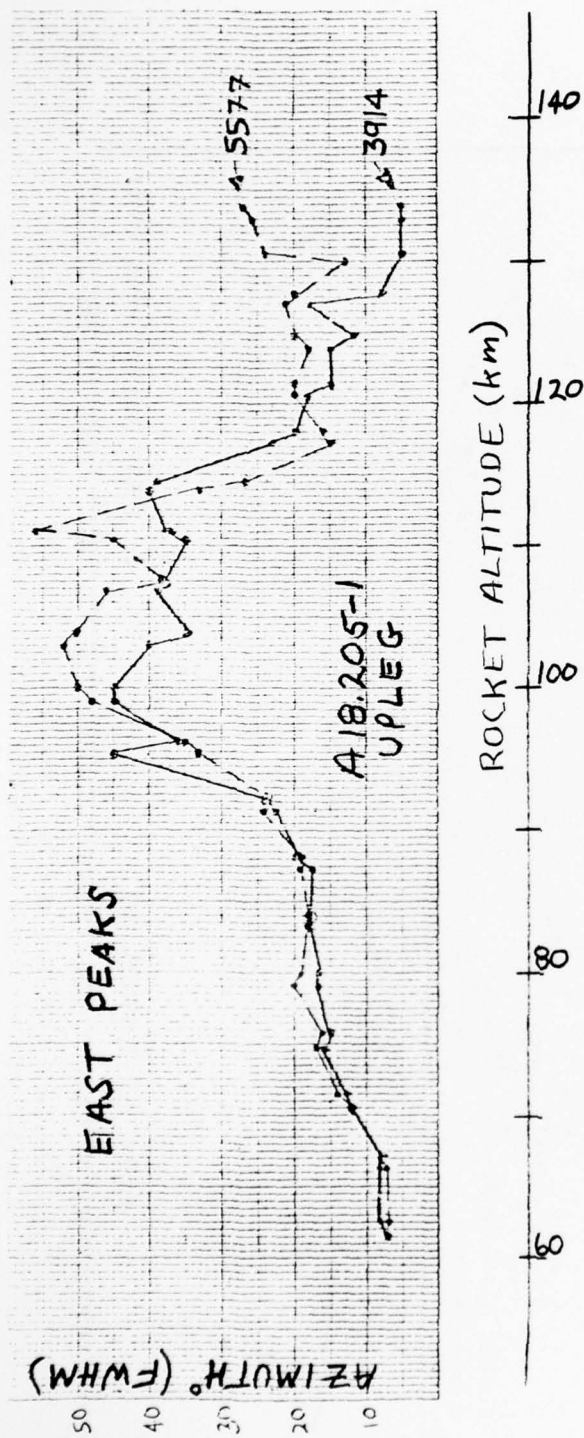


Figure 5. Altitude profiles of $\lambda 5577$ and $\lambda 3914$ east and west limb halfwidths with mean baseline backgrounds in Fig 2 subtracted, A18.205-1 upleg.

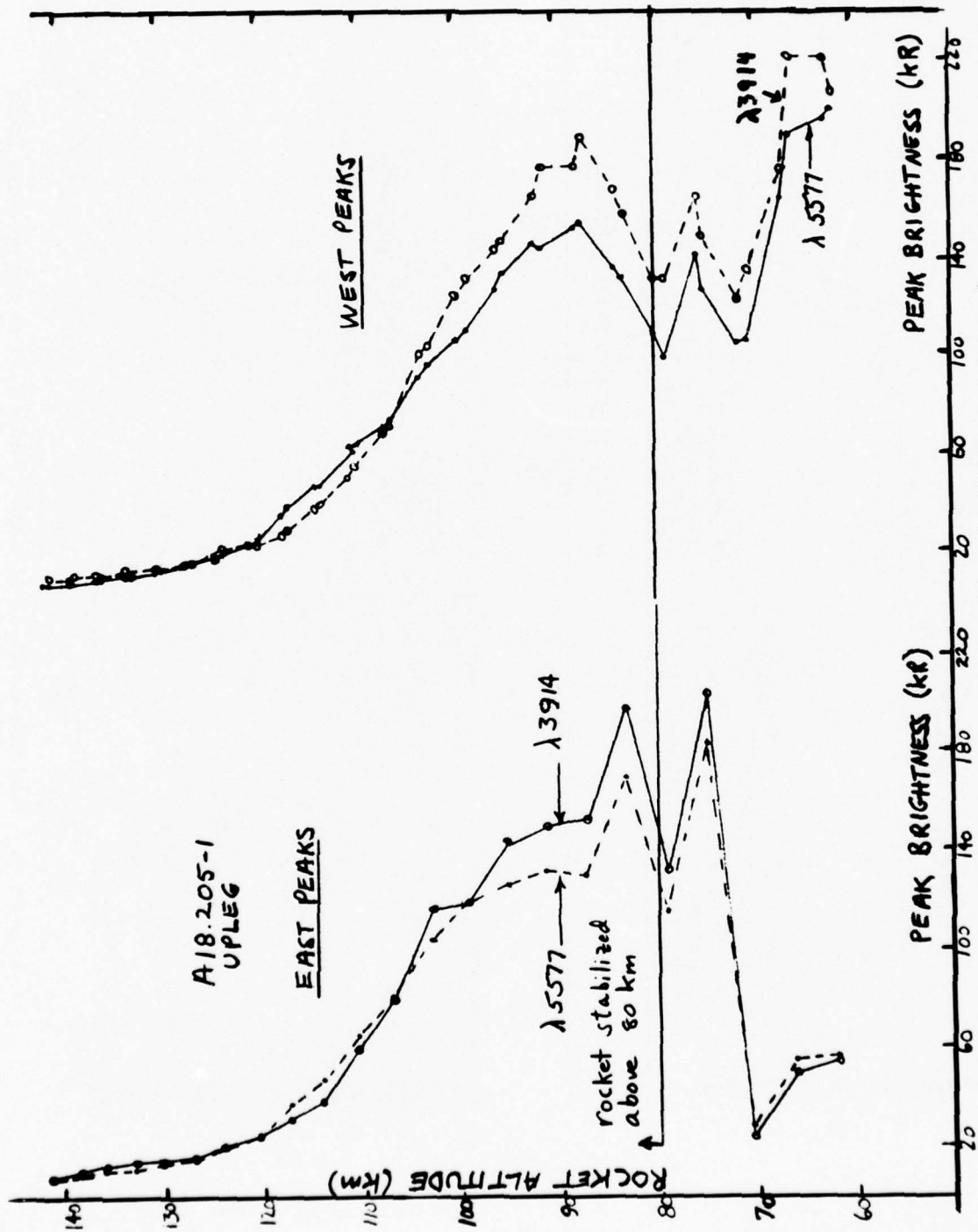


Figure 6. Altitude profiles of $\lambda 5577$ and $\lambda 3914$ east (a) and west (b) peak limb intensities with backgrounds included, A18.205-1 upleg.

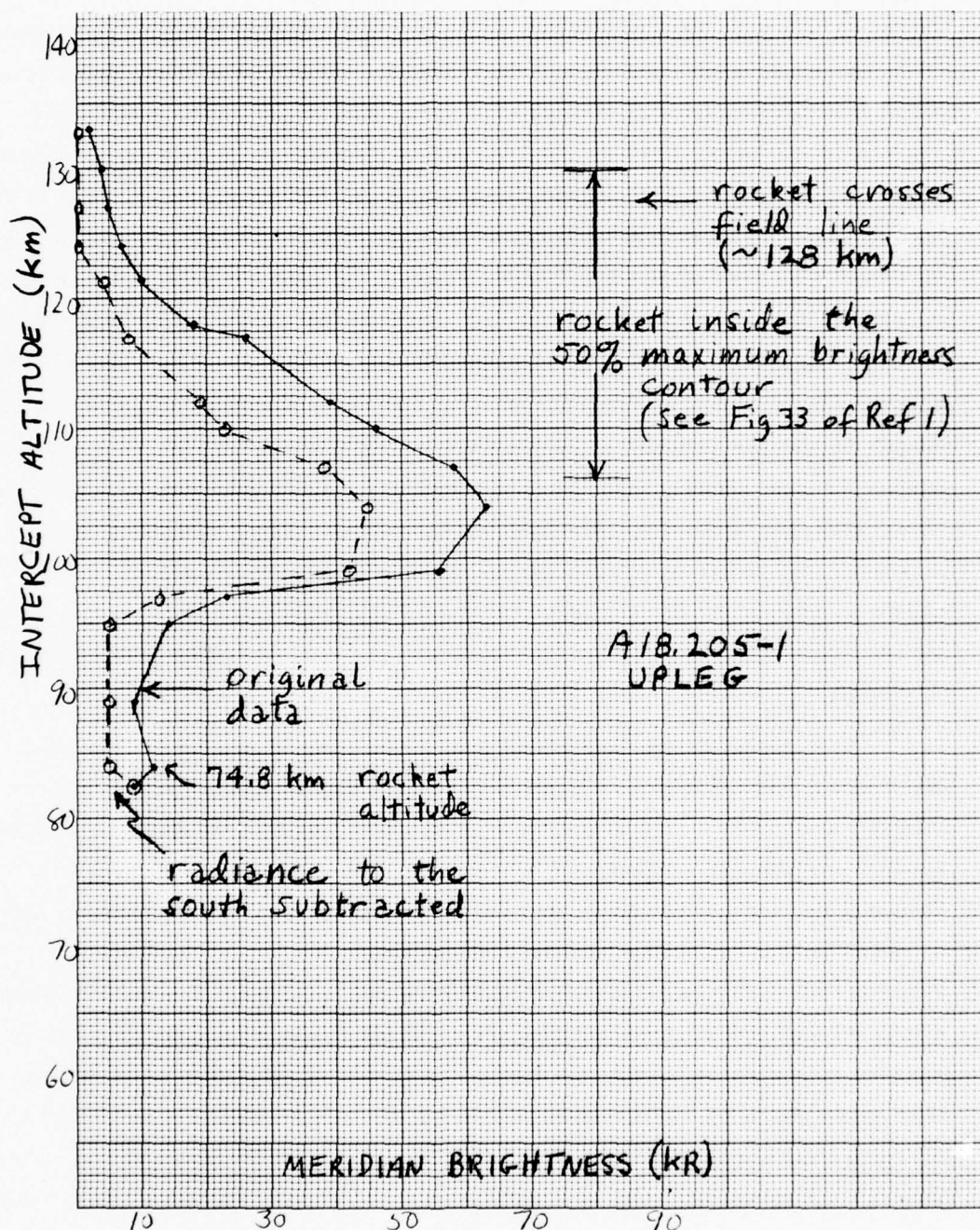


Figure 7. Intercept altitude profile of $\lambda 5577$ meridian brightness, A18.205-1 upleg.

Between 75 and 100 km rocket altitude, the ratio remains fairly constant at 0.85 (west limb) and 0.88 (east limb). Maximum limb radiances were reached at 85 km rocket altitude. Above 100 km, where the rocket is entering the arc, it increases rapidly to 1.2; then it starts to decrease at 115 km, again reaching 0.85 km when the rocket is N of the arc. The small difference between photometer elevation angles in the directions of the two peaks results in only a small difference in effective intercept altitude (our procedure for calculating intercepts will be explained further in the following section). When the radiances toward the south are subtracted (Fig 8b) the peak ratios again remain about the same between 75 and 100 km rocket altitude (0.84 west limb and 0.88 east limb), and increase rapidly above 105 km. With this "correction" procedure, however, falloff at higher altitudes is less certain. As noted previously, we shall not consider further here the issue of relative effective fluorescence-chemiluminescence efficiencies, or possible spatial differences between radiances in the two features (Ref 6).

The photometer designed to measure the N_2 Second Positive (0,2) band near 3800 Å showed limb peaks not substantially different from $\lambda\lambda$ 3914 and 5577. No detailed reduction of these data is included here, as the radiance distributions at present have somewhat secondary importance in interpreting infrared chemiluminescent radiation from aurora-excited air (the intensities do relate to N_2 triplet-state fluorescence at near-infrared wavelengths, and provide information about where the secondary electrons deposit their energy). Figure 9 summarizes some of the major features of the λ 3800 arc radiation. The peak ratio of radiance to λ 5577 is closely 0.14 between 75 and 100 km (backgrounds included), where maximum λ 3800 column intensity is ~ 20 kR in each peak. Azimuths of the Second Positive limb peaks lie very close to the OI peaks, and as expected the measured intensity toward geomagnetic north increases as the rocket approaches the arc.

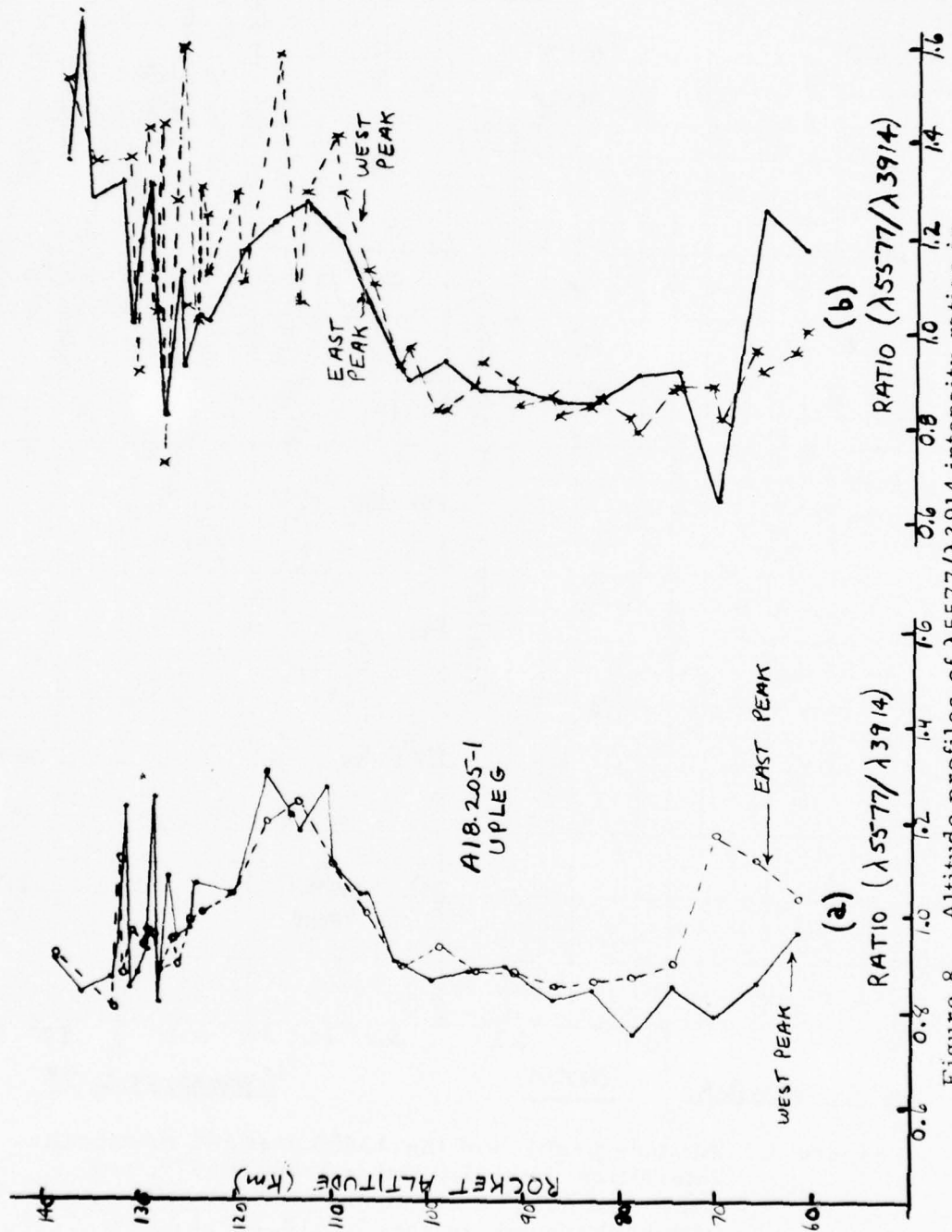


Figure 8. Altitude profiles of $\lambda 5577/\lambda 3914$ intensity ratios in both peaks, with background included (a) and radiance toward the S subtracted (b), A18.205-1 upleg.

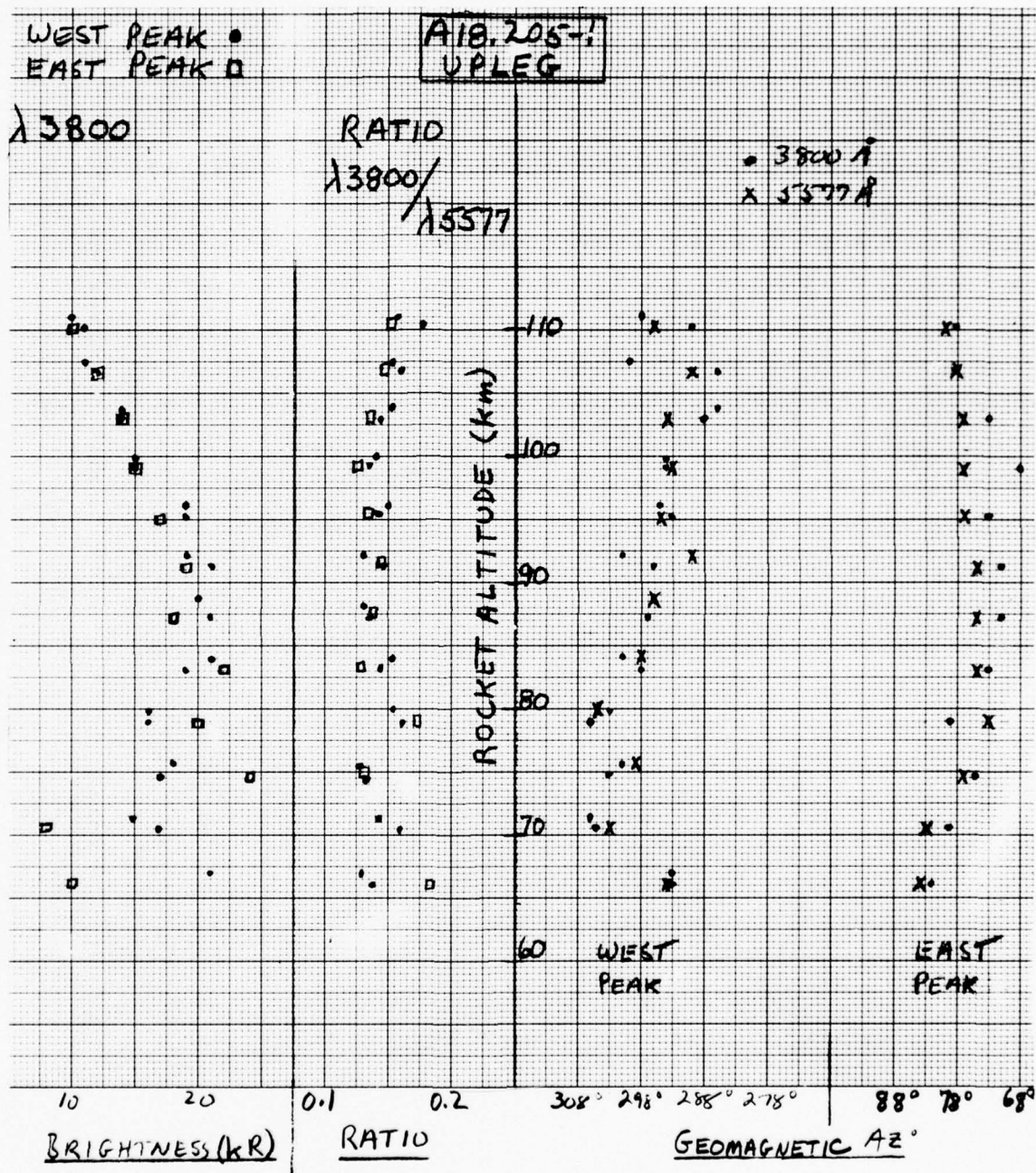


Figure 9. Altitude profiles of the $\lambda 3800$ east and west peak intensities, intensity ratios $\lambda 3800 / \lambda 5577$, and $\lambda 3800$ and $\lambda 5577$ azimuths of peak intensities, with backgrounds included, A18.205-1 upleg.

NI PRECURSOR FORBIDDEN LINES

Typical N^2D-^4S photometer azimuth scans, which show a radiance pattern generally following the $\lambda 3914$ fluorescence superposed on a moderately noisy background, are in Fig 10. Peaks east and west of the meridian persist until at least 130 km, with nearly equal maximum intensities. These peaks appear somewhat broader than those in $\lambda 3914$ or $\lambda 5577$, as was also observed from the 1972 multi rocket (see Fig 5 of Ref 1). The maximum column intensity of 475 R above the flat background south of the arc remains reasonably constant until the rocket enters the arc near 100 km, after which it drops rapidly to 170 R (Fig 11). These $\lambda 5199$ radiances are somewhat less than those observed in the 1972 experiment.

When the photometer points south of the arc, where its elevation angle is near 7° , $\lambda 5199$ intensity is about 90 R. This relatively flat "background" persists at all rocket altitudes, increasing only slightly to ~ 110 R at 103 km, and decreasing thereafter. It in fact remains lower throughout upleg than the radiance in the geomagnetic meridian at 13° instrument elevation angle. We subtracted the mean radiance toward the south to generate the $\lambda 5199$ altitude profile in Fig 11.

Azimuths of the N^2D peaks (Fig's 11 and 12) generally follow those of $\lambda \lambda 3914$ and 5577, as they did in the 1972 multi rocket experiment. This observation again suggests that leakage of "prompt" radiations may be contributing significantly to the doublet photometer's radiance signal. The ratio $N^2D/OI \lambda 5577$ in the east-limb peaks (Fig 13) is nearly constant at 4×10^{-3} between 75 and 100 km. Similarly, the west peak ratio to $\lambda 3914$ fluorescence increases slowly toward 4×10^{-3} at 103 km rocket altitude.

At 100 km, the lifetime of N^2D atoms is controlled by their reaction with O_2 , which has a quenching rate coefficient of $\sim 5 \times 10^{-12} \text{ cm}^3/\text{s}$. Taking $[O_2] = 1.5 \times 10^{-12} / \text{cm}^3$, 22 ion pairs per $\lambda 3914$ photon (see Section V), and 1 N^2D atom with radiative lifetime

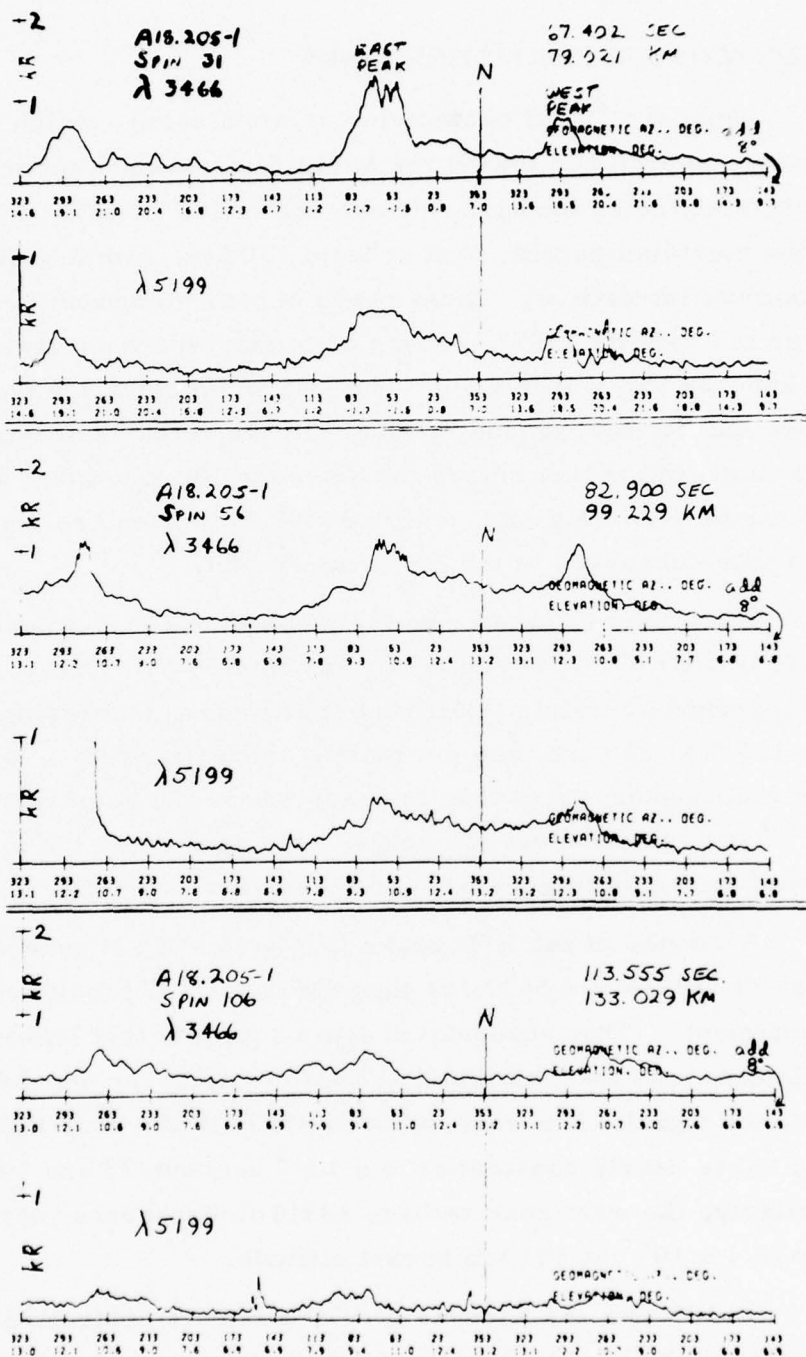


Figure 10. Three elevation-azimuth spin cycles on upleg of A18.205-1 showing the changing $\lambda 5199$ and $\lambda 3466$ angular distributions with altitude, A18.205-1.

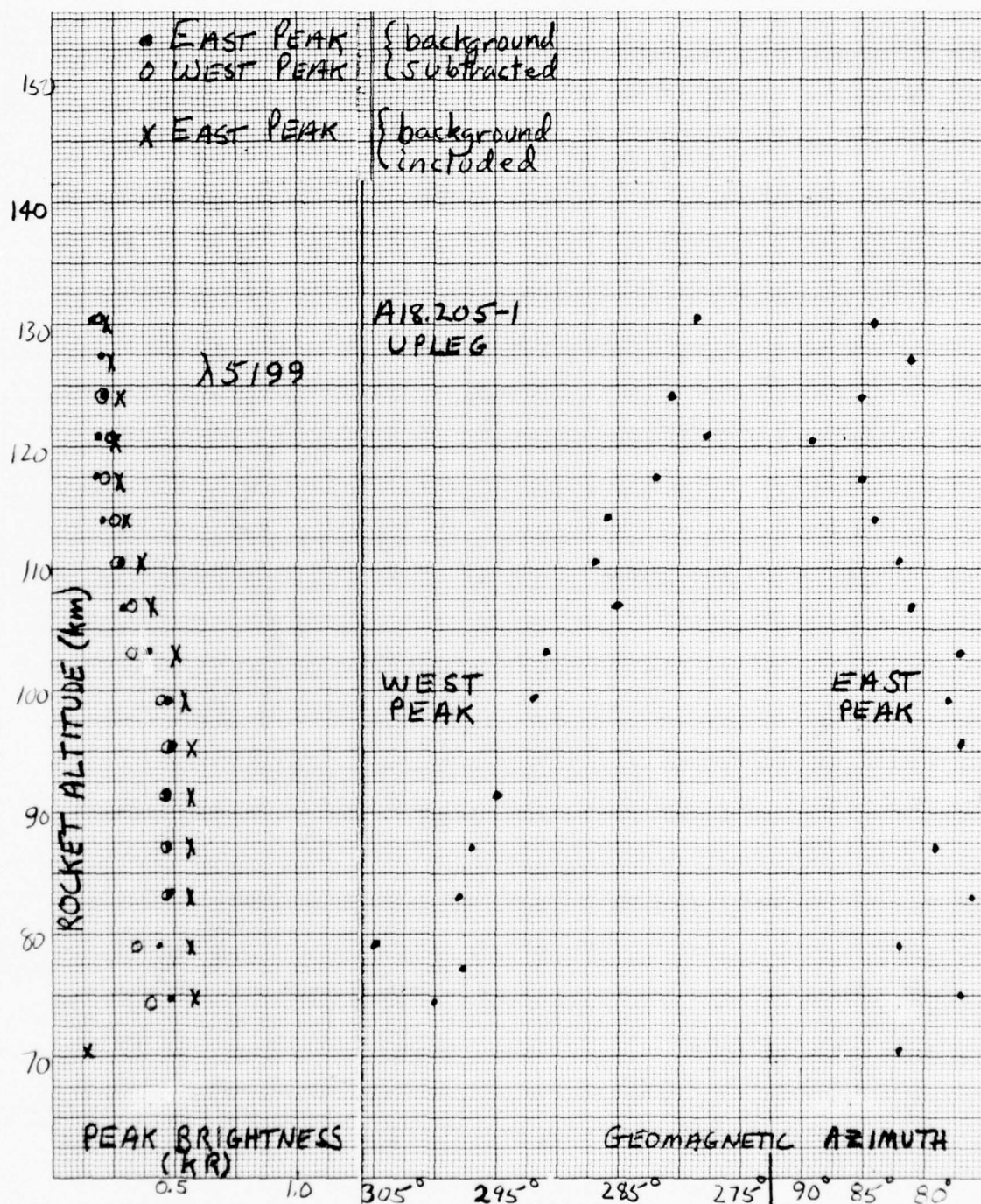


Figure 11. Altitude profiles of the $\lambda 5199$ east and west peak intensities and azimuth angles of peaks, A18.205-1 upleg. The background subtracted is the average radiance over the geomagnetic azimuth range 165° to 195° .

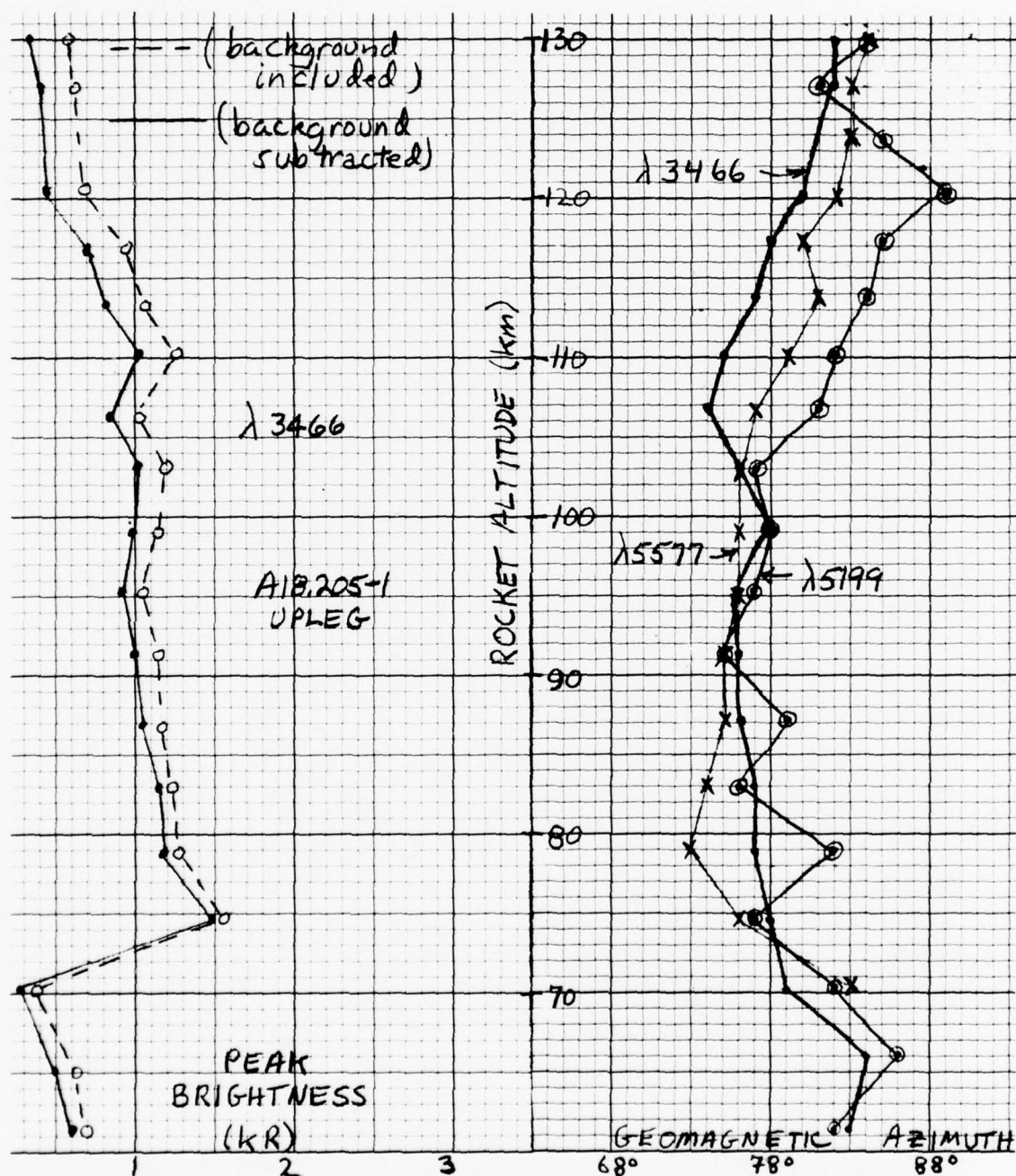


Figure 12. Altitude profiles of the $\lambda 3466$ east peak, and azimuth angles of the $\lambda 3466$, $\lambda 5577$, and $\lambda 5199$ east peaks, A18.205-1 upleg. Background defined as in Fig 11.

10^5 sec excited per ion pair, we find a volume emission rate ratio N^2D/N_2^+ (0,0) of 3×10^{-5} . Measured radiance ratios (Fig's 13 and 14) are two orders of magnitude higher. This large discrepancy, which was also observed in 1972, is again probably due to leakage in the photometer (Refer to Appendix 15 of Ref 1). It casts serious doubt on the accuracy of the $\lambda 5199$ radiance data in the presence of strong auroral fluorescence lines and bands.

The location of the limb maxima in the N^2P-^4S forbidden line also correlates fairly well with $\lambda\lambda 3914$ and 5577 , as Fig 12 indicates. The small differences in azimuth are probably due to imprecision in locating the maxima from scan data such as those shown in Fig 10. The $\lambda 3466$ spatial structure, however, more closely resembles that of $\lambda 5199$ in that the peaks are broad and the data somewhat noisy (Fig 10). Brightness to the south is 110 R up to 100 km rocket altitude, where it begins to increase and reaches about 225 R at 120 km. As expected, the meridian intensity also increases with altitude up to about 100 km, where it reaches a maximum of 550 R. At higher altitudes, radiances toward both north and south decrease, and at apogee their intensities are 170 R and 125 R respectively. As we noted, $\lambda 5199$ was also brighter in the north than south at the higher rocket altitudes.

Peak $\lambda 3466$ column intensity in the east limb, with background to the south both included and subtracted, is shown as a function of rocket altitude in Fig 12. The maximum limb radiance holds nearly constant at 1.15 kR (background included) between 80 and 100 km, and then gradually falls off to ~ 0.59 kR between 110 and 130 km.

The east peak ratio $\lambda 3466/\lambda 5577$ is minimum near 8.5×10^{-3} between 75 and 95 km rocket altitude, and then increases fivefold by 130 km (Fig 13). The similar $\lambda 3466/\lambda 3914$ ratio (not shown) is 7.3×10^{-3} up to 95 km. The theoretical ratio N^2P/N_2^+ First Negative (0,0), taken with the same rate coefficient for quenching on O_2 as N^2D 's, and $8/100$ N^2P atom (Ref 7) with radiative lifetime of 12 sec excited per ion pair, would be about 20×10^{-3} at 100 km altitude,

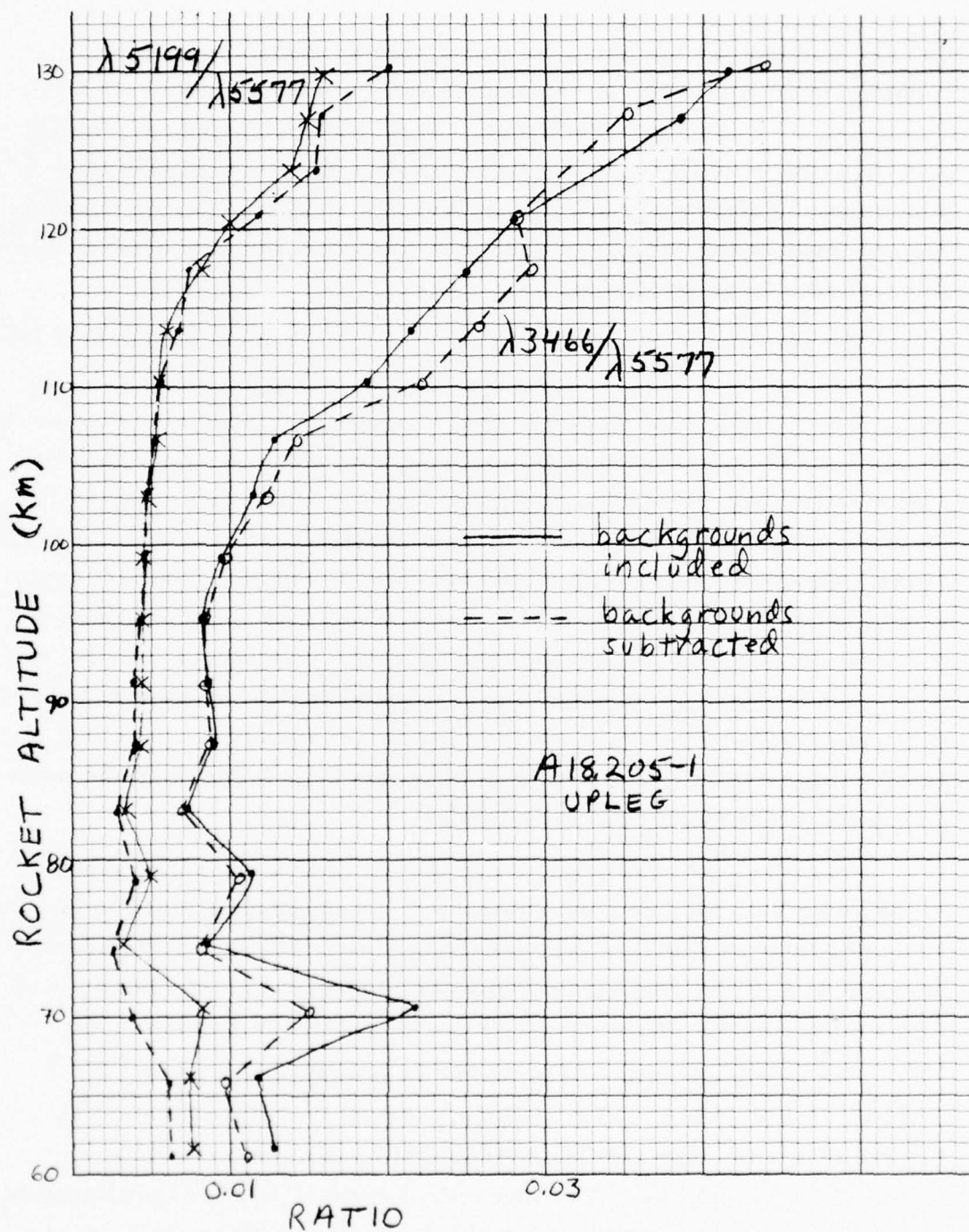


Figure 13. Altitude profiles of $\lambda 5199/\lambda 5577$ and $\lambda 3466/\lambda 5577$ intensity ratios, A18.205-1 upleg. $\lambda 5199$ and 3466 backgrounds defined as in Fig 11, $\lambda 5577$ backgrounds as in Fig 5.

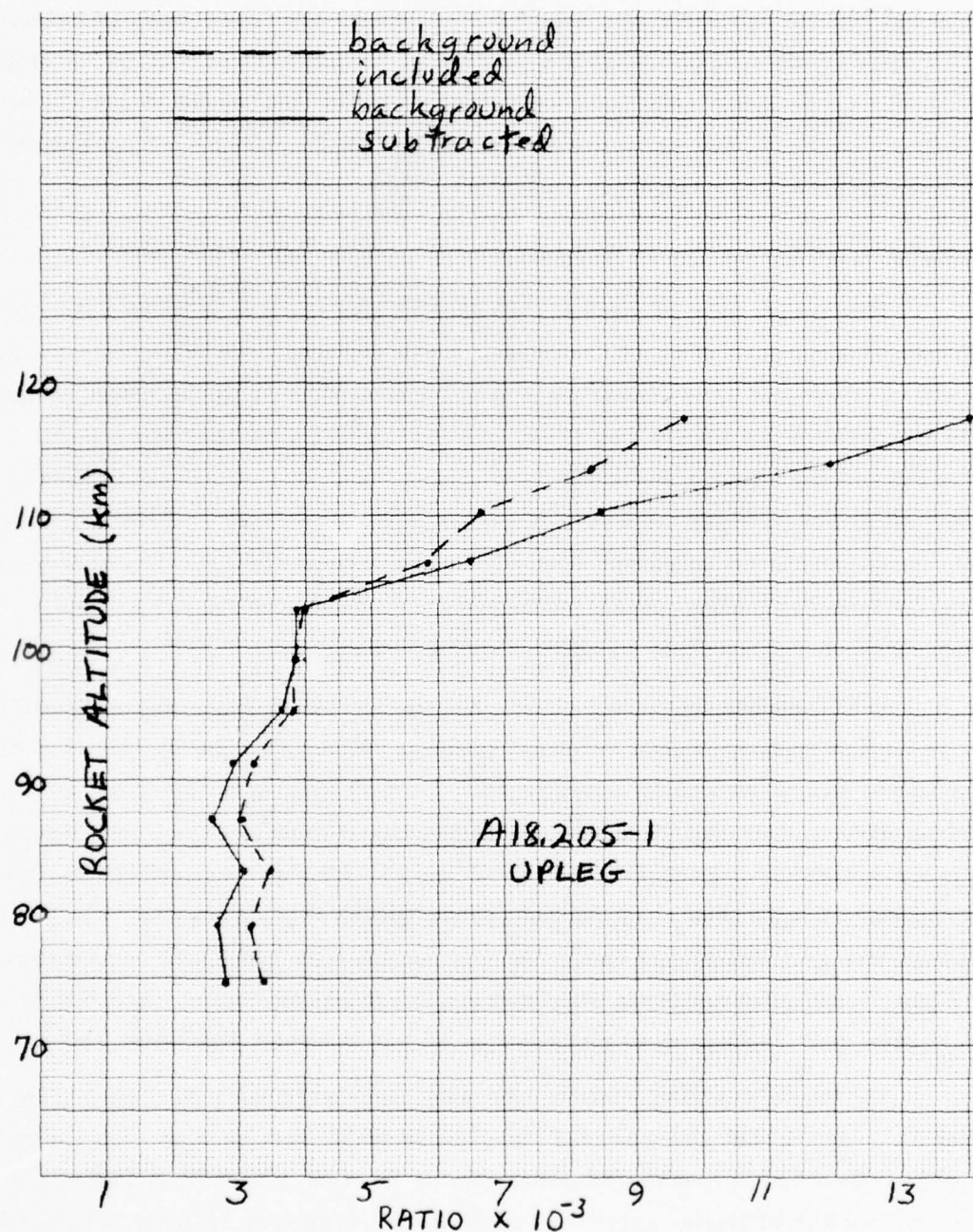


Figure 14. Altitude profiles of west peak $\lambda 5199/\lambda 3914$ intensity ratios, A18.205-1 upleg. Backgrounds defined as in Fig 13.

8×10^{-3} at 93 km altitude, and 3×10^{-3} at 85 km intercept altitude. The differently-shaped altitude profile of the measured ratios, coupled with the close geometric correspondence to $\lambda 3914$, again suggests some leakage in the $\lambda 3466$ photometer (refer to the discussion of potentially-overlapping aurora features in Ref 1).

VISIBLE AURORA ON DOWNLEG

The trajectory of rocket A18.205-1 left the arc's E-W axis more than 130 km south (Fig 1), increasing the projection of the instruments' field of view and thus lowering spatial resolution of the excited volume. Its brightness as measured from ground stations by this time had decreased by about a factor 2 from upleg, and was decreasing further beyond about 315 sec or 140 km rocket altitude (Fig 29 of Ref 1). As no arc-associated infrared emission was detectable, we discuss downleg data only briefly, principally toward understanding the angular distributions of surface brightness to be expected.

$\lambda 5577$ radiance distribution follows $\lambda 3914$ closely enough to allow it to define auroral input for this review. Four representative downleg radiance scans are shown in Fig 15. By 150 km, a broad glow of ~ 3 kR OI extends from 100° to 255° geomagnetic azimuth, where the photometer's elevation goes from 9° to 7° to 11° (not shown). The southward maximum brightness then increases as the rocket descends, the peak taking the general shape indicated by the scan at $110\frac{1}{2}$ km. At about 97 km, limb enhancement starts from a broad flat peak. At 96 km, the radiance had remained very close to 50 kR between 148° and 207° .

All these downleg maximums and their azimuths are shown in Fig 16 (recall that the auroral precipitation is decreasing with increasing time). The $\lambda 5577$ peaks maximize at 61 kR (SE) and 57 kR (SW) at 92 km rocket altitude; intercept altitude is of course higher, although it is lowered measurably by earth curvature. The large increase to 104 kR at 71 km in a narrowed SW peak is probably the westward surge feature visible in the PKR and EDO All-sky photographs (Fig's 43 and 44 of Ref 1). Otherwise, altitude-azimuth behavior of the fluorescence

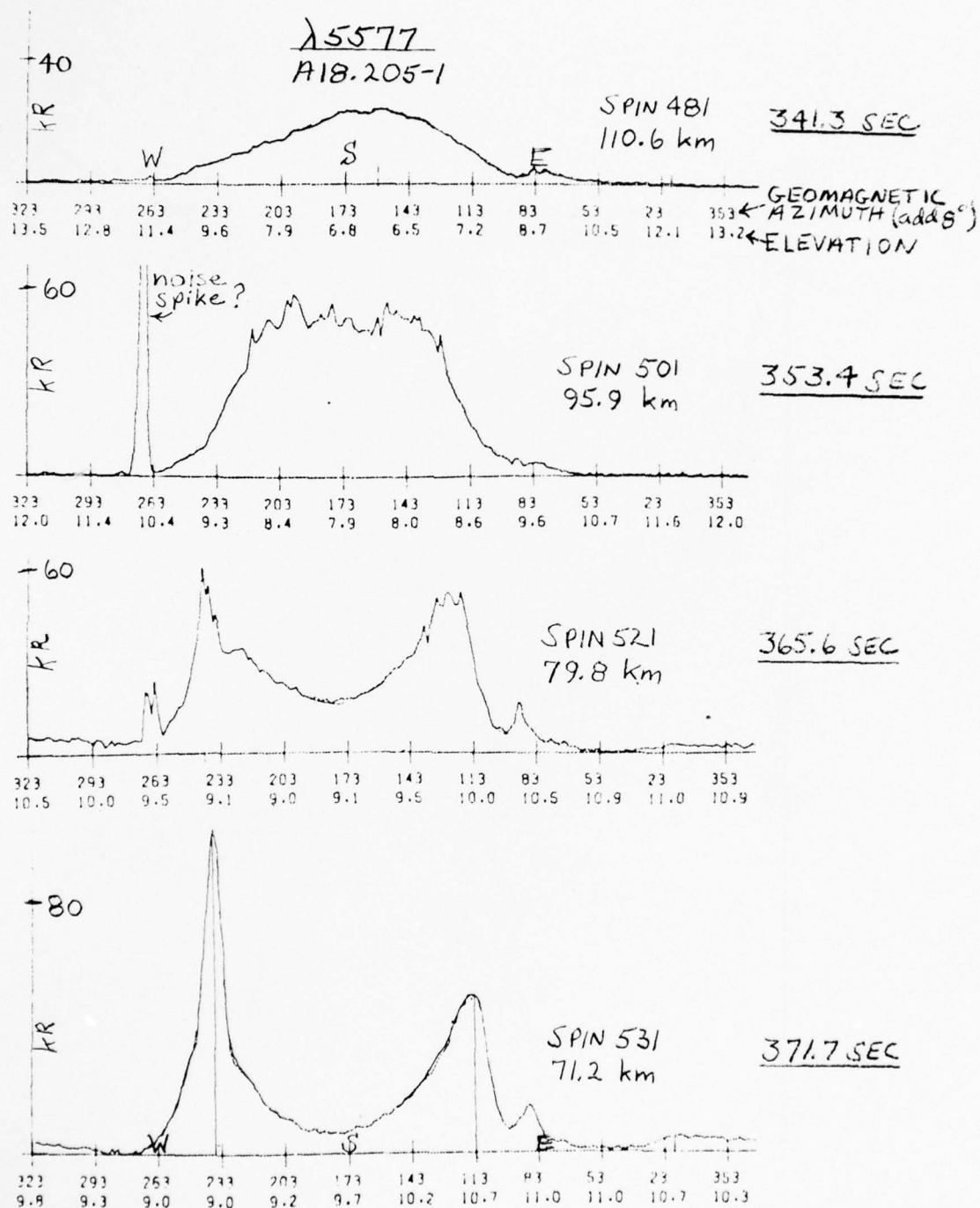


Figure 15. Four representative $\lambda 5577$ spin cycles on downleg of A18.205-1.

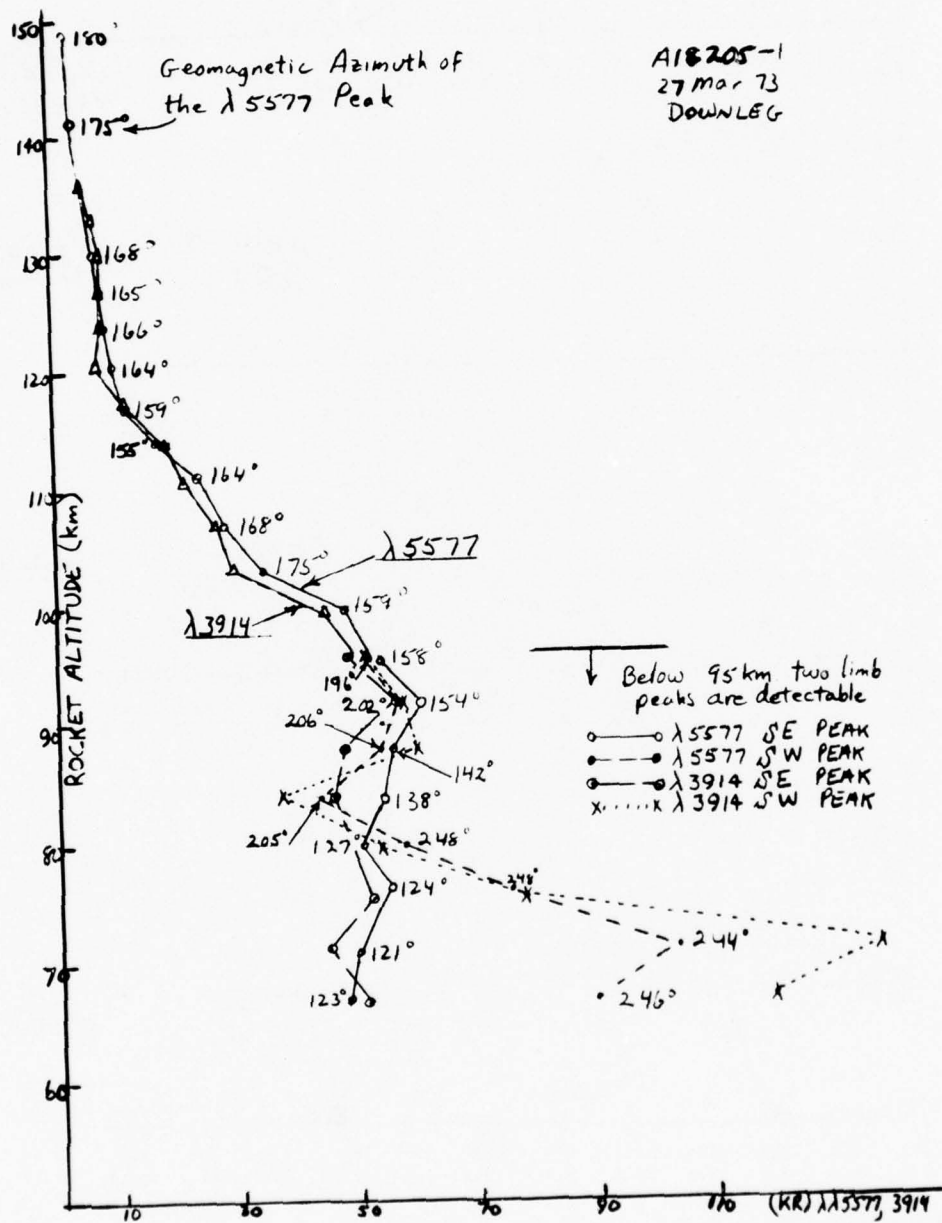


Figure 16. Altitude profiles of $\lambda 5577$ and $\lambda 3914$ peak intensities with backgrounds included, downleg A18.205-1.

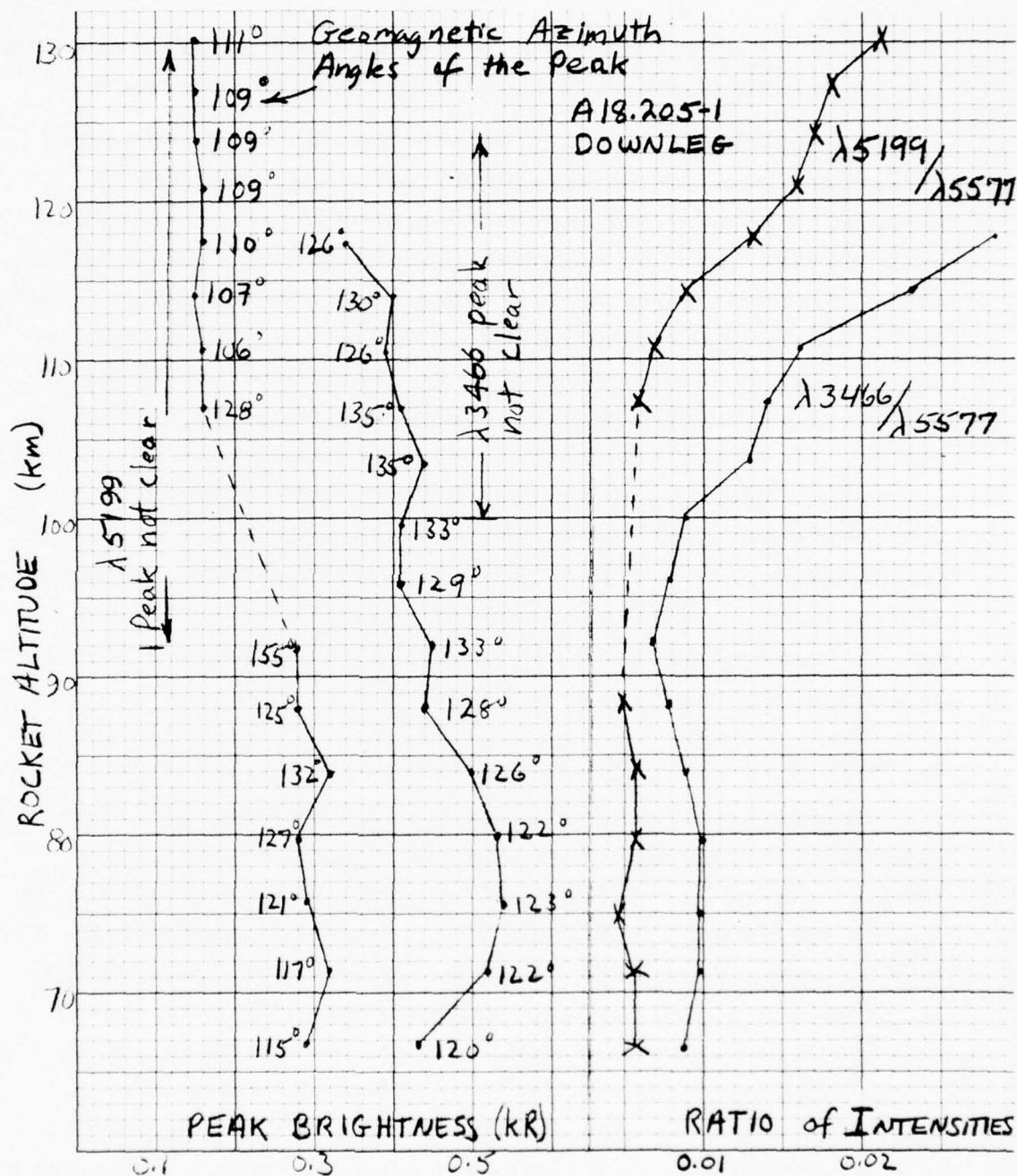


Figure 17. Altitude profiles of $\lambda 5199$ and $\lambda 3466$ peak intensities with backgrounds included, and ratios of peak intensities $\lambda 5199/\lambda 5577$ and $\lambda 3466/\lambda 5577$, downleg A18.205-1.

radiance distributions from N of the isolated tilted arc are qualitatively similar to those measured by a rocket ascending from the south.

The downleg N^2D and N^2P data contain information about the background intensities of these NO precursor species at auroral latitudes. Azimuth scans have broad maxima, whose intensities and peak locations cannot be accurately measured because of low signal/noise. Figure 17 shows our best estimates of behavior of these peaks. At 96 km, where low-contrast limbs first appear, the N^2D radiance is very close to 230 R between 105° and 245° (compare $\lambda 5577$'s flat southward maximum). Intensity toward the geomagnetic meridian is 125 R. The aforementioned sharp increase in the SW $\lambda 5577$ peak at low rocket altitudes is also clearly distinguishable in both the $\lambda 5199$ and $\lambda 3466$ data. Peak N^2P brightness reaches 500 R in a similarly flat maximum; its limbs have higher contrast detectable up to perhaps 100 km rocket altitude. The $\lambda 5199/\lambda 5577$ and $\lambda 3466/\lambda 5577$ limb-enhancement ratios (Fig 17) are similar in magnitude and in altitude at which increase occurs, to those observed on upleg.

5. $3\mu m$ NO FUNDAMENTAL -- BACKGROUND CONSIDERATIONS

A high background level in the $5.3\mu m$ NO vibrational fundamental band limits both the quantity and quality of measurements of this infrared emission's correlation with particle energy deposition in the upper atmosphere. Interference arises from what appears to be high frequency instrument noise, spin-correlated thermal radiation from the earth's limb similar to that seen from 1972 multi rocket A17.110-3, and a further thermal emission interpreted as coming from a solid object sporadically in the radiometer's field of view. A typical azimuth dependence is shown in Fig 18. For the previous ICECAP experiment, we manually smoothed each such $5.3\mu m$ angular distribution and interpreted the excess fluorescence-correlated radiation (over interpolated earth limb background) as emission from the auroral arc (see especially Fig XVIII-34 of Ref 1.) For A18.205-1,

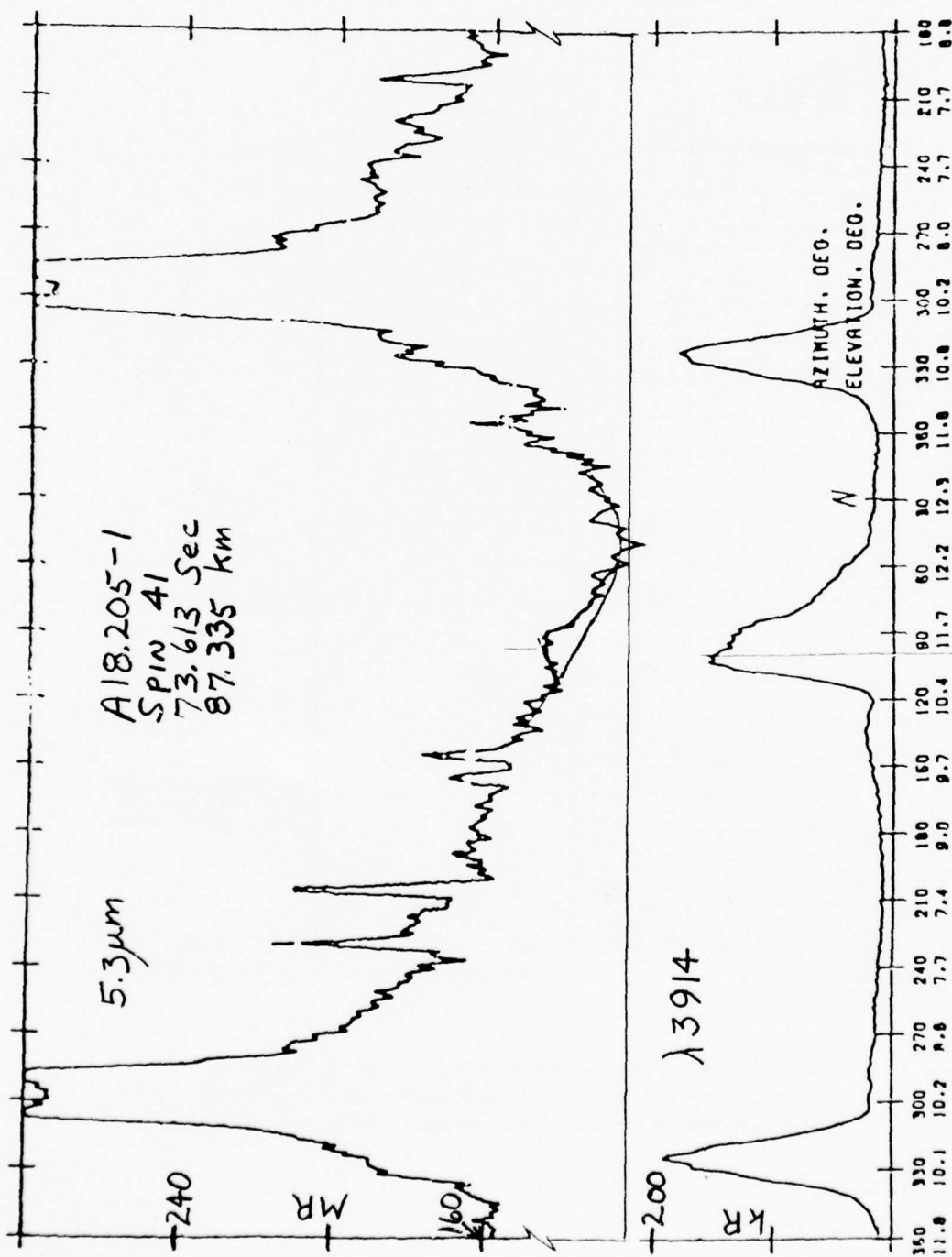


Figure 18. 5.3 μm elevation-azimuth spin cycle from A18.205-1 upleg showing the various noise backgrounds plus aurora-associated modulation near 70° E of geomagnetic N.

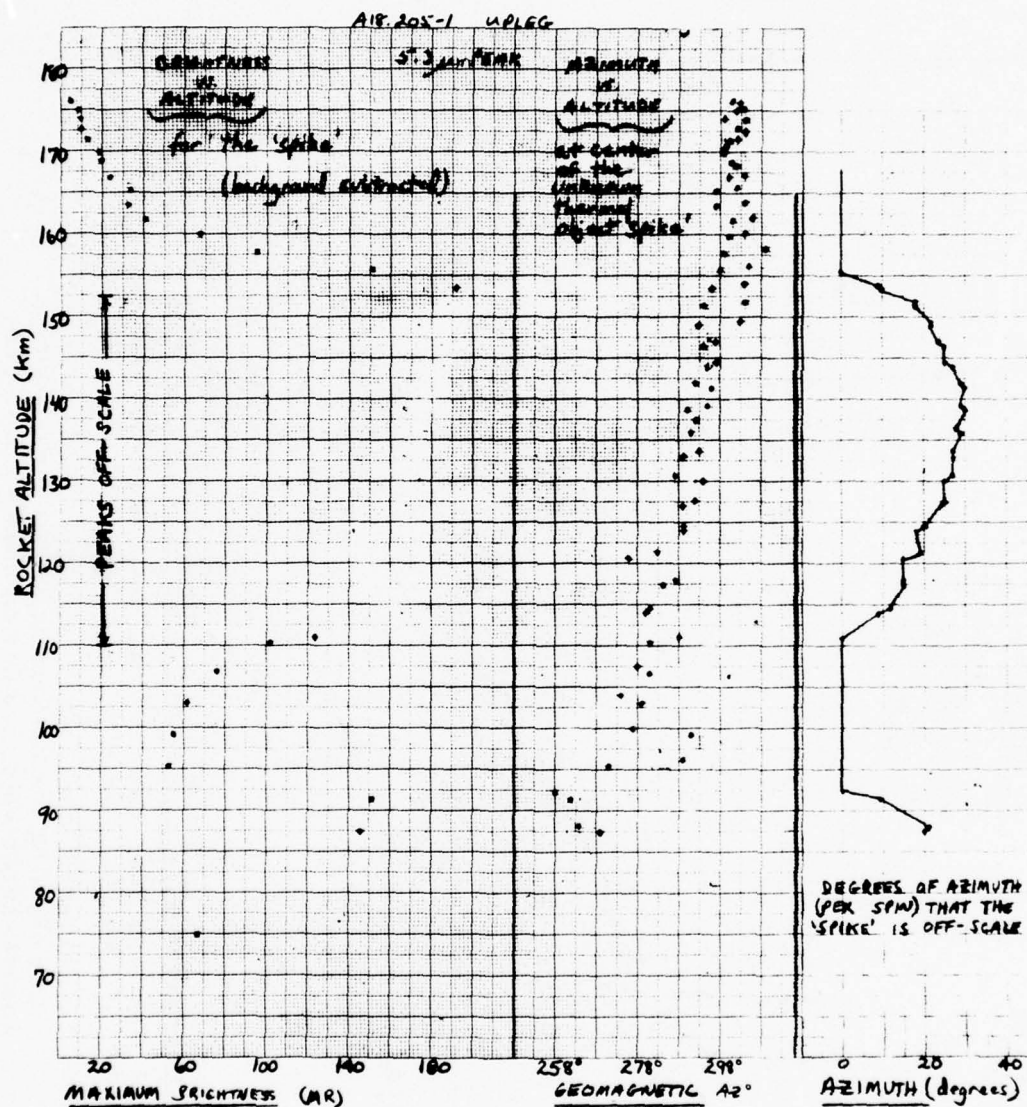


Figure 19. Altitude profiles of intensity of the $5.3\mu\text{m}$ "spike", azimuth angle of its center and number of degrees of azimuth (per spin) off-scale, A18.205-1 upleg.

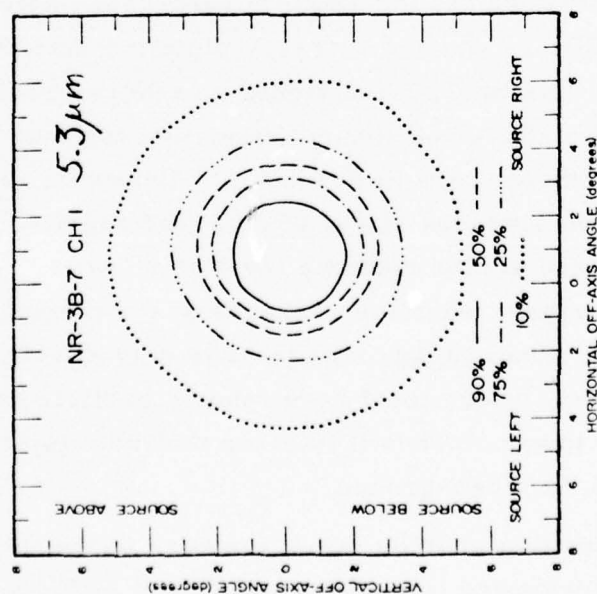
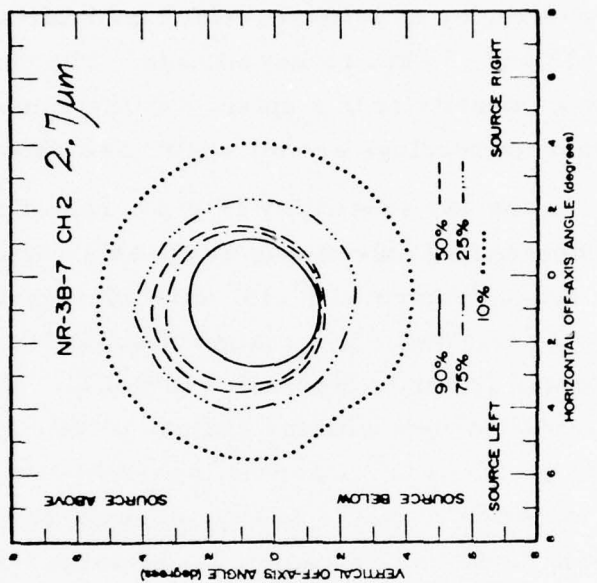


Figure 20. Polar diagrams of the angular sensitivity of A18.205-1's sideloooking dual channel radiometer (from Ref 3).

however, application of this procedure is inhibited by additional contamination over a broad region of azimuth, which goes off-scale (> 280 MR) between 113 and 153 km rocket altitude. The center azimuth angle and peak intensity of this spike, and the number of degrees of azimuth that its readings are off scale, are shown in Fig 19.

The radiometer's angular sensitivity (Fig 20, reproduced from Ref 3) appears to be decreasing only slowly at off-axis angles $\geq 5^\circ$. As the rocket spins, the instrument's 7° - 13° axial elevation angle variation would give rise to a van Rhijn change of about 2 if its angular field were sharply limited (refer to discussion in Ref 8). The convolution of the actual field of view with the altitude profile of "earth limb" $5.3\mu\text{m}$ radiance produces the observed low-fixed-frequency cyclical background variation. That is to say, off-axis radiation from lower altitudes "leaking" into the instrument is the source of this high background level.

To gain some further insight into this leakage, we have plotted in Fig 21 the (path length-like) cosecant of the radiometer axis' elevation angle against apparent radiant intensity at a high and a low rocket altitude, subtracting out the small aurora-associated pulse (original scans in Fig's 23 and 24a). These plots indicate that at fixed rocket altitude the $5.3\mu\text{m}$ background signal increases about linearly with the inverse of the sine of elevation angle, that is, with longer effective path length through the atmosphere. However, extrapolation to the zenith at the two altitudes shows offsets that are also considerably larger than the expected zenith radiance level of a few MR (refer to Fig 16 of Ref 2). Further, when the rocket is at the mesosphere altitude of 75 km, the mean background level is only a factor of $1\frac{1}{2}$ greater than at 176 km, where local atmospheric particle density is orders of magnitude lower. Thus it is clear that no simple model describes the cyclic $5.3\mu\text{m}$ background.

Figure 22 shows this altitude effect further, in the form of profiles of $5.3\mu\text{m}$ background intensity at minimum ($\sim 7^\circ$) and

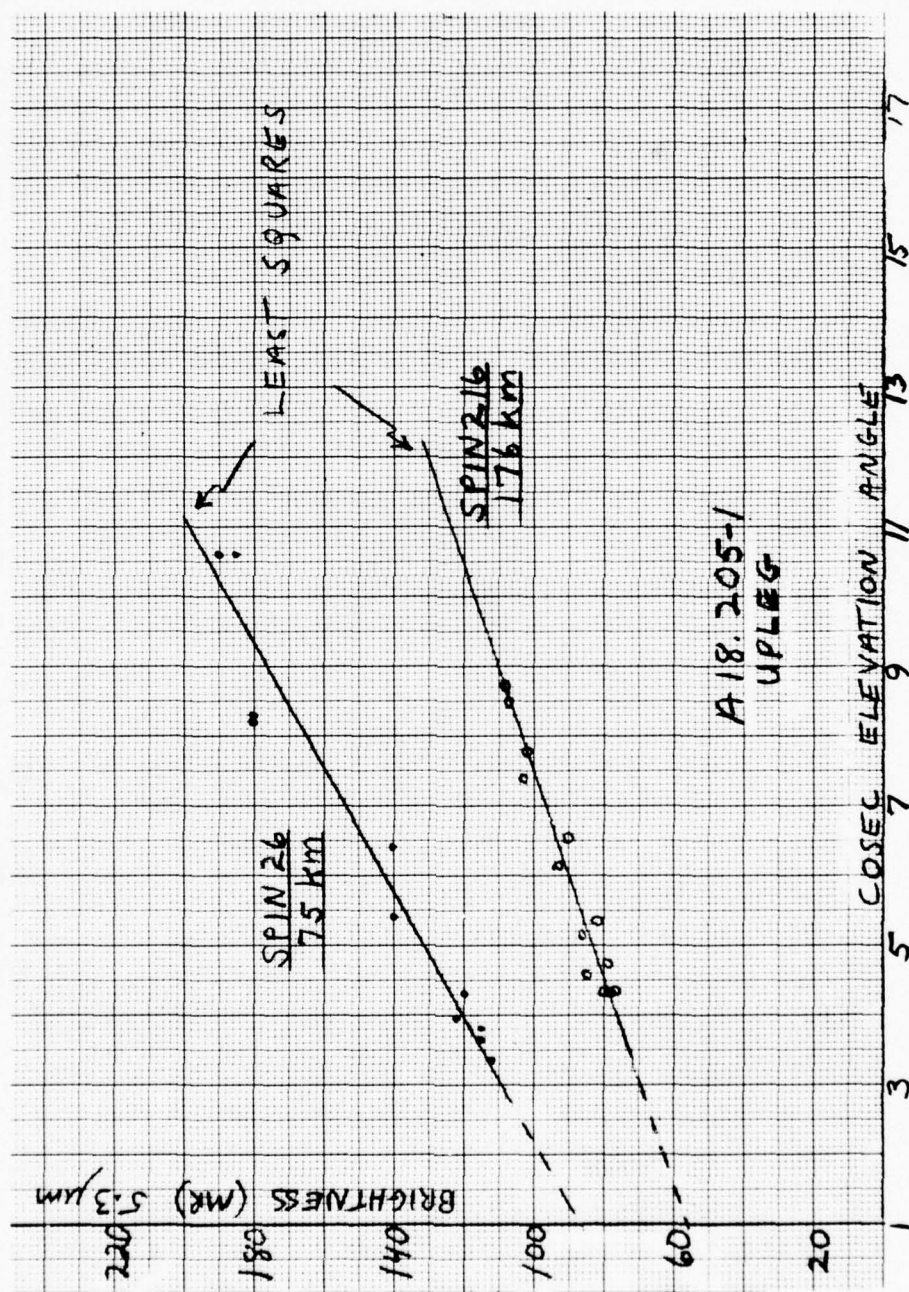


Figure 21. Apparent 5.3μm radiance plotted against cosec of 5.3μm radiometer axis' elevation angle at a high (176 km) and a low (75 km) rocket altitude, A18.205-1 upleg. Extrapolation of the least squares straight-line fits to the zenith indicates background intensities of the order to 60 to 90 MR (see text).

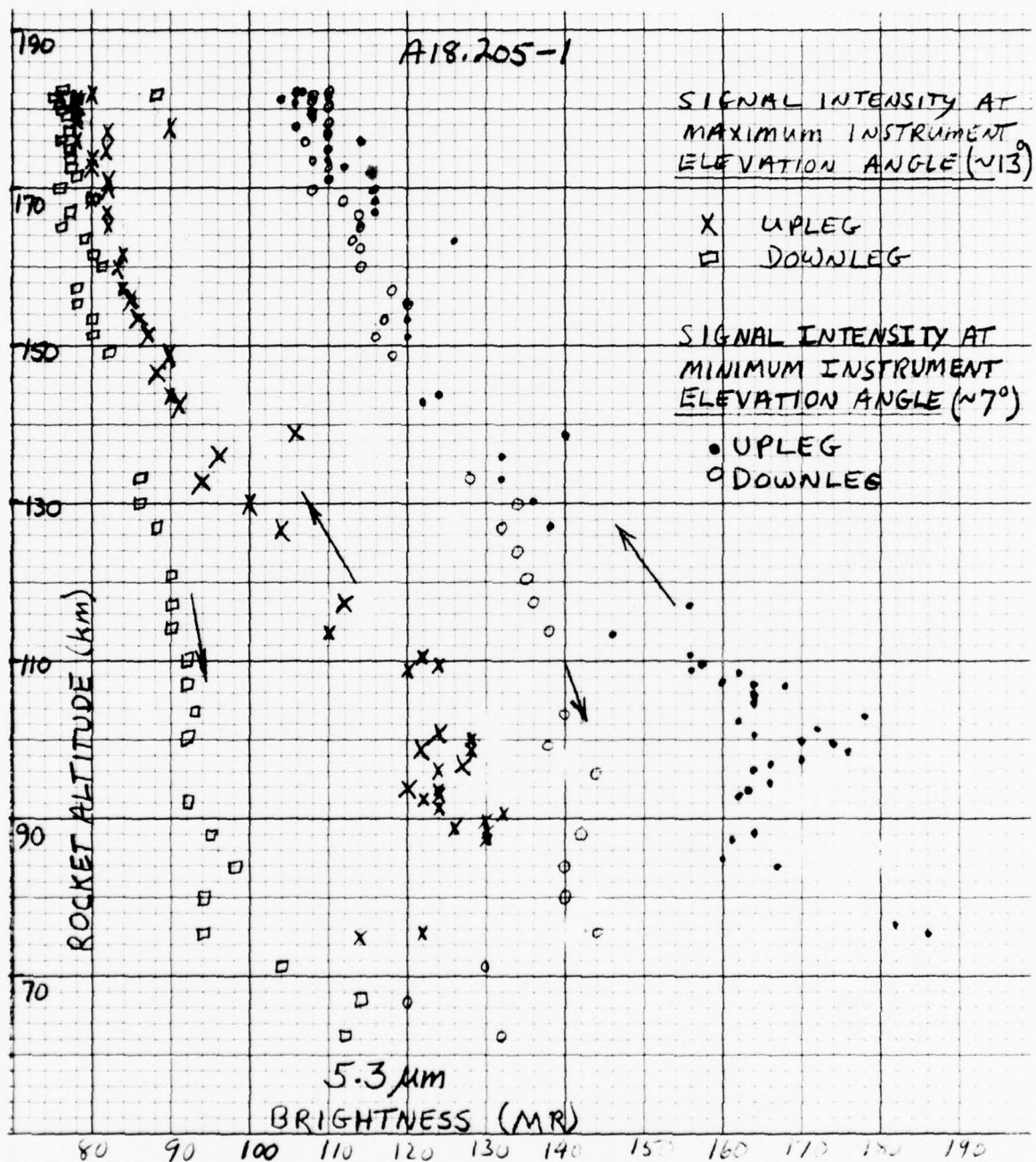


Figure 22. Altitude profiles of 5.3 μ m cyclic-background intensity at minimum (7°) and maximum (13°) radiometer elevation angle, A18.205-1 upleg and downleg.

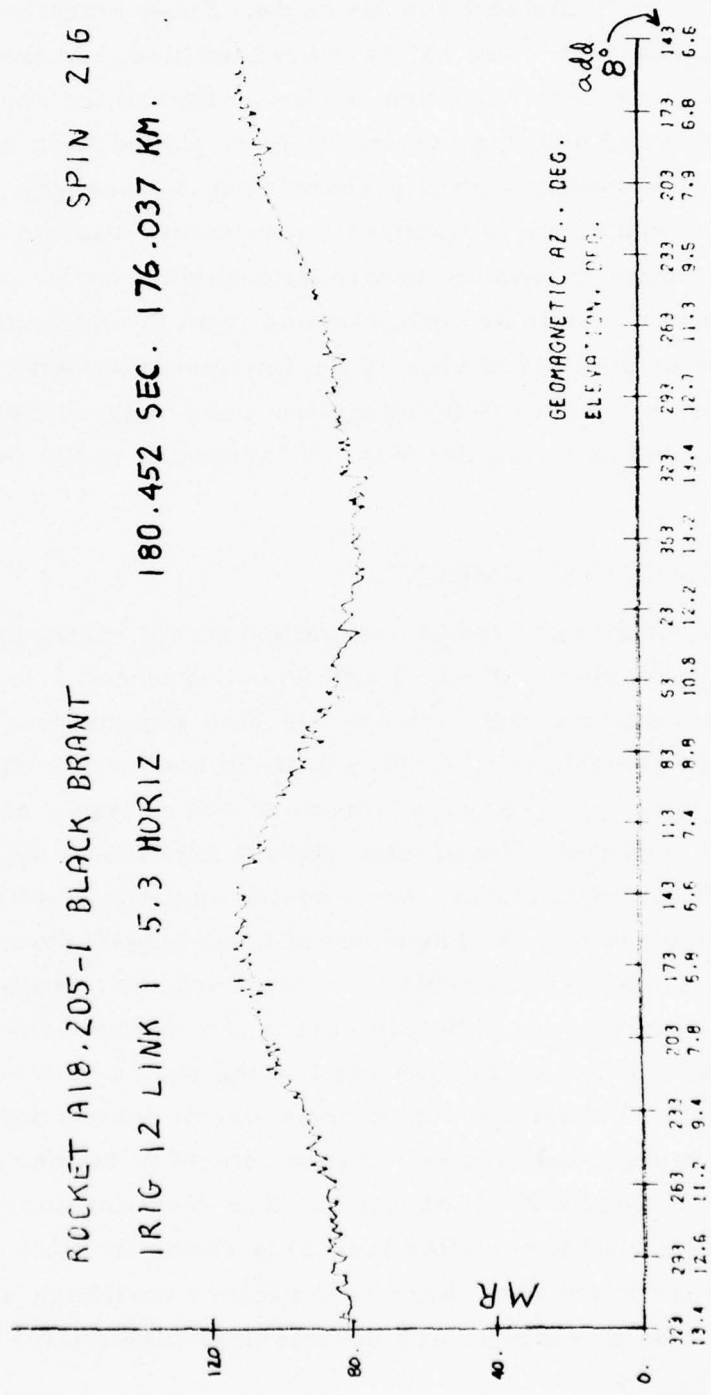


Figure 23. 5.3μm radiometer elevation-azimuth spin cycle at high altitude of A18.205-1 upleg, showing the remaining cyclical background signal.

maximum ($\sim 13^\circ$) radiometer elevation angle. Spins which had an obvious noise spike near 7° or 13° have been omitted. At the minimum elevation angle, where the direction of view is toward the south, the profiles for upleg and downleg are definitely displaced from one another below 130 km rocket altitude, and perhaps even up to apogee. A similar shift is seen at the radiometer's maximum elevation angle, where the instrument is pointing toward geomagnetic north. Although there may be some remaining contamination from the thermal emitter toward the edge of the field of view in the low-elevation data, the fact that offsets appear in opposite pointing directions suggest that these changes may be due to a slow decrease in sensitivity of the radiometer during flight.

5. $3\mu\text{m}$ ARC-ASSOCIATED EMISSION

Despite the high and erratic background levels, there appear in several low altitude spins (below 95 km) on upleg, excess $5.3\mu\text{m}$ signals associated with the arc's east limb near 70°E of geomagnetic N. These increases are generally similar to those observed in the 1972 multi data at times when the arc was north of and at higher altitude than the rocket, and thus offered long emitting columns at azimuths typically 60° from the meridian. We selected sections of azimuth scans from which we judged that the amplitude of these pulses above the smoothed earth limb baseline could be determined. We applied the criteria that 1) there be no obviously severe interference from the large spikes, and 2) the $\lambda 3914$ intensity be high over a narrow range of azimuth ($\sim 20^\circ$ - 30° FWHM), which permits discrimination against the low-frequency background (this latter requirement is further discussed in Section I and Appendix XVIII of Ref 1). The resulting narrow range of rocket altitudes (and times after launch) is shown in Table 2, along with data on range to the arc. Each of the eleven qualifying elevation-azimuth plots, plus an example of a submarginal case (Spin 40), is reproduced in Fig 24.

Table 2. Times of Best Overlap of $5.3\mu\text{m}$ and $\lambda 3914$ Enhancements - A18.205-1.

Spin	Time (sec after launch)	Rocket Altitude (km)	Horizontal distance from rocket to arc center's field lines in the meridian plane (km)	Distance from instruments to arc's east limb field lines at $\sim 70^\circ$ geomagnetic azimuth (km)	Intercept Altitude (km)
26 - 28	64.307 - 65.533	74.778 - 76.467	40	117	~ 93 km
37 - 47	71.131 - 77.333	84.045 - 92.131	32 - 21	94 - 62	103 - 104

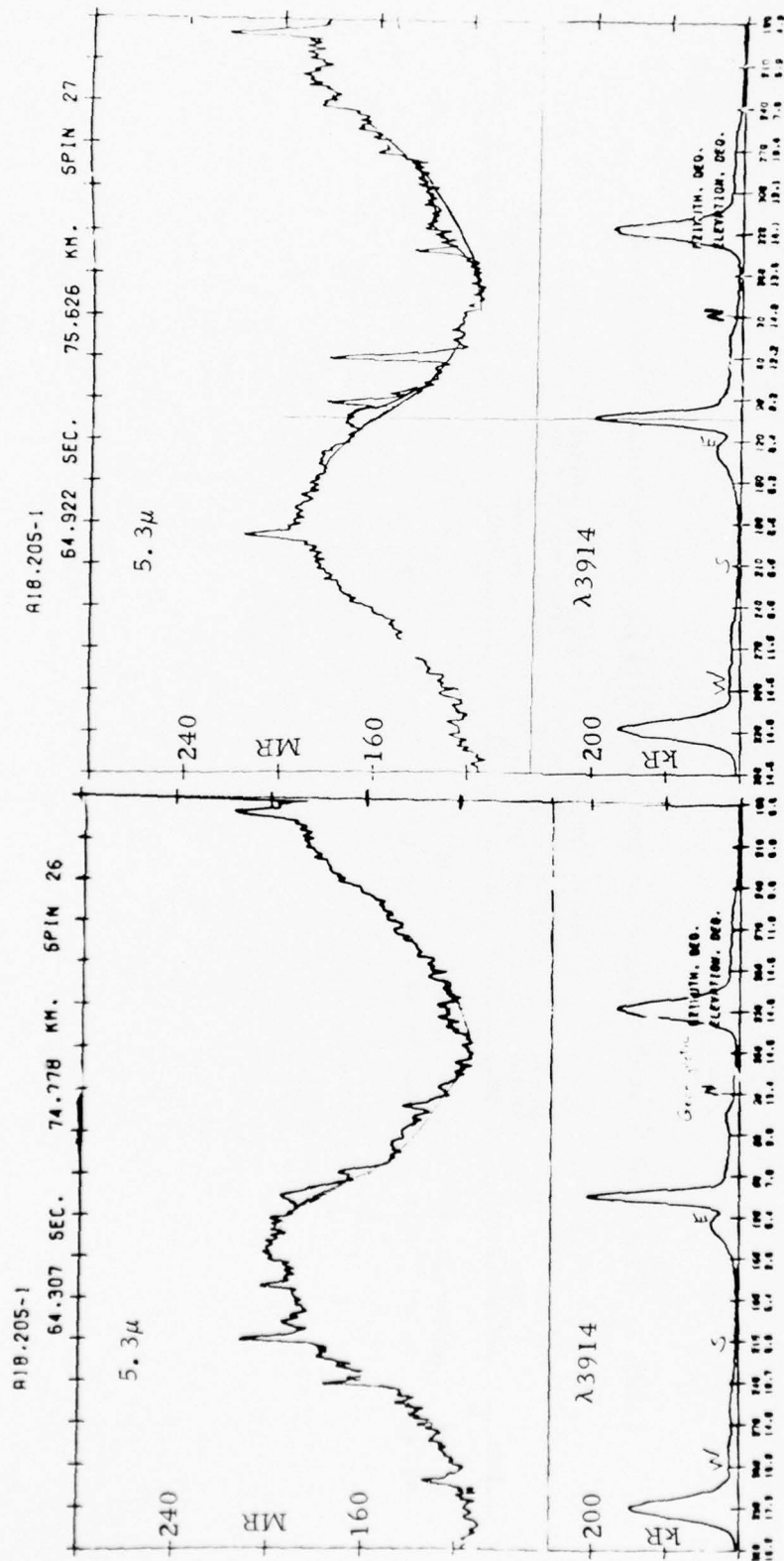
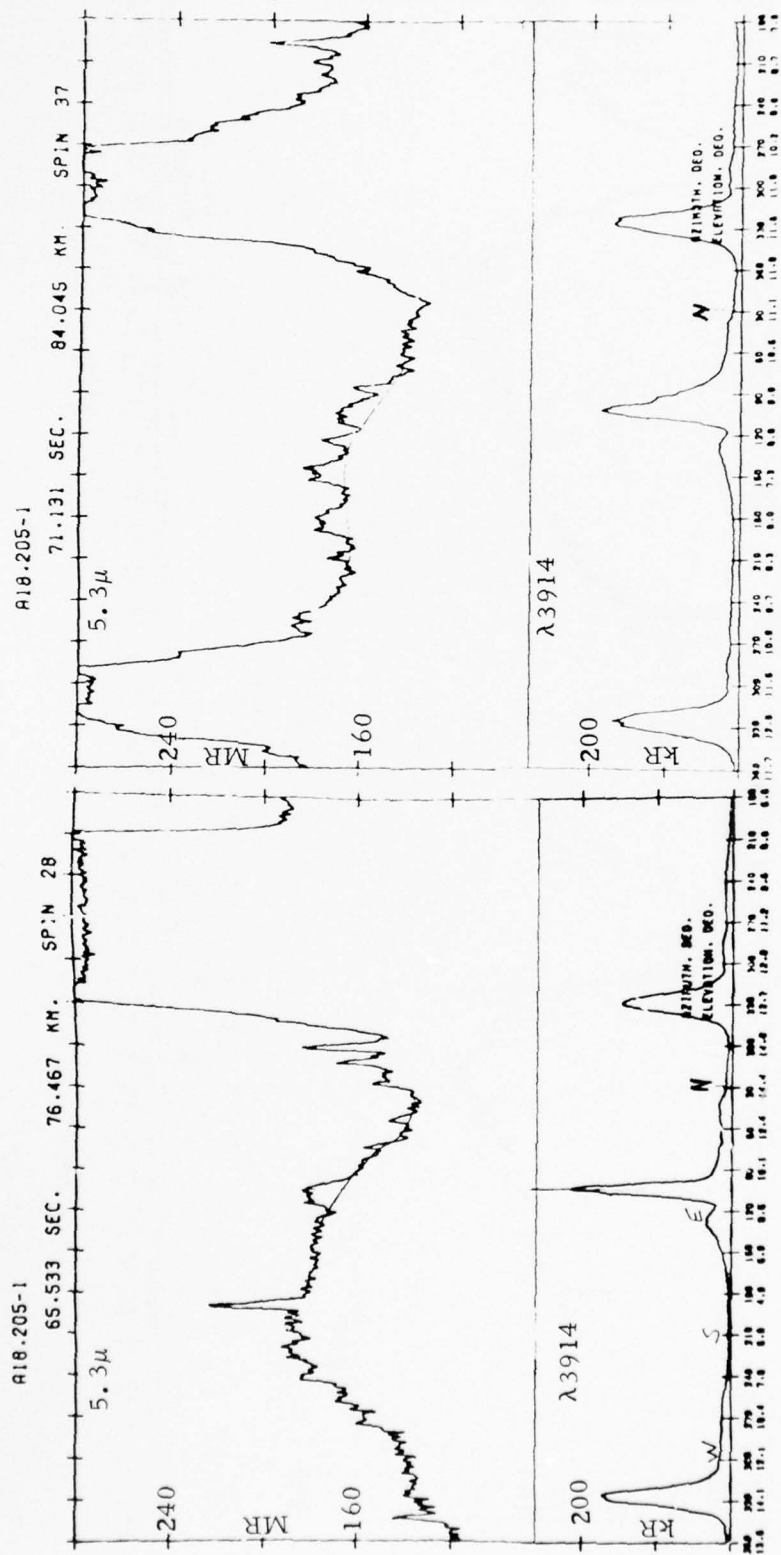
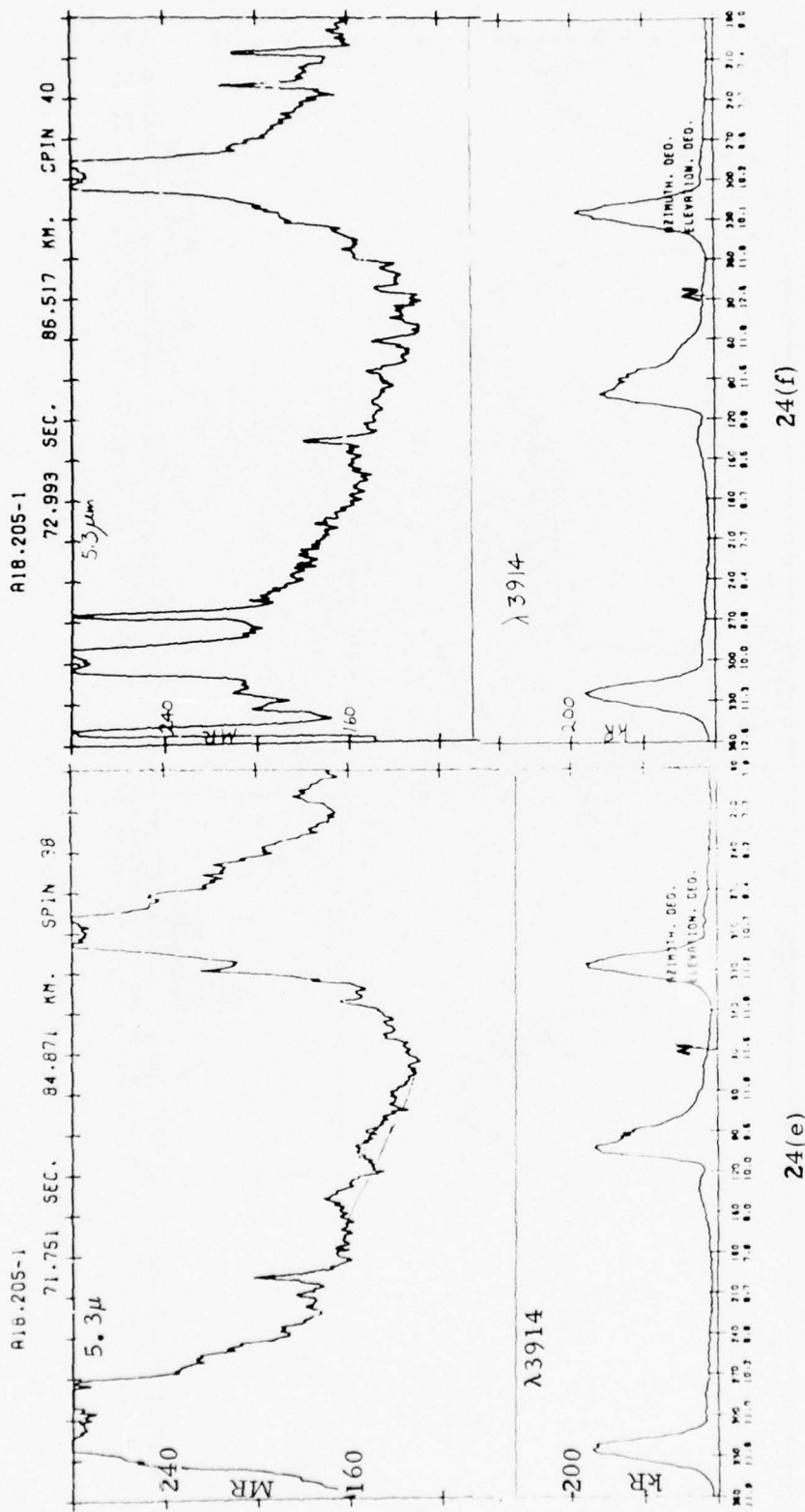


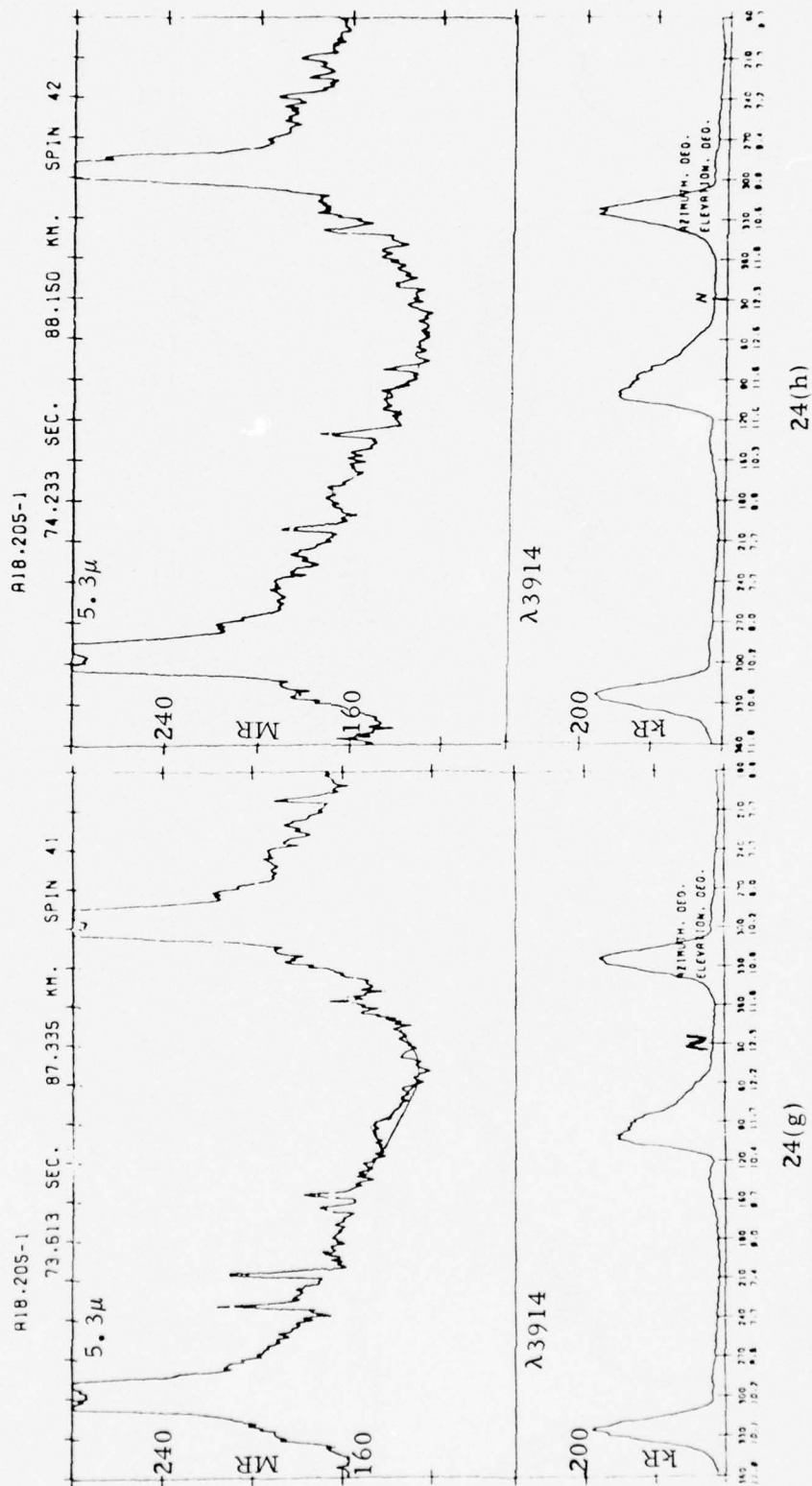
Figure 24a-1 Twelve elevation-azimuth spin cycles of $5.3\mu\text{m}$ and $\lambda 3914$ radiance distributions from A18.205-1 upleg, indicating correlation of the two features at low rocket altitude and further illustrating the various backgrounds. Spin 40 defines a limiting case without sufficient aurora-associated modulation for inclusion in the scatter plot in Fig 25.

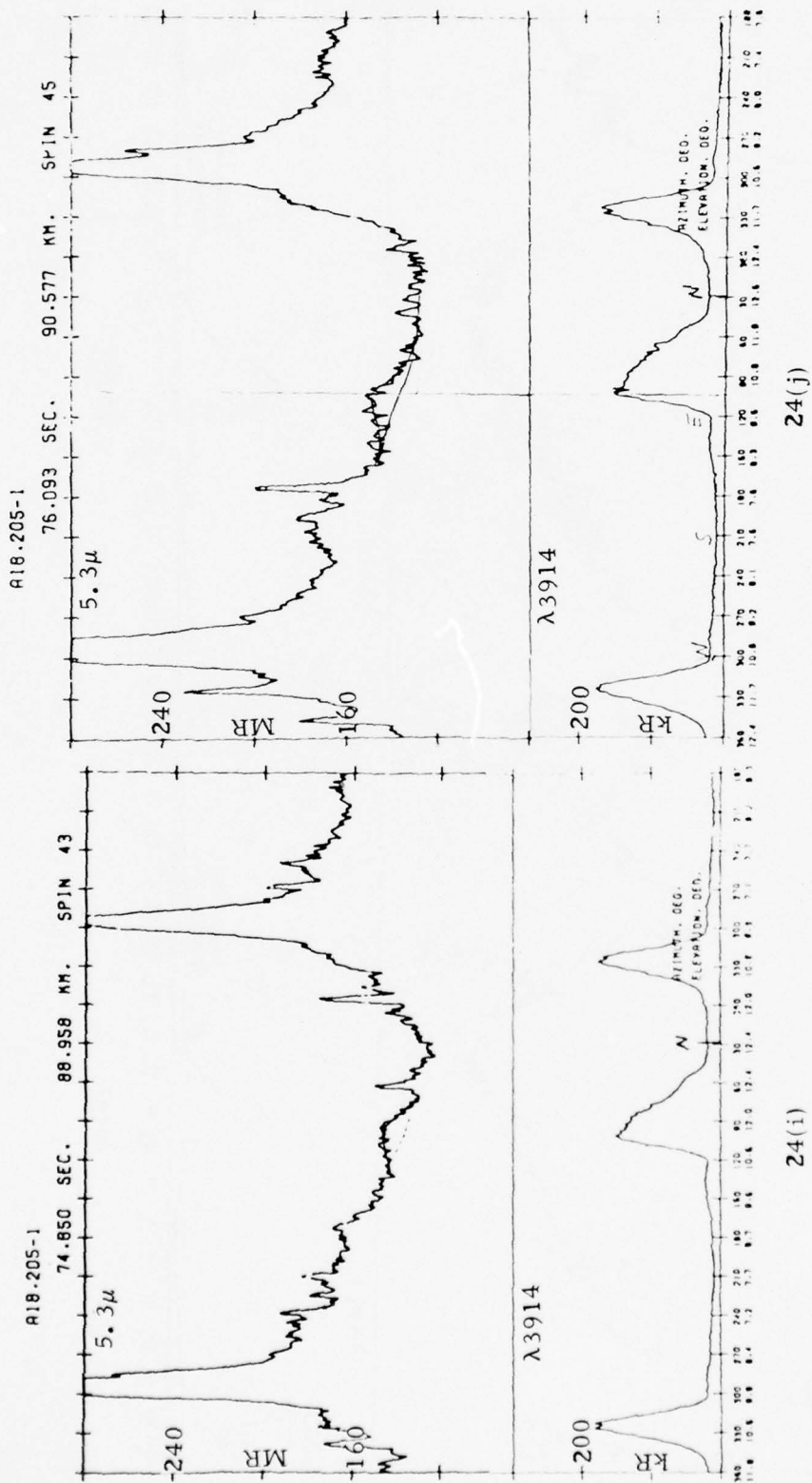


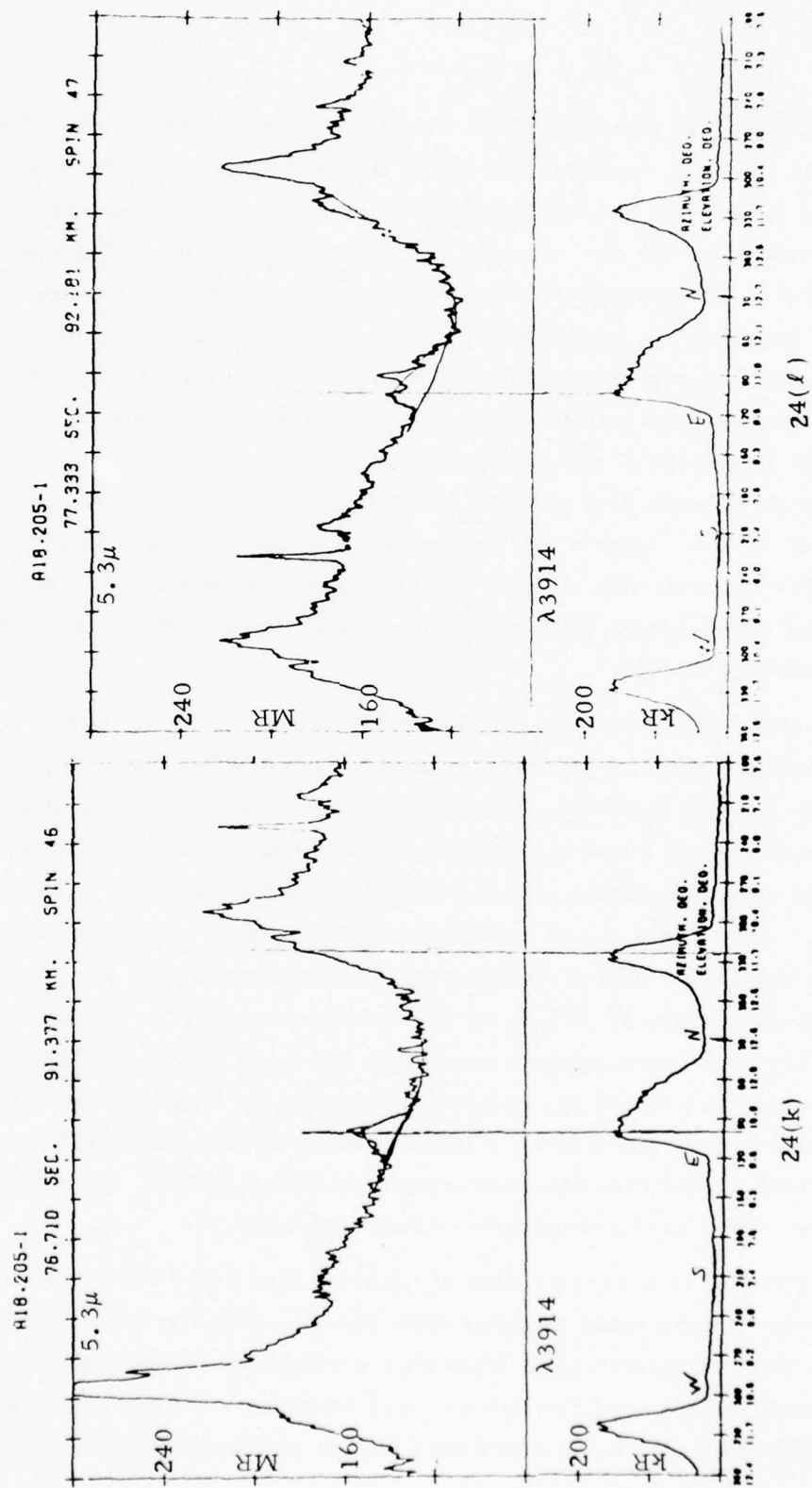
24(d)

24(c)









To calculate the altitude at which the radiometer's field of view intercepts the arc, we first projected the trajectory into the meridian plane and measured the horizontal distance to the field line (at 77° dip angle) drawn through the arc's brightness "center" (as defined by Fig 1). The typically 12° instrument elevation in the meridian direction has the effect of raising this intercept by ~ 7 km above the rocket's altitude when this altitude is between 74.8 and 76.5 km (Spins 26-28). Outside the meridian plane, a computation taking into account earth curvature places the intercept of the radiometer's field of view with the arc's east limb field lines at a point 117 km distant, and at an auroral altitude of 93 km. Similarly, for rocket altitude between 84 and 92 km (Spins 37-47) the distance from the radiometer to the arc's field lines at 70° E of geomagnetic N is typically 74 km, making the intercept altitude about 103 km.

At the three lowest rocket altitudes (near 75 km, Figures 24a-c), the azimuthal extent of detectable excess $5.3\mu\text{m}$ signal is comparable to that of the $\lambda 3914$ peaks. Although the signal-to-noise ratios are not sufficiently high to allow a detailed comparison of azimuth dependence within the arc-associated pulses, the $5.3\mu\text{m}$ peak appears to be about 5° broader. This angle would correspond to a spatial spread of about 11 km at the arc. The directions of the peak intensities also correlate very closely (within 3° - 5°). As the rocket passes 77 km, the thermal emitter begins to contaminate seriously the west limb (see Fig 24d). Some correlation remains, however, between the enhancements near 70° E (Fig's 24d-f); these show a trend toward $5.3\mu\text{m}$ peaks that are slightly less broad than the corresponding $\lambda 3914$ peaks. Maximum radiances above background are included in Table 3.

Figure 25 is a scatter plot of these $5.3\mu\text{m}$ and $\lambda 3914$ peak excess intensities. Three least squares straight-line fits are indicated, two of which were forced to pass through the origin and thus assume direct proportionality between the two auroral features over the small altitude range included. With the somewhat higher readings from higher-

Table 3. Azimuth Angles and Intensities of $\lambda 3914$ and $5.3\mu\text{m}$ Excess Radiances, A18.205-1 upleg

<u>Spin</u>	<u>Time (sec after launch)</u>	<u>Rocket Altitude (km)</u>	<u>Geomagnetic Azimuth (degrees)</u>	<u>$\lambda 3914$ Brightness (background subtracted) (kR)</u>	<u>$5.3\mu\text{m}$ Brightness (background subtracted) (MR)</u>
26	64.309	74.778	73 300	205 163	13.5 8.0
27	64.921	75.627	73 300	189 170	11.0 11.0
28	65.533	76.467	73	208	14.5
37	71.131	84.045	73	181	12.0
38	71.750	84.870	73	159	10.5
41	73.614	87.355	71	140	9.0
42	74.231	88.147	72	139	9.0
43	74.850	88.958	73	138	10.0
45	76.092	90.576	74	141	12.0
46	76.709	91.375	70	139	17.0
47	77.331	92.178	75 296	146 150	15.0 12.0

Spins	Rocket Altitude (km)	Distance from instruments to arc's east limb field line at $\sim 70^\circ$ geomagnetic azimuth (km)	Intercept Altitude (km)
o 26 - 28	74.8 - 76.5	117	~ 93
• 37 - 43	84.0 - 89.0		
x 45 - 47	90.6 - 92.2	93 - 62	103 - 104

A18.205-1
UPLEG

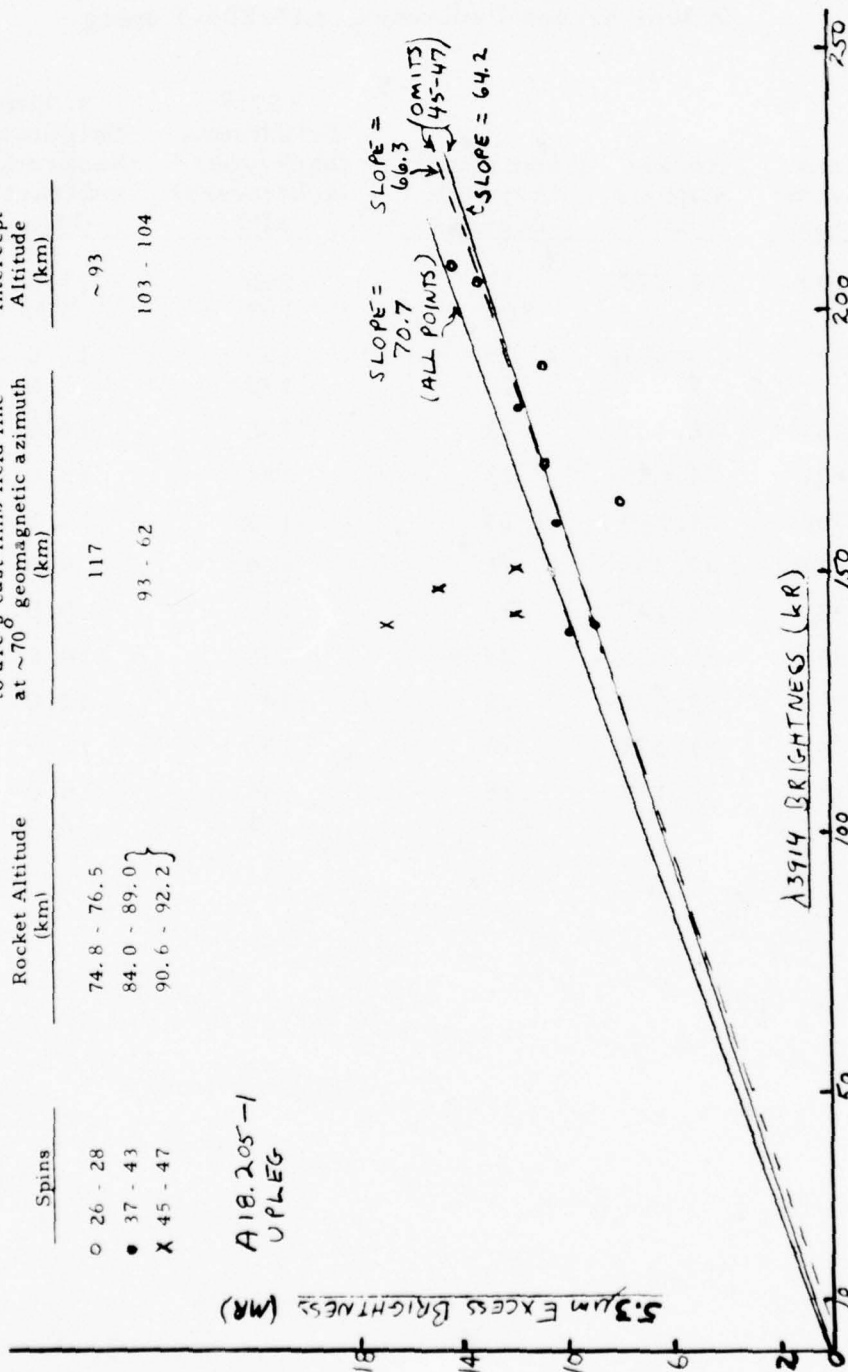


Figure 25. Scatter plot of excess 5.3 μ m and $\lambda 3914$ intensities from A18.205-1 upleg traces in Fig 24, with supporting information on range to and intercept altitude on the arc. The three sloping lines are least squares straight-line fits described in the text.

altitude Spins 45-47 omitted the $5.3\mu\text{m}/\lambda_{3914}$ ratio (of column photon intensities) determined from the slope of the line through the origin is 64.2. The least squares fit to these same points gives 66.3 photons/photon. Adopting a mean ratio of 65, and taking a value of 21.5 ion pairs per λ_{3914} photon as determined by the HAES PRECEDE experiment (see Section V), we get ~ 3 NO fundamental photons within the radiometer's passband per ion pair in air between 93 and 103 km. If the data for 104 km intercept altitude are included, the ratio would appear to increase by less than 10%. This change, however, is probably not significant in light of the experimental uncertainties and poorer confidence limits of the latter fit.

A low-resolution spectrum (Figure 26) (Ref 9) for $T_{\text{vib}} = 5000$ K and $T_{\text{rot}} = 225$ K indicates that about one-third of the $\Delta v = 1$ sequence's spectral intensity lies within the radiometer's bandpass. We have assumed here that the radiometer calibration refers to its response to a continuum of constant spectral radiance summed between its half-response points. This leads to a lumped-parameter figure of 9 NO vibrational fundamental photons per ion pair in the altitude region 93-103 km. Other assumptions about the initial vibrational population of NO molecules (Fig 13 of Ref 1, Fig2-9a of Ref 5) would of course result in different effective ratios. For example, if we assume that only $v = 1$ is populated (more on this in the following subsection), the radiometer detects about three-fourths of the spectral intensity, giving an efficiency of 4 NO fundamental (1,0) photons per ion pair.

Recalculation of our 1972 multi ratio (p 28 of Ref 1) using the 5000 K NO synthetic spectrum and $21\frac{1}{2}$ ion pairs per λ_{3914} photon, gives 3 NO photons produced per ion pair. This factor of 3 difference in effective fluorescence efficiencies between the 1972 and 1973 experiments turns out to be very close to the ratio of mean $5.3\mu\text{m}$ intensities measured from the two rockets, as a comparison of the ordinate scale of Fig 24 with that of Ref 1's Fig 9 clearly shows.

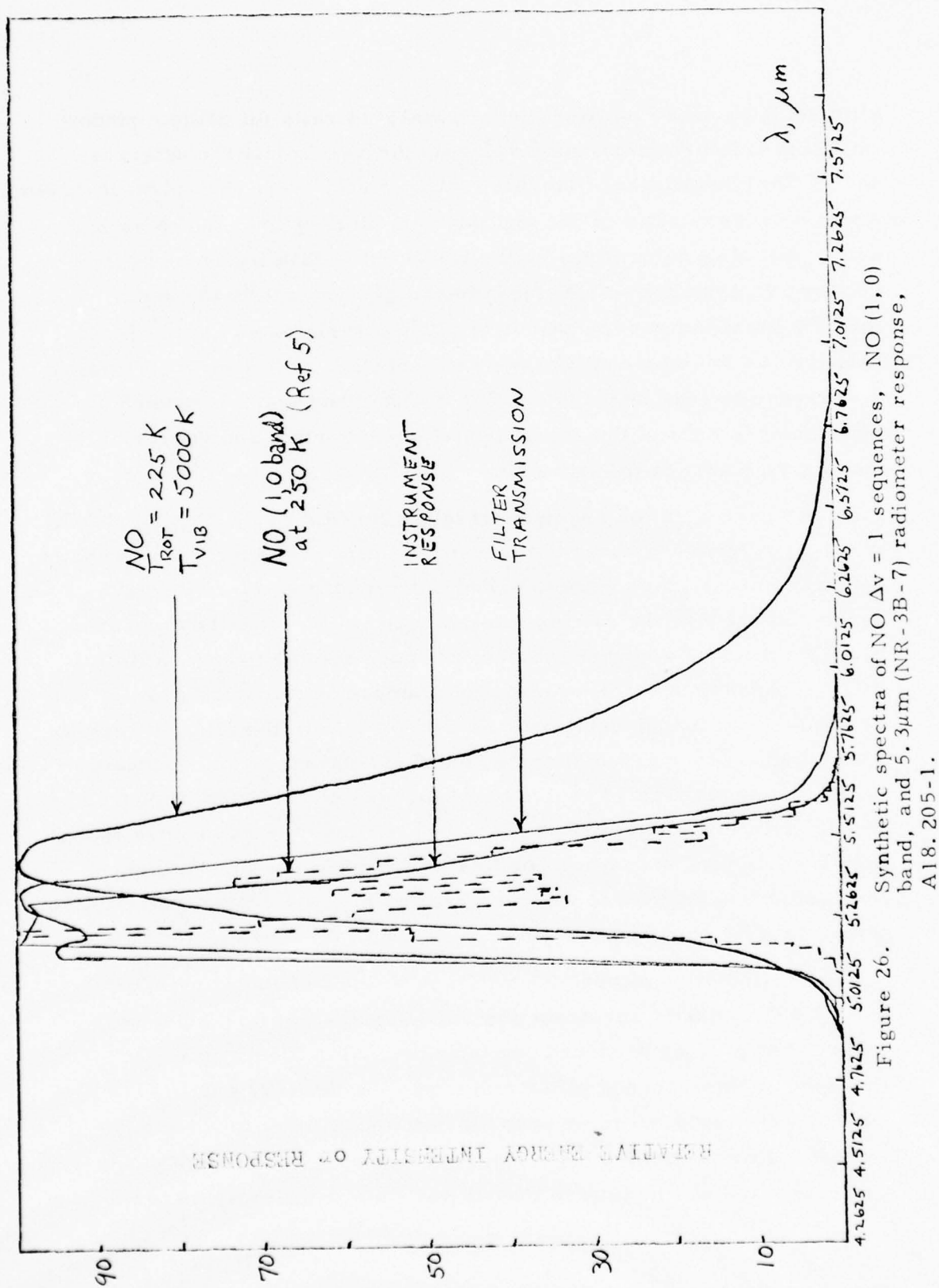


Figure 26.

(In both experiments, the typical $\lambda 3914$ auroral-limb radiance was ~ 170 kR.) This observation suggests that the difference may be an effect of the absolute calibration of the radiometer.

On downleg, as we noted earlier, the $\lambda 3914$ and $\lambda 5577$ fluorescence signals show a broad glow to the S building up to ~ 50 kR OI as the rocket descends below 100 km. The minimum range to the arc's inclined field lines at 90 km rocket altitude is about 135 km (Fig 1), and thus the perpendicular projection on the arc of the 5° instrument field is 12 km. Away from the meridian direction, where the limb enhancements lie, the projection is about a factor 2 greater (more in the horizontal than in the vertical). Inspection of the downleg $5.3\mu\text{m}$ radiometer traces shows no enhancement above the nominal 120 MR background. High frequency noise superposed on this slowly-varying background sets an upper limit of about 5 MR of excess $5.3\mu\text{m}$ radiation that could be visually undetectable in the plots of radiance as a function of azimuth. Therefore as many as 4 in-band NO photons per ion pair could actually be excited. That is to say, on downleg the A18.205-1 sidelooking rocket data give only an upper limit to the number of NO fundamental vibrational quanta, which is comparable to the number measured on upleg.

2. $7\mu\text{m}$ NO OVERTONE

The $2.7\mu\text{m}$ horizontal radiometer signals, though they too are contaminated with various types of noise, also seem to be showing some auroral modulation. Examples of two spins at altitudes in and above the range where excess $5.3\mu\text{m}$ radiation was seen are given in Fig 27. Both the spin-correlated repetitive limb modulation (85.7 km) and the erratic pulsations decrease more rapidly with altitude than the similar backgrounds returned by the $5.3\mu\text{m}$ radiometer. Above ~ 125 km the radiance has become nearly constant at 1-2 MR over most of the spin, but with intense (> 100 MR) steep spikes (130 km). The azimuth angles of the spikes' centers

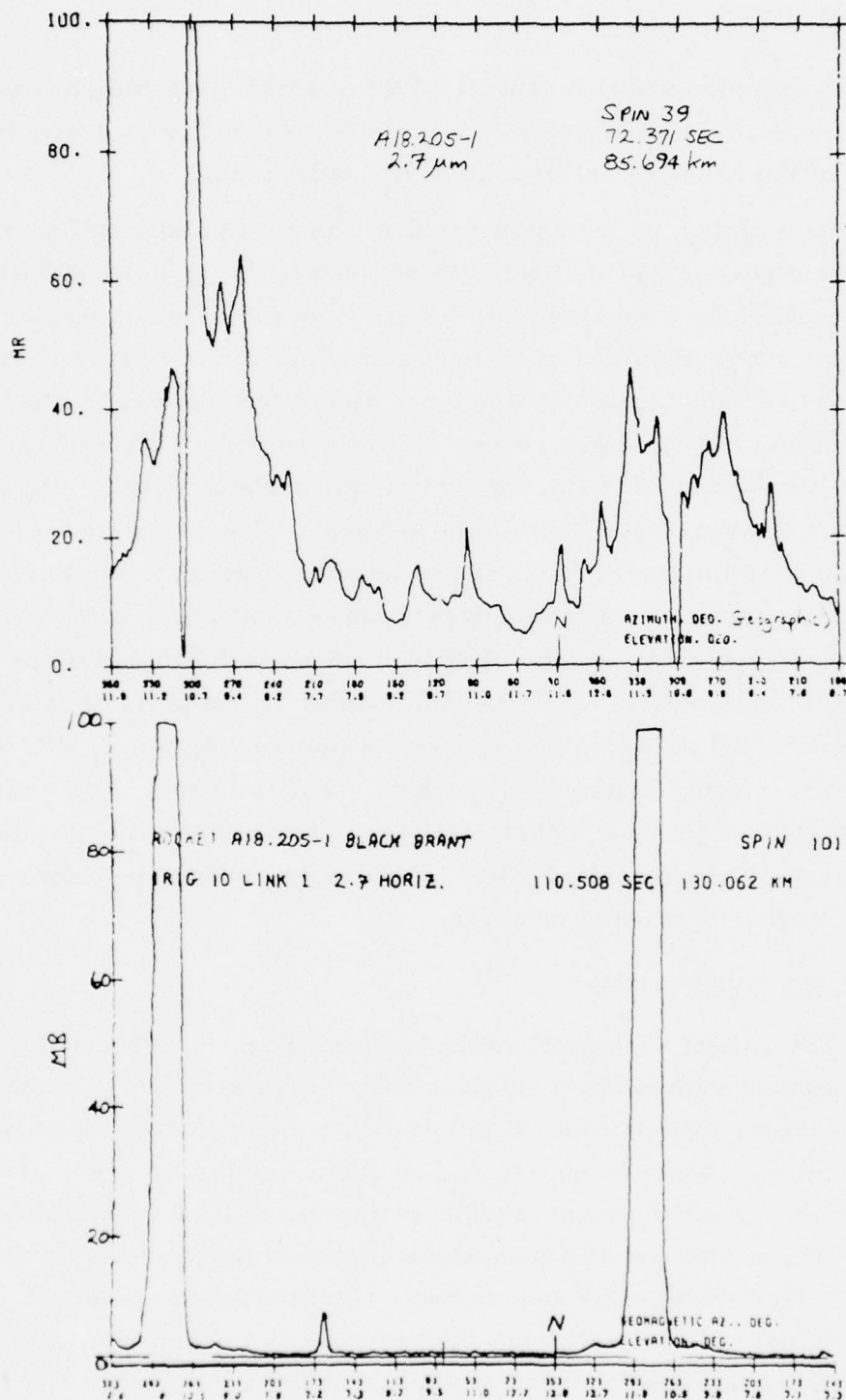


Figure 27. 2.7 μ m elevation-azimuth spin cycles from two altitudes of A18.205-1 upleg showing the various noise backgrounds including large spikes believed to be caused by a thermally-emitting object in the field of view.

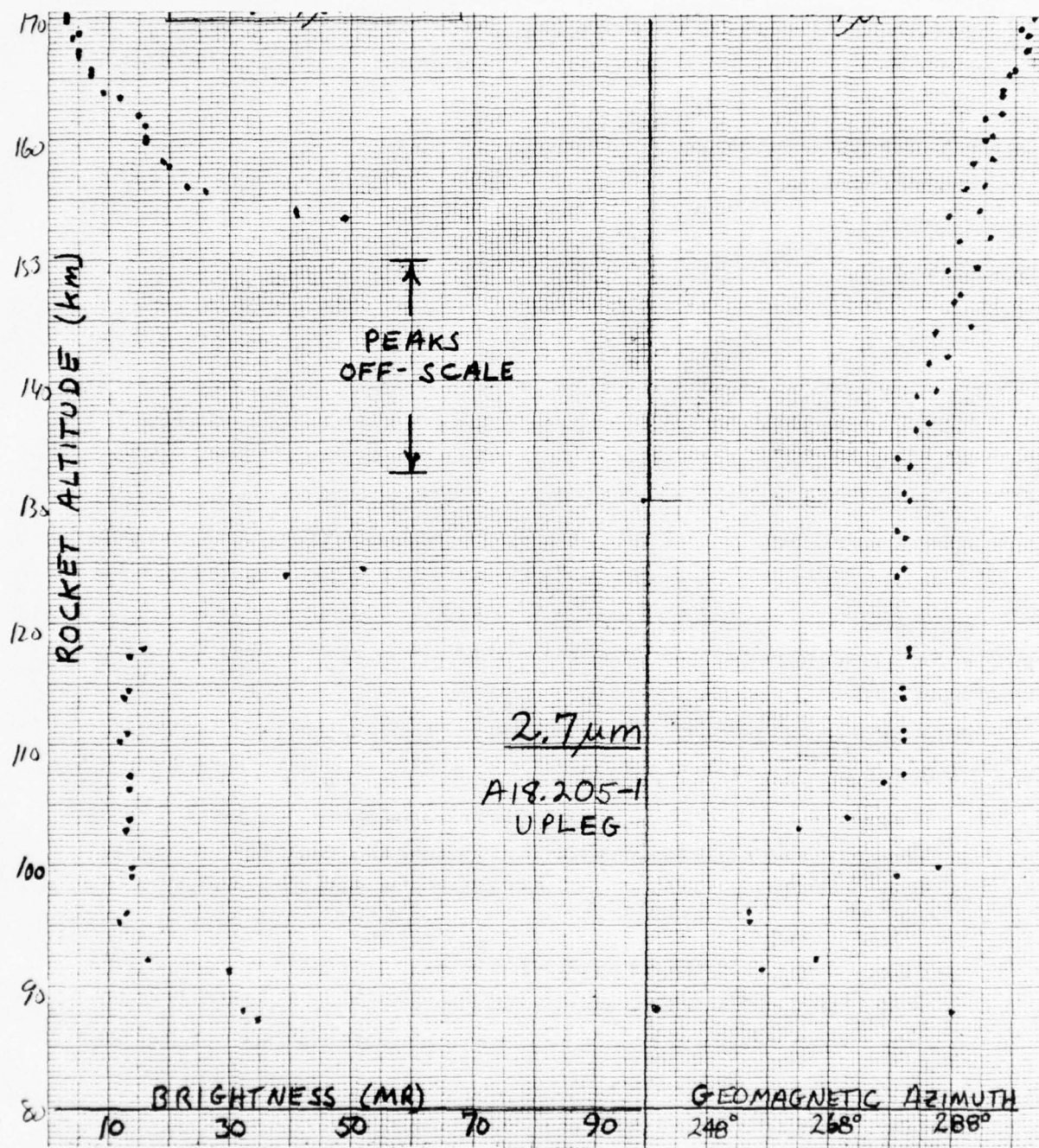


Figure 28. Altitude profiles of intensity of the 2.7 μ m "spike" and its center geomagnetic azimuth, A18.205-1 upleg.

correlate closely with those observed at $5.3\mu\text{m}$. Figure 28 shows these azimuths and maximum intensities above background as defined below. The large peaks, which are off-scale between 130 and 150 km rocket altitude, have an average FWHM of $\sim 12^\circ$ of azimuth in this altitude region, making them narrower than the corresponding $5.3\mu\text{m}$ spurious signals. Note from Fig 1 that most of the arc emission is at lower altitudes than the rocket when this interference is most prominent.

We have reproduced in Fig 29 those few cycles that may be considered, on the basis of the criteria we applied to the $5.3\mu\text{m}$ data, to show auroral enhancement. The altitude range of the rocket at these times is 88-92 km, and horizontal distance to the field line in the meridian plane is about 23 km. The radiometer's field of view intercepts the axial line of the arc at a line-of-sight distance of ~ 73 km, and at an altitude of 103 km. The mean intensity of the four smoothed excess $2.7\mu\text{m}$ signals above our estimation of background, which we have indicated by dotted lines, is 7.3 MR. Peak intensity of the corresponding $\lambda 3914$ pulses remained at about 150 kR over this $2\frac{1}{2}$ sec span. These limited data points lead to a mean $2.7\mu\text{m}/\lambda 3914$ photon ratio of 49, but provide no significant information about the proportionality of the two features.

Taking again 21.5 ion pairs per $\lambda 3914$ photon, we get 2.3 in-band $2.7\mu\text{m}$ quanta per ion pair at ~ 100 km auroral altitude. We shall assume that all this radiation is NO overtone. Our synthetic spectrum calculated for $T_{\text{vib}} = 5000$ K and $T_{\text{rot}} = 213$ K (Ref 2) indicates that about 88% of the $\Delta v = 2$ system intensity is detected by the wide band radiometer, whose half-power points lie at 2.42 and $3.11\mu\text{m}$ (Ref 3). The result is 2.6 NO overtone photons excited per ion pair in E-region air, which is an effective fluorescent conversion efficiency of $3\frac{1}{2}\%$. Compare 2 $\Delta v = 1$ photons/ion pair, p47.

As discussed in the following Section, the overtone excitation efficiency derived from the downleg portion of multi A18.219-1

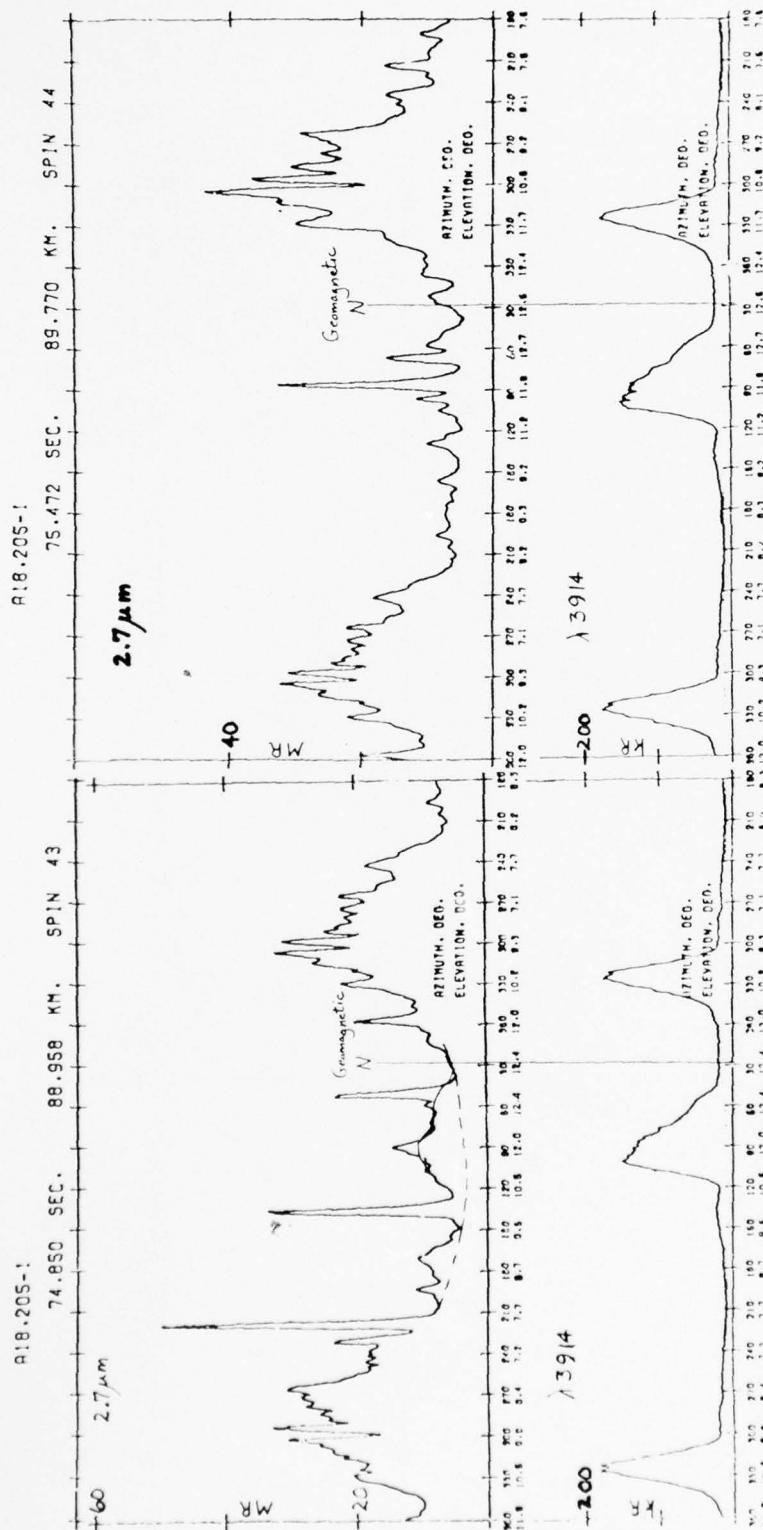
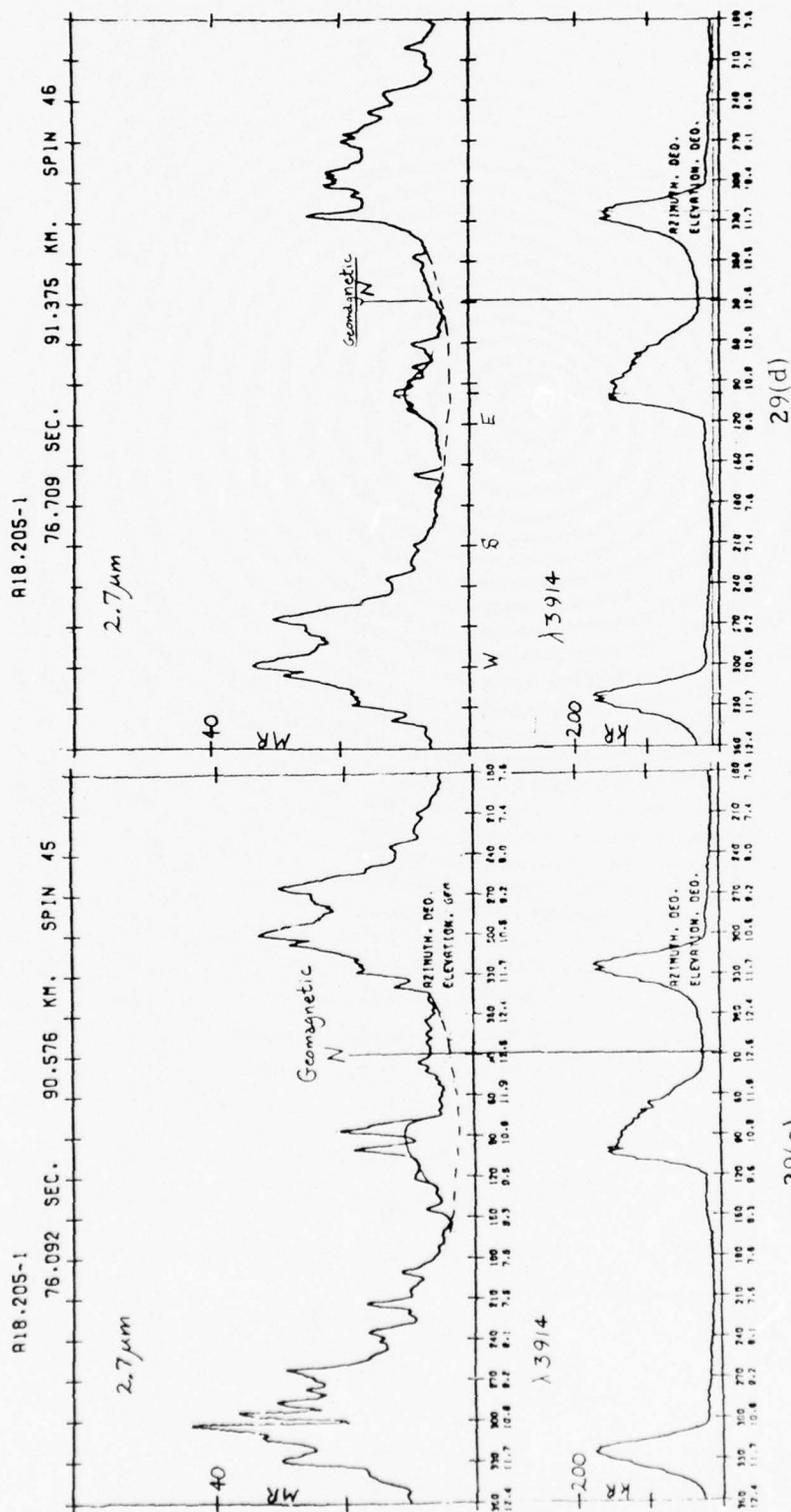
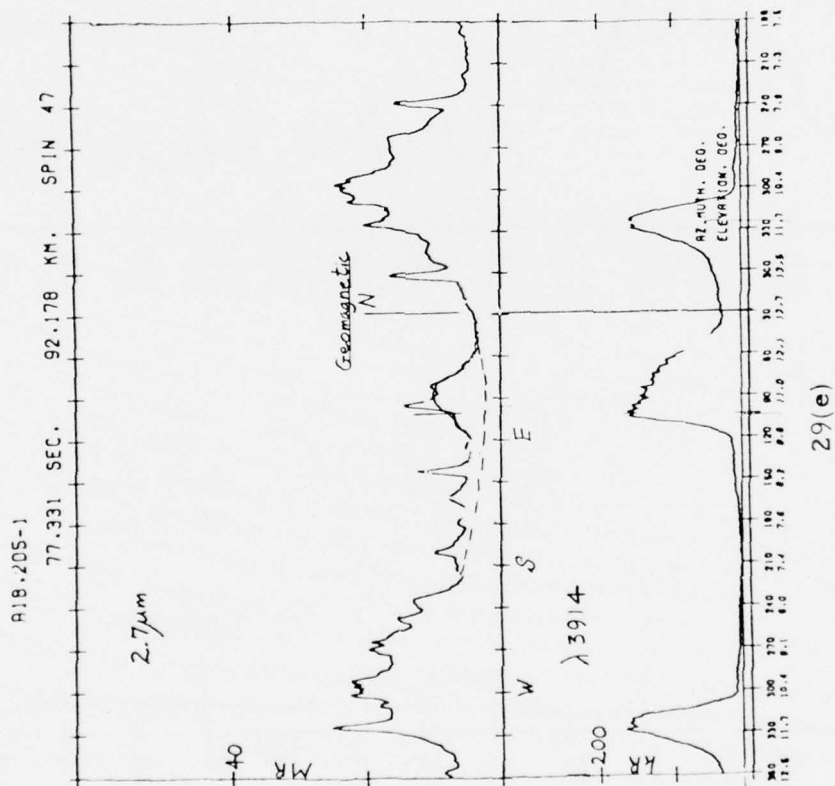


Figure 29a-e. Five elevation-azimuth spin cycles of 2.7 μ m and λ 3914 radiance distributions from A18.205-1 upleg, indicating the correlation of the two features at low rocket altitude. Spin 44 defines a limiting case without sufficient aurora-associated modulation for inclusion in the ratio calculated in the text.





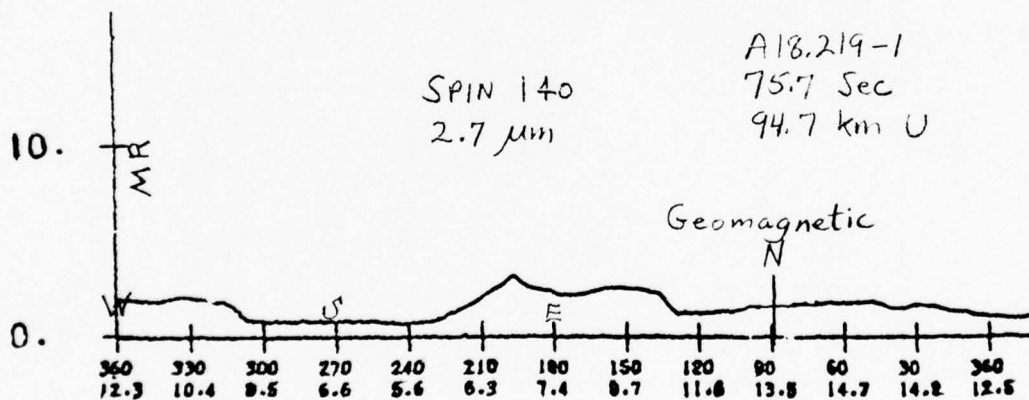
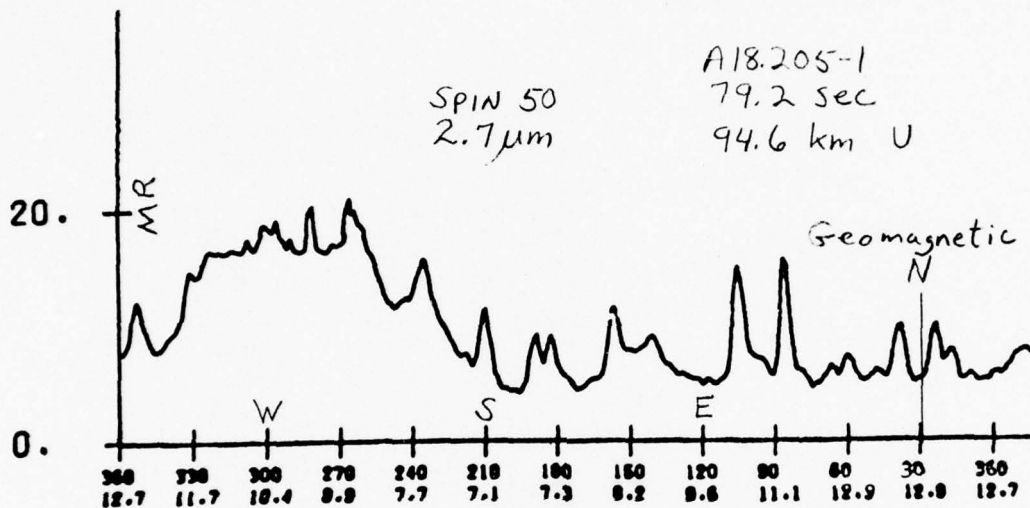


Figure 30. Comparison of 2.7 μ m side-looking radiometer scans from multi rockets A18.205-1 and A18.219-1 near 95 km on upleg, showing the higher mean radiance levels in the 1973 data. True geographic azimuth for A18.219-1 is 60° less than shown on the abscissa.

(ICECAP 74) was 0.6%. However, the mean $2.7\mu\text{m}$ background levels measured from the 1974 rocket (Fig 30), particularly above 90 km, are consistently 4 to 5 times less than those from A18.205-1. This again suggests that the discrepancy between the two experiments may be due to some error in absolute calibration. Our analyses of ICECAP 75 aircraft observations (Ref 2 and Section IV) indicates that 0.8% of the energy deposited by auroral electrons is eventually radiated as NO overtone photons.

On the downleg segment of A18.205-1, no enhancements in the $2.7\mu\text{m}$ radiometer were visually detectable. Starting at about 159 km, numerous "noise" spikes appear, and between 146 and 133 km the density of these spikes increases markedly (see Fig 31a). Later between 133 km and 66 km, where data taking stops, only a few random spikes with peak intensities of 20-60 MR appear (Fig 31b).

COMMENTS ON ARC-ASSOCIATED EMISSION AT 5.3 and $2.7\mu\text{m}$

Two potential causes of the excess $5.3\mu\text{m}$ radiation associated with the arc are 1) reaction of N atoms with O_2 molecules exciting $\text{NO}^\dagger(v \geq 1)$ (Ref 1), and 2) buildup of [NO] in the dosed region increasing the rates of atom interchange reactions $\text{NO} + \text{O}' \rightarrow \text{NO}^\dagger(v = 1) + \text{O}$ and scatter of earthshine (Ref's 5 and 10). (The volume rate of interchange reactions also increases with [O] and temperature (Ref 2).) Fig 26 indicates that the radiometer is biased towards radiation excited by the latter mechanisms, since it detects about $2\frac{1}{2}$ times as many of the (1,0) quanta as generally longer-wavelength $\Delta v = 1$ cascade quanta from $\text{N} + \text{O}_2$ chemiluminescence.

Despite this detection bias, the excess $5.3\mu\text{m}$ radiances follow the $\lambda 3914$ fluorescence peaks very closely, thus indicating that they are caused by relatively "prompt" reactions. As Fig 24 shows, the azimuth angles of the peak intensities correlate very closely (within 5°), as do the angular widths. A similar proportionality of maximum intensities is shown in Fig 25. The characteristic time for chemi-

luminescent emission from NO in IBC II aurora at 100 km altitude (following "standard" aerochemistry) is ~ 10 sec. Therefore if the arc remains stable at this time scale, the location and intensity of $5.3\mu\text{m}$ infrared emission would appear to follow the energy input.

Radiations depending on the NO concentration, on the other hand, depend on the time integral of the dose rate. We would expect any $5.3\mu\text{m}$ enhancements resulting from processes 2) to be "smeared" by upper-atmospheric winds and diffusion in the time needed to build up [NO]. Specifically, at typical arc altitudes, transport by winds along with a diffusive spread of a few km in that time (Page VIII-5 of Ref 1) would result in about 50 km displacements in 1000 sec. The close geometric and intensity correspondence of the visible prompt air fluorescence with infrared emission is inconsistent with such movements. Furthermore, as noted in Ref 2, typical $5.3\mu\text{m}$ zenith brightnesses from ~ 100 km under relatively quiet auroral conditions are of the order of 1 MR which, with the van Rhijn gain from the instrument viewing angle of 10° , would result in ~ 5 MR measured radiance. Since the observed excess $5.3\mu\text{m}$ radiances are typically 10 MR, a factor of about 3 increase in [NO] in the arc would be required to explain the infrared data on the basis of atom interchange plus earthshine scatter. At least 2000 sec of predosing would have been needed to provide such a buildup (Appendix VIII of Ref 1), which wasn't the case (see the All-sky photographs, and Fig 2-22 of Ref 5).

Strong enhancements seen by the sidelooking $2.7\mu\text{m}$ radiometer (p 52) provide further supportive evidence that $\text{N} + \text{O}_2$ chemiluminescence is the primary source of the excess $5.3\mu\text{m}$ radiances. NO overtone radiation of course requires population to the $v = 2$ vibrational state, the volume rate of which by reactions 2) is negligible. Although the possibility exists that some contribution may be coming from increases in [NO] in the dosed region, the resolution of the experiment is not sufficiently high to allow its assessment.

SECTION II

PARTIAL REDUCTION OF PHOTOMETER AND RADIOMETER DATA FROM MULTI- EXPERIMENT ROCKET A18.219-1

INTRODUCTION

Black Brant A18.219 1, the third of ICECAP's multi-instrumented rockets, was launched from Poker Flat on 25 Feb 1974 at 0738:30. Its purpose was to provide information about short wavelength-infrared radiation resulting from bombardment of air by energetic charged particles. We present here some of those data from the side-looking radiometers and photometers that, following a "quick-look" examination, appear to have the most direct application to nuclear-effects simulation. Reference is made to our reductions of data similarly obtained from the 1972 and 1973 multi rockets (Section I of Ref 1 and Section I of this report), which contain information on procedures for accessing the data, geometric relationships between the arc and rocket, and other aspects of these HAES tests.

A preliminary characterization of the 25 Feb auroral ionosphere is presented in Appendix VII of Ref 2, and more complete ground-support data in Ref's 11 and 12. Fig 32 shows the rocket's trajectory against the moving arc (and later, multiple arcs), along with its peak radiance viewed from PKR (some rocket locations and auroral intensities have been corrected on Fig 32's original version in Ref 2.) Meridian scanning photometers (Ref 11) and All-sky photographs (Ref's 1 (p 86), 2, 12, 13 and Section III of this report) show a system of weak arcs merging to form a single broad, relatively stable arc just north of PKR approximately 2 minutes before launch. The arc's peak $\lambda 5577$ intensity at PKR was ~ 150 kR at this time, and it remained above 50 kR during all of the data-taking period with the exception of ~ 30 sec near apogee. In the first 80 sec after launch the arc's "center" moved northward at about $1/2$ km/sec, which is about twice the rocket's horizontal velocity, as Fig 32 shows. Between 140 and

210 sec the arc moved back southward to just N of its zenith angle at launch, so that the rocket crossed the arc center's field line at 175 km altitude (160 sec). Then the arc again moved very rapidly to the N as a westward surge developed (Ref 12), recrossing the rocket's trajectory on downleg at ~180 km at 260 sec. Onboard scintillator data (Ref 5) show strong enhancements of energy flux at the rocket during these two crossings. A second arc of generally comparable brightness intensified over FYU near 220 sec, so that on downleg the side-looking instruments viewed two broad arcs plus other complex auroral structure to the north (see in particular the FYU All-sky photographs in Figure 55 and in Ref 13).

The instrument doors were opened at 64 km. Rocket stabilization was achieved by 86 km on upleg, with the rocket's major axis tilted 4° from the zenith toward a (southeast) azimuth near 130° (Fig 33), with the assumptions expressed in the next subsection. The instruments viewed the aurora at elevation angles not substantially different from those of A18.205-1, though the spin rate of 2.0 rev/sec was more than a factor two higher and the rocket's northward range a factor 2 lower. Destabilization began at 86 km on downleg, where the sidelooking data stop at 82 km. The most obviously arc-associated infrared emission is observed on downleg.

No enhancements were detectable in any of the photometer or radiometer azimuth plots during the two high-altitude crossings of the arc. Thus the energetic charged particle beam introduced no measurable spurious signals from these instruments. More importantly, even though the ionosphere plasma properties measured onboard the rocket cannot be directly coordinated with remotely-sensed infrared data, to the extent that the primary energy spectrum holds constant the scintillator data can determine an altitude profile of energy input in the arc.

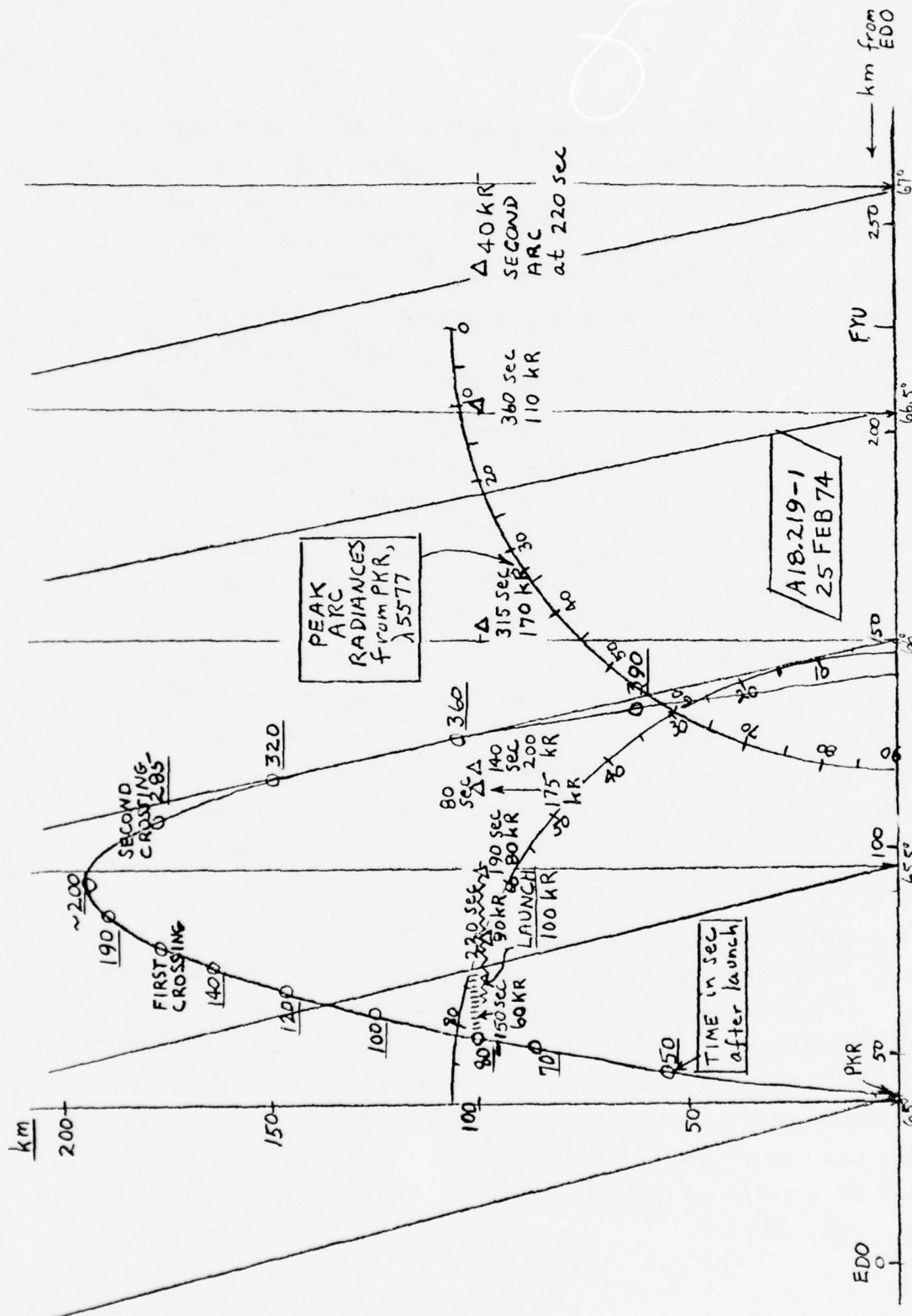


Figure 32. Trajectory of A18.219-1, with location of arc "centers" and maximum $\lambda 55.77$ radiance seen from PKR. Centers are 100-km altitude intercepts along the zenith angle at which meridian-plane radiance was maximum.

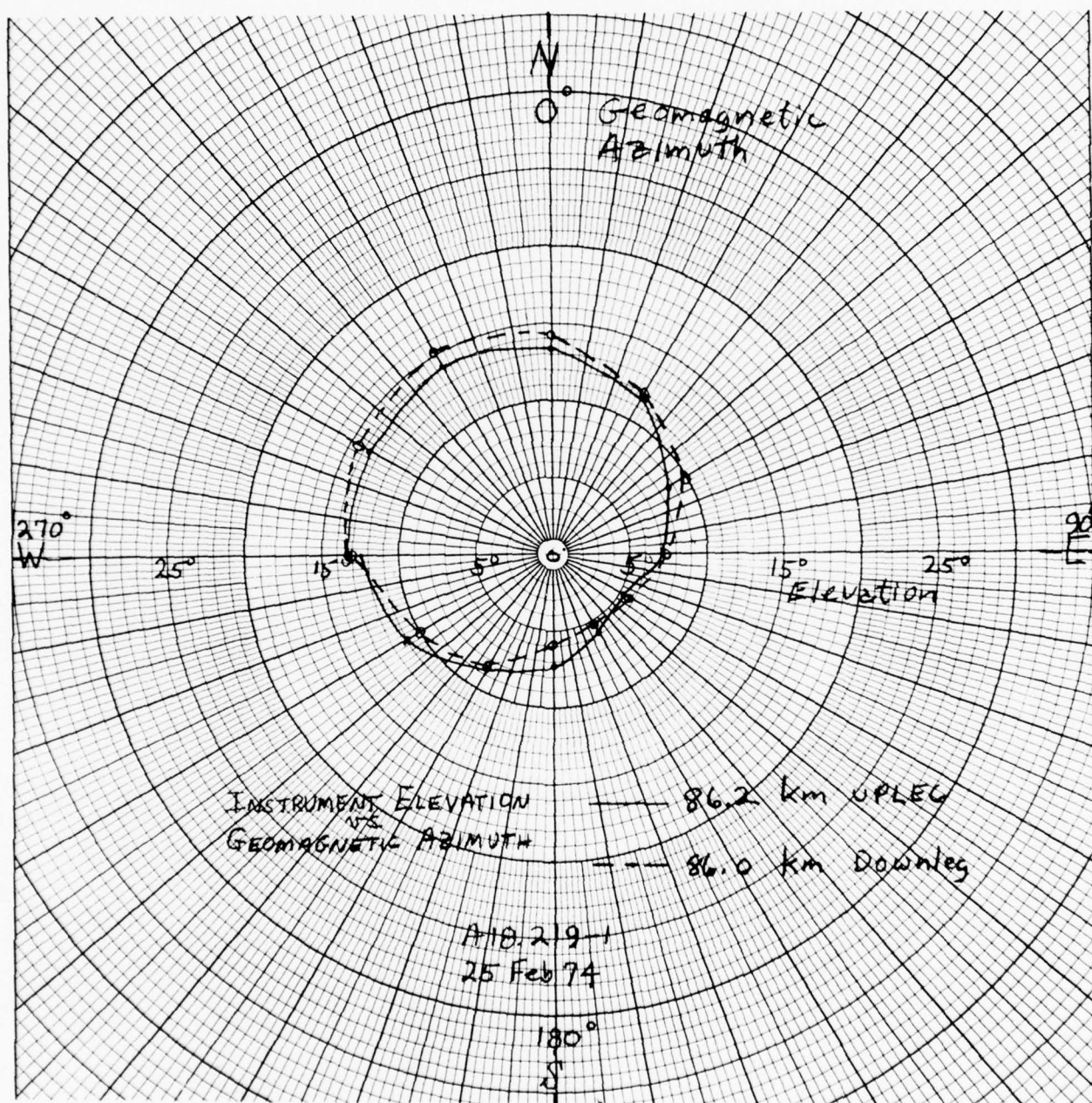


Figure 33. Elevation vs. azimuth of the side-looking photo-meters and radiometers after A18.219-1 stabilized.

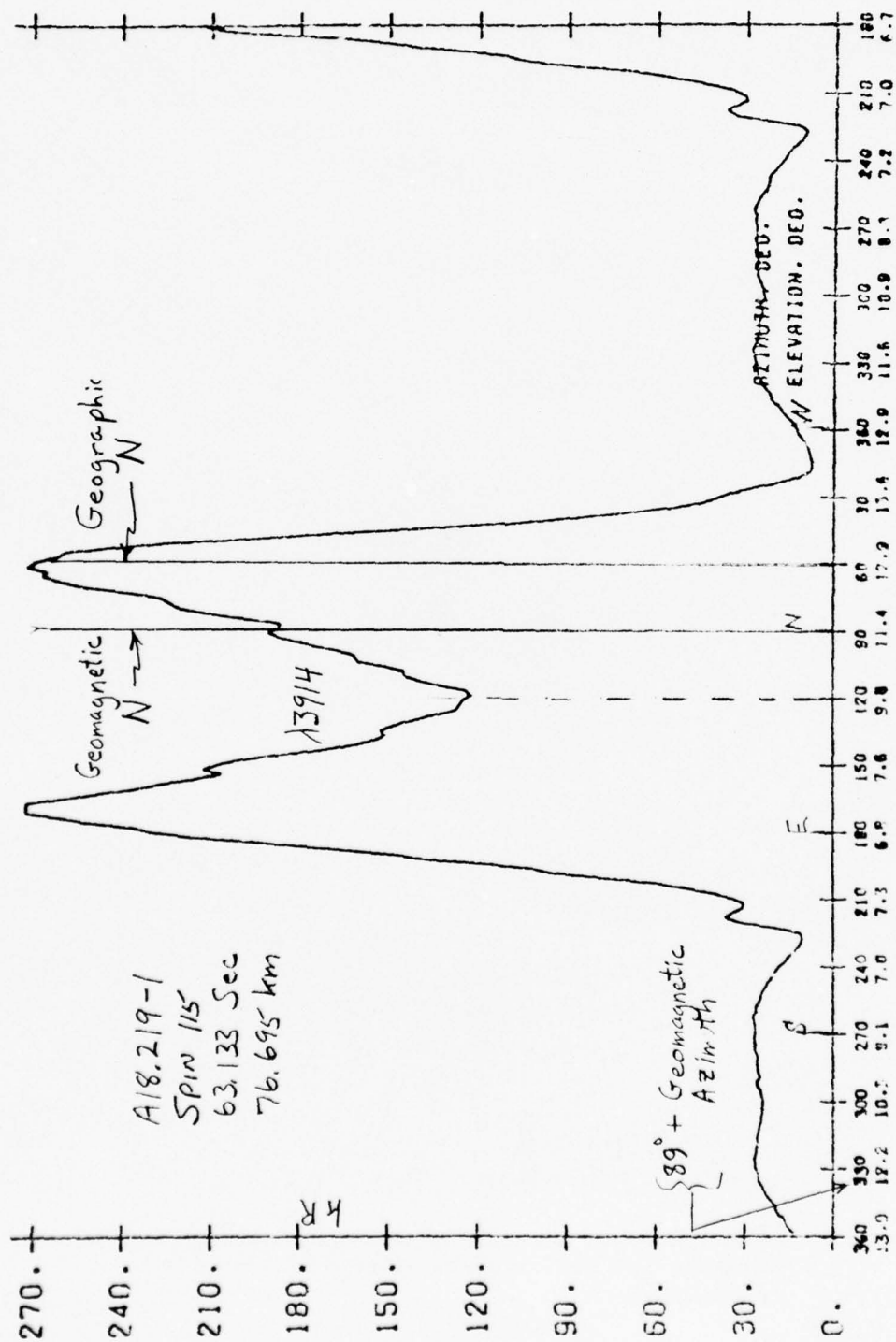


Figure 34. Representative elevation-azimuth scan from A18.219-1 showing the location of geomagnetic N as determined in the text.

INSTRUMENT ELEVATION AND AZIMUTH

The azimuth angles of the radiance data as received were not consistent with the geometry of the arc and location of the rocket instruments. This inconsistency was tentatively resolved with the aid of the known relative positions of emitting region and photometers on upleg. A gyro-system offset of 60° in azimuth was identified (Ref 14), making the azimuths consistent with those inferred from the onboard magnetometer. As shown in Fig 34, geomagnetic N is then placed at 89° on the original azimuth scale.

Our preliminary reduction assumes no similar slip in the instruments' elevation angles. While errors in elevation have little effect on these preliminary findings about $2.7\mu\text{m}$ and $4.3\mu\text{m}$ emission excited in auroras, accurate pointing is needed to understand the spatial distribution of excitation, ranges to and altitudes of emitting features, and infrared backgrounds at low altitudes. This offset can in all probability be corrected by fitting an approximately-known elevation angle dependence of background radiance, that is, by correlating using a model such as the one adopted in Fig 21.

UPLEG DATA - ENERGY INPUT FROM $\lambda 3914$ and $\lambda 5577$

Since some arc-associated infrared data maybe obtainable from this section of trajectory, and as a check on instrument performance and aurora intensities, we compiled some preliminary upleg radiance distributions.

The familiar east and west limb enhancements appear between 70 and 88 km rocket altitude (Fig 35). Maximum $\lambda 3914$ column intensity reaches ~ 280 kR in both limbs near 73 km, where the rocket is 63 km horizontally from the arc "center's" field line in the geomagnetic meridian plane. At 88 km, this horizontal range is 60 km so that with the typical (apparent; see previous subsection) 14° instrument elevation the intercept altitude in the meridian becomes 102 km. By this rocket altitude the two peaks have merged into a broad north-

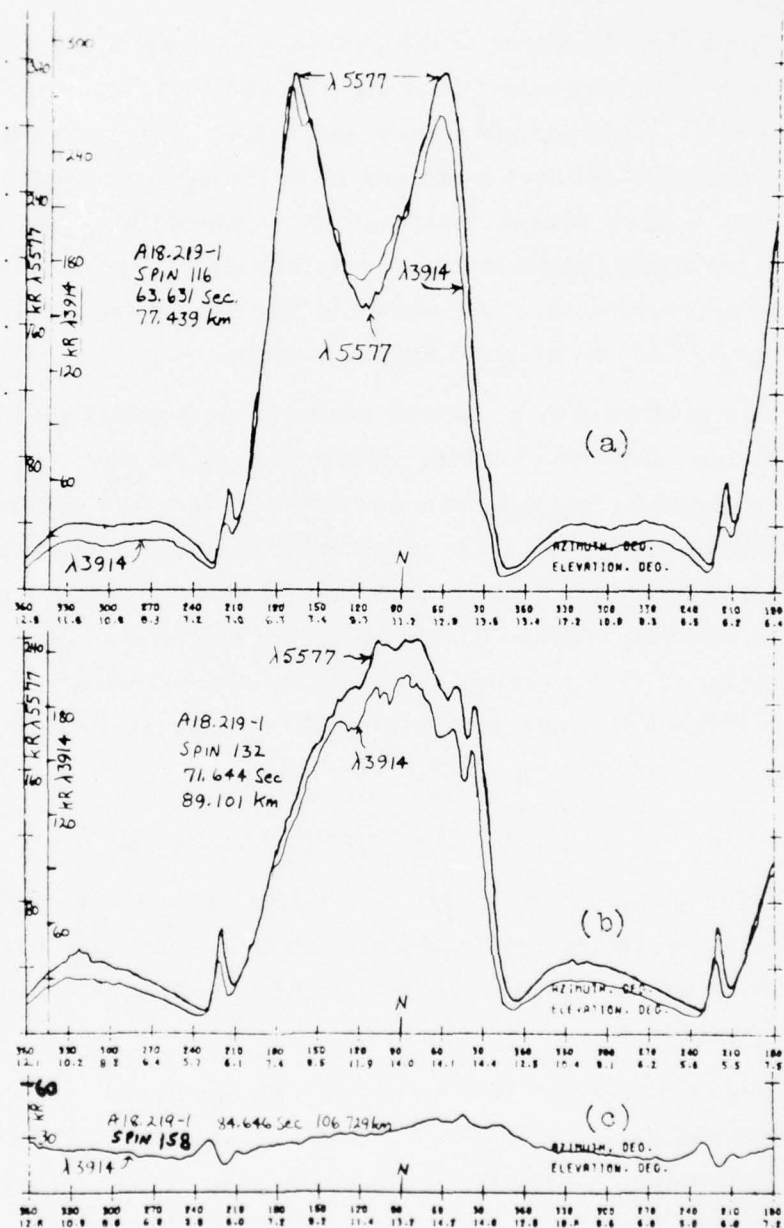


Figure 35. Three elevation-azimuth spin cycles on upleg of A18.219-1 showing the changing λ_{5577} and λ_{3914} angular distributions with rocket altitude. East and west limb enhancements remain resolvable below 88 km, compare Fig 2.

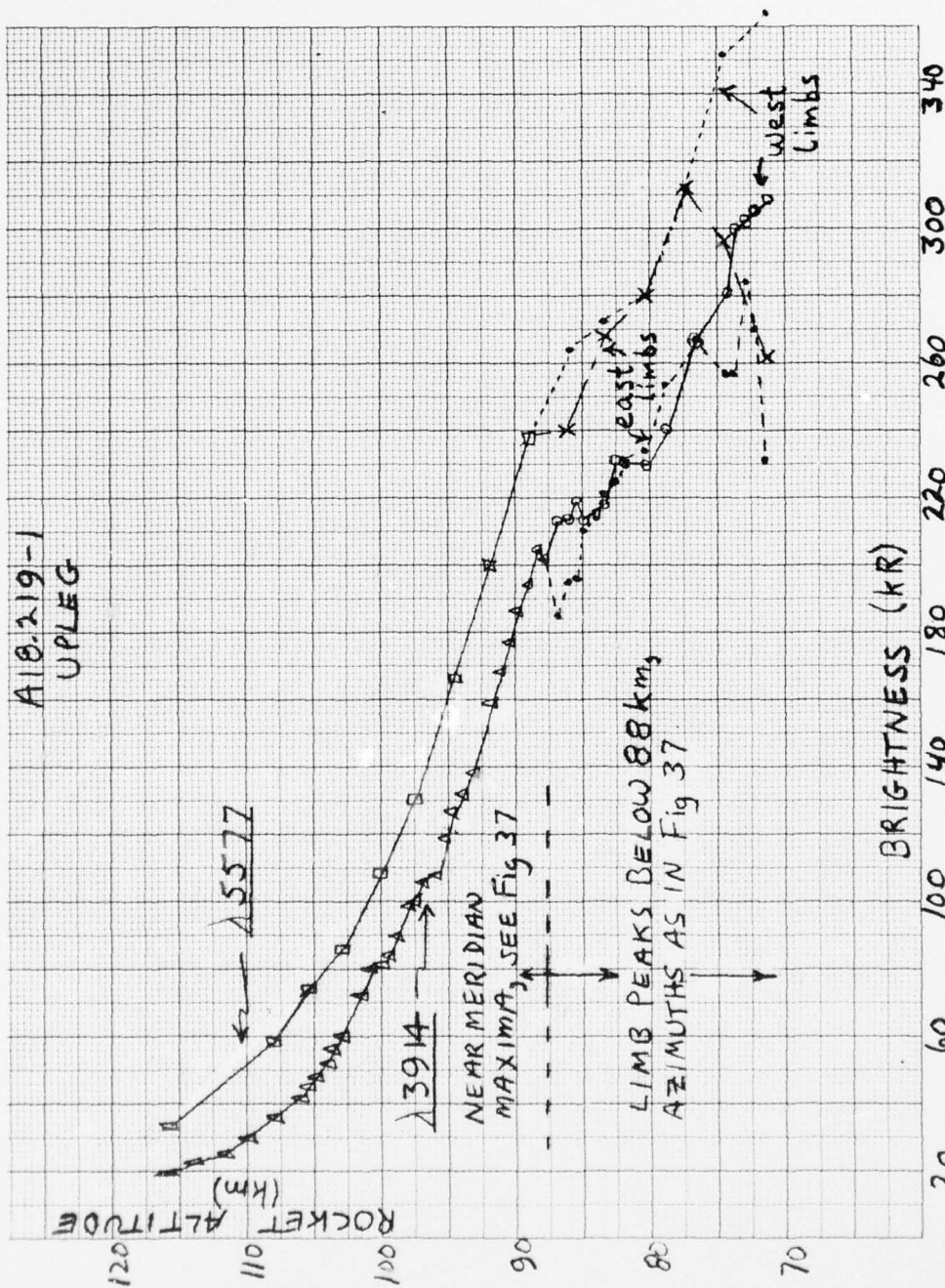


Figure 36. Altitude profiles of the 5577 and 3914 peak intensities with backgrounds included, A18.219-1 upleg.

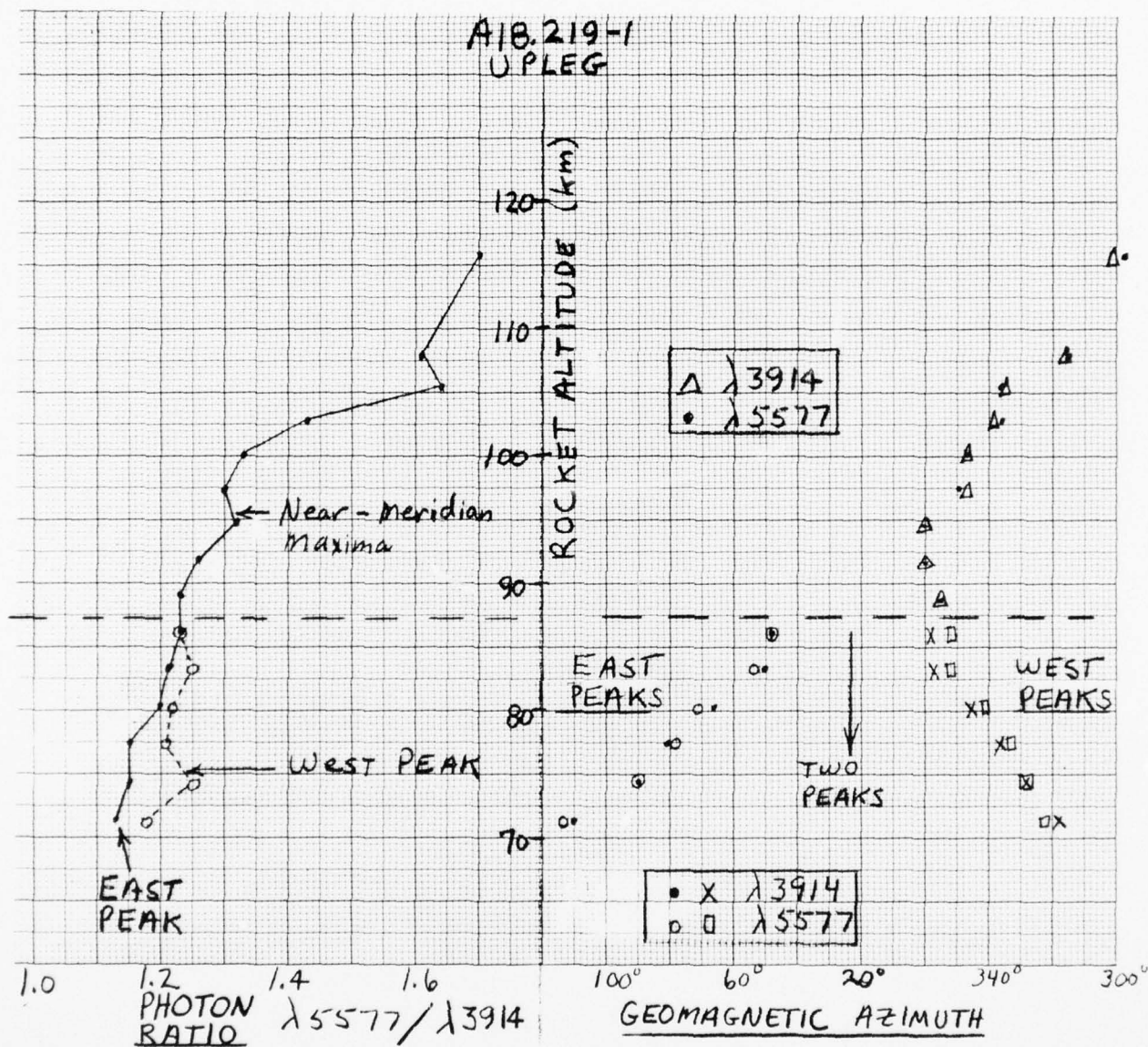


Figure 37. Altitude profiles of azimuths of $\lambda 5577$ and $\lambda 3914$ peak intensities, and $\lambda 5577 / \lambda 3914$ intensity ratios with backgrounds included, A18.219-1 upleg.

ward glow extending about 180° in azimuth with a maximum near the meridian direction (Fig 35). $\lambda\lambda 3914$ and 5577 altitude profiles of this central peak and (below 88 km) limb maxima are plotted in Fig 36, and the azimuth angles of all these maxima in Fig 37. As the rocket altitude increases the azimuths of the limb peaks approach the meridian, a behavior opposite to that observed from the 1972 and 1973 multis (see Fig 3). This is probably a combined effect of the northward motion of the distant arc and the elevation angle distribution of the photometers' azimuth scans.

The lower radiance (~ 30 kR $\lambda 3914$ at 90 km, 12 kR at 115 km) toward the southwest is due to the additional auroral structure seen over PKR near 60 sec (Ref 11). At apogee $\lambda 3914$ intensity is near-uniform and less than 1 kR (at all azimuths).

The $\lambda 5577$ photometer showed similar radiance distributions (Fig 35) with maximums below 88 km altitude; 312 kR (east limb) and 364 kR (west limb) (Fig 36). Azimuth angles of the peaks are closely correlated with those of $\lambda 3914$ (Fig 37), and again limbs converge to a single central maximum above 88 km. Ratios of peak column intensity (backgrounds included) up to 116 km rocket altitude are shown in Fig 36. Between about 72 and 92 km (80 - 106 km "best estimate" intercept altitude) the ratio increases slowly about a mean value of 1.2. Above 92 km it increases rapidly, reaching 1.6 at 105 km (compare Fig 8a of Section I).

UPLEG - NI FORBIDDEN LINES

The $\lambda 3466$ $N^2P - ^4S$ forbidden line radiance distributions (Fig 38) differ from $\lambda\lambda 3914$ and 5577 in that identifiable limb enhancements remain to about 135 km rocket altitude, holding near fixed azimuths (Fig 38 and 39); and the peak intensities in the west limb between 75 and 100 km are a factor $\sim 1\frac{1}{2}$ higher than those in the east limb (Fig 40). At 85 km rocket altitude the maximum column intensity ratio $\lambda 3466 / \lambda 3914$ is about 7×10^{-3} , which is close to that measured from A18.205-1 (p 34).

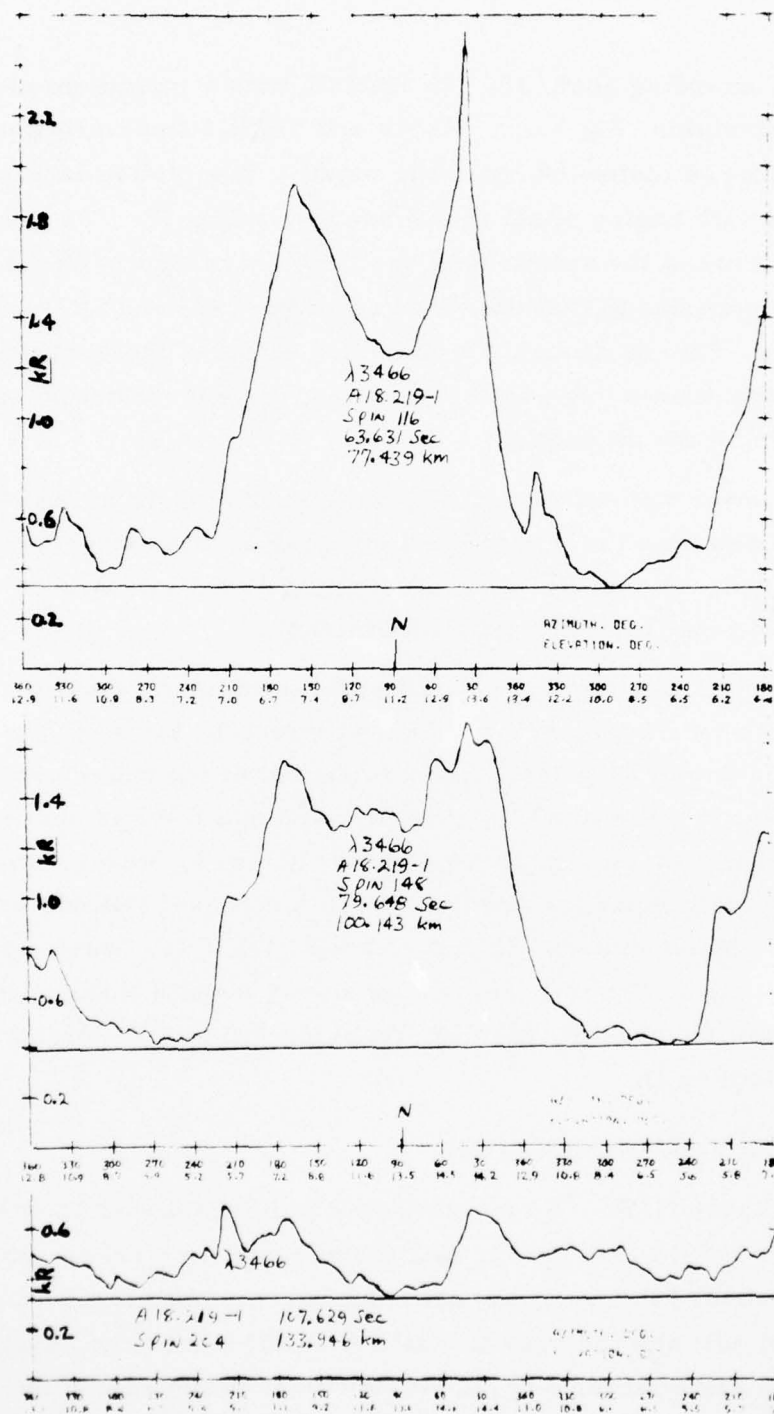


Figure 38. Three elevation-azimuth spin cycles on upleg of A18.219-1 showing the changing $\lambda 3466$ angular distributions with rocket altitude.

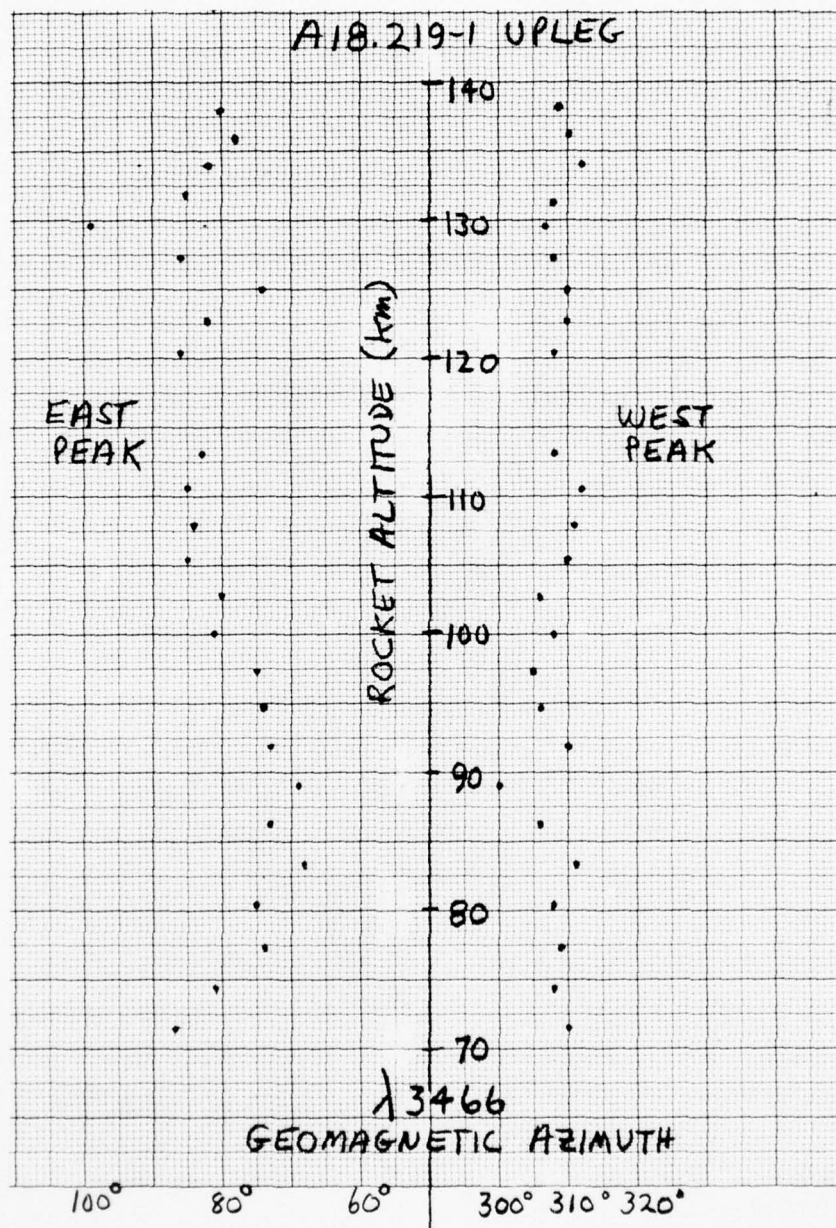


Figure 39. Altitude profiles of azimuth angles of $\lambda 3466$ east and west limb enhancements, A18.219-1 upleg.

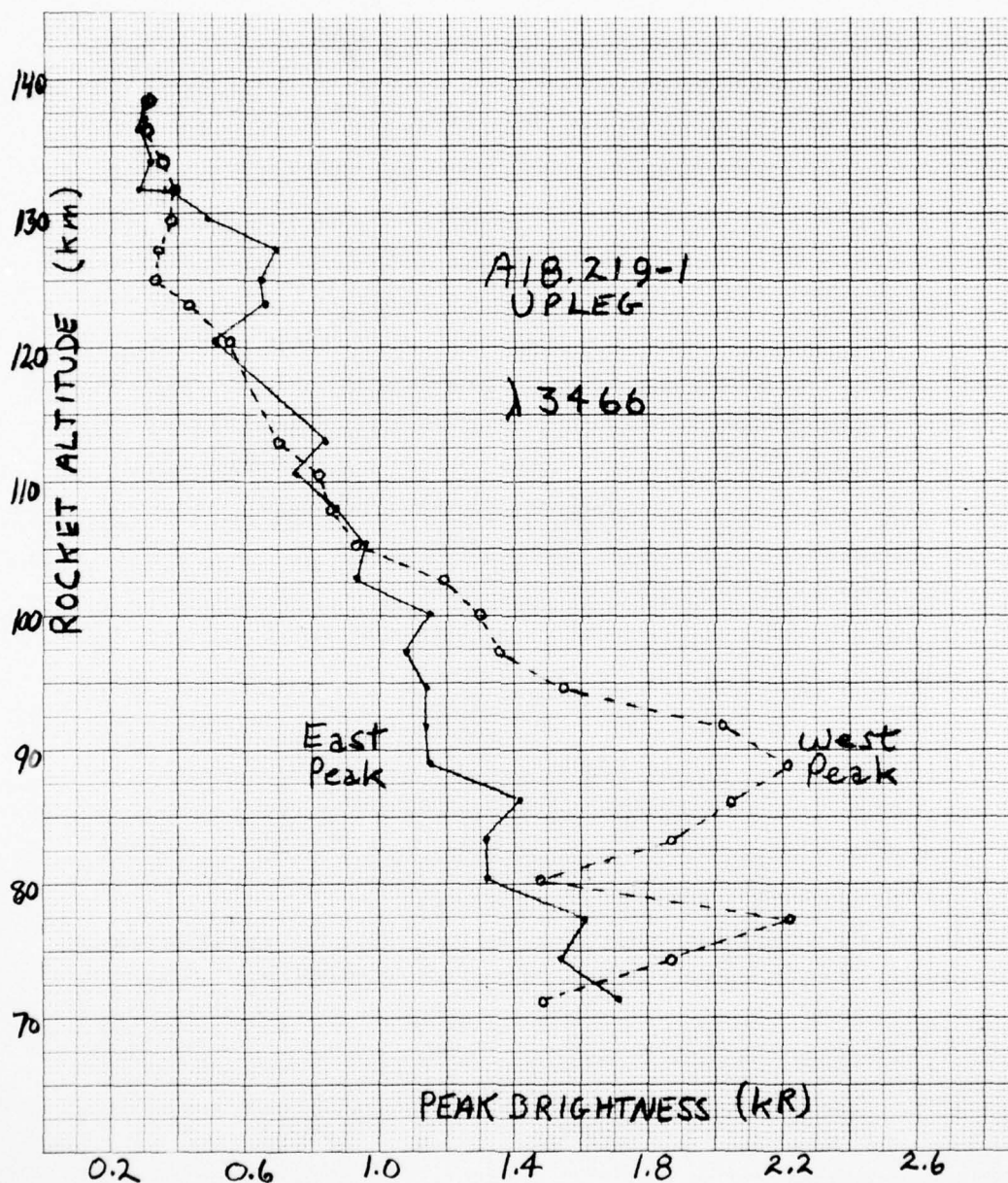


Figure 40. Altitude profiles of the $\lambda 3466$ east and west peak intensities, with mean baseline backgrounds in Fig 38 subtracted, A18.219-1 upleg.

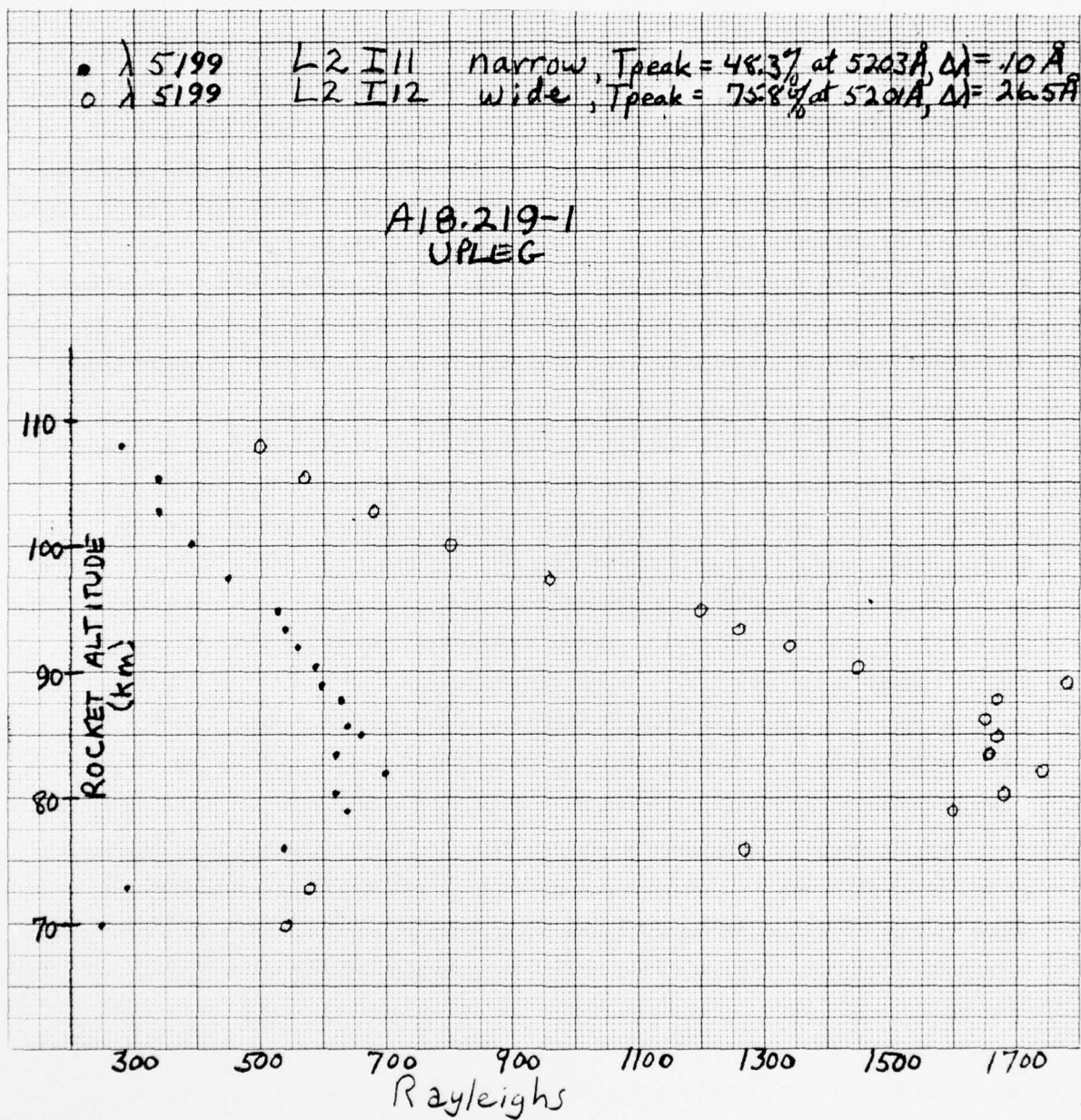


Figure 41. Altitude profiles of the $\lambda 5199$ meridian intensities measured by the wide- and narrow-band filter photometers, without correction for backgrounds, A18.219-1 upleg.

The two $\lambda 5199 \text{ N}_2^+ - ^4\text{S}$ photometers applied wide-band ($26\frac{1}{2} \text{ \AA}$ FWHM) and narrow-band (10 \AA FWHM) filters to permit subtraction of unwanted fluorescence (principally from the N_2^+ First Negative (0, 3) band, Fig 17 of Ref 1). Azimuth scans by each instrument also show limb-associated enhancements, unlike $\lambda 3466$ to altitudes of only about 86 km. To indicate typical uncorrected radiance levels, we plotted altitude profiles in the meridian (Fig 41). These intensities, ratioed to Fig 35's near-meridian $\lambda 3914$ intensities (see also Fig 11), indicate less fluorescence leakage in the narrow channel, as would be expected.

UPLEG -- $4.3\mu\text{m}$ and $2.7\mu\text{m}$ RADIOMETER DATA

Both radiometer scans showed numerous erratic pulsations up to 80 km rocket altitude. Between 80 and 87 km, both also develop large spikes regularly separated by 180° . These are off-scale ($> 50 \text{ MR}$) for about 40° in azimuth at $4.3\mu\text{m}$. By 91 - 92 km rocket altitude, the erratic pulsations have subsided. Then at 110 km a single spike (from what may be an object in the field of view) first appears near the geomagnetic meridian, off-scale at $4.3\mu\text{m}$ over $\sim 25^\circ$ in azimuth. Some evidence of this (spurious) emission is present almost to apogee in both radiometer signals.

The $4.3\mu\text{m}$ radiometer above 91 km sees a broad flat maximum to the N, where its (apparent) elevation angle is also near maximum. This "hump" lies in the same general direction as the $\lambda 3914$ increase in Fig 35b. Mean intensity over a spin cycle is $3\frac{1}{2} \text{ MR}$ by 110 km rocket altitude. The rough correlation of $4.3\mu\text{m}$ intensity with the broad arc-associated air fluorescence toward the north is under further investigation. These azimuth scans also contain information about the altitude profile of angular distribution of $4.3\mu\text{m} \text{ CO}_2$ thermal (plus vibroluminescent) radiation in the auroral ionosphere.

At $2.7\mu\text{m}$, the mean intensity at 93 km (after the pulsations have disappeared) is about $1\frac{1}{2} \text{ MR}$, also generally higher to the N than S. A broad $2.7\mu\text{m}$ increase centered near 45° W of N begins at about

98 km and reaches 6.5 MR by 106 km, with an azimuth angle dependence similar to the air fluorescence in Fig 35c. The correlation of these upleg $2.7\mu\text{m}$ radiance distributions with precipitation-indicating air fluorescence, and other features of the high-altitude background in this wavelength band, are also under further investigation. (As we noted earlier, we examined the downleg infrared data first because of their more obvious association with auroral activity.)

DOWNLEG -- CORRELATION OF $2.7\mu\text{m}$ EMISSION WITH AIR FLUORESCENCE

Between rocket altitudes of 120 and 95 km, the $2.7\mu\text{m}$ angular distribution shows good correlation with $\lambda 3914$ over complete azimuth scans as well as (perhaps more strikingly) in bright isolated auroral features. We have reduced some of these radiance data to ratios, as summarized in later Fig 51. The $4.3\mu\text{m}$ azimuth distributions also show some potentially useful auroral relationship, and therefore we have included a very preliminary reduction (subsection following).

As we noted earlier, the rocket re-intercepted the arc's field line near apogee (280 sec) as the arc was moving to the N in connection with the westward surge phase of a magnetospheric substorm. The mean northward transport rate of the intensely-irradiated auroral volume was about 1 km/sec, four times the rocket's horizontal speed, as the radiometers descended toward 110 km between 300 and 360 sec. A second broad arc had intensified over FYU by 220 sec. Meridian photometer scans from PKR for the time period 335 - 370 sec (Fig 42) show this development. The S edge of the bright auroral region was then of the order of 100 km N of the descending rocket, a range comparable to that on downleg of A18.205-1, although the arc's field lines are tilted in an opposite sense.

$2.7\mu\text{m}$ and $4.3\mu\text{m}$ radiance scans near 102 km, typical of those between ~115 and 95 km, are compared to $\lambda\lambda 3914$ and 5577 in Fig 43 and Fig 44. At these rocket altitudes the $2.7\mu\text{m}$ intensities are more

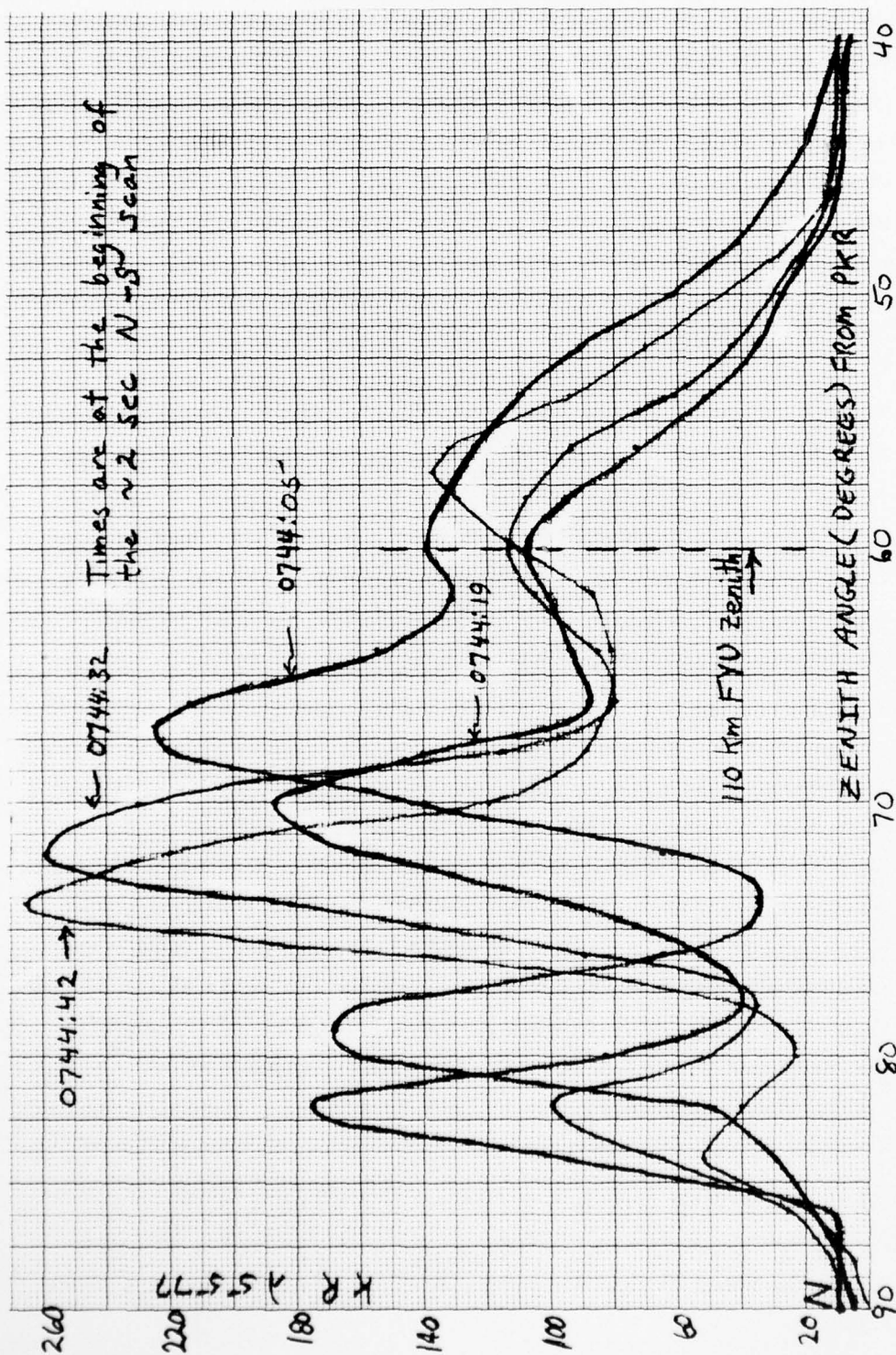


Figure 42. $\lambda 5577$ meridian photometer scans from PKR showing the complex auroral structure during downleg of A18.219-1.

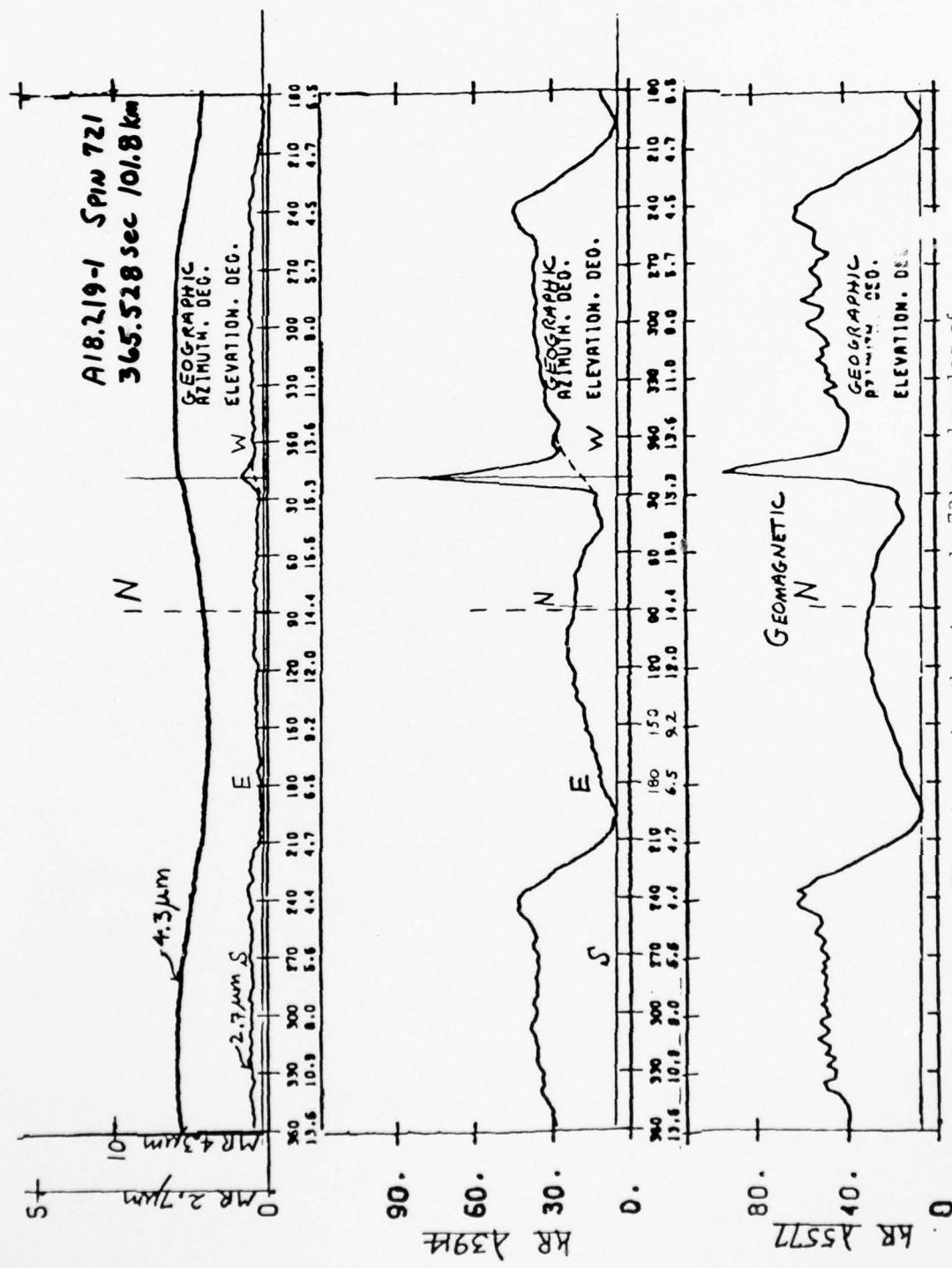


Figure 43. Elevation-azimuth spin cycle 721 on downleg of A18.219-1 comparing $\lambda 3914$, $\lambda 5577$, $2.7\mu m$ and $4.3\mu m$ radiance distributions near 102 km rocket altitude. The dashed lines establish backgrounds for the altitude profiles in Fig 47.

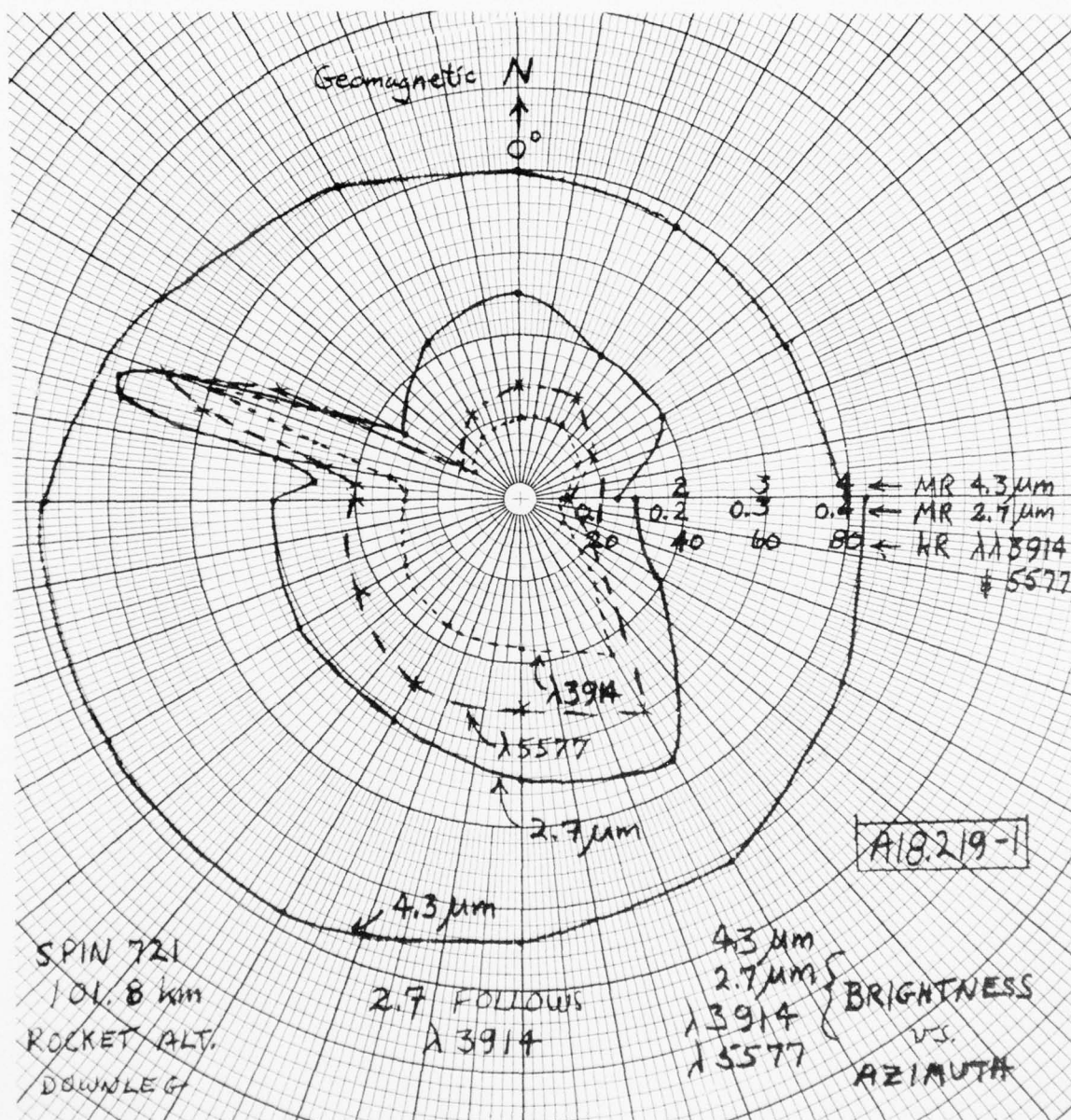


Figure 44. Polar plot of Fig 43's four radiance distributions near 102 km, A18.219-1 downleg.

or less following the prompt air fluorescence at all azimuths. In particular, the peaks near 70° W line up, as do the broad enhancements to N & S.

This narrow peak first appears in the $\lambda\lambda 3914$ and 5577 azimuth scans at about 135 km rocket altitude (337 sec) and persists until cessation of data taking at 82 km. The similar enhancement at $2.7\mu\text{m}$ is visually detectable in the scans between 120 and 94 km. These isolated peaks may be enhancements associated with the westward surge, or a limb effect of the 17° eastward azimuth angle of the trajectory's plane; they are not obvious from the All-sky photographs. (Compare the increase in intensity in the west limb from downleg A18.205-1 at low altitudes, Fig's 15 and 16.)

Before treating these isolated peaks we first plotted (Fig 45) the $2.7\mu\text{m}/\lambda 3914$ ratio for two complete consecutive spins near 102 km altitude, including all "backgrounds." Toward the meridian this ratio is about 12, and then it increases briefly to 22 just N of the spike where $\lambda 3914$ decreases. The low photon ratio 7 at the peak of the spike proper may be due to spatial filtering of the $2.7\mu\text{m}$ "microradiance" by the broader (and perhaps slower) radiometer instrument. Continuing toward the south and southwest, where typical $\lambda 3914$ radiance is 35 kR, we find a ratio about 9. Then due east (near 90°) it again briefly increases to ~ 24 where $\lambda 3914$ decreases more rapidly than $2.7\mu\text{m}$, which may be due to some infrared background or off-axis contribution (at apogee, where the sky radiance is expected to be very small, the radiometer signal was negligible compared to this "background" at 102 km). We note that when the infrared radiance is $\gtrsim 400$ kR (except in the narrow western spike) the photon ratio is 10 - 12.

The azimuth angles of the $2.7\mu\text{m}$ peaks follow $\lambda 3914$ (Fig 46), offset by a few degrees to the west. We plotted altitude profiles of these peaks and their ratio to $\lambda 3914$ (Fig 47) with and without backgrounds defined as indicated by the dashed interpolations in Fig 43. The $\lambda 5577$ peak's altitude profile, along with the ratio $\lambda 5577/\lambda 3914$ at peak

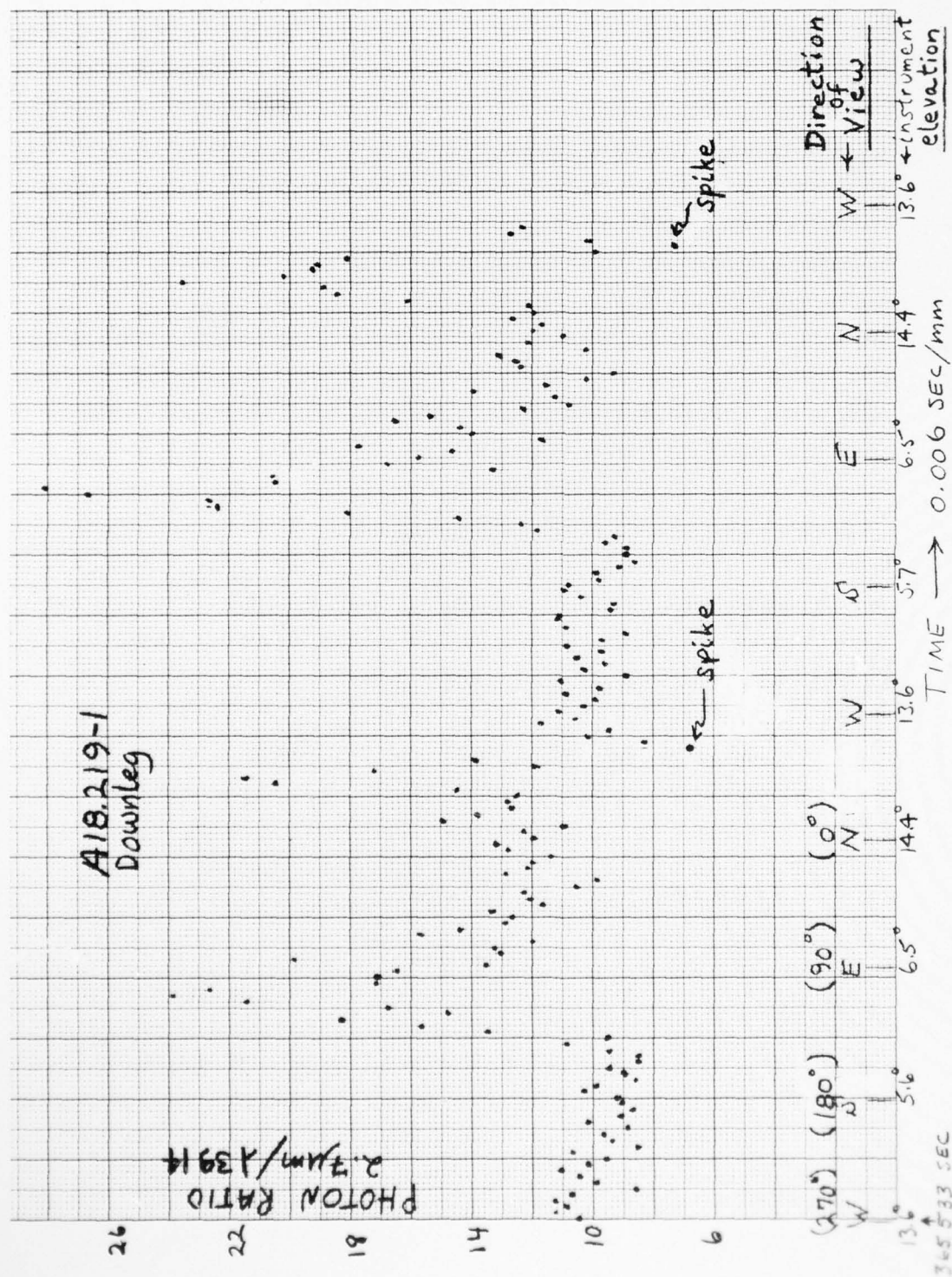


Figure 45. Azimuth profile of 2.7 μ m/ λ 3914 intensity ratios with backgrounds included for spins 721 and 722, A18.219-1 downleg. Original data in Fig 43.

AD-A047 376

PHOTOMETRICS INC LEXINGTON MASS

F/G 4/1

DATA REDUCTION AND AURORAL CHARACTERIZATIONS FOR ICECAP III. HA--ETC(U)

JAN 77 I L KOFSKY, D P VILLANUCCI, R B SLUDER DNA001-76-C-0161

UNCLASSIFIED

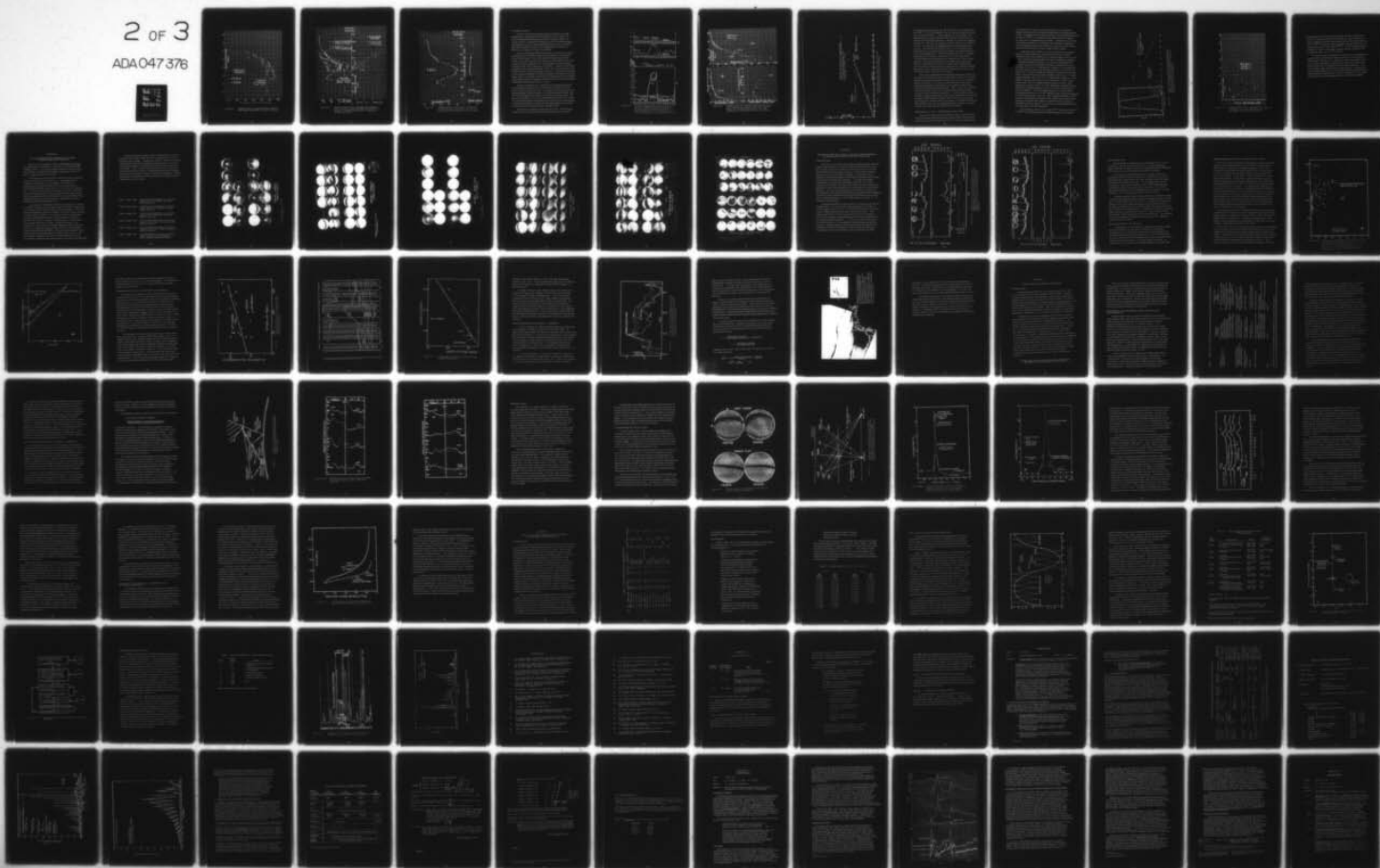
PHM-02-77

DNA-4220F

NL

2 OF 3

ADA047376



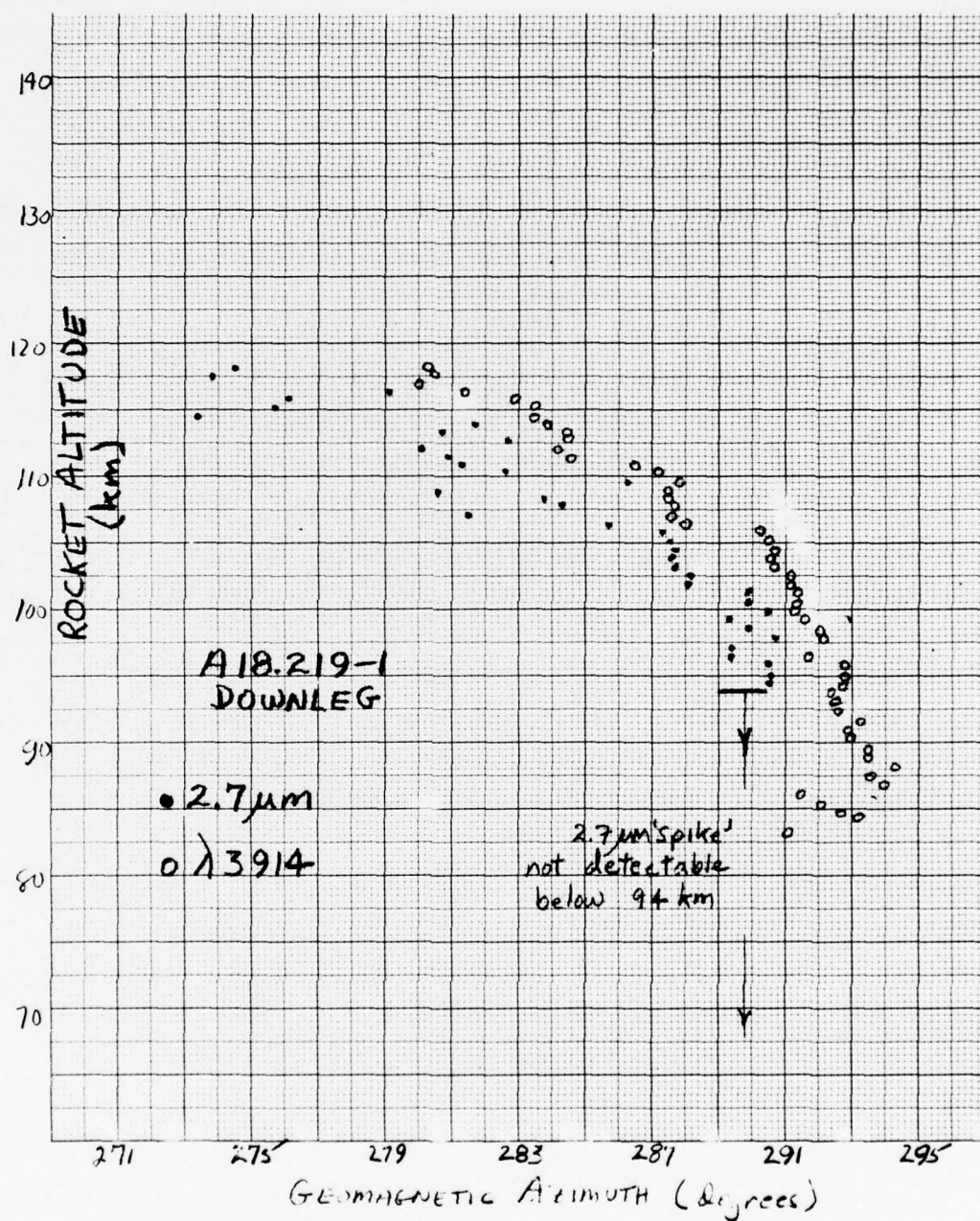


Figure 46. Altitude profiles of azimuths of the 2.7 μ m and λ 3914 spikes near 70° W, A18.219-1 downleg.

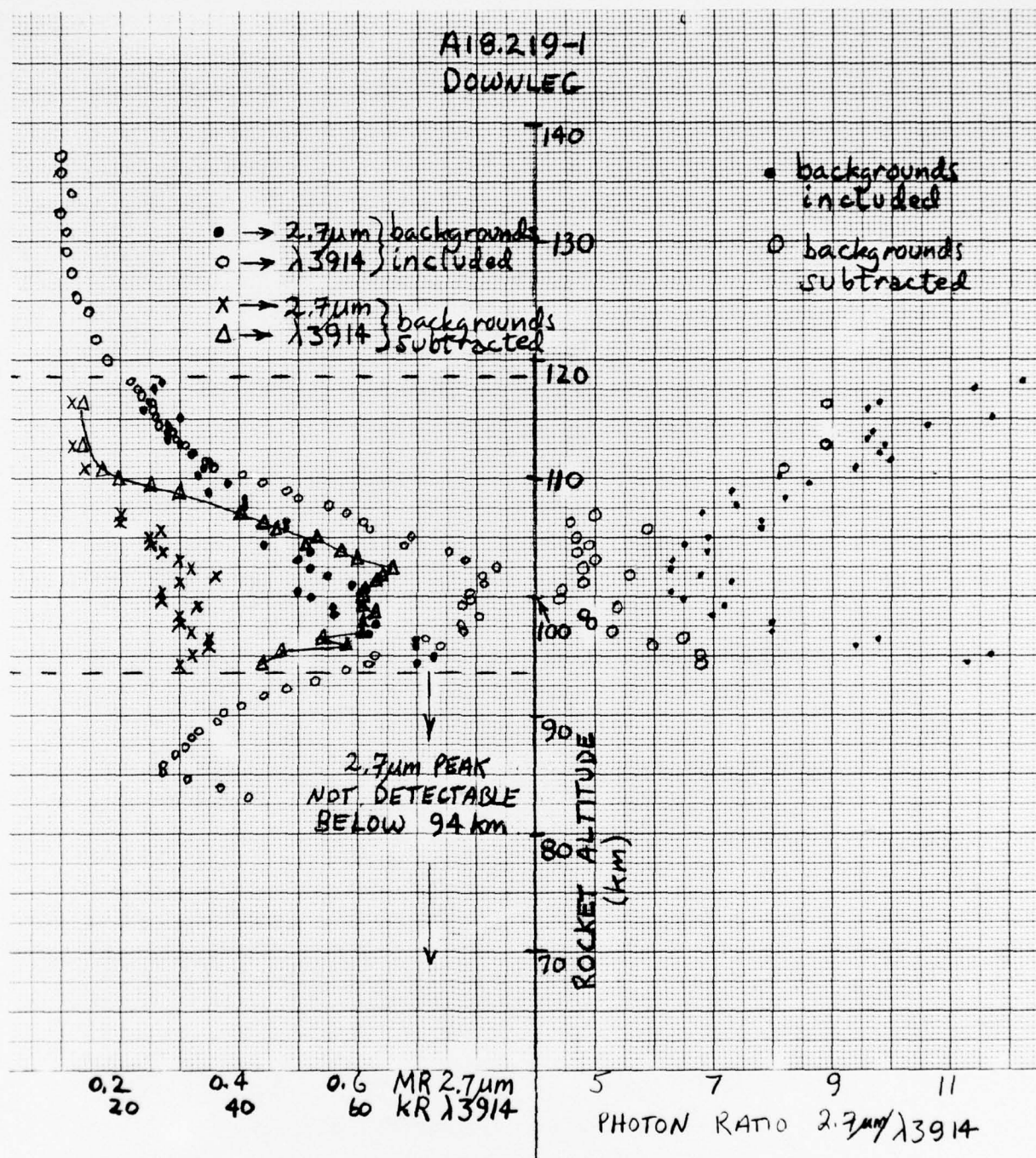


Figure 47. Altitude profiles of the 2.7μm and λ3914 westward spike intensities and 2.7μm/λ3914 ratios, A18.219-1 downleg. Background subtraction is explained in the text and Fig 43.

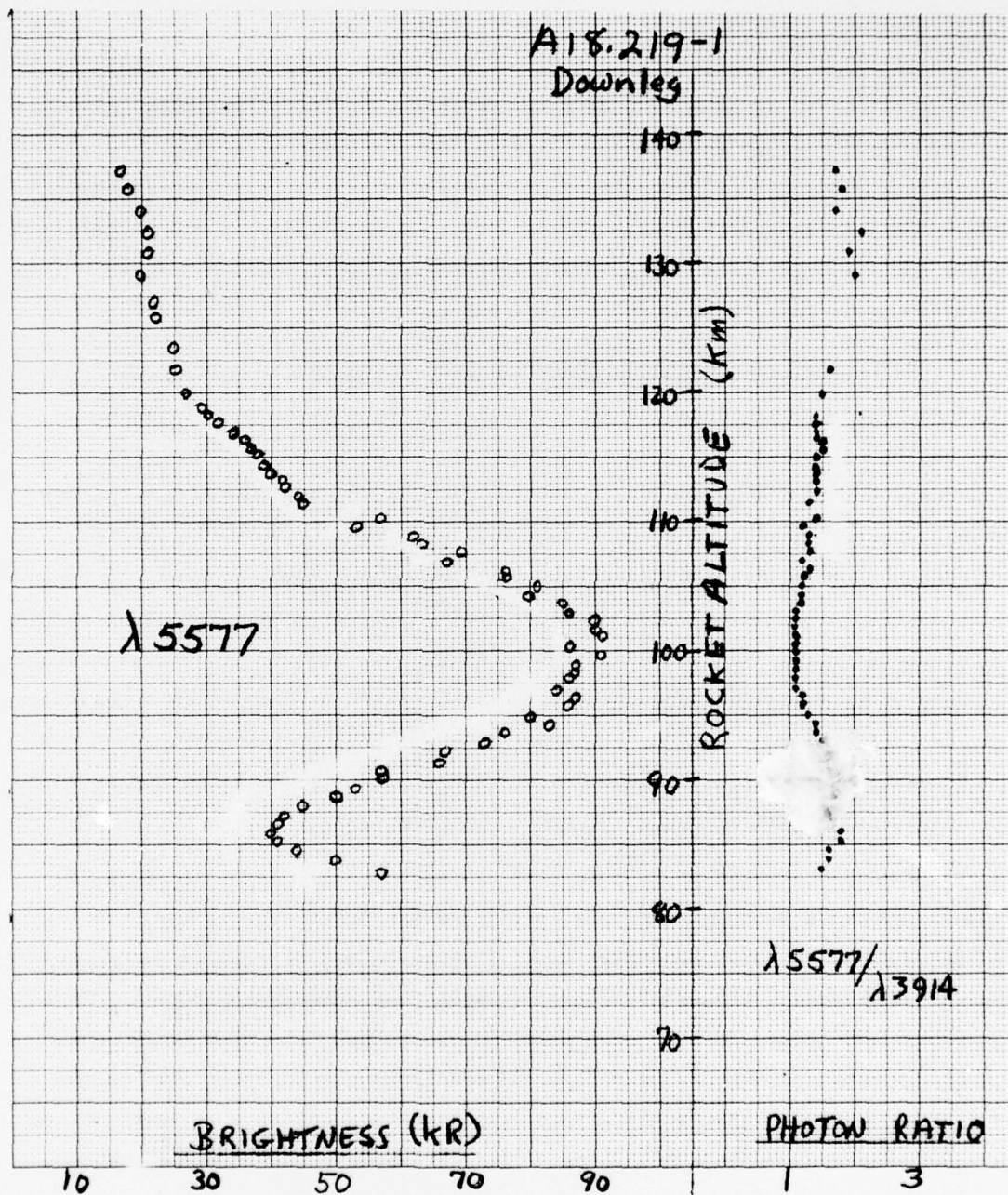


Figure 48. Altitude profiles of $\lambda 5577$ peak intensity, and $\lambda 5577 / \lambda 3914$ ratio in the spike near $70^\circ W$, with background included, A18.219-1 downleg.

are shown in Fig 48.

The low contrast of the $2.7\mu\text{m}$ pulses (they become virtually undetectable in scans below 94 km and above 117 km), and the uncertain background subtractions even when contrast is higher, of course results in considerable ambiguity in Fig 47's altitude profiles. The apparent factors-of-two altitude dependence of the $2.7\mu\text{m}/\lambda 3914$ peak ratios could be an effect of the "background" as well as the difference in response of the two instruments.

At lower downleg altitudes (below 95 km), the intensity correlation extends over a smaller range of azimuth angles, as the typical scans in Fig 49 show. The $2.7\mu\text{m}$ intensity toward the southwest increases (Fig 49a), and by 85 km the mean $2.7\mu\text{m}$ radiance level over a spin cycle has reached about 2.5 MR and shows even less general correlation with the air fluorescence (Fig 49b). Between 88 and 82 km secondary $2.7\mu\text{m}$ peaks develop near 345° , close to the direction of the $\lambda 3914$ west limb, which we included on Fig 51. The cyclically-varying $2.7\mu\text{m}$ radiance generally increases with apparent radiometer elevation angle (refer to our earlier comments on the validity of these elevations), in the opposite sense to expected van Rhijn increases in the OH airglow fundamental bands (about a factor 6, Ref 8).

We also compiled $2.7\mu\text{m}$, $\lambda 3914$ and $\lambda 5577$ altitude profiles for the meridian direction with the rocket between 120 and 83 km (138 - 98 km intercept altitude) (Fig 50). The scan in Fig 43, typical of these altitudes shows a broad increase in the $\lambda 3914$ radiance extending from 315° to 105° geomagnetic azimuth; its maximum intensity stays $\sim 10^\circ$ east of the meridian. The $2.7\mu\text{m}/\lambda 3914$ photon ratio (Fig 50c) is about 10, with altitude effects presumably due to the inclusion of background. A preliminary attempt to subtract the flat backgrounds such as shown in Fig 43 resulted in generally lower meridian ratios.

Figure 51 is a summary scatter plot of $2.7\mu\text{m} - \lambda 3914$ downleg intensities from several azimuths, without background corrections.

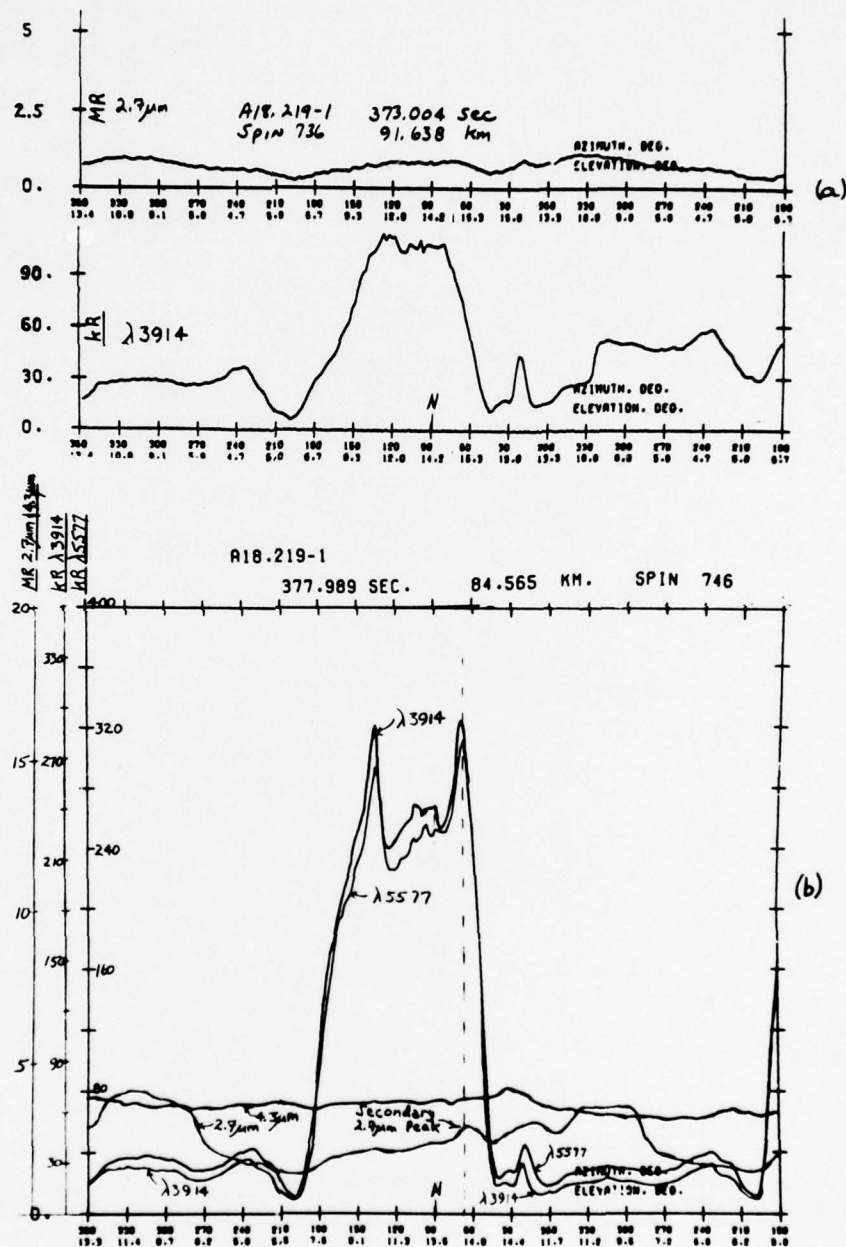


Figure 49. Elevation-azimuth spin cycles on downleg of A18.219-1 showing (among other features) the decreased correlation of 2.7μm radiance with λ3914 between 91½ and 84½ km and the increased 2.7μm intensity toward the southwest.

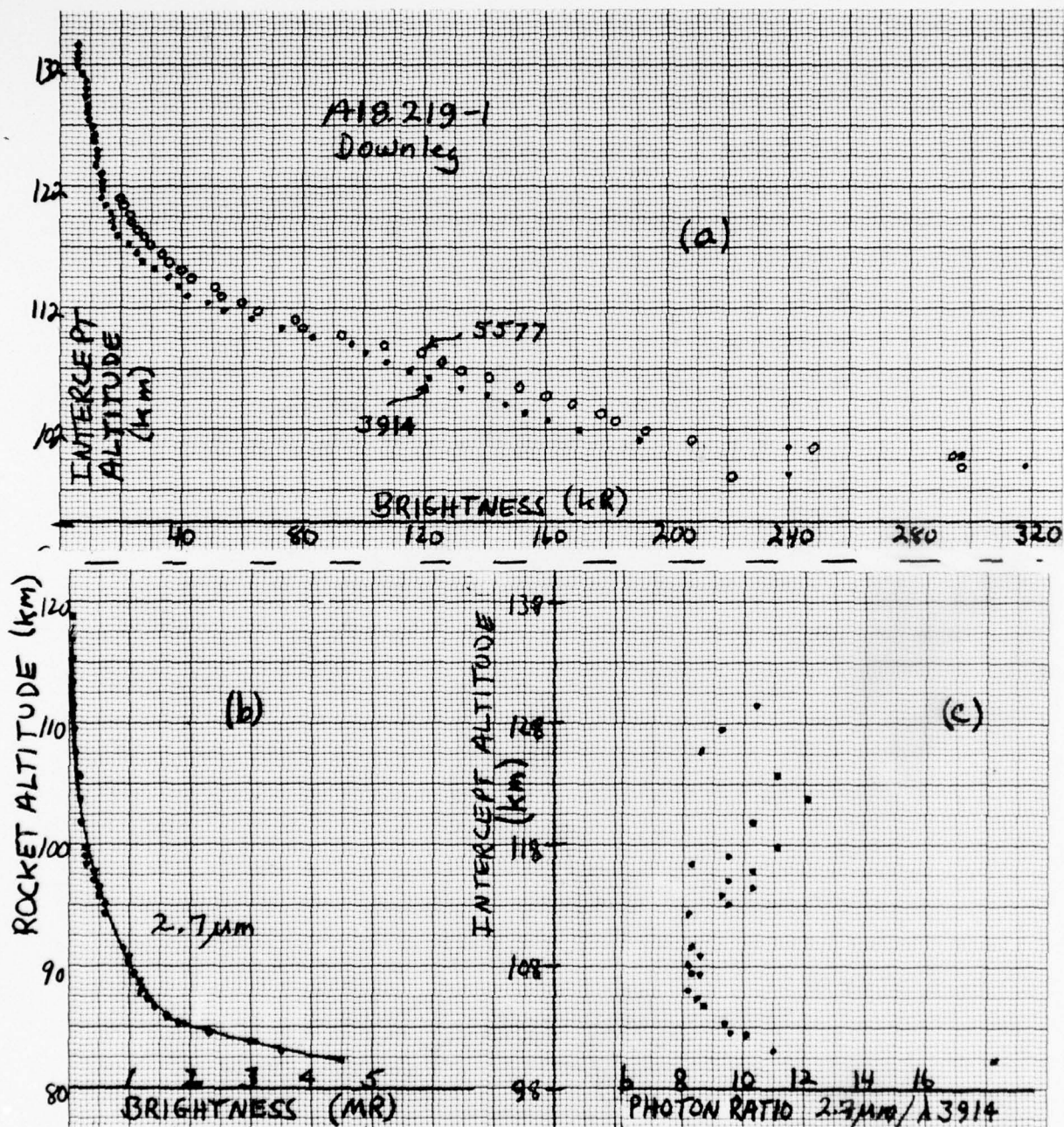


Figure 50. Altitude profiles of meridian intensities for (a) λ 3914, λ 5577 and (b) 2.7 μm , and (c) 2.7 μm / λ 3914 intensity ratios, with backgrounds included. Intercept altitudes were calculated as described in the text.

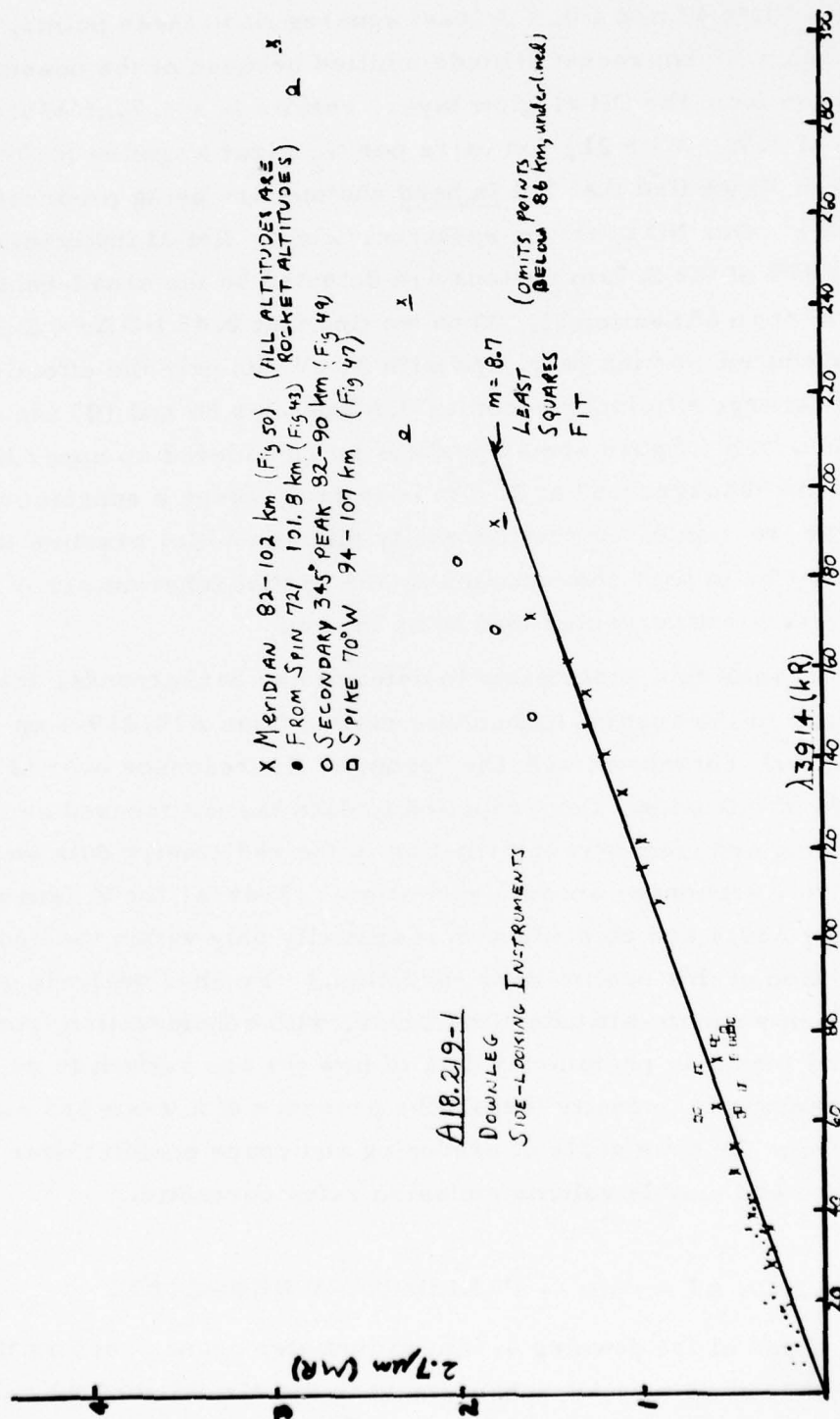


Figure 51. Scatter plot of 2.7μm and λ3914 intensities with backgrounds included, A18.219-1 downleg.

It includes the isolated spike near 70° W (Fig 47), the secondary peak near 345° (15° W), meridian data (Fig 50), and the complete spin cycle 721 (in Fig's 43 and 45). A least squares fit to these points, with data below 86 km rocket altitude omitted because of the possible contribution from the OH airglow layer, results in a $2.7\mu\text{m}/\lambda 3914$ photon ratio of 8.7. With $21\frac{1}{2}$ ion pairs per N_2^+ First Negative (0,0) quantum (Section V) we find that 0.4 in band photons are being produced per ion pair. Our NO overtone spectrum (Fig 3, Ref 2) indicates that about 88% of the $2.7\mu\text{m}$ photons are detected by the broad-band radiometer (see p 65, Section I). Thus we find that $0.45 \text{ NO } \Delta v = 2$ photons are produced per ion pair, and with 34 eV/ion pair the effective $2.7\mu\text{m}$ energy efficiency becomes 0.6% between 86 and 107 km rocket altitude. This figure should perhaps be considered an upper limit since the "background" at $2.7\mu\text{m}$ is in many cases a substantially greater fraction of the total intensity than the $\lambda 3914$ baseline (although this may be in part compensated by the partial inherent error in the 70° W spike ratios, which tend to be lower).

Despite this uncertainty in determining backgrounds, the $2.7\mu\text{m}$ radiance in the auroral ionosphere viewed from A18.219-1 on downleg seems well correlated with the "prompt" fluorescence over at least a decade of intensity. Our reduction to date has not focused on the predosing and transport information in the radiometry data on this relatively stationary auroral excitation. (That is, the $2.7\mu\text{m}$ emission may lag $\lambda 3914$ and coincide with it spatially only within the broad resolution of this preliminary reduction.) Further analysis of these elevation-azimuth-altitude-time scans, with consideration from the All-sky and meridian photometer data of how the arc system is moving and changing in intensity (recall the presence of a westward surge) can determine the time scale of predosing and space scale(s) over which infrared and visible volume emission rates correlate.

RADIATION AT $4.3\mu\text{m}$ -- PRELIMINARY REDUCTION

Some of the downleg $4.3\mu\text{m}$ radiometer scans, such as the one in Fig 43, show a small enhancement in the direction of the narrow $\lambda 3914$ (and $2.7\mu\text{m}$) limb peaks near 70° W. This low-contrast pulse,

if it is indeed arc-related, would be caused by some "relatively prompt" process such as vibrational fundamental chemiluminescence of NO^+ , secondary electron impact excitation of and vibrational luminescence transfer to $\text{N}^{14}\text{N}^{15}$, or excitation of CO_2 (001) by electron impact (or some as yet unexplained fast reaction). It might also be an effect of telemetry crosstalk or of leakage in the radiometer, perhaps of the NO fundamental-band emission above $5.3\mu\text{m}$ (the $2.7\mu\text{m}$ radiance seems too low to produce a large enough spurious signal).

Ignoring for this tentative review the possibility of instrument effects, and discounting CO_2 emission because of its uncertain excitation and low transmission in the long slant paths to the arc limb, we first assume the excess signal to be due to radiation in the NO^+ fundamental vibrational sequence. Fig 52 shows calculated $\text{NO}^{+\dagger}$ emission spectra for two population models (smoothed from Ref 5) overlaid on the A18.219-1 radiometer's response curve (assuming it to be the same as the vertical-pointing radiometer's on A18.205-1). About 0.16 of the NO^+ fundamental photons are detected by the radiometer if the aerochemical reactions populate states up to $v = 10$ with equal probability, and 0.39 if the (1,0) band alone is emitted. A very tentative estimate of the excess $4.3\mu\text{m}$ radiation is $1/6$ MR, which would result in $2R$ NO^+ fundamental detected per R $\lambda 3914$. This figure gives a photon ratio ($4.3\mu\text{m}$ NO^+ fundamental emitted)/($\lambda 3914$) of about 12 for equal population, and $4\frac{1}{2}$ if the first vibrational state only is populated. The corresponding figures for effective chemiluminescent efficiency are 0.6 NO^+ photon/ion pair and 0.5% (energy), and 0.2 NO^+ photon/ion pair and 0.2%. Any attenuation between arc and rocket by coinciding CO_2 rotational lines would increase these ratios. Reference is made to the smaller $4.3\mu\text{m}/\lambda 3914$ ratio measured in EXCEDE II (Ref 15), which is uncorrected for (possibly large) losses due to geometry and time dependence.

The abundance relative to N_2 of the $\text{N}^{14}\text{N}^{15}$ isotope is 0.72×10^{-2} . If $\text{N}^{14}\text{N}^{15}$ is the "relatively prompt" radiating species, its effective

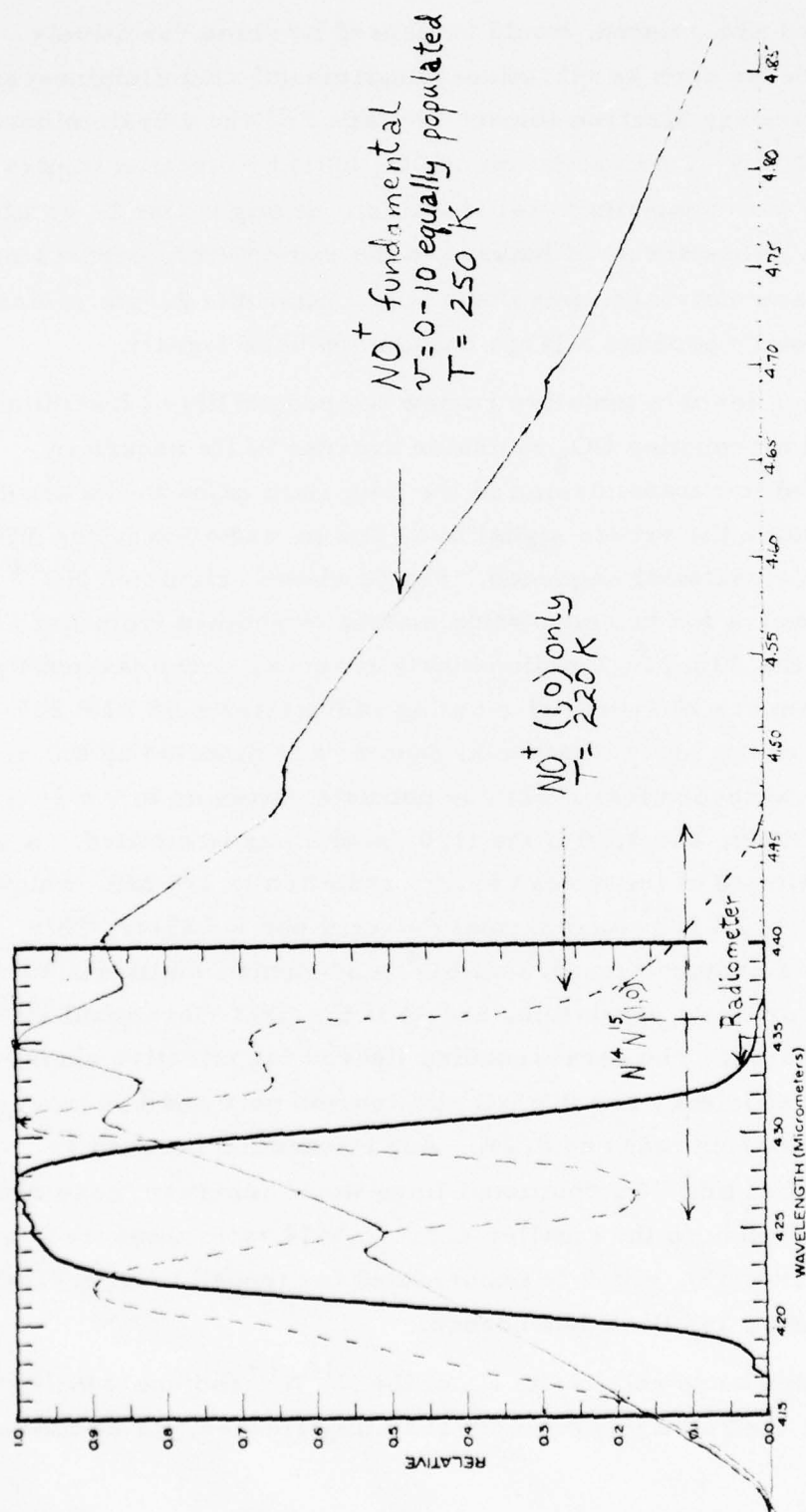


Figure 52. Calculated spectra of NO⁺ vibrational fundamental with v = 0 - 10 equally populated and NO⁺ (1,0) band only (from Ref 5), and relative response of A18.219-1's 4.3μm radiometer.

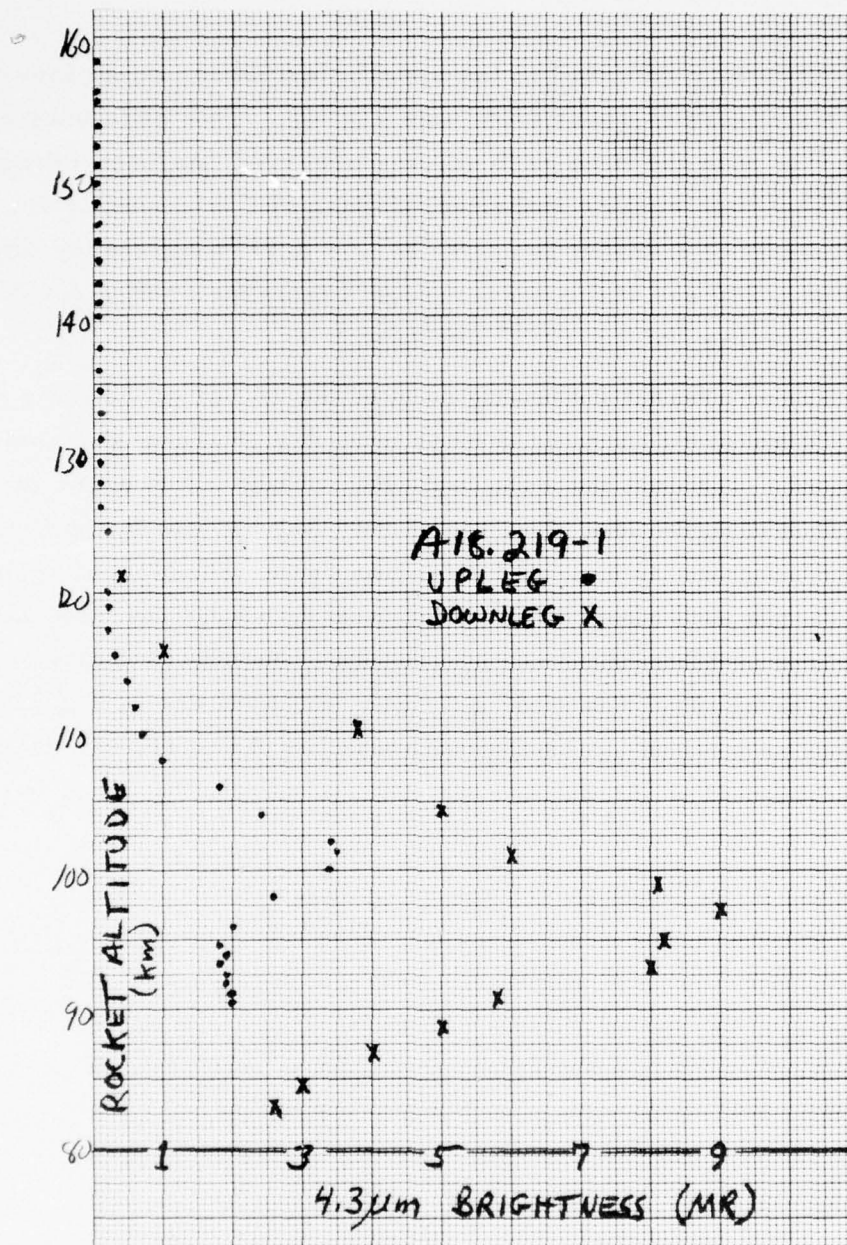


Figure 53. Altitude profile of the 4.3 μ m radiances measured at the fixed radiometer elevation angle $\sim 8^\circ$, geomagnetic azimuth 210° , A18.219-1.

emission efficiency referred to the specific excitation conditions of A18.219-1's aurora is about 1/3% (see Fig 52). This efficiency of course varies with the time each volume observed has been predosed, and the $N^{14}N^{15}$ molecule's radiative lifetime and rate coefficient for vibrationaluminescence transfer from $N^{14}N^{14}$. A 1/3% efficiency implies a halflife of ~ 200 sec if the near-resonant transfer coefficient has its expected value of $2 \times 10^{-12} \text{ cm}^3/\text{sec}$.

We are at present reviewing each of the 100 or so downleg scans between 120 km and 82 km for further evidence of arc-associated enhancement. The data (as on upleg) also contain information on the CO_2 radiance distribution, despite the fact that the van Rhijn-type gain is shifted from its expected elevation angle dependence. (The $2.7\mu\text{m}$ radiance data show the same general offset.) Downleg and upleg altitude profiles of the $4.3\mu\text{m}$ radiant intensity measured at the fixed radiometer elevation of 8° near 211° azimuth are in Fig 53 (for comparison to vertical-pointing profiles in Ref 5 and elsewhere).

SECTION III

ALL-SKY PHOTOGRAPHIC RECORDS OF AURORAS PROBED FROM ICECAP ROCKETS

Fig's 54-59 are montages of All-sky photographs illustrating the optical aurora into which were launched recent ICECAP-HAES sounding rockets. A set of nine similar displays for eight previous rocket probes, plus quick-look montages preliminary to Fig's 54 and 55, appear in Fig's 36-46 of Ref 1.

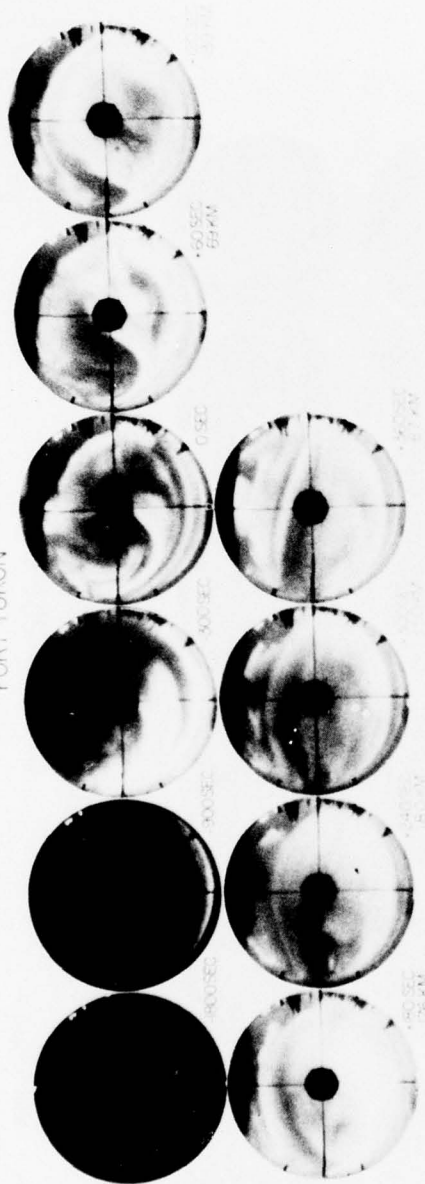
The rationale for these pictorial overviews of auroral development is presented in Section III of Ref 1. Principally they are intended to communicate, to data analysts and others, the morphology of the natural charged-particle precipitation that is simulating high-altitude nuclear effects. At one level, the montages represent an archival record of the program; at another, they help indicate the magnetospheric substorm's phase and the spatial distribution of predosing; and they act as guide to the original Poker Range photograph sequences and complementing, quantitative meridian photometer scans available to data users.

The present set of displays is a compromise between a standardized format to allow ready intercomparison of ICECAP's auroras and a description useful to each individual rocket investigation. Selecting from the photographic data base available - which for various reasons is itself a design constraint - we show views from Fort Yukon and one of the southern Range stations, at matching times intended to illustrate test-specific predosing - launch decision - actual launch - 100 km upleg penetration - apogee - downleg penetration. We adjusted time scales to monitor rapidly-changing auroral conditions (A18.219-1), align with segments of data on the auroral ionosphere limited by rocket tumbling (HIRIS), and correspond to altitude regions in which particularly useful data were acquired (WS 610.27-1). We also included a montage for a "quiet" auroral condition (NJ-74-1), as a baseline to illustrate the reproduction of a near-dark sky background.

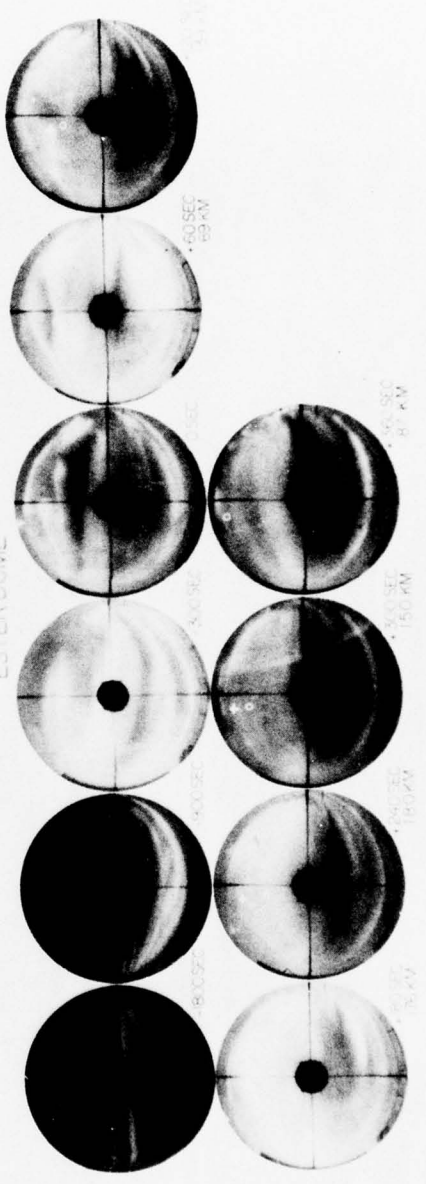
Aurora is printed in positive (light), with geomagnetic N at the top of the frames and E to the left (as to a ground observer facing S looking up at the zenith). Projections of both the instrument-carrying rocket and the intercept of the magnetic field line through it with the 100-km altitude plane, near which much of the radiation originates, are marked. Ref 1's caveats on interpretation of these projections onto two dimensions of the three-dimensional optically-thin radiating volume and of the intensity response of the quasi-logarithmic, clipping film detector (of which the printed report shows an eighth generation reproduction) of course apply.

- Figure 54(page 109). Visible-auroral distribution for ICECAP rocket A18.116-1, HIRIS I, launched 0916:30 21 Feb 74.
- Figure 55(page 110). Visible-auroral distribution for ICECAP rocket A18.219-1, '74 Multi, launched 0738:30 25 Feb 74.
- Figure 56(page 111). Visible auroral distribution for ICECAP rocket NJ-74-1, Quiet CVF, launched 0801:00 11 Apr 74.
- Figure 57(page 112). Visible-auroral distribution for ICECAP rocket IC 519.07-1B, '75 Multi, launched 0748:10 12 Mar 75.
- Figure 58(page 113). Visible-auroral distribution for ICECAP rocket IC 630.02-1A, HIRIS II, launched 0805:20 01 Apr 76.
- Figure 59(page 114). Visible auroral distribution for ICECAP rocket WS 610.27-1, RF/Langmuir Probe, launched 0928:20 01 Apr 76.

FORT YUKON



ESTER DOME



A18116-1 HIRIS I
0916 30 21 FEB 74

DIRECTION TO - Rocket, + - 100km Intercept
of field line through rocket

NO DATA

ESTER DOME

1. 148 SEC 170 KM

2. 408 SEC 134 KM

3. 68 SEC 84 KM

4. 28 SEC 19 KM

5. 900 SEC

6. 176.8 SEC

7. 388 SEC 70 KM

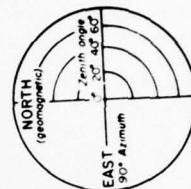
8. 348 SEC 124 KM

9. 308 SEC 163 KM

10. 268 SEC 187 KM

11. 228 SEC 196 KM

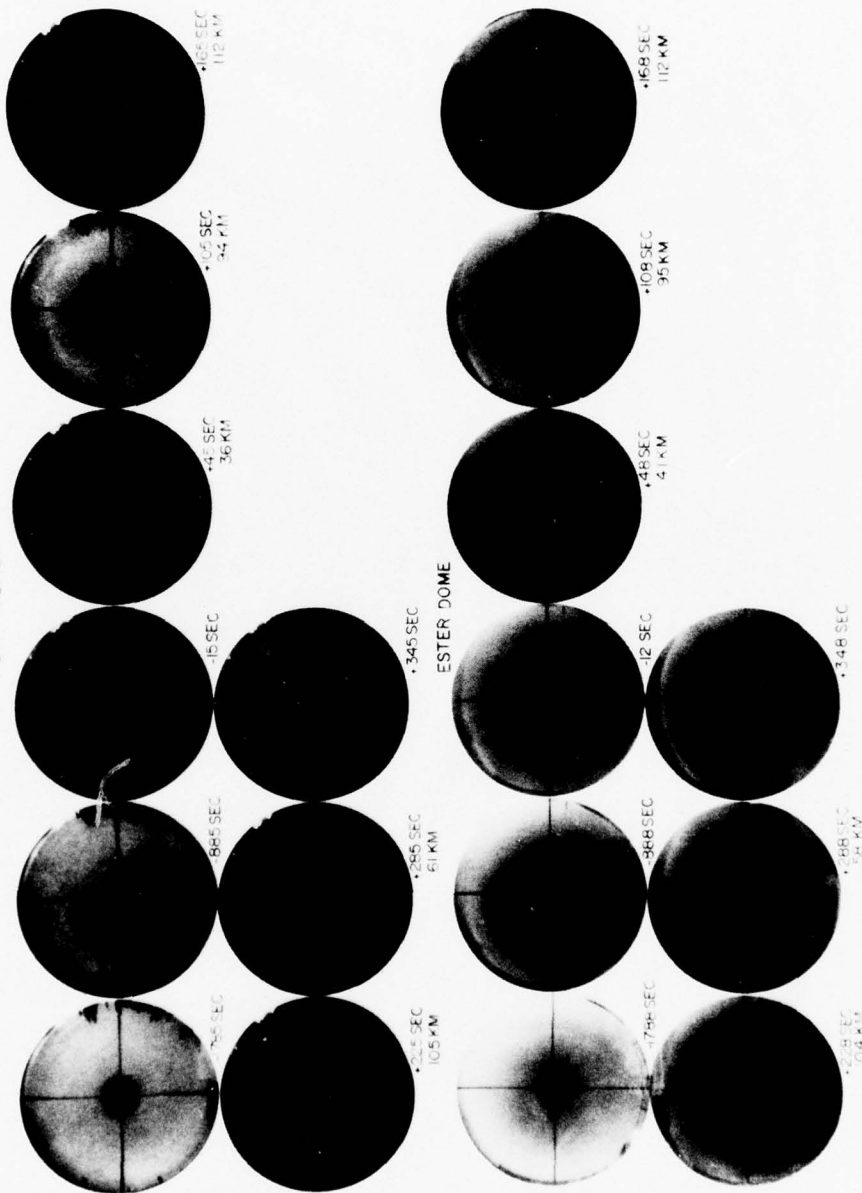
12. 188 SEC 190 KM



A18 219-1 '74 MULTI
073830 25FEB 74

DIRECTION TO ○ - Rocket, + - 100km Intercept
of field line through rocket

FORT YUKON



NJ-74-1 QUIET CVF
0801:00 01APR 74

DIRECTION TO - Rocket, + - 100km Intercept
of field line through rocket



Figure 1 consists of 12 circular frames arranged in two rows of six. The top row shows the flare's development from -140 SEC to +267 SEC. The bottom row shows the flare's decay from +248 SEC to +303 SEC. Each frame is labeled with its time relative to the flare maximum and the corresponding speed of the solar wind in km/sec.

Time (SEC)	Speed (km/sec)
-140	140
-52	110
+8	110
+68	78
+109	107
+267	90
+248	103
+299	114
+303	103

CHITANINA

-14.4 SEC
55 KM

-16 SEC
55 KM

-76 SEC
55 KM

-136 SEC
55 KM

-916 SEC
55 KM

-1416 SEC
55 KM

-164 SEC
125 KM

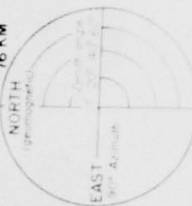
-224 SEC
116 KM

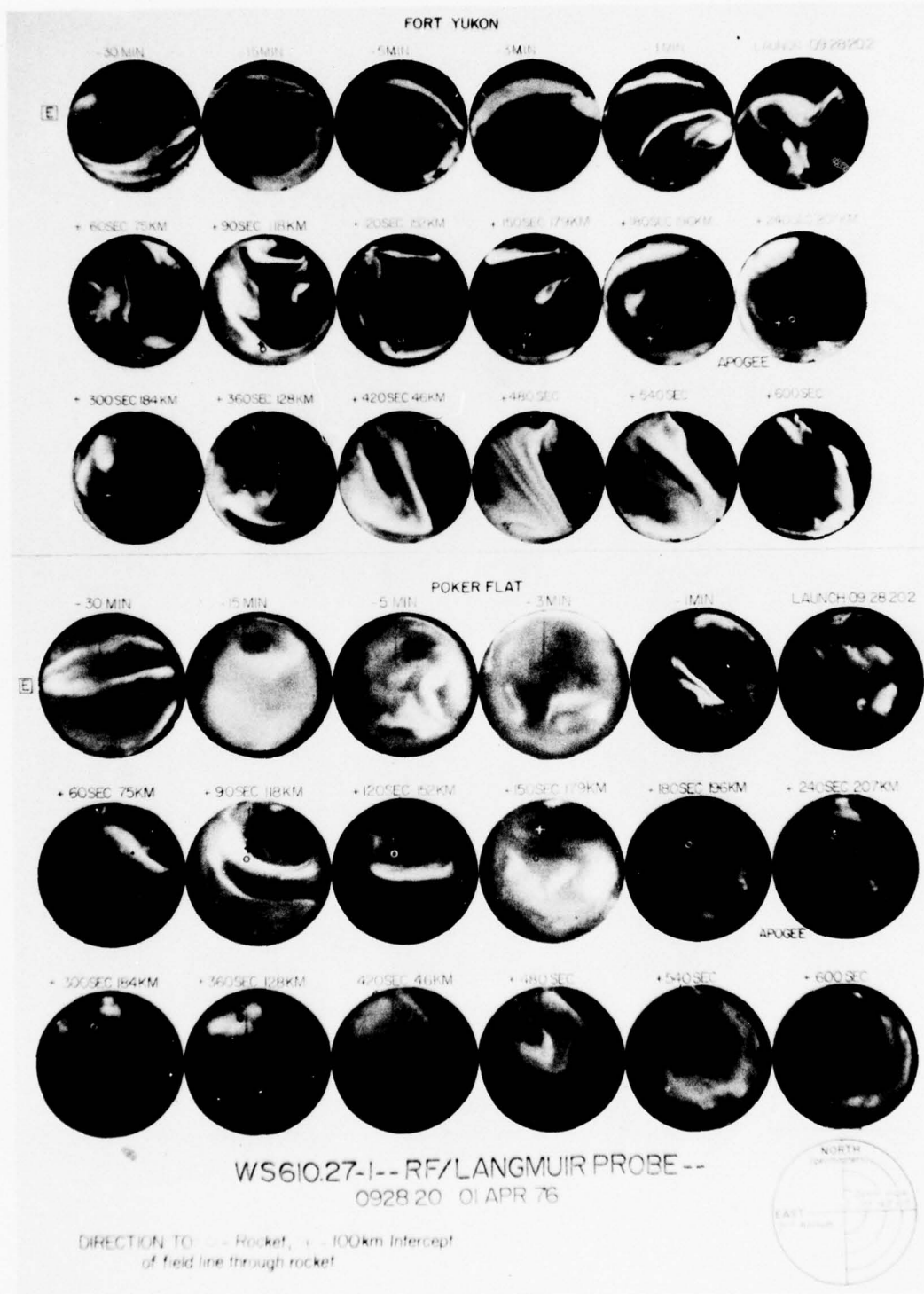
-248 SEC
103 KM

-267 SEC
95 KM

IC 630.02-1A HIRIS II
0805:20 01 APR 76

DIRECTION TO - Rocket, + 100km Intercept
of field line through rocket





SECTION IV

ANALYSIS OF ICECAP's 10 MAR 75 AIRCRAFT MEASUREMENTS OF AURORA-ASSOCIATED RADIATION NEAR $2.8\mu\text{m}$

INTRODUCTION

Reference is made to our 1975 analysis of the partially calibrated radiance data from KC-135 aircraft mission ICECAP 4 (Section III of Ref 2), whose result was an effective efficiency of $2/3\%$ for exciting NO vibrational overtone quanta in aurora. The derivation required adoption of a mean Arctic winter atmosphere, along with some 15 explicitly stated interpretations of instrument performance and assumptions about the atmosphere's radiations. The model atmosphere provides the necessary post-calibration of the $2.83 \pm \frac{1}{2} 0.155\mu\text{m}$ radiometer, and allows correction of the measured SWIR radiances for absorption of NO overtone photons by air molecules above the aircraft platform. The derived chemiluminescence efficiency is sensitive to the atmosphere selected principally through its absolute thermal radiance, to which the signal enhancements associated with aurora were ratioed, and secondarily through its ($\sim 75\%$) zenith transmission of the $\Delta v = 2$ sequences' rotational lines.

Laboratory-calibrated $2.8\mu\text{m}$ radiometer data have since become available (Ref 16), and are shown with supporting aircraft data in Fig 60 (compare Fig 19 of Ref 2). In this Section we derive from these a more reliable effective NO overtone emission efficiency. The updated yield turns out to be very close to the one we calculated in Ref 2, thus providing a reassuring indication of the appropriateness of our assumed model atmosphere. (It is also very close to the figure derived from A18.219-1's downleg arc-radiometry data, Section II.) The more complete analysis in addition gives further insight into the simulation by aurora of excitation of infrared by nuclear particles, and suggests several improvements in the aircraft test procedure.

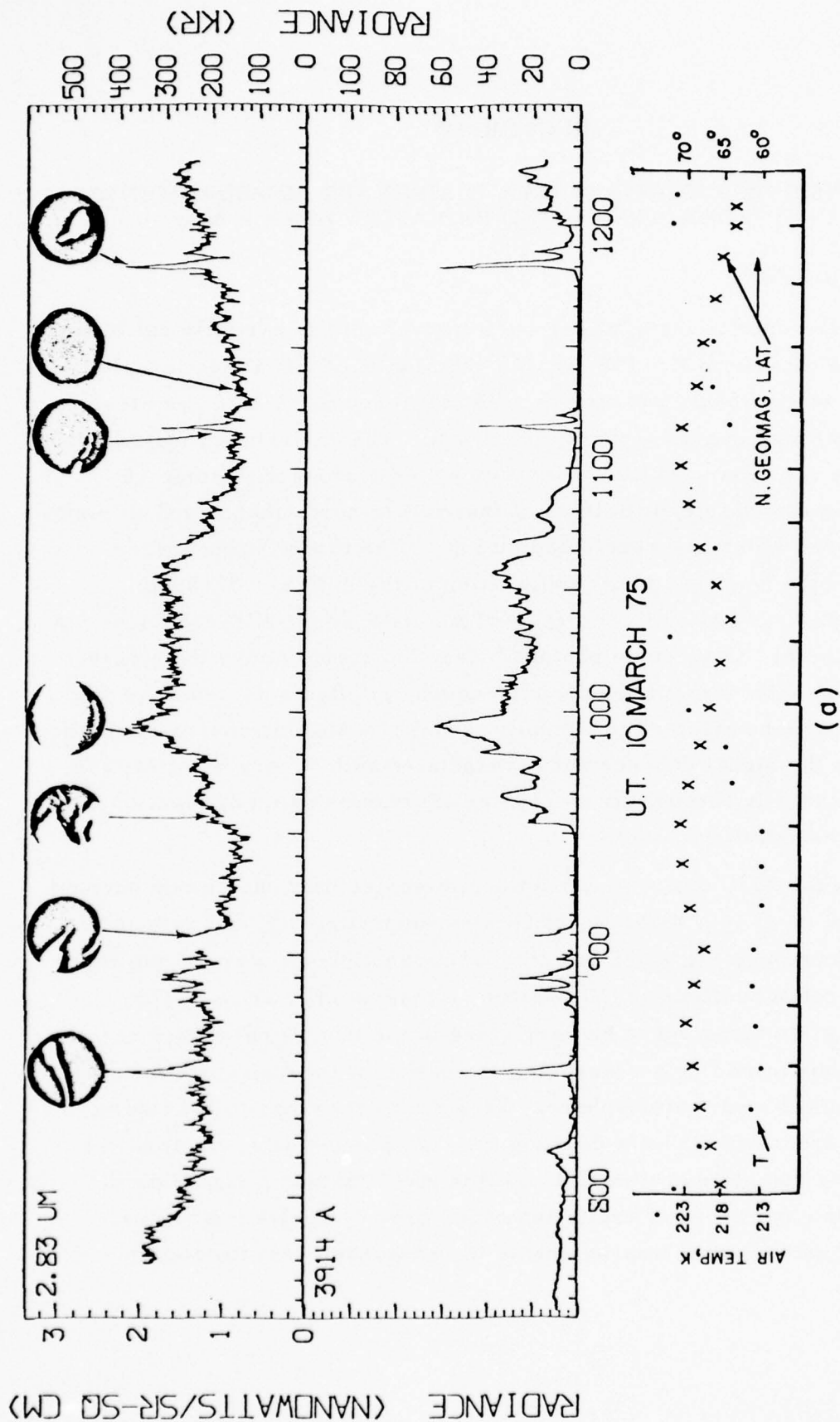
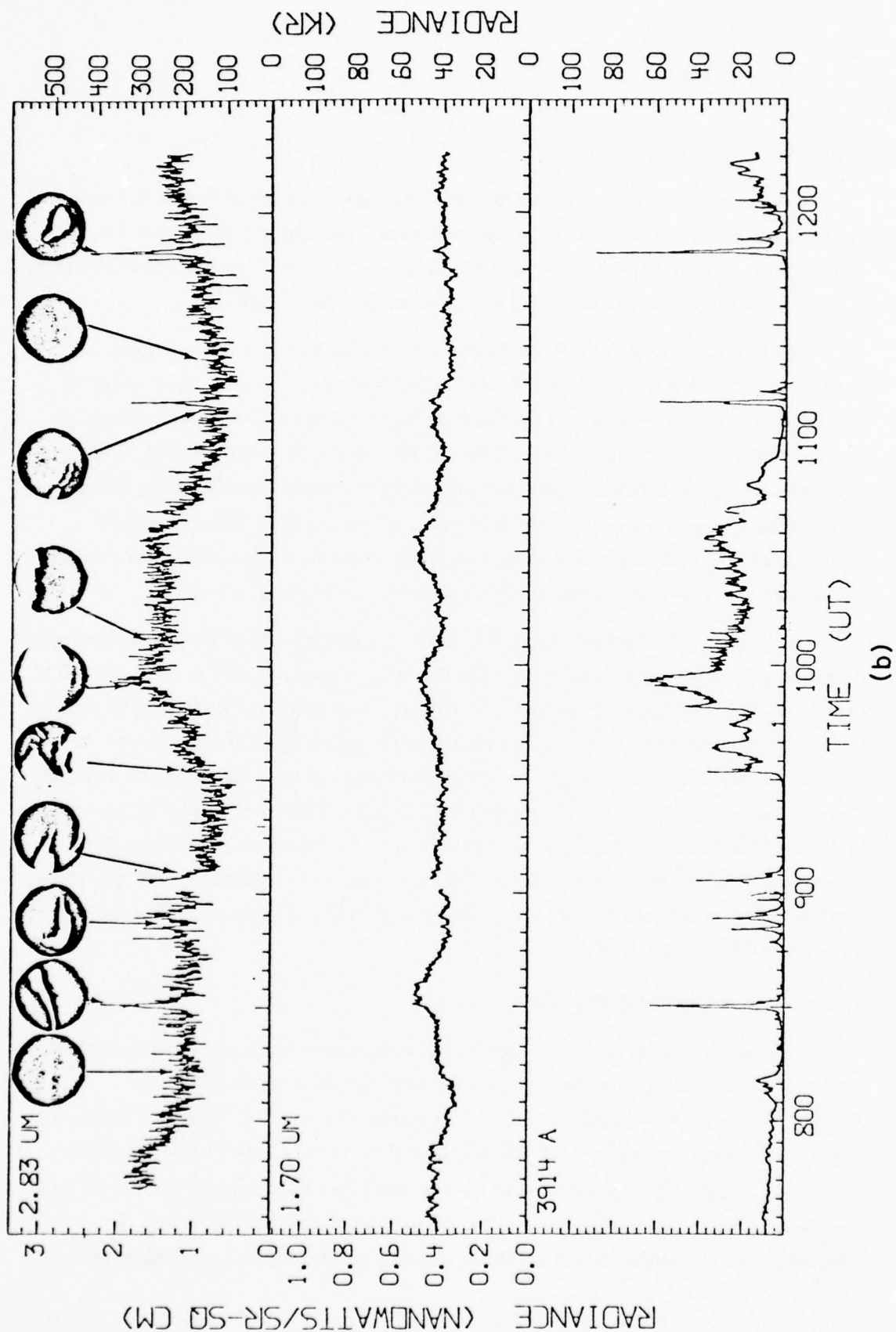


Figure 60a, b. ICECAP-4's zenith radiance data with 0.05 Hz bandwidth (half-power) low-pass filtering (a) and 0.0125 Hz filtering (b). The temperature and latitude data are from the aircraft navigator's flight log.



DATA REDUCTION

With exceptions as noted below, we again adopted Ref's 2 interpretations of how the instruments perform, assumptions about the absolute spectral intensities of auroral, airglow, and thermal radiations, and procedures for accessing and processing the flight data.

The $2.8\mu\text{m}$ and $\lambda 3914$ radiance traces in Fig 60b were first manually smoothed to damp the typically 5%-amplitude, $\frac{1}{2}$ min-period fluctuations that remained after the prior low-pass (linear) filtering of the instrument readings in Fig 60a. The smoothed data were then sampled at $2\frac{1}{2}$ min intervals starting at 0745, without adjusting times by matching isolated peaks as was done previously. This is about equivalent to applying a ~ 2 min sampling aperture outside of arc-like structures. The resulting scatter plot is shown in Fig 61a.

We then subtracted from the $2.8\mu\text{m}$ radiometer signal the contribution of hydroxyl (principally the (1,0) band), applying the factor (58 kR)/(45 kR $1.7\mu\text{m}$ radiance) derived in Ref 2. We omitted $\lambda 3914$ data points below 2 kR since the $2.8\mu\text{m}$ readings associated with them appear to lie within the fluctuations in thermal background and thus would reduce the accuracy of slope determination. (In addition they apply to generally higher altitudes, as discussed in Section V.) Also omitted are data before 0805, for the reason given in the next subsection. The resulting scatter plot is shown in Fig 61b, which like Fig 61a is a calibrated version of Refs 2's Fig 20.

SELF-CONSISTENCY OF THE DATA

These plots have some qualitative features that provide insights into the simulation, its instruments, and the data presentation. Among these are the anomalous placement of the point labeled 1150, the group lying upper left of the dashed line in Fig 61a (omitted from Fig 61b), and the apparent separation between data points taken during and outside the breakup phase of a magnetospheric substorm. In addition the $2.8\mu\text{m}$ radiances show a weak tendency to correlate with

(latitude-dependent) outside air temperature at the aircraft.

The 1150 UT point lies below the least squares fit lines because the optical arc's peak appears about 1 min before the similarly-shaped infrared peak. The aircraft is flying geomagnetic S at this time. Similarly, the isolated $\lambda 3914$ enhancements at 0831 (aircraft turning N \rightarrow S) and 1110 (aircraft moving S) convolve with the photometer's field to reach peaks $\sim \frac{1}{2}$ min before $2.8\mu\text{m}$ maxima that are otherwise closely similar. If this offset is caused by infrared emitting species actually lying S of the prompt fluorescence, their horizontal separation would be ~ 10 km, which is less than one radiometer field-of-view projected on the aurora. (The displacement might also be interpreted as ~ 40 km vertically in arcs tilted 13° from the vertical.) A more probable explanation of these shifts is that they are an artefact of the recording or presentation of data from the aircraft radiometer and/or photometer, most likely related to signal integration times. They thus give a measure of the precision with which readings from the two instruments can be compared, that is, of the resolution with which visible-infrared spatial correlations (and to some extent, the effect of predosing) can be measured.

In this regard, we note (Fig 60b) that low-pass filtering reduces the peak radiances in isolated arcs; to the extent that this attenuates both signals equally, it introduces only second-order errors in the effective chemiluminescence efficiency. Offsets of less than about one half-width are also somewhat self-compensating, as high ratios on one side partially counterbalance low ratios on the other.

We turn next to the series of data points lying upper left of the dotted line in Fig 61a, which are all from the 20 min before 0805, when the radiometer's readings were decreasing rapidly and the photometer's slowly. The aircraft, which took off from the runway at 0716, requires a nominal 20 min to reach 25 kft altitude where radiometer cooling is initiated; operating temperature is reached 30 min later. This sequence places the start of reliable radiometer operation somewhat

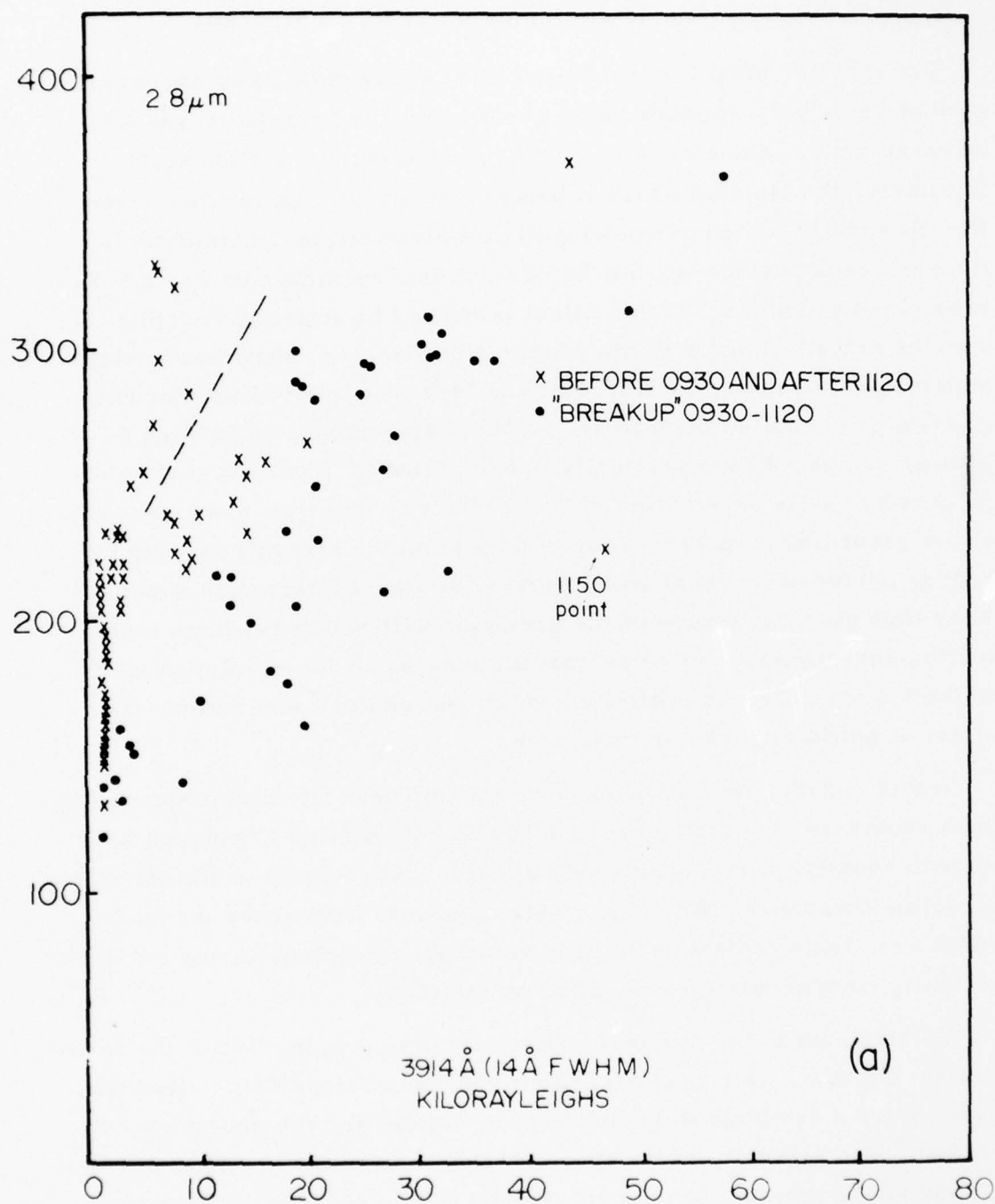
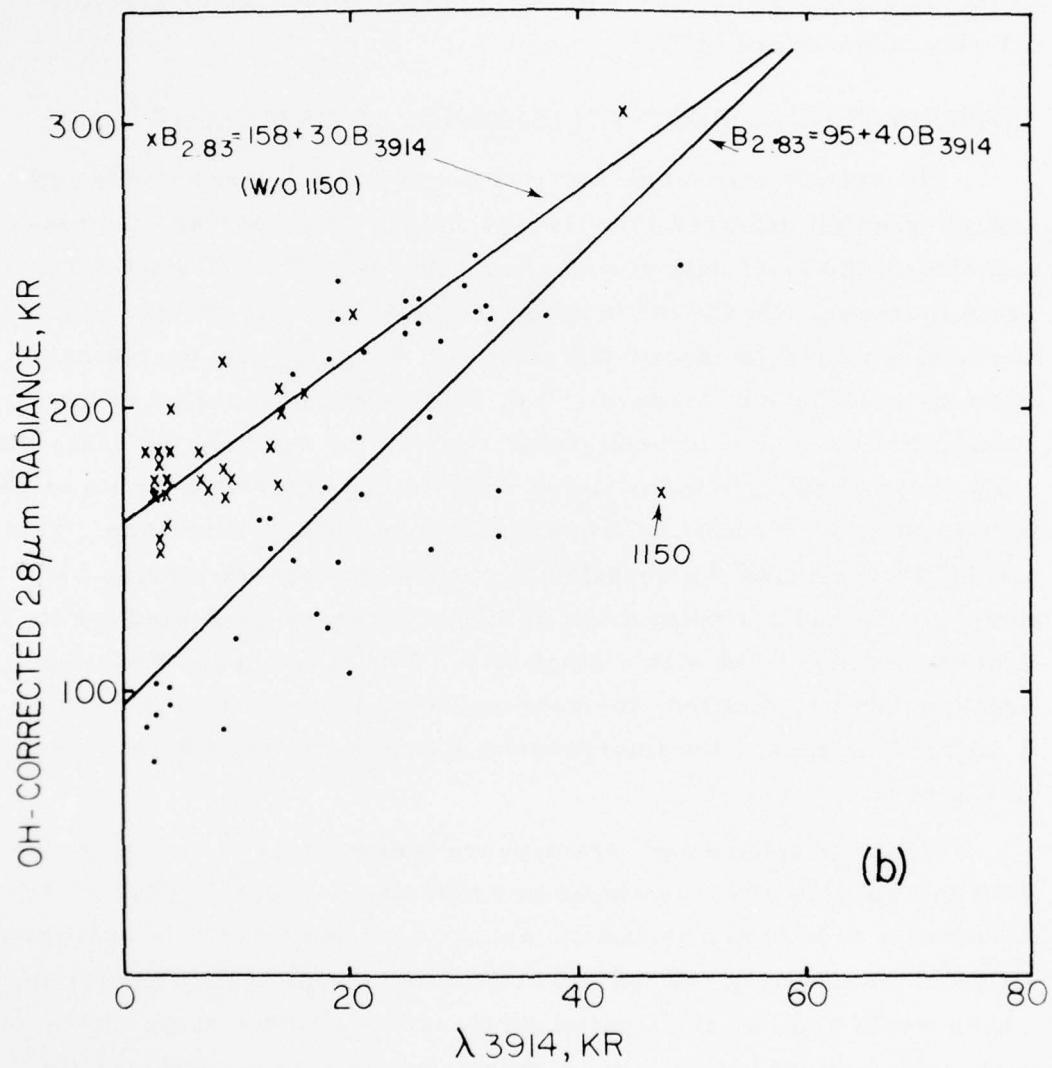


Figure 61a, b. Scatter plots of ICECAP-4's zenith radiance data before (a) and after (b) correction for OH airglow. The procedure in sampling the data from Fig 60b is described in the text. The straight lines in Fig 61b are least-squares fits to the breakup (lower) and non-breakup (upper) data points.



after 0800, which is the time when the aircraft entered orbit north-bound at Point A in Fig 21 of Ref 2 (near Fairbanks). In consideration of this potential source of error, we omitted from further analysis all data taken before 0805.

TEMPERATURE EFFECTS ON INFRARED SKY RADIANCE

The outside air temperature at the aircraft (bottom of Fig 60b) is high when the infrared level is high before 0805, during the breakup, and also in the brief data period after 1200 when the radiometer readings again increase. On the other hand, the local air temperature is if anything anticorrelated with the relatively high, aurora-unrelated infrared radiances between 0815 and 0905; and the intercept of the straightline fit to the breakup phase's points (on Fig 61b) indicates that their thermal background is lower than for the other data points on the scatter plot, continuing the trend just before and after breakup. Taking all the data, we find the correlation coefficient between outside air temperature and a 5-point mean of $2.8\mu\text{m}$ radiance corrected for its OH contribution is $+0.54$ with a slope of $5.9 \text{ kR}/^{\circ}\text{K}$ (Fig 62). When the breakup data are omitted, the corresponding figures are $+0.59$ and $5.0 \text{ kR}/^{\circ}\text{K}$ (compare the fluorescence-correlated intensity increases in Fig 60).

The troposphere and stratosphere temperature structure above PKR in Feb-Mar 1975 is shown in RAOB data, Table 4 (Ref 17). Substantial day-to-day variations appear near the aircraft's operating altitude, presumably related to vertical movement of the tropopause. These would suggest also spatial temperature changes along the flight path, which might be tentatively considered as leading to the shifts in the $2.8\mu\text{m}$ thermal "baseline" in Fig 60. On the other hand there are only small variations above $\sim 15 \text{ km}$ altitude, from where may come radiation in optically thin water vapor lines that contribute to the infrared signal. The aircraft data point suggests that on the night of 10 Mar the temperature profile above PKR was approaching that

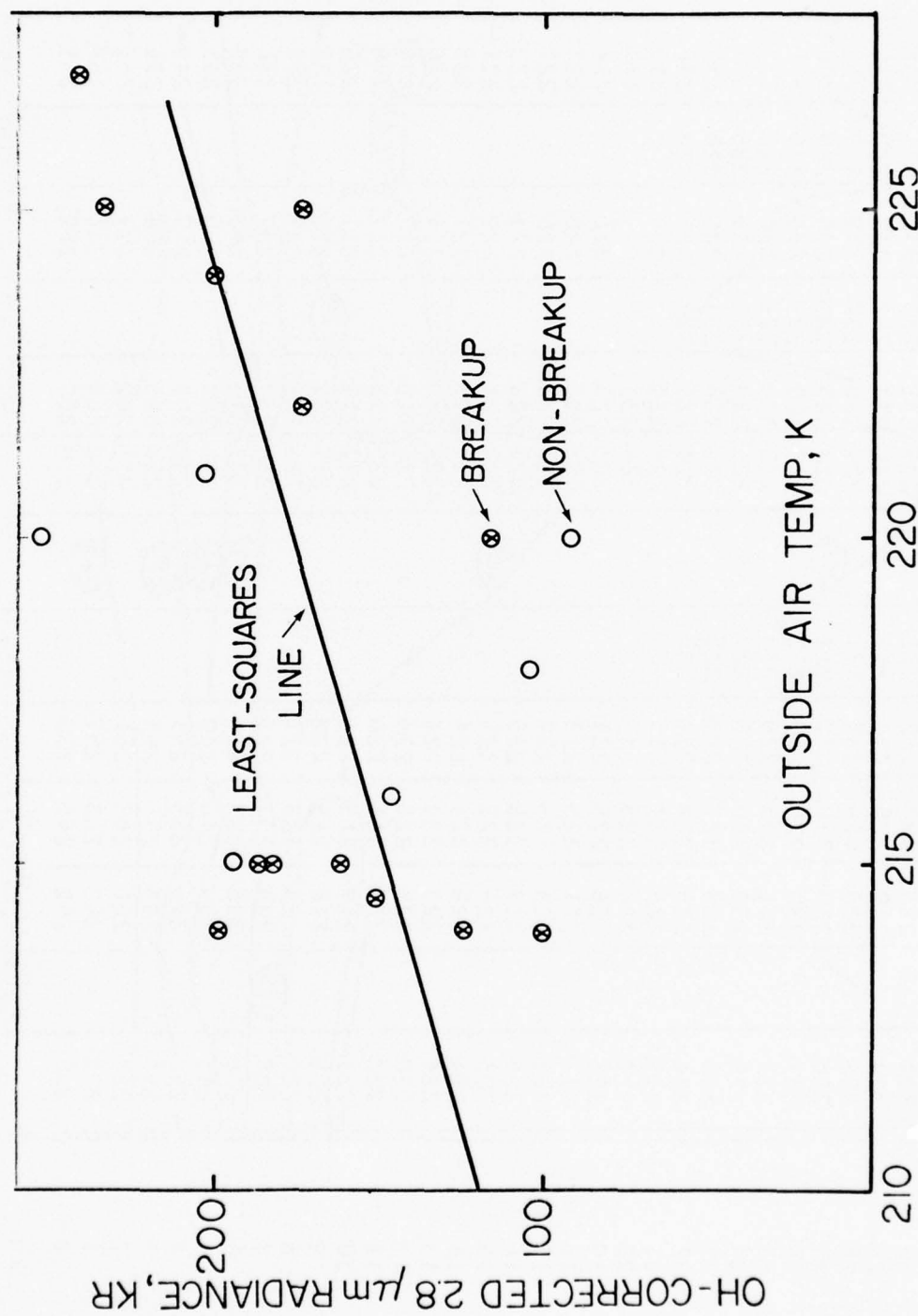


Figure 62. Scatter plot of five-point averages of 2.8 μ m radiance and outside air temperature at the aircraft for ICECAP-4.

Table 4. RAOB Temperatures Over Poker Flat Research Range, ICECAP 75

km	27	28	1	2	3	4	5	6	7	8	9	10	11
30	224	223	229	232	231	225	231	233	235	231	236		
29	224	229	229	233	231	220	233	232	237	230	236		
28	225	229	229	233	231	224	230	234	239	229	233		
27	226	230	230	232	232	223	223	240	239	229	230		
26	227	230	229	229	232	223	228	239	235	223	231		
25	227	231	223	229	230	223	227	235	230	220	231		
24	228	230	230	223	227	226	223	231	229	228	231		
23	228	228	225	227	227	225	226	231	229	228	230		
22	224	225	224	227	226	224	225	227	229	228	230		
21	225	225	224	215	224	225	224	225	209	228	230		
20	225	226	225	215	225	223	223	223	216	226	230		
19	225	226	225	221	225	223	223	223	226	227	224		
18	223	221	225	215	222	222	224	222	222	221	225		
17	223	228	225	227	223	223	223	223	224	221	226		
16	225	227	226	225	225	223	223	223	224	222	222		
15	225	226	227	225	224	223	221	223	222	221	225		
14	224	226	224	224	224	225	220	224	221	221	226		
13	224	223	224	225	224	225	219	225	217	230	228		
12	220	223	226	225	225	223	213	223	212	IC 4	226		
11	222	223	223	226	225	222	213	222	211	226	226		
10	221	223	221	226	221	222	213	222	220	223	223		
9	219	217	215	221	221	219	221	220	220	223	235		
8	220	218	215	222	222	224	229	228	228	231	238		
7	226	229	223	223	223	230	237	237	237	238	245		
6	236	236	233	239	239	237	245	243	250	249	254		
5	243	239	246	240	243	243	253	257	264	261	268		
4	250	246	253	255	247	253	255	262	266	261	268		
3	256	253	256	255	252	253	255	262	266	261	268		
2	264	261	263	261	253	262	265	250	257	257	261		
1	272	263	263	267	262	265	253	250	257	257	261		
0	265	262	256	253	253	250	253	250	257	257	261		

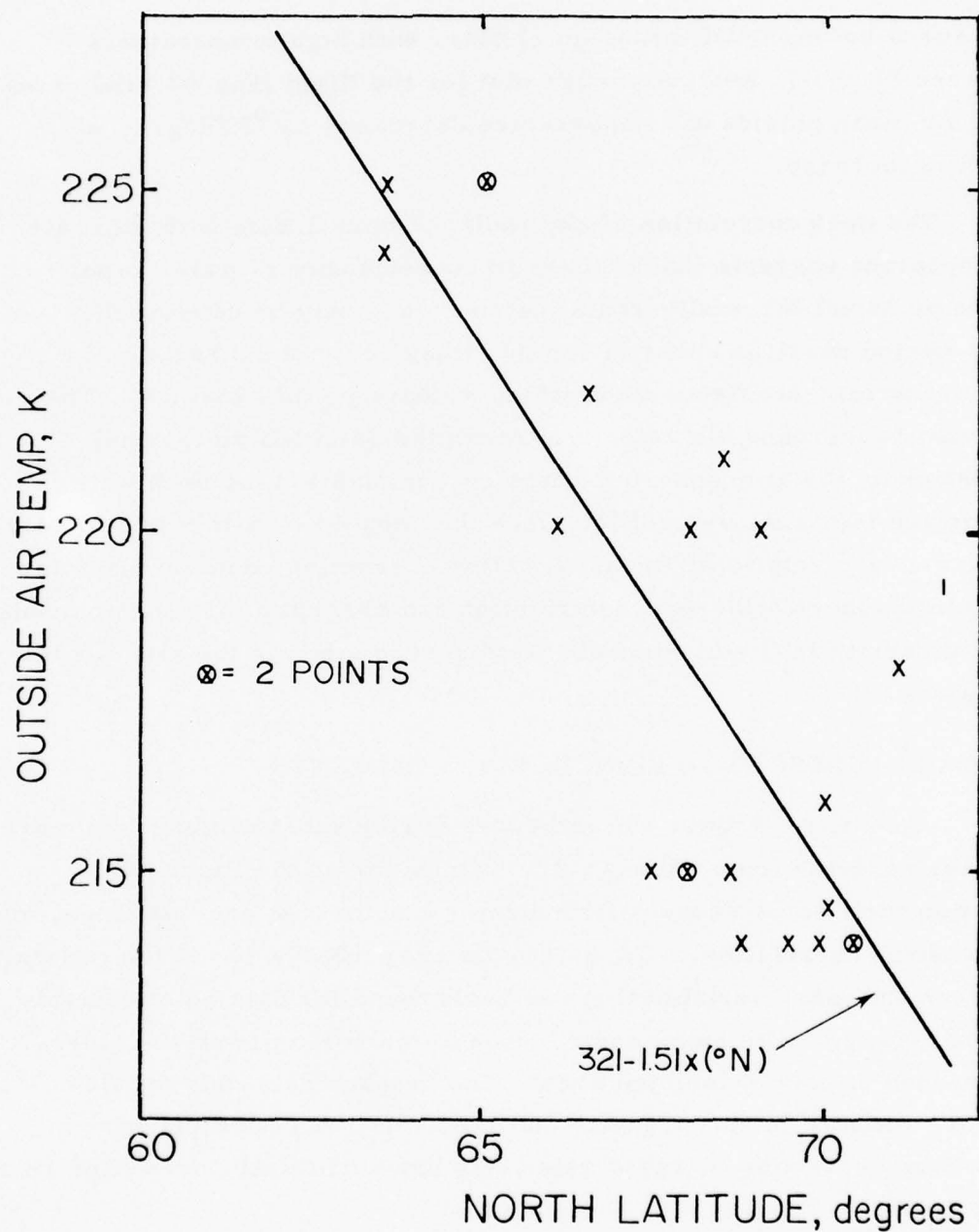


Figure 63.

Scatter plot of outside air temperature and latitude of ICECAP-4.

measured by the RAOB probe on 11 Mar, with high temperatures between 11 and 15 km. A scatter plot for the flight (Fig 63) indicates that the mean outside air temperature decreases $1\frac{1}{2}^{\circ}\text{K/degree}$ of latitude increase.

The weak correlation of sky radiance near $2.8\mu\text{m}$ with local air temperature suggests that changes in concentration of water vapor - the principal thermally radiating species - may be causing the long-period baseline shifts in Fig 60 (they could of course also be due to instrument effects about which we have no information). The thermal background and effective transmission of NO vibrational radiation by the atmosphere require re-computation for each water vapor and temperature profile, since they depend on a mix of optically thick and thin rotational lines. A better correction could be made for the stratosphere's thermal contribution and absorption if spectroscopic data on zenith H_2O emission-absorption were taken in the aircraft test missions.

CHEMILUMINESCENCE EFFICIENCY, COMMENTS

As Fig 61 shows, the radiances during substorm breakup more or less separate from those at other times during the flight. In addition their least-squares fit indicates a somewhat greater slope, and also better correlation. These effects are probably due to the generally greater and more variable thermal background for data points outside of the breakup, with some contribution to the spread from the aforementioned offsets of isolated arcs. The breakup data thus provide a more reliable ratio. We note that they apply to a hard primary spectrum depositing energy at relatively low auroral altitudes (Ref 18 ; Section V).

As a further qualitative check on the correlation between the two radiance distributions, we plotted peak-normalized, background-corrected data for the breakup period (Fig 64). These plots, perhaps even more compellingly than the isolated arcs outside the breakup

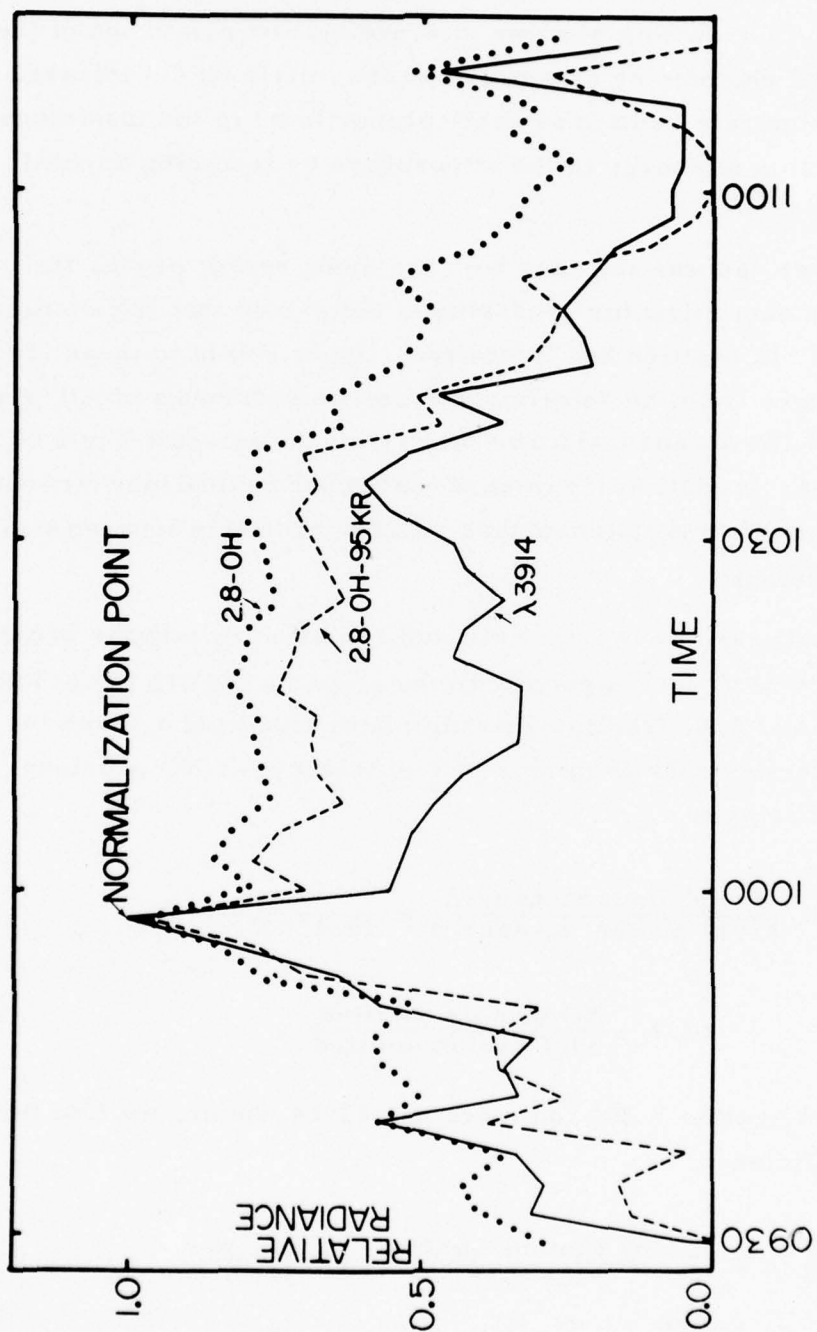


Figure 64. Zenith radiances during ICECAP-4's breakup normalized to the peak at 0957 $\frac{1}{2}$. The 95 kR subtracted on the dashed trace refers to the background intercept in Fig 61b.

phase in Fig 60, indicate that the $2.8\mu\text{m}$ chemiluminescence with a few exceptions "follows" the prompt auroral fluorescence in the aircraft's zenith. To within what we interpret as the resolution of the radiometer and photometer data provided, the (nitric oxide) infrared column emission rate remain sensibly proportional to the instantaneous rate of deposition of energy in the atmosphere by incoming auroral particles.

However, as was the case with the multi rocket probes the radiance-scan data allow for predosing in the period that the auroras remain "fixed" in position and intensity. Upper limits to these effective integration times could be determined from the sequences of All-sky photographs of IC-4's auroral forms taken from the aircraft (Fig's 60,65) and ground stations. In addition the radiance data when refined may turn out to contain further information about the spatial relationship between visible and infrared emissions.

We shall assume that the infrared radiation rate in the breakup has reached equilibrium. Applying to the slope in Fig 61b the 0.748 transmission and 0.42 fraction-in-radiometer passband derived in Ref 2, the effective chemiluminescence efficiency for NO overtone photons then becomes

$$4.0 \frac{\text{NO photons measured}}{\lambda 3914 \text{ photon measured}} \times \frac{1}{(0.42)(0.75)} =$$

$$12.7 \frac{\text{NO photons emitted}}{\lambda 3914 \text{ photon emitted}} .$$

Adopting from Section V $20\frac{1}{2}$ ion pairs per $\lambda 3914$ photon, we find for the energy efficiency

$$\begin{aligned} \frac{12.7}{20.5} &= 0.62 \frac{\text{NO photons emitted}}{\text{ion pair}} \times \frac{1 \text{ ion pair}}{34 \text{ ev}} \\ &\times \frac{1.234}{2.8} \frac{\text{ev}}{\text{quantum}} = 0.8\% . \end{aligned}$$

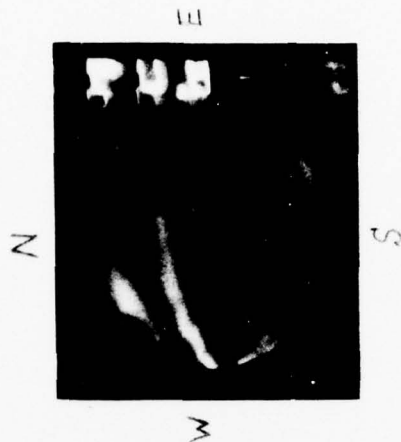


Figure 65. Aircraft location (X) on the DMSP record of optical-NIR aurora in the Alaska sector for 0856-0858 10 Mar 75, with aircraft All-sky photograph for 0858:09 (conclusion of turn to N). The DMSP scanning-image is composed from a single sweep over the scene as the satellite moves in the direction of the raster lines.

This figure is very close to the 2/3% derived in Ref 2, for which we inferred an absolute calibration for the $2.8\mu\text{m}$ radiometer, used all the flight data points, and adopted as inverse fluorescence efficiency 18 ion pairs/ N_2^+ First Negative (0,0) band quantum. It is also very close to that from A18.219-1's sidelooking radiometry data, Section II.

Our analysis has shown the importance of time resolution and identification to the accuracy of visible-infrared spatial correlations. The effect of what appears to be thermal radiation from the atmosphere above the aircraft, while not onerous in IC-4, can be reduced in higher-resolution tests by simultaneous measurement of water vapor emission. In addition radiance measurements in more than one direction would remove the inherent space-time ambiguity that hinders assessment of predosing.

SECTION V

ENERGY INPUT IN AURORAL SIMULATIONS

INTRODUCTION

To scale and apply ICECAP's infrared data in predictive codes, the energy input to the auroral ionosphere must be known. Particle counters, plasma probes, and coaligned air-fluorescence photometers onboard some of the rockets measure the largely "prompt" ionization by incoming charged particles. Measurements over much longer times and broader regions can be made from the ground, principally by photometers and Thomson-scatter radars. Data from other remote sensors, which can be applied toward general characterizations of the disturbed high-latitude ionosphere, have much poorer time and space resolution.

"Predosing" in a period comparable to the time for excitation and/or storage of an atmospheric infrared radiation contributes to its measured intensity (as we showed in Appendix VIII of Ref 1). The in situ rocket measurements are in general too brief and localized to provide sufficient information about this prior energy input. $4.3\mu\text{m}$ $\text{N}_2 - \text{CO}_2$ vibrational quanta (originally excited by soft secondary electrons) are trapped with e-folding times of $\sim 1 - 10$ min in the E-region (Ref 19); LWIR O_3 vibrational chemiluminescence depends on the mesosphere's energy-absorption history in the several hrs required for free O atoms to combine with O_2 ; and emission in NO's 2.7 and $5.3\mu\text{m}$ vibrational bands follows the increase in concentration of its precursor N atoms, volume emission rates from which are in turn determined by the predosing. Clearly, some time period of auroral power input appropriate to a feature's excitation and storage mechanism(s) must be adopted to define its effective fluorescence efficiency

$$\frac{\text{Energy output in infrared radiation from a volume of air}}{\text{Energy input by ionizing particles to that volume}}$$

Errors in this ratio's denominator have of course the same effect on the accuracy of results from defensive system codes that make use of HAES data, as do errors in measurement of the aurora-associated infrared radiances. Indeed, the precision required in calibrating infrared instruments, which is an important cost factor, need not be much better than the precision to which the energy input into the upper atmosphere can be measured. We have therefore made a preliminary review of the two principal methods for remotely sensing this energy, and of the present interpretation of column ionization rates in aurora in terms of accepted models for exciting NO⁺.

PHOTOMETRY AND INCOHERENT RADAR BACKSCATTER MEASUREMENTS

Nominal characteristics of the two methods for determining auroral power input – from the column emission rate in air fluorescence bands, and from the density of free electrons indicated by their incoherent backscatter at UHF – are listed in Table 5. The tabulation is designed only to help assess the accuracy and "utility" of dose-rate information under various conditions, and is not intended as an exhaustive critique of the two techniques. It does not consider their other capabilities for plasma-diagnosis (in particular, the radar can determine energy taken from ionospheric electric fields, proton fluxes and buildup of some critical chemical species can be measured optically, and both the radar and spectrophotometers can infer winds and temperatures), or make explicit recognition of the possibilities for complementary measurements (as underscored in the recent joint paper by radar and optical groups, Ref 20).

The two methods and their application to HAES measurements from aircraft platforms are discussed further in Appendix II. To review briefly, the photometric method applies narrow-angle "telescopes" to determine the aurora's apparent surface radiance in optical features that indicate the flux, energy spectrum, and types of incoming particles. Familiar examples are the Alaska multi-

Table 5 . Characteristics of Ground-Based Measurements of Auroral Particle Energy Input

	Photometric Method	Thomson-scatter Radar Method
Accuracy of Theoretical Basis of Measurement	Good for column (altitude) integral, Reasonable for altitude profile (Appendix II). Equilibrium assumption needed for profile applying $\lambda 6300$, uniformity across field line needed for profile	[e]: Good in arc, poor-to-fair in weak drizzle region, α : Fair-to-maybe good. Equilibrium assumption needed to apply $Q = \alpha [e]^2$ (Ionization rate = recombination coefficient x square of electron density)
Time/Space Resolution (compare to time/space variations of aurora, and times for wind drift)	* $\sim 1/3$ min per meridian scan with 2° circular field gives $\lesssim 10\%$ precision at IBC 1: Good if 2° field OK	~ 5 min per scan, with 0.6° circular field. Error [e]-dependent; usually Poor time, good space
Degradation by Lower Atmosphere	Can be serious outside bright regions (see text)	Essentially none
Threshold	Can readily be $2 \times$ $< 1/50 \text{ erg/cm}^2 \text{ sec}$	$\sim 1/5 \text{ erg/(cm}^2 \text{ sec)}$ for scan** conditions in Row 2 above
Other Considerations	Can't operate by day or when clouds present Portable, airborne if required Absolute calibration straight- forward and self-contained Limited F-region information	All-weather operation Fixed installation Absolute calibration needs outside reference** Good lower F-region information 7^{**} $\sim \$10$
COST	$\sim \$10^5$	

* Referred to 2 inch diameter aperture single detectors, such as in Alaska network

** Referred to DNA 617 monostatic radar at Chatanika, AK; space/time tradeoffs of course are possible

wavelength photometers that scan in the meridian plane, and video-based and related devices with multiple focal plane detectors for measuring two-dimensional radiance distributions. (All-sky cameras with radiometrically calibrated film can be also considered as multiplexed photometers, with wavelength-time-intensity resolution lower than that of the more expensive electro-optical sensors.)

Radiance in bands of the First Negative (B-A) system of N_2^+ is usually adopted as the basis for measuring column ionization rates, because the ratio of cross-sections for populating N_2^+ 's B and X states remains nearly independent of charged-particle energy and the principal bands are both intense and more or less isolated from other auroral features. The column intensity decreases somewhat as the energy spectrum of the aurora-exciting electrons softens, a 25% effect between characteristic energy parameter 20 keV and 1 keV (Fig 7 of Ref 21). In addition the appropriate energy input refers to that range of (lower) altitudes in which infrared-chemiluminescent reactions are favored. These "fundamental" uncertainties can be reduced sharply if the primary energy spectrum is known, as we will show later in this Section (p 149). Larger errors are introduced by scattering of auroral light in the lower atmosphere, which we will also review in further detail; these too are in principle subject to correction.

The inherently high time-space resolution and threshold performance of photometers (Rows 2 and 4 of Table 5) makes even relatively inexpensive installations effective on most auroral activity, including $\sim 1 - 20$ sec pulsating forms (Ref 22) in which electron concentration (which radar scatter measures) may not follow the precipitation. Photometers measure F-region emission from metastable species that are collisionally quenched at lower altitudes, such as O^1D and N^2D atoms and even $N^+ 2P$ ions; however, since the low-lying upper states can be populated by other mechanisms the measurement may not relate directly to electron-impact excitation (Row 5).

In contrast to spectroscopic remote sensing, the interpretation of power input results from incoherent radar backscatter has received rather little critical attention in the refereed scientific literature. The range information contained in the radar pulse returns provides altitude profiles of volume ionization rate. As we note in Appendix II, the measured quantity is electron concentration, and the procedure involves an estimate of the effective recombination coefficient applicable to the ionosphere's species concentrations and the assumption that an equilibrium electron density obtains (free electron production rate \approx destruction rate). There does not appear to be sufficient experience, disinterested expert analysis, or cross-calibration to assess absolute accuracy over all dose rates and histories. As a partial cross-calibration (see also Ref 20), we shall compare line integrals of volume ionization rate derived from the radar sounder to those derived from scanning photometry (p 140).

SCATTERING AND BUILDUP IN THE LOWER ATMOSPHERE

As we pointed out in Ref 1 (p 57), the apparent auroral radiant intensities must be corrected for those photons that are out-scattered and absorbed by molecules and aerosols in the troposphere. For example about half the $\lambda\lambda 4278$ and 3914 quanta are singly-scattered from a vertical path to sea level even under clear, dry weather conditions (Table 2 of Ref 1). Rayleigh and Mie scattering not only reduce the brightness in the direction of isolated auroral forms, but also contribute to the sky's apparent radiance at other viewing angles. This "flare light" mimics excitation by particle precipitation, and must also be corrected for to determine accurately the predosing.

The need to consider troposphere scatter and extinction when interpreting aurora was already well recognized in the early 1950's. Approximate compensation procedures, based on S. Chandrasekhar's 1950 treatise "Radiation Transfer," are outlined in Chamberlain's 1961 text (Ref 23). These methods have been most recently used to

improve $\lambda 5577/\lambda 3914$ column emission ratios measured from ground stations (Ref 24). They are of course applicable in auroral simulation of nuclear-particle deposition in the atmosphere as well as to auroral morphology.

The fundamental transfer equation (2.16 of Ref 23) is of the form

Actual upper-atmosphere radiance =

$$\frac{\text{Apparent radiance} - \text{Inscattered "radiance"}}{\text{Narrow-beam atmosphere transmission}}$$

as illustrated in Fig 66. Determining the in-scattered component involves integrating the brightness over the upper hemisphere, which in principle can be done from All-sky photographic images. It also requires some knowledge of the ground albedo and of course of the atmosphere's attenuation and scattering coefficients. (Evidence of the role of upwelling radiation is given both by DMSP photographs and the observation that the high-latitude winter airglow remains intense even under thick overcast, presumably because of multiple scattering of photons between snow and cloud deck.) Both these geophysical factors may vary within the (~ 200 km) region in which scattering makes a significant contribution to sky radiance.

The radiative transfer model adopted and the atmospheric-optics data input to it must be complete enough to promise results sufficiently accurate for the specific auroral simulation. For those HAES applications in which nearly-"prompt" emissions from isolated arcs are measured, a simple exponential attenuation (Ref 1) probably provides adequate correction. In extended substorm breakups, however, applying narrow-beam attenuation would in general give less accurate assessment of particle input than no correction at all. Where long-period predosing is a factor - as in interpreting CO_2^+ emission -, or when measurements are made at low zenith angles from the ground, consideration of inscattering would definitely improve

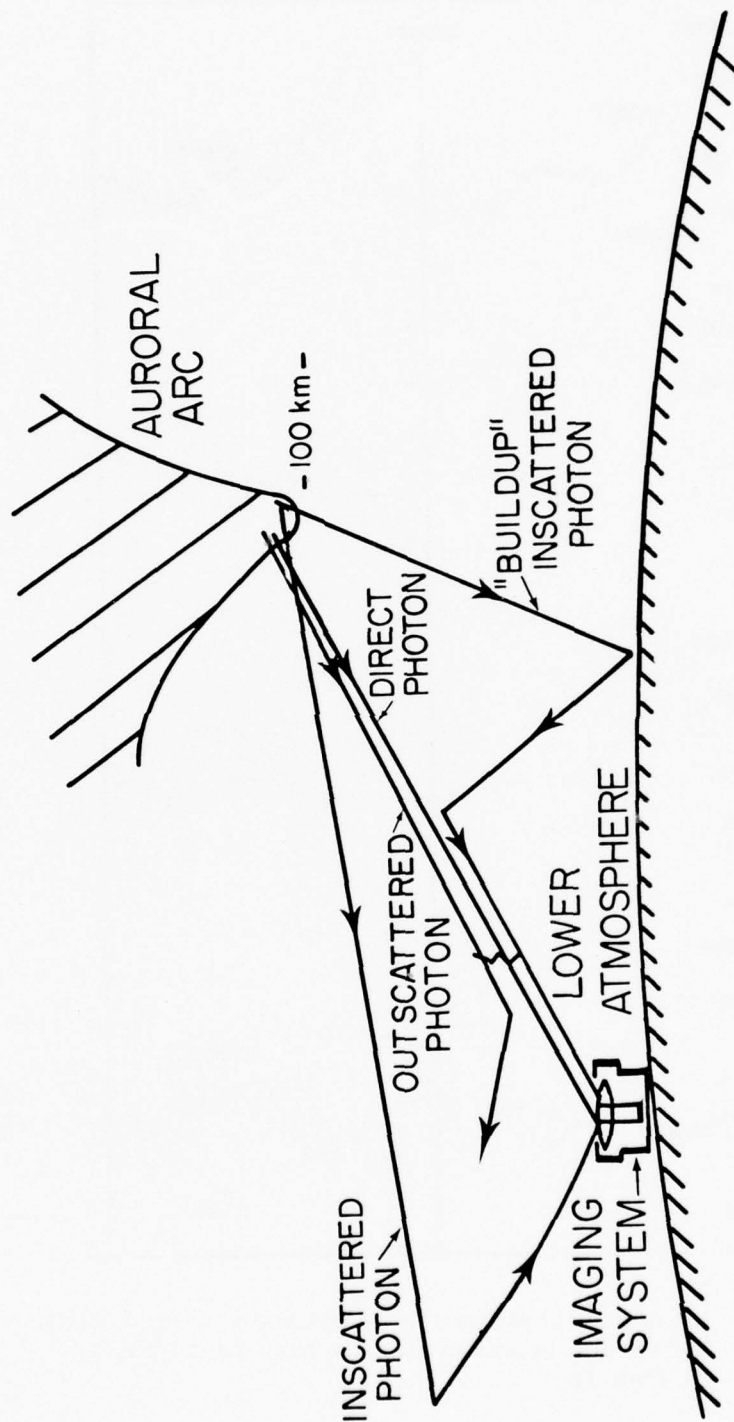


Figure 66. Schematic diagram of photon scattering and buildup in the atmosphere between auroral form and sensor.

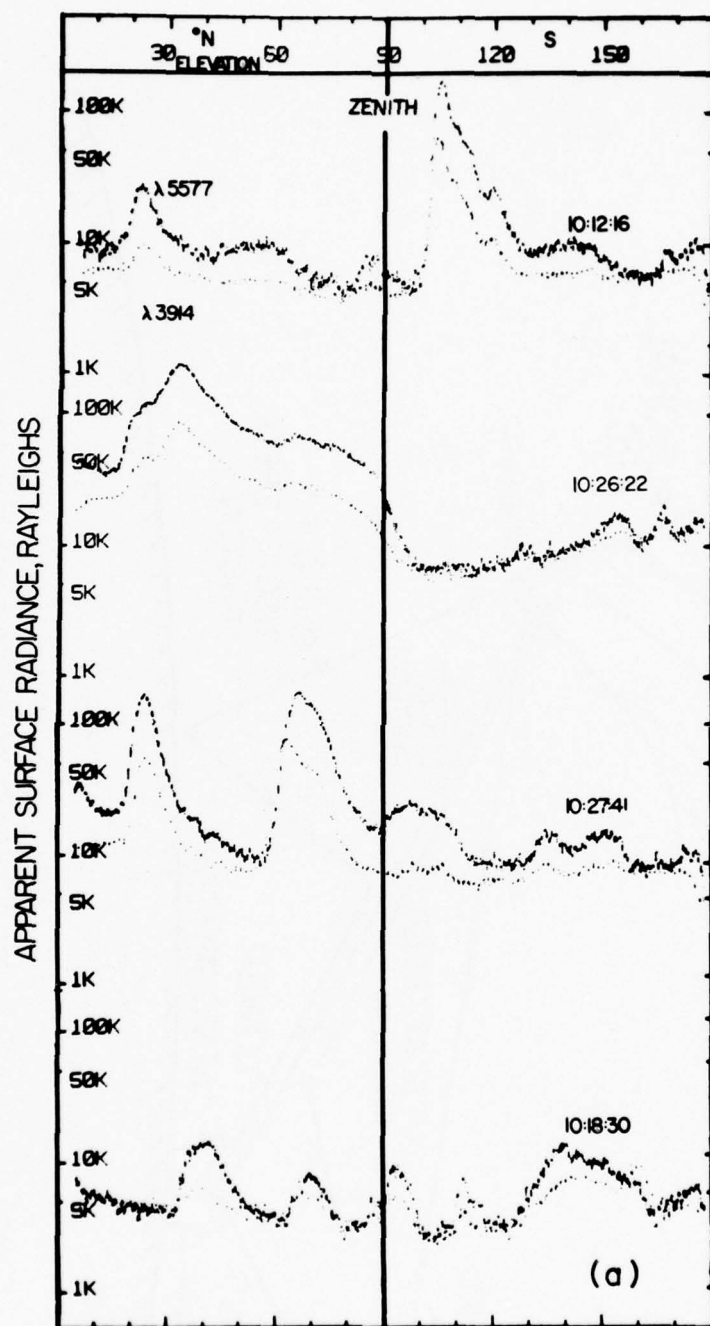


Figure 67a, b. Meridian photometer scans with (a) and without (b) strong isolated arc forms, from PKR 21 Feb 76.

HAES data quality.

This "buildup" is as expected present in much of ICECAP's meridian photometer scan data. The sky near Poker range is generally bright whenever intense auroral arcs are within $\sim 70^\circ$ of the zenith, as is indicated by the example scans in Ref 1. While some of this emission may be excited by "inverted V" drizzle precipitation (Ref's 5 and 25), the actual radiance distribution suggests that some also must arise simply from scattering. This is further illustrated by the low dynamic range of $\lambda 3914$ radiance and the decreased $\lambda 5577/\lambda 3914$ column intensity ratios in ICECAP 76 meridian photometer scans when arc forms were present, Fig 67a (Ref 26). The uncorrected green/blue ratio varies between its "canonical" value of 2 in arcs and 1 (or even less) outside them, for peak $\lambda 3914$ arc radiances between ~ 10 and 100 kR. In contrast, when as in Fig 67b the sky's radiance is more nearly uniform (to within a factor ~ 3 except in some small arcs near the northern horizon) the ratio away from the horizons remains very close to 2 for mean $\lambda 3914$ between 6 and 1/4 kR.

The decreased apparent $\lambda 5577/\lambda 3914$ ratio outside arcs (Fig 67a) is consistent with the greater Rayleigh (and Mie) scattering of shorter-wavelength photons. In the absence of high-contrast auroral forms (67b) the effects of buildup from scattering tend to average out, with some increase in $\lambda 3914$ toward the horizons and strong hints of van Rhijn enhancements (67a and b). (The somewhat higher ratio in the least-intense aurora (lowest frame in Fig 67b) is most probably due to the contribution of $\sim 1/5$ kR $\lambda 5577$ continuum nightglow, and the relatively enhanced $\lambda 3914$ near the lower northern borders of narrow arcs lying within $\sim 60^\circ$ of the zenith (Fig 67a) is most likely due to increasing quenching of O^1S toward lower altitudes.) We estimate the typical N_2^+ -band inscattered intensities in the subsection following, using actual arc and drizzle measurements by the DNA 617 radar.

A brightening is frequently observed over Poker Flat in the few minutes before the arrival of southward-moving arc systems (that is, during the substorm expansion phase), and is a factor in the decision on when to launch rocket probes. Some of this radiation is probably due to scattering in the troposphere of light from arcs at high zenith angles. The contribution excited by particle precipitation could be determined by the radar or photometrically from aircraft altitude, where the buildup intensity in the zenith is small.

A COMPARISON OF SPATIAL SCANS

To assess further this inscattered photon contribution and investigate incoherent scatter radar's performance in determining energy inputs, we compared results from a DNA 617 radar scan in the meridian plane to those from scanning photometers at Poker Flat Research Range. This procedure is similar to that in Ref 20, which compared the time dependences of auroral power inputs derived with instruments coaligned toward geomagnetic zenith.

Some reduced Chatanika radar meridian scans are available for the night of 12 Mar 75 Z (Ref 27), when the Geophysical Institute's Fort Yukon and LMSC's Chatanika meridian scanning photometers were in operation under clear-sky conditions (the Ester Dome unit was inoperative). The photometers present views from ground stations separated by 186 km of the auroral sky surrounding the reasonably well isolated IBC II-III arc near Chatanika zenith ($\sim 60^\circ$ of FYU) at 0840, also shown in Fig 68. The radar's electron density data and the photometers' projections are shown in Fig 69.

We first converted these electron densities to energy deposition rates applying an effective recombination coefficient of $3 \times 10^{-7} \text{ cm}^3 \text{ sec}^{-1}$ at all altitudes (Ref 20), and then summed these manually along zenith angle lines from both stations. We added a $\frac{1}{2} \times 10^5 \text{ electrons/cm}^3$ contour at high altitude (which contributes a few percent to the column

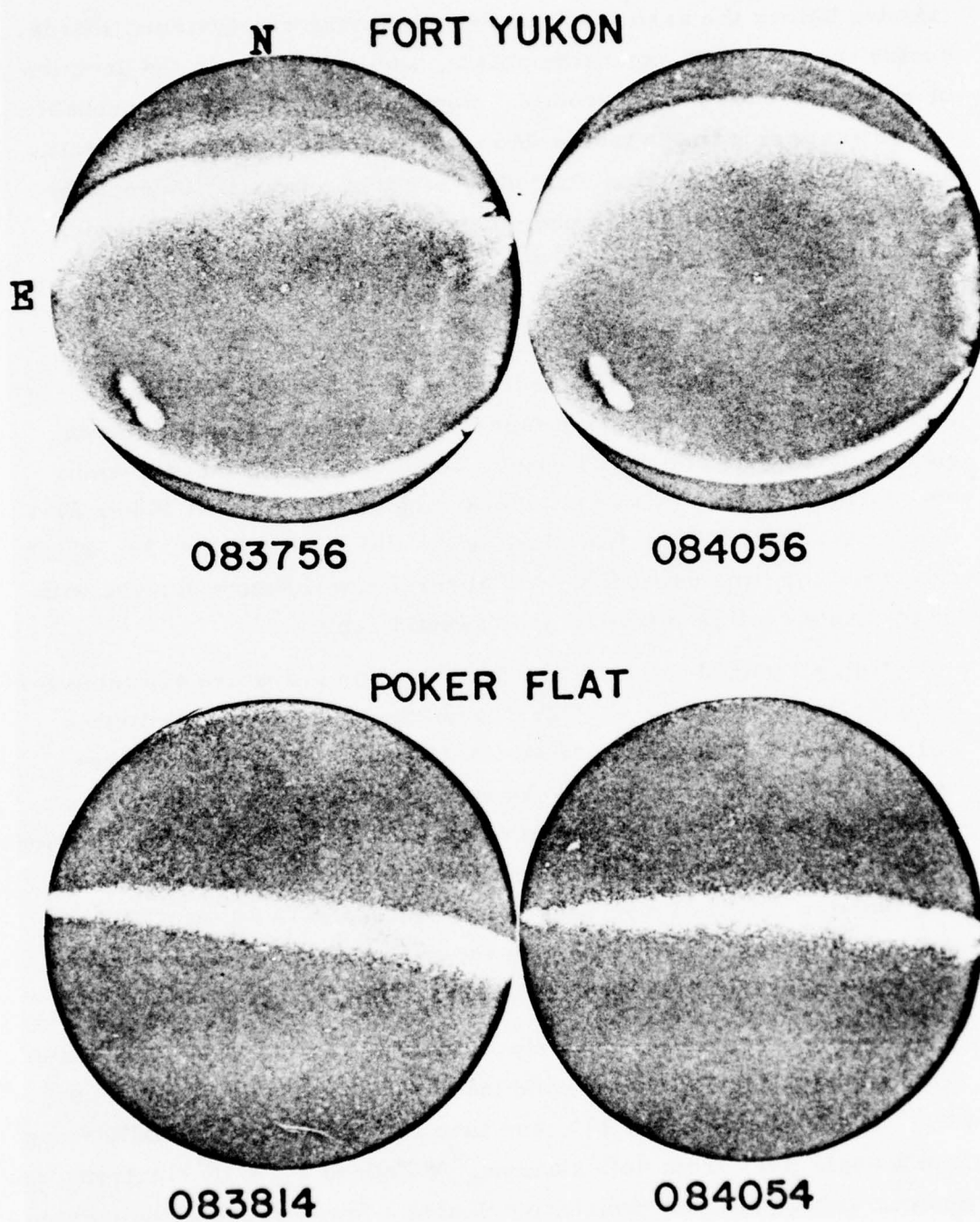


Figure 68.

All-sky views of the isolated arc over PKR and the arc N of FYU, 12 Mar 75.

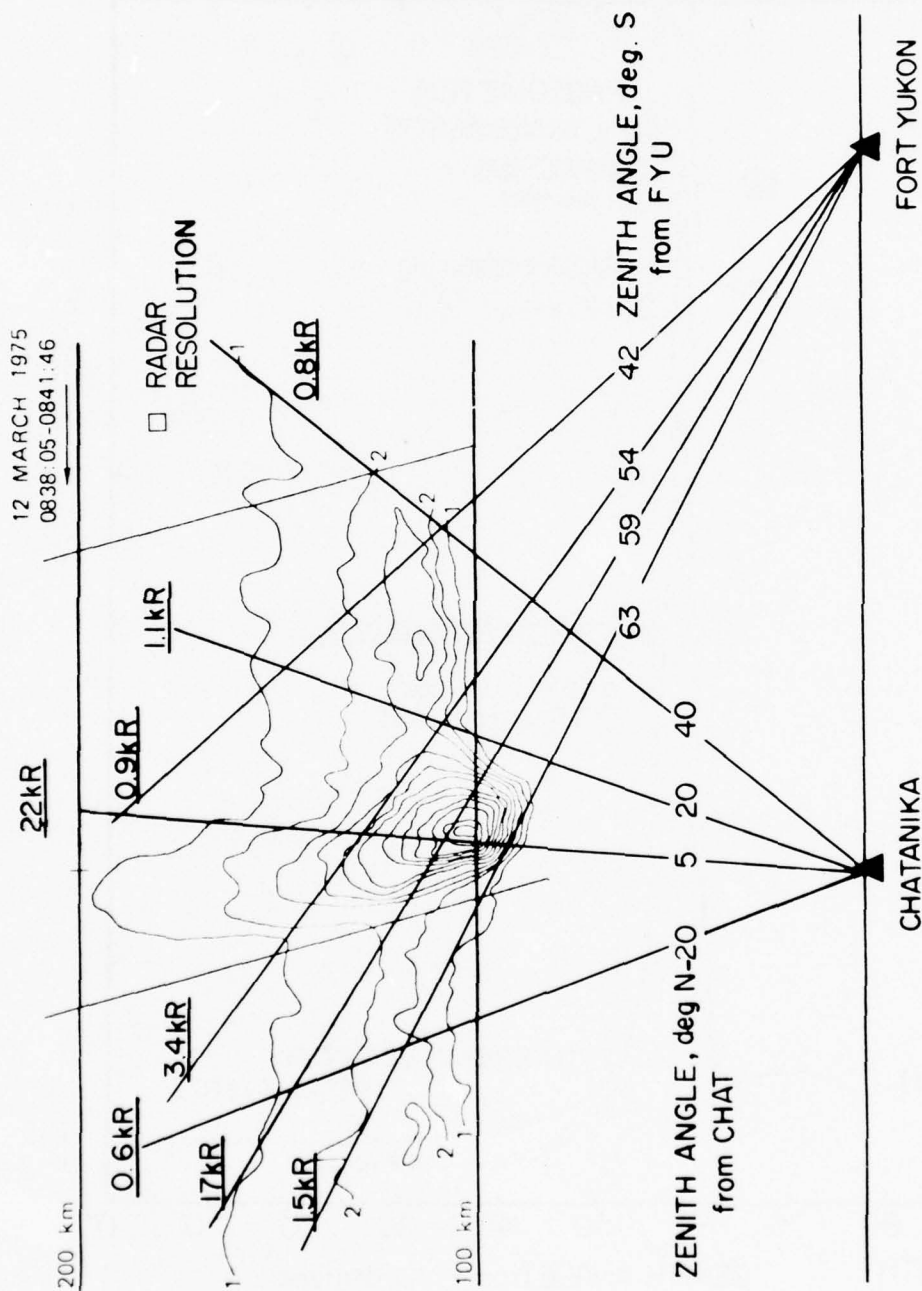


Figure 69. Contours of meridional-plane electron density on 12 Mar 75 at Chatanika, AK (from Ref 27), with column integrals converted to $\lambda 4278$ radiance at FYU and PKR as described in text.

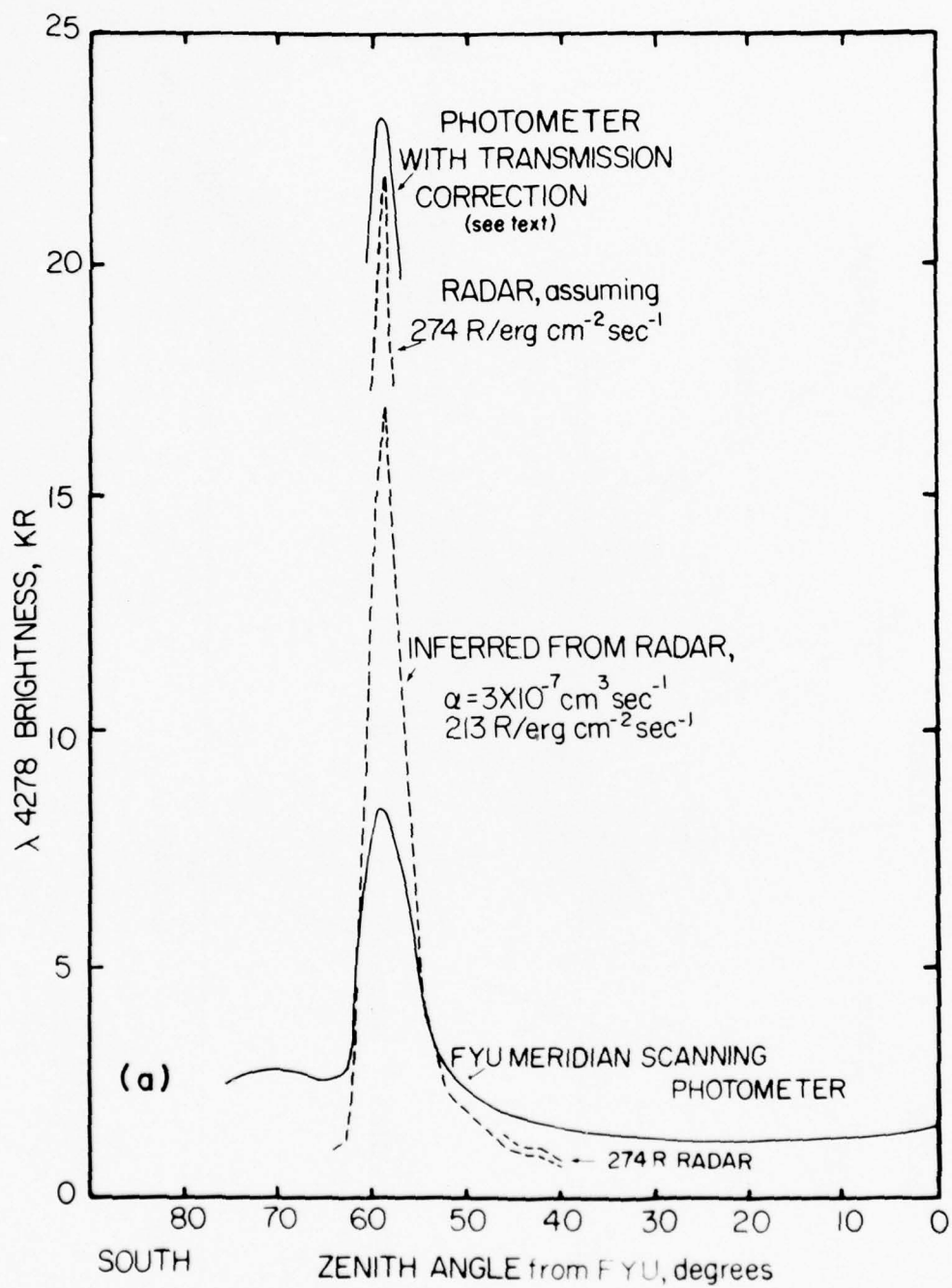
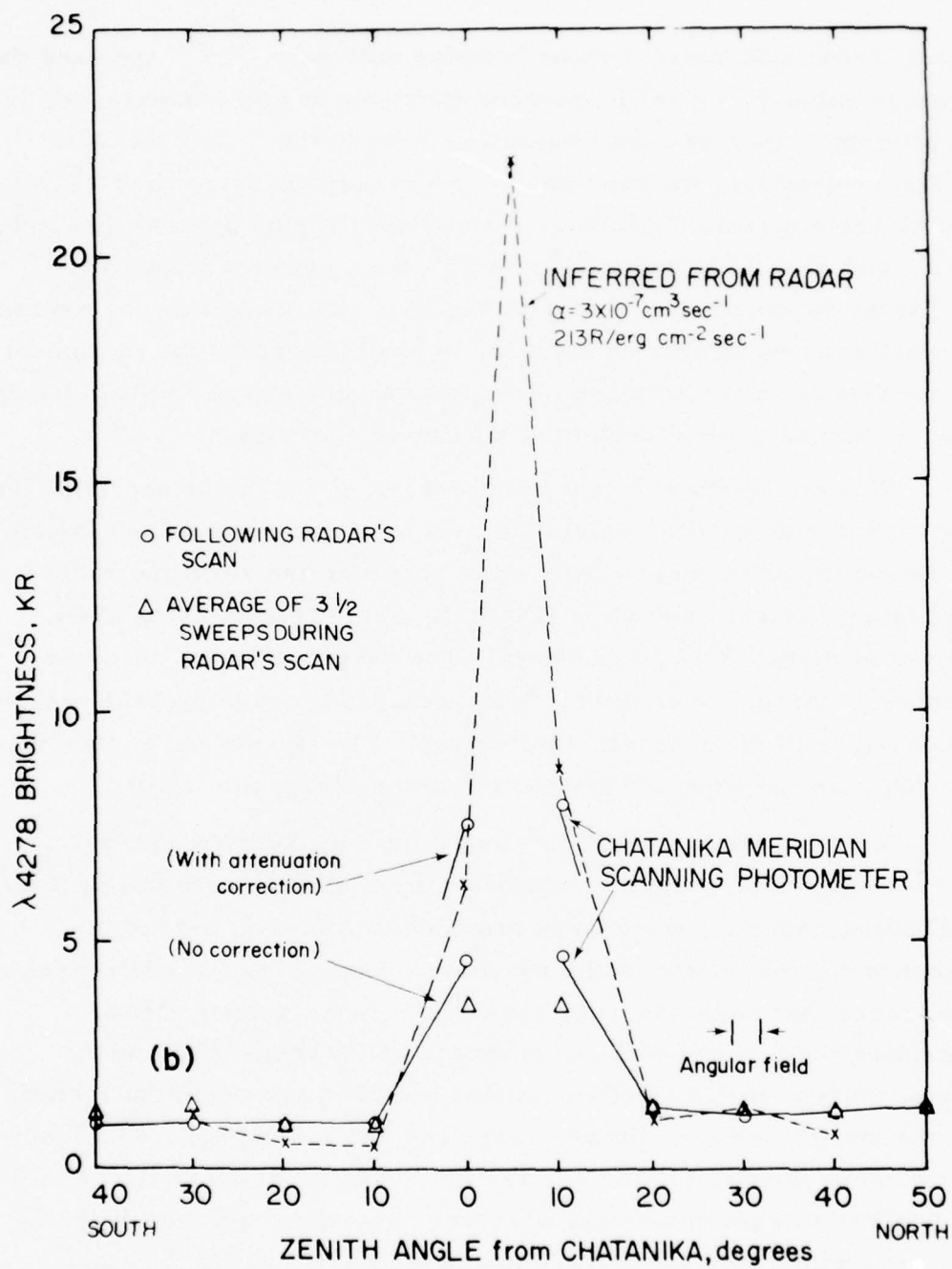


Figure 70a, b. Comparison of measured $\lambda 4278$ meridian radiance distribution at FYU (a) and PKR (b) with calculation from Chatanika radar's electron density profiles, 0840 12 Mar 75.



sum), drew in an extra contour between each pair given, and used the average value of $+d[e]/dt$ between each pair of new contours, all in an attempt to increase the integration's precision. For the Fort Yukon projections, we summed volume deposition rates each 2° in zenith angle outside the intensely-irradiated region between 40° and 54° S, and each 1° between 54° and 62° , thus encompassing the 73° of Chatanika-zenith data (refer to Fig 69). In composing the Chatanika projections, we integrated each 10° in zenith to match the increment in the data from the stepping photometer there, and in addition added one column near the direction of maximum densities.

We applied the efficiency factor 213R of $\lambda 4278$ per $\text{erg}/(\text{cm}^2 \text{ col sec})$ adopted in Ref 20, which converts to 25 ion pairs/ $\lambda 3914$ photon, to derive the absolute abscissa scale shown on the resulting radar-equivalent "brightness" plots (Fig 70). Some results using 274R, or 19 ion pairs/ $\lambda 3914$, are shown. The "best" effective efficiency figures, averaged over the arc's altitude profile, are probably 22 and 245R (refer to the subsection following). The two dashed segments on Fig 70a span the expected ionization/photon conversion ratio.

We read the radiances measured by Fort Yukon's $\lambda 4278$ (N_2^+ First Negative (0,1) band) photometer from copies of its photographed CRT output signals, which were provided to AFGL as part of the Geophysical Institute's range-support package. Fig 71 shows four of the ten traces that cover the time span of the radar's much slower meridian scan, along with intermediate calibrations (photometer signal voltage-to-CRT deflection) that had been placed on the record by the station operator between 0816 and 0817. The individual traces show some variation in the sky radiance distribution S of FYU zenith, in qualitative agreement with what was observed from the Chatanika optical station, and substantial northward movement of the other intense arc near 40° N. (For example, the radiance near 10° S held between 1.35 and 1.65 kR.) We judged the southward intensities sufficiently constant to obviate the need for developing a procedure to

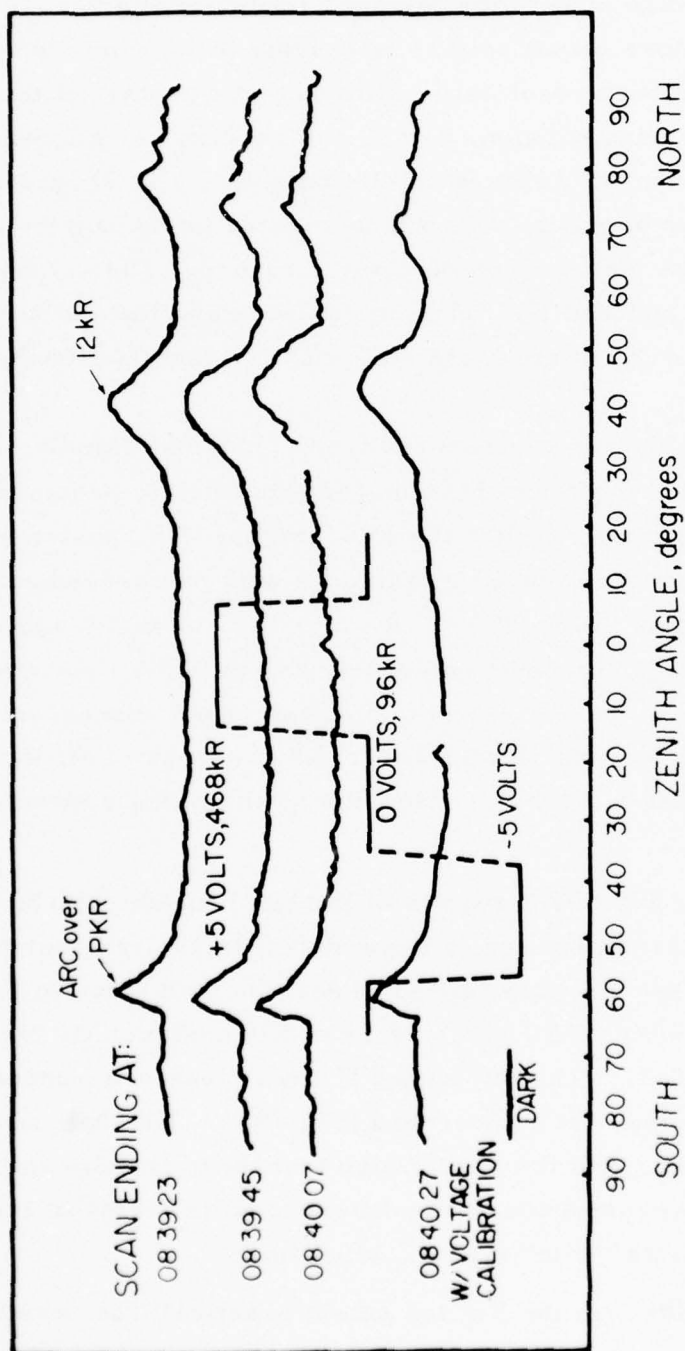


Figure 71. Meridian scans in $\lambda 4278$ from Fort Yukon, 12 Mar 75.

"match" times with those along the radar's 221-sec sweep, and to allow use of an average of the four radiance traces in Fig 71.

The photometer, whose output voltage is roughly logarithmic with scene radiance, had been absolutely-calibrated at the start of the winter auroral observing season, a radiance reading being supplied each 0.25 volt between its limits ± 5 volts output. Fig 71 gives some estimate of the precision with which auroral intensities can be read from the Alaska meridian photometer's record. The solid lines in Fig 71 show the reduced FYU photometer scan and the arc's peak intensities corrected for narrow-beam attenuation (only) following Table 2 of Ref 1.

The meridian photometer records from Chatanika (kindly provided by R. Sears of LMSC) appear to have better photometric precision though less angular precision than the FYU traces. The photometer steps in 10° increments, compiling radiances with one second sampling time at each step, thus taking 80 sec to cover 160° in zenith angle. For the reduction Fig 70b we both interpolated between the records from individual cycles that spanned the position on the incoherent-scatter radar's angular scan (circles) and took averages of all the photometer's readings at each direction during the radar's sweep (triangles).

Within the arc over PKR results of the two procedures show the same good spatial agreement, and to some extent intensity agreement, reported in Ref 20 for the time dependences. On both sides of the arc region, however, the FYU photometer shows consistently higher power inputs (Fig 70a). The difference if any is less pronounced when the (near-isolated) arc is overhead (Fig 70b). We shall review these findings briefly, with the recognition that there is substantial further scope for interpretation of the differences (in terms of instrument performance as well as "true" signal intensities).

We first consider (to the limited extent practical) the possibility that the excess apparent radiances at FYU are due to instrument

effects such as flare in the photometer or a systematic error in the radar's results at low electron densities. There does not appear to be sufficient total emission from the arcs to produce the observed large (and "smooth") signals by internal scattering in a reasonably-well-designed photometer telescope. To check on the radar's consistency, we reviewed our reduction of the data in Fig 69 for both precision at high and low mean electron densities and possible effects due to variation with altitude of the effective recombination coefficient α . Since most of the contribution to all the FYU line integrals comes from a narrow range of ionosphere altitudes, an altitude dependence (Ref 20) would not be the cause of the apparently low radar results outside the arc. A decrease in α with electron density would be required to reduce the higher "contrast" in the radar's column energy deposition measurement.

Assuming no further serious instrument errors, it would appear that FYU's ~ 1 kR photometry excess N of $\sim 52^\circ$ S is in-scattered from the arcs. The increase in $\lambda 4278$ radiance near FYU's southern horizon is also not well reproduced by the radar column integrals taken from Chatanika station; however the mean level could be fit in a very rough sense, after van Rhijn correction, to the Chatanika radiances S of the arc (which are themselves generally higher than the radar results).

It is instructive to estimate the zenith sky radiance at FYU originating from photons scattered from the two isolated arcs. These cover $\sim 1/10$ the solid angle of upper hemisphere (Fig 68), and have a mean surface radiance of ~ 15 kR after correction for the $\sim 1/3$ narrow-beam transmission of the lower atmosphere. If (to a very rough approximation) the remaining $2/3$ or 10 "kR" is considered spread uniformly over the remaining $9/10$ solid angle, the apparent sky radiance will be ~ 1 kR, which is indeed quite near that observed between 0° and 40° S. The radiation transport method in Ref 22 is in effect a quantification and rationalization of this very simple approximation procedure.

The radiances measured outside the arc by the 10^0 -stepping photometer at Chatanika (Fig 70b) show smaller, if any increases over the radar sums. This may be due to the presence nearby of only a single arc lying toward the zenith, with the second arc ~ 300 km northward contributing little flare light to the sky over PKR. Since the arc's peak $\lambda 4278$ radiance is not sampled, we cannot ascertain its "contrast" over the local auroral sky or improve the estimate of buildup intensity over that in the preceding paragraph. In any case, however, it is clear that applying a simple outscattering correction to optically-measured power inputs outside the isolated arc - nearly a factor 2 at typical 30^0 zenith - would exacerbate both the Chatanika and FYU differences. This observation further indicates the presence of substantial scattered light in the exo-arc photometer signals at both stations.

This preliminary discussion, as we mentioned earlier, leaves considerable room for further and even different interpretation of the differences in results from the two common procedures for measuring auroral power inputs. At a minimum the comparison has served to show that predosing measured by ground photometry may be spuriously increased (as well as decreased) by scattering of auroral photons in the atmosphere.

RATIOS OF IONIZATION TO N_2^+ FLUORESCENCE TO NO CHEMILUMINESCENCE

The changing composition of the atmosphere at altitudes above ~ 90 km has an effect on the apparent vertical-column intensity of NO vibrational radiation in aurora, which though not large might otherwise be interpreted as due to changes in the chemiluminescence with density or temperature(or dosing). We therefore show here, in a preliminary way, how the infrared emission depends on the altitude profile of the primary electrons' energy deposition, and thus on their energy spectrum as well as total column rate of ionizations.

The atmosphere's relative concentration of N_2 molecules decreases with increasing altitude in the region where most auroral charged-particle energy is absorbed, while the relative O-atom concentration increases. Therefore fluorescence in the N_2^+ First Negative band system (the commonly-applied indicator of auroral intensity) decreases, while the rate of quenching by ground-state O of N_2^+ atoms (which, according to present models, excite NO^+ when they react with O_2 molecules) increases. That is, there appears to be both less energy deposition and less chemiluminescent emission, so that if no correction is made the net result is only a second-order effect on the simulation. Nonetheless since the infrared yield may also depend on unknown aeronomic factors, changes attributable to atmosphere composition must be considered in interpreting HAES measurements of NO^+ altitude profiles and - in particular - in extrapolating them to the β -patch at lower heights in the atmosphere.

To illustrate these ideas more quantitatively, we compiled the integrals over altitude of auroral energy deposition profiles and the resulting averaged effective efficiencies for $\lambda 3914 N_2^+$ First Negative (0,0) band emission in Fig 72. The volume ionization data refer to a model "Maxwellian" primary electron spectrum (the form discussed in Appendix II and Ref 21) with characteristic energy 2.3 keV, and the substantially harder spectrum exciting the arc of 27 Mar 73 as measured by multi rocket A18.205-1's particle counters (Ref 4). $\lambda 3914$ excitation efficiency profiles output from the ARCTIC code (Ref 28) were weighted by ionization profiles from Ref's 27 and 4 respectively to derive $\lambda 3914/(\text{ion pair})$ ratios in a vertical column (such as apply to ICECAP's aircraft measurements, Sections IV and VI). The $\lambda 3914$ photon yields measured at low to moderate altitudes in the PRECEDE rocketborne electron-accelerator test (Ref 29) agree very well with ARCTIC's calculations ($21\frac{1}{2}$ ion pairs/ $\lambda 3914$ to 100 km, increasing to 23 at 123 km, 24 at 140 km and 28 at 186 km). These latter altitude-localized efficiencies of course

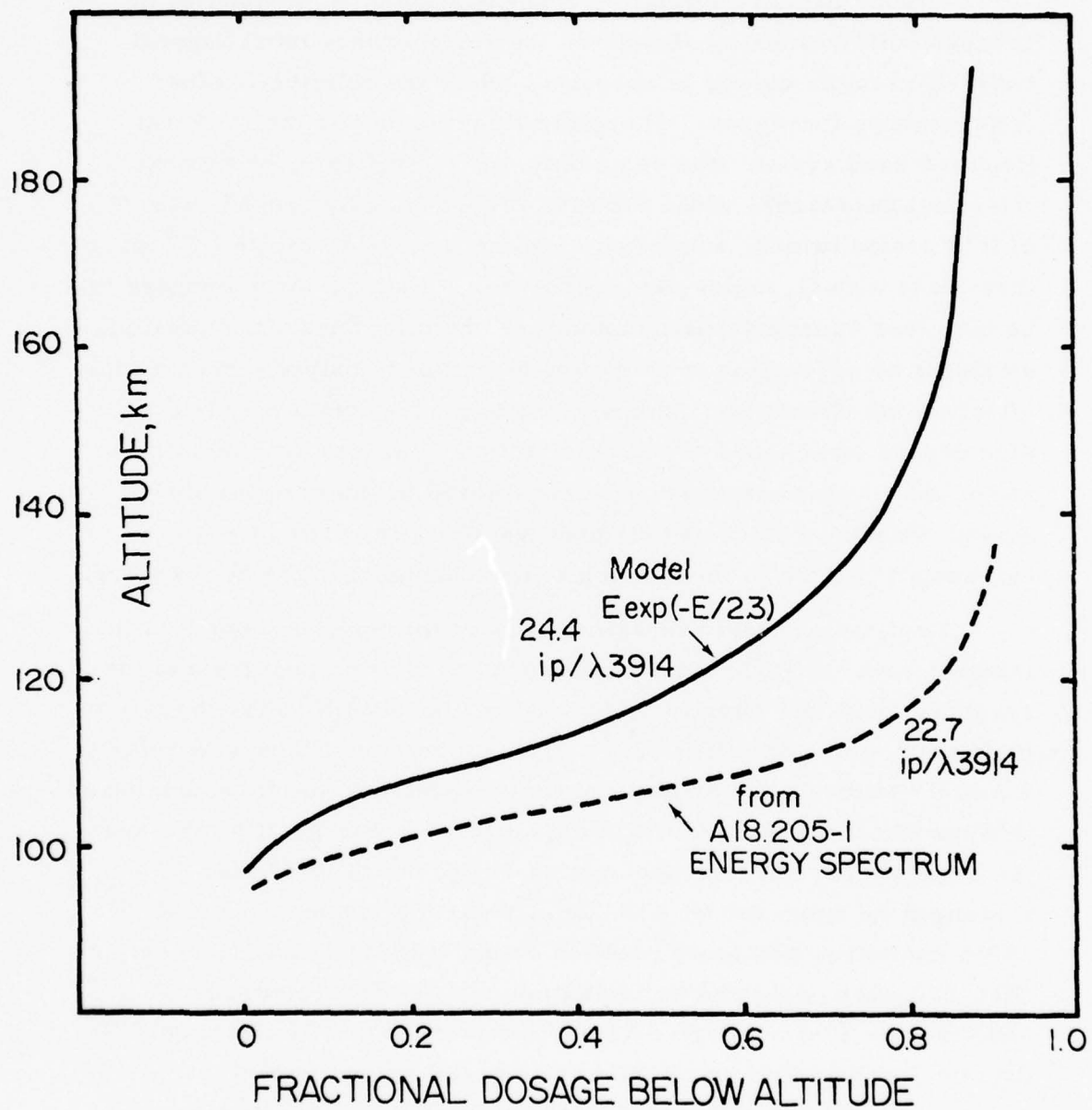


Figure 72. Column integral of volume energy deposition rate for two primary electron energy spectra.

apply directly to side-looking radiometry of auroral arcs from multi-instrumented rockets (Sections I and II).

In present models of the chemistry of air following partial ionization, N^2D atoms originating from dissociations of N_2 molecules react with ambient O_2 molecules to excite NO^+ . At altitudes above 140 km, however, N^2D becomes preferentially quenched by the increasingly abundant O^3P atoms (Ref 30). Thus (in terms of current aeronomy) ionization above ~ 140 km should be subtracted when calculating from auroral data NO^+ chemiluminescent efficiency ratios applicable to nuclear excitation. This introduces about a 25% correction (in the number of effective ion pairs/ $\lambda 3914$ photon counted) for soft primary electron spectra, and 10% for the hard spectra typical of bright auroral arcs (Ref 31) and breakups from which almost all the useful aircraft NO^+ data are in any case derived (refer to Fig 61). For HAES measurements in the aircraft's zenith, then, a reasonable inverse fluorescence efficiency figure becomes $0.9 \times 22.7 = 20\frac{1}{2}$ ion pairs/ $\lambda 3914$.

It could of course be argued that since N_2 is the source of N^2D , the rate of ionizations plus direct (and "secondary" EUV-produced) dissociations of N_2 below ~ 140 km is a more physically appropriate measure for quantifying NO vibrational intensities. The ratio of this quantity to total column excitations of $\lambda 3914$ photons is about 15 in bright aurora. In any case, the measure selected for expressing NO chemiluminescence "efficiencies" carries some implications about the aeronomy that the simulation is designed to clarify.

SECTION VI

ICECAP 76 AIRCRAFT MEASUREMENT PROGRAM AND AURORAL RADIANCES DATA

INTRODUCTION

A series of measurements of short wave infrared emission from aurora was made in conjunction with ICECAP 76 by AFGL's IR-Optical Flying Laboratory (USAF NKC-135A S/N 55-3120). The aircraft's operating plan, with an outline of its instrument configuration and ground coordination and a discussion of program goals, is reproduced in Appendix I. Background information on the radiometers and photometers is given in Section III and in Ref 2's Section IV and Appendix II, in which the ICECAP 75 aircraft program is described. Particular reference is made to Ref 2's Fig 21, which projects the flight tracks in this report's Tables A1-4 and -5 against the mean midnight auroral oval; its discussion of the overlap of the auroral ionosphere observed from the aircraft on the region accessible to Poker Research Range's coordinating ground instruments; and its review of the sensitivity of the radiometers to known aurora and airglow features. As stated in more detail in Appendix I, the purpose of these measurements was to investigate processes leading to emission of vibrational radiation from nitric oxide, in particular its altitude dependence, emission spectrum, and spatial correlation with charged-particle precipitation.

Table 6 lists and gives background information on ICECAP 76's 8 SWIR-aurora missions, plus 9 missions flown for other purposes. Moon age was 28 days at the first flight (ICECAP 3), and auroral simulation measurements continued in the next moon-down period, in which age was 25 days on 25 Mar (ICECAP 16). Cross-auroral arc flights took place near or west of the 257°E geomagnetic longitude line through Poker Range (as shown in Fig 21 of Ref 2), and parallel-arc flights were generally along lines of constant geomagnetic longitude.

Table 6. Log of Flights NKC-135 53120, ICECAP 76.

IC-76	Date	Mission - Function	USAF Base		Take-off	Land	Times		PhotoMetrics Equipment Operated	Time		Radar Overlay
			Take-off	Land			Take-off	Land		Data Start	Data End	
1	22 Feb	Ferry	Pease	Eielson	1438	2020			Wide Angle 1VN Photometer	1422:30	2056	No
2	26 Feb	Sunrise + Day Airglow	Eielson	Eielson	1518	2145			All Sky Photometer	1422:30	1503	No
3	28 Feb	Cross Auroral Arc	Eielson	Eielson	0704	1220			All Sky Photometer	0730	1222	Yes
4	29 Feb	Cross Auroral Arc	Eielson	Eielson	0745	1210			All Sky Photometer	0730	1222	Yes
5	01 Mar	Cross Auroral Arc	Eielson	Eielson	0752	1250			All Sky Photometer	0758	1146	Yes
6	03 Mar	Day Airglow, Sunset, Aurora	Eielson	Eielson	0110	0800			Photometer	0804	1211	Yes
7	04 Mar	OH Spatial Variation	Eielson	March	0910	1340			Wide Angle 1VN All Sky Photometer	0141	0442	Yes
8	04 Mar	Day Airglow	March	Eielson	1543	2205			Wide Angle 1VN All Sky Photometer	0418:20	0725	Yes
9	07 Mar	Cross Auroral Arc	Eielson	Eielson	0830	1230			Photometer	0346	0725	No
10	08 Mar	Parallel Auroral Arc	Eielson	Eielson	0630	1038			No participation by PhotoMetrics			No
11	13 Mar	Arctic Backgrounds	Eielson	Eielson	2025	2400			All Sky Photometer	0843	0930	Yes
12	15 Mar	OH Spatial Variations	Eielson	Eielson	1230	0745			All Sky Photometer	0843	1203	Yes
13	21 Mar	OH Time/Space	Hickam	Hickam	0635	1053			All Sky Photometer	0642	1006	Yes
14	22 Mar	Day Airglow	Hickam	Eielson	1830	0417			Photometer	0648	1004	Yes
15	23 Mar	Arctic Backgrounds	Eielson	Eielson	2032	0017			1 VN 25mm lens 1 VN 10mm lens	On-Off Times in Table 7		No
16	26 Mar	Parallel Auroral Arc	Eielson	Eielson	0630	1242			All Sky Photometer	1257	1610	No
17	28 Mar	Parallel Arc + Sunrise, Ferry	Eielson	Pease	0552	1310			All Sky Photometer	1257	1612	No
									1 VN 25mm lens 1 VN 10mm lens	0643	1145:45	No
									All Sky Photometer	0655	1145:29	No
									All Sky Photometer	1841	0142	No
									1 VN 10mm	2247	0136	No
									On-Off Times in Table 7			No
									All Sky Photometer	0654	1211	Yes
									All Sky Photometer	0656	1202	No
									All Sky Photometer	0612	1049	No
									All Sky Photometer	0612	1047	No

The navigator's reduction of his flight logs to geographic latitude and longitude of the aircraft measurements is continuing.

INSTRUMENTS

Refer to Table A1-1 for a listing of the coaligned, zenith-pointing spectroradiometers. The principal changes from ICECAP 75's aircraft program are

- addition of a high-resolution interferometric spectrometer covering the wavelength region $1.17 - 3.1\mu\text{m}$;
- broadening and shifting of the passband of the $2.8\mu\text{m}$ radiometer that measures NO-OH-thermal emission, to FWHM wavelengths $2.84 - 3.04\mu\text{m}$ (Ref 32; note that the broadening is less than the original plan states, and the shift of central wavelength is also small);
- addition of a multi-channel sequencing photoelectric photometer (Table A1-2; further operational data, including wavelengths and angular sensitivity, temperature effects, and calibration procedures, are given in Ref 33), which provides, along with the usual auroral intensity data, information about emission altitudes as outlined in Appendix II;
- replacement of the auroral fluorescence-contaminated $1.57\mu\text{m}$ radiometer with one designed to measure O_2 ${}^1\Delta - {}^3\Sigma$ emission near $1.27\mu\text{m}$;

- reduction of angular fields, to improve spatial resolution for infrared-visible correlation tests.

The All-sky camera was operated with 4 sec exposures on EK 2475 high-speed monochrome film. 1V-N cameras noted in Table 6 provided boresight information for sidelooking infrared instruments used in other than auroral missions, as shown in Table 7. The All-sky's useful field of view was reduced to $\sim 120^\circ$ circular by the flat window plate needed to meet aircraft safety requirements, which resulted in only a small decrease of its effectiveness in assessing brightness distributions and substorm development.

Table 7. 1V-N Camera Operation Times for IC 11 and 15.

IC 11		IC 15	
<u>Data Start</u>	<u>Data End</u>	<u>Data Start</u>	<u>Data End</u>
22 03:00	22 06:00	21 11:30	21 13:56
22 07:10	22 08:20	21 15:24	21 18:18
22 10:00	22 12:20	21 24:55	21 27:38
22 28:25	22 29:29	21 28:53	21 31:44
22 30:23	22 32:50	22 16:40	22 20:12
22 33:20	22 39:04	22 20:55	22 23:52
22 56:50	22 58:12	22 29:56	22 32:32
23 03:53	23 05:20	23 16:35	23 21:16
23 06:28	23 09:50	23 24:16	23 26:46
23 15:49	23 21:50	23 27:12	23 30:10
23 25:50	23 28:05		
23 28:44	23 31:10		

DNA 617 RADAR COORDINATION, OPERATION

To determine altitude profiles of energy deposition in auroral forms observed from the aircraft, we coordinated the incoherent scatter radar's el-az scan with the flight path. We worked with the DNA 617 staff to develop the geomagnetic meridian-plane scanning mode whose projection against the aircraft instruments' effective field of view is shown in Fig 73.

The 0.6° FWHM radar beam moves at a constant angular speed of $0.28^\circ/\text{sec}$ (nominal setting is $0.3^\circ/\text{sec}$), which with a 5.0 sec integrating time results in a zenith angle resolution of about 2° . To minimize loss of radar data during the time needed to reprogram its scanning mode, we planned a fixed repetitive program covering N and S $65\frac{1}{2}^\circ$ segments centered at $8\frac{1}{2}^\circ$ N zenith angle. (At elevation angles below $\sim 30^\circ$, the radar's signal/noise decreases rapidly.) This provides a series of coincidences (Fig 73), as an approximation to continuous coverage were the radar readily programmable to follow the aircraft instruments' intercept on the auroral E-region. The antenna's automatic scan is limited to elevation at any azimuth, almucantars, or individual three-position mode. The aircraft is of course constrained to fly at nearly constant airspeed to maintain the high operating altitudes needed for good infrared auroral data. At Chatanika's zenith, the angular speed of its ($\sim 5^\circ$) instrument fields is $\sim 0.13^\circ/\text{sec}$. A little less than 2 min of data is lost, or at least seriously degraded, in each reversal of flight direction.

For reasons of rocket range safety most of the cross-arc flights were placed near a geomagnetic meridian passing 100 km W of PKR. Thus the instrument fields "overlap" only to the extent that the primary auroral electrons, energy spectrum remains essentially constant over distances of 100 km. The radar's altitude distribution data are presumably applicable to stable auroral arcs, whose maximum surface brightness is typically near-uniform over hundreds of km E-W.

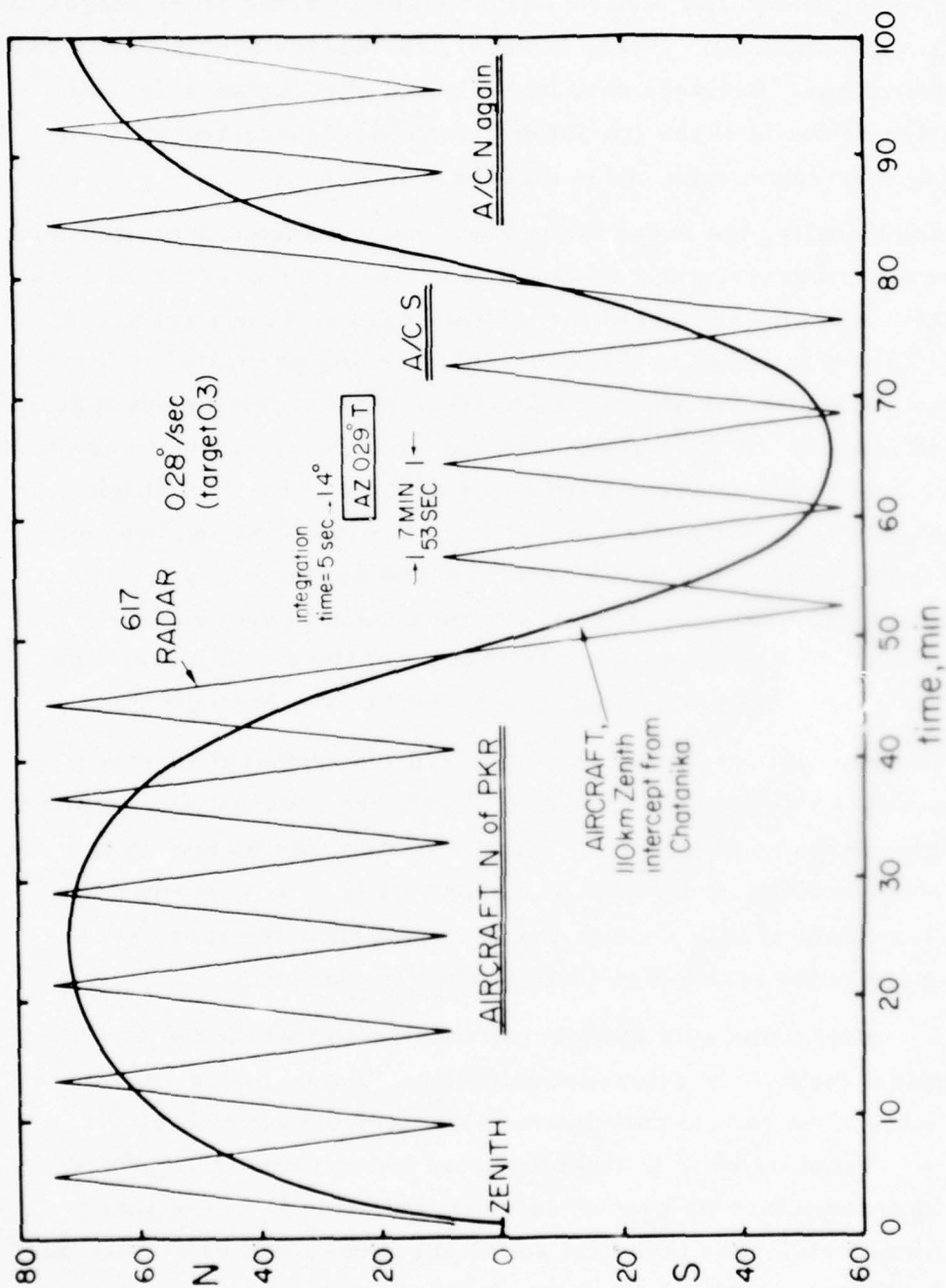


Figure 73. Zenith angles of DNA617 radar beam and projection from radar of intercept of aircraft radiometer fields with 110 km altitude plane.

Spatial homogeneity may also be adequate during some other phases of substorm development. Often, however, the energy spectrum can vary over tens of km. Radiance data from the All sky cameras provide qualitative evidence of the spatial distribution of characteristic incoming electron energy, as is discussed in Ref 31 .

Additionally, the radar facility was not continuously available to the aircraft program, since it was also tasked to support the rockets (ICECAP's and other projects'). Actual support of the first seven auroral flights is shown in Table 8 (IC17, being partially for ferry purposes, operated far off Poker Range). Most of the meridian scans extended over 54° or 70° rather than 131° zenith angle, and in addition much of the radar's observing time was devoted to the 3-position "electrojet" mode (Appendix I of Ref 1). Any coordination between aircraft and radar in the latter case would be sporadic and fortuitous, as is indicated by the plan view of effective instrument fields in Fig 74. Details of overlap await location of the aircraft from the navigator's log, along with reduction of the All-sky photographs.

To maximize coordination with the incoherent-scatter radar in the presence of its competing requirements, we followed the operation procedure shown in Figure 75. The final decision on operating mode is the responsibility of the DNA 617 staff. Data, and perhaps even worse continuity of experiment, are lost each time the radar's pointing and pulse length distribution mode is changed.

Communication with the aircraft was again maintained by the Geophysical Institute's Telecommunications Center, using various radio links. The ground coordinator also used the set of control points separated by 10 min flight time, as is indicated in Appendix I; he could order a turn or even mission cancellation at one of these navigation points. The technical and flight crews stood by at Eielson AFB starting at ~ 2000 LT on those nights that the Range's magnetometers suggested later auroral activity, awaiting launch instructions from the ICECAP ground controller (J.W. Reed, Maj. USAF, of AFGL's OPR branch).

Table 8. Missions Supported by DNA 617 Radar
(Preliminary Data)

IC76-, Date	Radar Mode	Time	Overlap on Aircraft
3, 28 Feb	Pre-planned meridian scans [*] Truncated ^{**} meridian scans 3-Position ⁺	0801-0940 0943-1001 1001-1220	Very good Fair Poor
4, 29 Feb	Truncated meridian scans 3-Position	0720-0929 0931-1210	Fair. A/C 60 n.m. Poor W
5, 01 Mar	3-Position Truncated meridian scans 3-Position	0551-0942 0943-1103 1103-1250	Poor Fair. A/C W Poor
6, 03 Mar	Truncated meridian scans 3-Position	0510-0720 0723-	May be good A/C Landing
9, 07 Mar	3-Position Truncated meridian scans 3-Position	0624-0910 0912-1049 1049-	A/C Takeoff May be good
10, 08 Mar	3-Position Truncated meridian scans Az 044° T after 0938	0630-0927 0927-1211	Poor May be good
16, 26 Mar	8-Position ⁺⁺ Truncated meridian scans Az 044° T, 36° to 90° E ^ℓ 3-Position, not as above ⁺⁺⁺ Truncated meridian scans Az 044° T, 36° to 90° E ^ℓ	0644-0911 0917-1017 1017-1140 1140-1208	Fair Fair Fair Fair

* Refer to Figure 73.

** Generally from ~ 100° to ~ 30° E^ℓ (measured from N horizon) on 029° T azimuth.

⁺ 67° elevation (measured from N horizon), 029°, 154°, 264° T. The antenna is moved each 3 min, and the A/C field may fortuitously intercept the region it measured.

⁺⁺ 76½°, 209°; 62°, 272°; 52°, 280°; 76½°, 209°; 62°, 145°; 52°, 137°; 76½°, 209°; 62°, 209°, with 2 min dwell.

⁺⁺⁺ 63.2°, 044°; 62°, 270°; 62°, 148°, with ~ 3 min dwell.

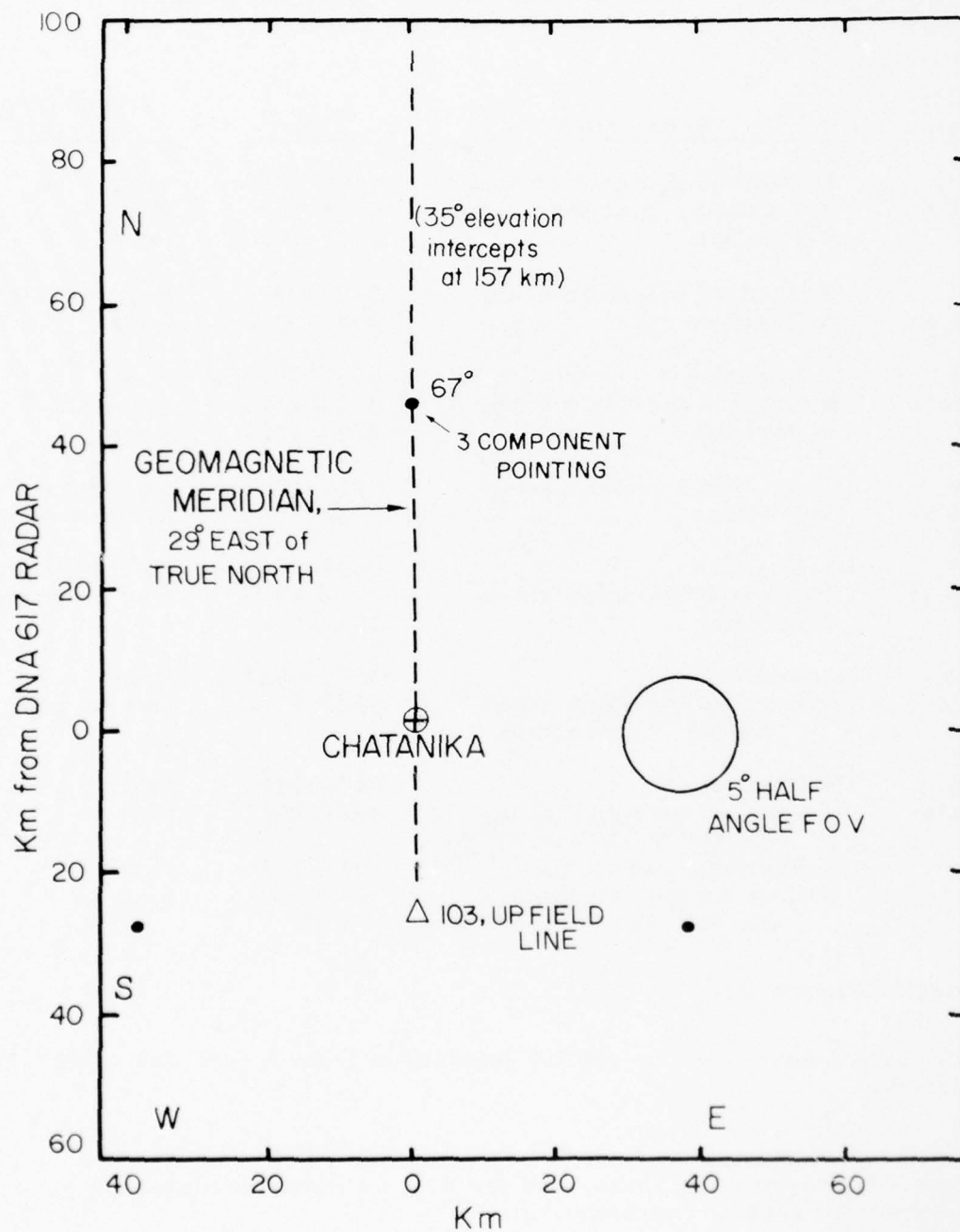


Figure 74. Plan view of radar and aircraft field intercepts at 110 km altitude, ICECAP 76.

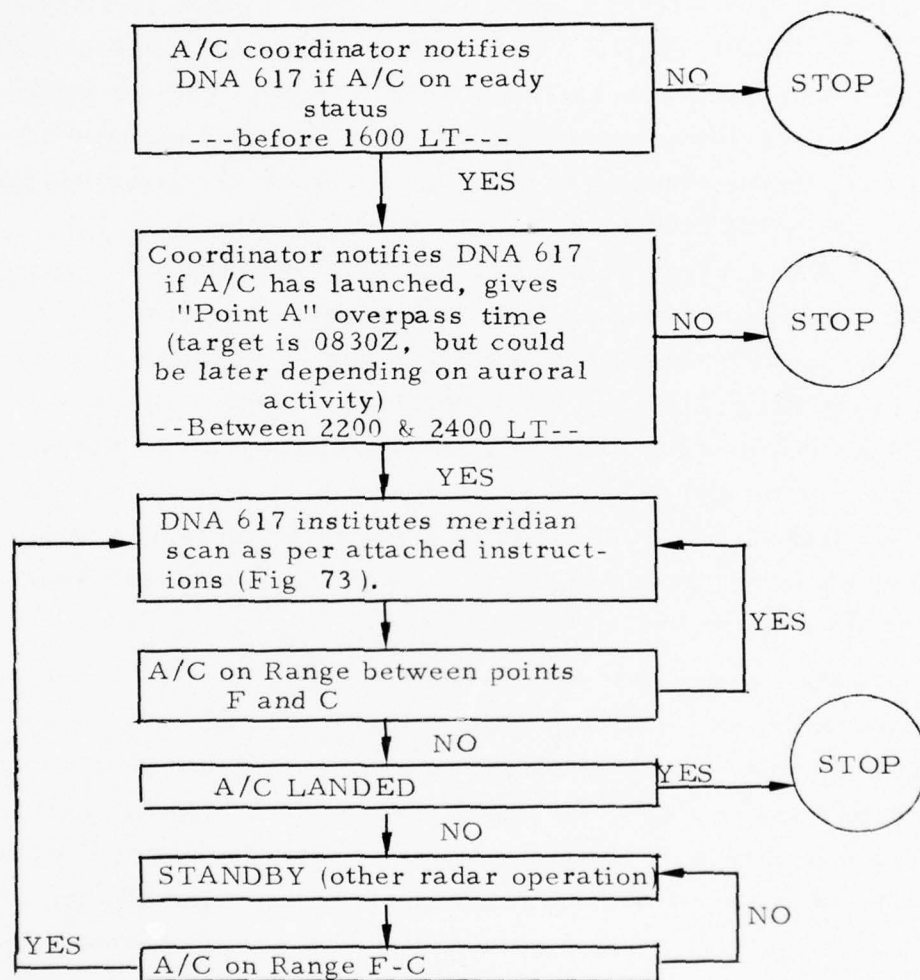


Figure 75. Operating cycle for aircraft-radar coordination, ICECAP 76.

PHOTOMETER MEASUREMENTS

PhotoMetrics operated the 12-channel photometer described in Table A1-2 and the All-sky camera (under USAF Contract F19628-76-0150, DNA MIPR 76-519/WU23). The airborne photometer had been previously calibrated against a uniform low-brightness light source. This calibration was checked in the field by comparing its aurora and airglow readings to those from some of the zenith-pointing photometers on the ground as the aircraft was passing over Poker Range. (In this process we learned that the $\lambda 5577$ radiances reported from the two different meridian scanning photometers at PKR's Hilltop station were within 20% of one another.) PhotoMetrics also kept both the Range staff and the Atmospheric Sciences Laboratory (WSMR) groups informed about aircraft flight schedules. The Range records meridian photometer and All-Sky camera data at PKR and FYU when tasked, and ASL supports the ICECAP measurements by launching sounding rockets to determine atmospheric temperature and water vapor profiles (refer to Section V).

An example of zenith radiance data taken by the aircraft photometer is given in Fig 76, and of a reduced flight record from one channel in Fig 77. The readings are being entered by teletype into AFGL's central computer, to permit both convenient qualitative comparison to similarly plotted radiometer data (such as in Fig 60) and later quantitative analyses (for example determining altitude profiles by the procedure in Appendix II). The computer facility of course allows ready access to the photometer data in virtually any format, including plots at arbitrary time scales. Signal/noise ratios in data from the $2.8\mu\text{m}$ radiometer (as communicated informally by the group in charge) are at present setting our priority in reading the ~ 34 hr of auroral-region photometer chart records. The status of this data reduction is shown in Table 9.

Table 9. Status of ICECAP 76's Aircraft Photometer Data

<u>IC 76</u>	<u>Duration Data</u>	<u>Status</u>
5	4:07	5 channels * entered in computer and plotted
10	3:20	5 channels tabulated and entered in computer
16	5:20	5 channels tabulated
6	5:20	5 channels tabulated
9	3:20	1 channel (4278) tabulated
4	3:50	None
3	4:50	
17	4:35	

* $\lambda\lambda$ 5577, 6300, 4278, 5310, 5199, all calibrated.

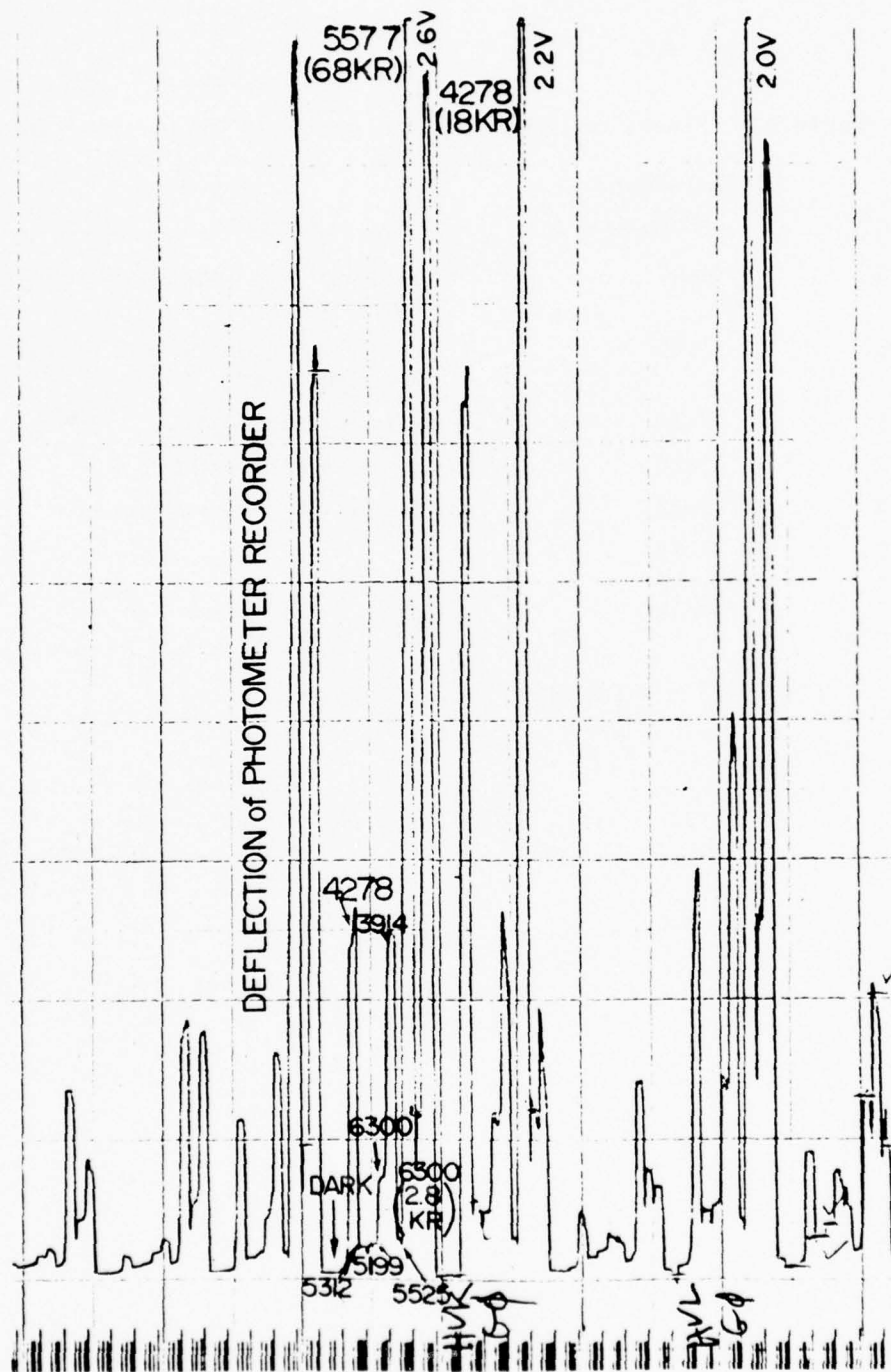


Figure 76.

Example of zenith radiance recordings from the 12-channel aircraft photometer, ICECAP 76.

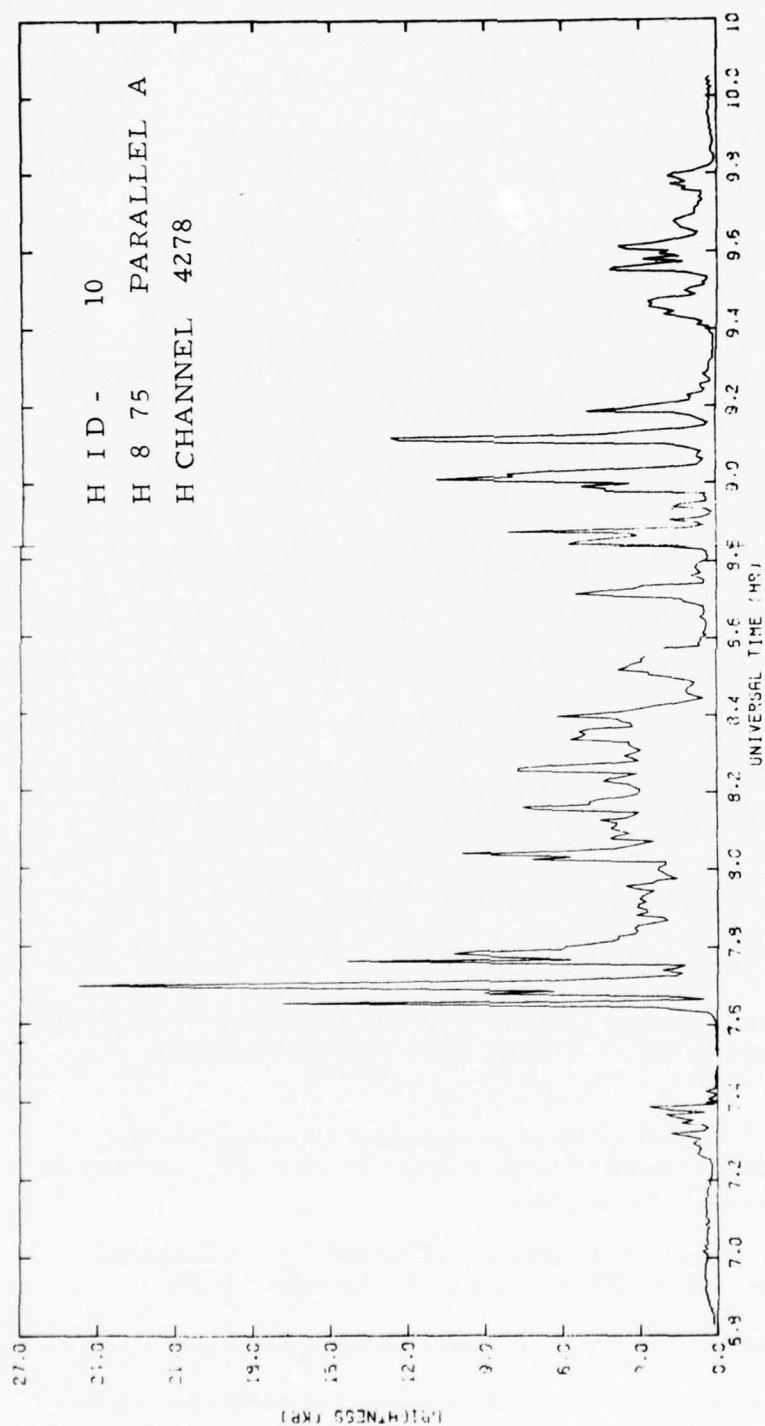


Figure 77. Example of a zenith radiance plot from one photometer channel, ICECAP 76.

REFERENCES

1. I. L. Kofsky et al., Data Reduction and Auroral Characterizations for ICECAP, HAES Report No. 4, DNA 3511F (10 April 75).
2. I. L. Kofsky, R. B. Sluder, and C. A. Trowbridge, Data Reduction and Auroral Characterizations for ICECAP II, HAES Report No. 27, DNA 3789F (25 October 75).
3. D. A. Burt and C. S. Davis, Rocket Instrumentation for ICECAP 73A Auroral Measurements Program - Black Brant 18.205-1, HAES Report No. 3, AFCRL-TR-74-0195 (February 74).
4. D. H. Archer and P. W. Tarr, Auroral Simulation Studies, HAES Report No. 6, DNA 3567T (22 April 75).
5. P. W. Tarr and D. H. Archer, Auroral Simulation Studies in Support of ICECAP and EXCEDE, HAES Report No. 24, DNA 3785F (30 September 75).
6. M. Henrist, J. Geophys. Res. 78, 2310 (1973).
7. H. S. Porter et al., J. Chem. Phys. 65, 154 (1976).
8. W. F. Grieder and L. A. Whelan, Geometric Aspects of Rocket Photometry, HAES Report No. 41, AFGL-TR-76-0046 (February 76).
9. J. Rogers, private communication, 1976.
10. T. Degges, Appl. Opt. 10, 1856 (1971).
11. Aeronomy Observatory, Ground Support Data Report in Support of Black Brant 18.219-1 Flight, Utah State University, (2 September 1974).
12. G. J. Romick, Report on the Geophysical Description and Available Data Associated with Rocket PF-BB-72, University of Alaska, p.22 (23 July 74).
13. P. D. Perreault and M. J. Baron, ICECAP 74 - Chatanika Radar Results, DNA 3871T, pp 58-59 (October 1975).
14. AFGL Data Reduction Staff, private communication.
15. R. R. O'Neil et al., EXCEDE II, AFGL-TM-OPR-03, 1976.

16. R.J. Huppi and A.T. Stair, private communication, Apr 1976.
17. R. Olson, private communication, Feb 1976.
18. R.H. Eather, S.B. Mende, and R.J.R. Judge, J. Geophys. Res. 81, 2805 (1976).
19. J.B. Kumer, "Analysis of 4.3 μ m ICECAP Data," HAES Report No. 19, AFCRL-TR-74-0334, (July 1974)
20. V.B. Wickwar, M.J. Baron and R.D. Sears, J. Geophys. Res. 80, 4364 (1975).
21. M.H. Rees and D. Luckey, J. Geophys. Res. 71, 5181 (1974).
22. A. Omholt, The Optical Aurora, Springer, NY, 1971.
23. J.W. Chamberlain, Physics of the Aurora and Airglow, Academic Press, N.Y., 1961, Chapter 2.
24. W. Sawchuk and C.D. Anger, Planet. Space Sci. 24, 896 (1976).
25. L.A. Frank and K. Ackerson, J. Geophys. Res. 76, 3612 (1971).
26. K.D. Baker, private communication, Feb 76.
27. R.R. Vondrak and M.J. Baron, Radar Measurements of the Latitudinal Variation of Auroral Ionization, to appear in Radio Science, Oct 1976.
28. D. Archer, private communication, Feb 1976.
29. R.R. O'Neil, E.R. Huppi, and E.T.P. Lee, Paper SA56, A.G.U. Dec 75, p. 1035.
30. D.F. Strobel, E.S. Oran, and P.D. Feldman, J. Geophys. Res. 81, 3745 (1976).
31. C.S. Deehr, J.D. Winningham, F. Yasuhara, and S.-I. Akasafu, J. Geophys. Res. 81, 5527 (1976).
32. R.J. Huppi, private communication, 06 Dec 76.
33. I.L. Kofsky et al., Sky Background Measurement Program, AFCRL-70-0032, 30 Nov 69.

APPENDIXES

TABLE OF CONTENTS

<u>Appendix Number</u>	<u>PhotoMetrics PIC-Number</u>	<u>Topic</u>	<u>Page</u>
I	61, 11 pp	Operating Plan for Coordinated Aircraft and Ground Measure- ments on the Auroral Ionosphere, ICECAP 76	I-1
II	69, 6pp	Optical Method for Determining Altitude of Aurora for Investigations of NO ^f and Other IR Backgrounds	II-1
III	73a, 13 pp	Review of the Space and Time Variations of the Natural Hydroxyl Airglow	III-1

ABSTRACTS AND EXPLANATORY NOTES

Three of the working memorandums in which we reported shorter-term support projects to DNA, AFGL, and directly to other HAES groups are reproduced here. Some minor changes from the original communications have been made to clarify references and standardize the format.

I (61) -- Operating Plan for Aircraft, Radar Support

Goals, instrument configuration, flight profiles, and support data requested from Poker Range's ground-based instruments for the ICECAP 76 aircraft program are presented. AFGL's IR/Optical Flying Laboratory's missions are listed, and the Thomson-scatter radar's operating procedure is

described in Section VI. PhotoMetrics maintained communication about the aircraft's status with the ground-support groups (radar, RAOB, radiometer, meridian photometer plus All-sky camera).

In addition PhotoMetrics participated in planning, at Poker Range, the DNA 617 radar's support of ICECAP 76's rockets. Procedures agreed on were as follows.

- For EXCEDE -- ensure very low level particle bombardment and E-layer electron density ("quiet" auroral conditions) by measurements near the rocket's trajectory.
- for HIRIS -- determine predosing and instantaneous particle precipitation in the spectrometer's field with the program
 - a. Up to 2 min before launch: scan in zenith angle in the azimuth plane of the rocket's trajectory; -
 - b. At 2 min: point at the rocket's 100-km upleg intercept; -
 - c. At apogee (3 ~ min after launch): move to the 100 km downleg intercept; -
 - d. When rocket reaches ~60 km altitude on downleg: end radar support.
- For the dual CO₂ rocket investigation -- measure particle precipitation in and near the stable auroral arc by meridian scans between zenith and 35°N elevation.

6

The CO_2^+ radiation measurements were not supported by radar measurements of the auroral-ionosphere wind profile partly because these winds are expected to change during the ~ 12 min required using the short multipulse mode, and partly to avoid data loss during the change from meridian scanning mode, which would be repeated for each rocket launch delay (in addition the 3-position radar data require substantial computer time to process into wind drift vectors).

II (69) -- Spectroscopic Determination of Auroral Altitudes

Remote sensing of altitude profiles of auroral-particle energy deposition by radiometric spectrometry of emission features, and its application to ICECAP's aircraft measurements of aurora-associated infrared radiation, are reviewed.

III (73a) -- Variations in the Hydroxyl Airglow

The natural fluctuations in OH background intensity ($\Delta v = 1$, $2.8 - \sim 4\mu\text{m}$; $\Delta v = 2$, $1.2 - \sim 2\mu\text{m}$) are reviewed. Variations are observed with latitude, season, solar zenith angle, magnetospheric activity, and warming of the stratosphere, which are only sparsely documented and not well explained by theoretical models.

MEMORANDUM

DATE: 09 Feb 76

TO: ICECAP Distribution List FROM: I. L. Kofsky

SUBJECT: Operating Plan for Coordinated Aircraft and Ground Measurements on the Auroral Ionosphere, ICECAP 76

Background: AFGL's IR/optical Flying Laboratory NKC-135A 553120 will fly a series of missions from Eielson AFB starting 20 Feb 76 in connection with DNA's High Altitude Effects Simulations tests. This memorandum outlines the goals of the flight program, the aircraft's instrument configuration and mission profiles, supporting data requested from ICECAP and Alaska-network ground facilities (in particular, the Chatanika radar), and coordination procedures.

The 1975 ICECAP aircraft program is reviewed in the attached Appendix. It indicated that NO vibrational overtone radiation near $2.8\mu\text{m}$ associated with optical auroral forms could be detected from jet transport altitude by filter radiometry; and that averaged over energy-deposition altitude, $\sim 1/2$ NO $\Delta v=2$ system photon is emitted per ion pair (tentative figure from one flight analyzed in forthcoming HAES Report 27; refer to my pre-planning memo of 02 Oct 75). Reference is also made to the Test Plan for A/C 53120 operations 15 Feb - 30 Mar 76 prepared by Major J. W. Reed (23 Jan 76), which lists operational support, scheduling, and technical requirements and gives the flight profiles included here as Tables 4 and 5.

A. Goals of Aircraft-Coordinated Test Program

The primary goal is to derive lumped-parameter absolute spectral yields of nitric oxide vibrational radiation for input to predictive computer models of weapons effects, while providing understanding of the processes that excite this infrared background/foreground in air bombarded by energetic particles. Measurements on the high latitude ionosphere will determine

- 1) altitude dependence of NO volume emission rate, with support of altitude profiles of energy deposition rate from the DNA Project 617 incoherent-scatter radar and (secondarily) ground and aircraft photometry of optical features that indicate the spectral index of the aurora-producing electrons;
- 2) spectral distribution in the $\Delta v = 2$ system, using an interferometric spectrometer behind the aircraft's LN_2 -cooled chopper;
- 3) spatial structure and correlation with visible fluorescence forms, whose radiance distribution is measured by narrow-angle photometers.

* See p I-11

The radiometer measurements will also indicate departures of absolute radiance from linearity with column energy deposition rate, and effects of predosing, if any. The usual coordinating measurements of NO precursor radiations and auroral-ionosphere parameters are planned.

The flights will also provide information on

- 4) OH Meinel band fluctuations and waves, since latitude and longitude profiles of hydroxyl nightglow zenith intensity are required for interpreting the $2.8\mu\text{m}$ radiance data. (Any further OH measurements would be on a non-interference basis.)

B. Aircraft Instruments

Table I-1 gives specifications of the radiometers, photometers, and spectrometer, all of which are mounted in the aircraft to point to the zenith. Further particulars on the instruments marked *, operated in ICECAP 75, are given in the Appendix. Note that the $2.0\mu\text{m}$ radiometer has been removed, and the auroral fluorescence-sensitive $1.57\mu\text{m}$ filter replaced by a $1.27\mu\text{m}$ O_2 Δ filter channel. For reference, we have included as Figures I-1a and I-1b model synthetic spectra for $2850\text{--}3750\text{ cm}^{-1}$ ($3.50\text{--}2.67\mu\text{m}$) from HAES Report 27. Fig I-1a is the zenith spectral radiance from beneath aurora having $10\text{ kR N}_2^+(0,0)$ First Negative band intensity, with the OH cascade normalized to $150\text{ kR}(1,0)$ band intensity and thermal emission/absorption by the lower atmosphere similarly scaled to expected values. The slowly-varying OH contribution to radiometer signals near $2.8\mu\text{m}$ can be subtracted by reference to the OH overtone radiometer reading, leaving the NO overtone and a comparably slowly-varying thermal emission component largely removable by reference to the sky radiance in the absence of auroral excitation (as further described in HAES 27 and the references in the Appendix).

The $2.8\mu\text{m}$ radiometer's filter width and field of view will be adjusted to meet the somewhat conflicting requirements of spatial (Item 3) and intensity (Item 1) resolution. For the spatial correlation measurements the field will be reduced to 2° or 5° circular (depending on S/N realized), and the filter passband widened to $2.5\text{--}3.05\mu\text{m}$ to compensate partially for the radiometer's loss of geometric throughput. The projection of a 2° field at auroral altitude is $\sim 3\text{--}1\frac{1}{3}\text{ km}$, and the aircraft's 220 m/sec forward speed sweeps one such field in $\sim 15\text{ sec}$.

The interferometer's expected NESR of $1 \times 10^{-11}\text{ w}/(\text{cm}^2\text{ ster cm}^{-1})$ should provide useful NO overtone spectra in IBC III auroral breakups (refer to Fig 1). It is mounted behind the external cold chopper, which interrupts the signal at 1578 Hz . The raw spectral transform and a reference interferogram of a 5842.49 \AA laser are recorded at 300 Hz . See E. R. Huppi, J. W. Rogers, and A. T. Stair, Jr., Applied Optics 14, 1466 (1974) for further details of instrument and cold-chopper construction.

The 12 channel photometer (Table I-2) is the unit used in AFCRL-OPR's 1968-1972 aircraft program, from which considerable experience with interpretation of filter channel readings has been gained. Filters were selected to decrease the $\lambda 3914$ sampling interval to 8 sec , increase dynamic range (sensitivity is otherwise controlled manually), and provide auroral predosing and spectral index information. The sampling interval for monitoring auroral particle flux can of course be reduced to $\sim 1/10\text{ sec}$, by holding the filter wheel on a single channel.

Table I-1. Zenith-Pointing Spectroradiometers[†] On A/C 53120, ICECAP 76

INSTRUMENT, A/C STATION	SPECTRAL FWHM	FULL FIELD OF VIEW	APERTURE DIAMETER	FRAMING TIME, SEC	DETECTOR	SENSITIVITY, COMMENTS
*Radiometer E-09, 510	2.5 or 2.85 -3.05 μ m	2° or 5°, or 10° -- See text	2 in	<1 when signal high	InSb with cold filter, LN ₂ -- Cold Chopper (NO + OH + Thermal)	
*Dual Radiometer E-15, 540	1.27 μ m \pm 0.05, 1.7003 μ m \pm $\frac{1}{2}$ 0.0773 μ m		2 in		PbS -40°C	NESR 4 kR at 10° field, OH (1.57) & O ₂ Δ (1.27)
Type III - 1 Interferometer E-09, 510	1.17 - 3.1 μ m	4° f/1 lens with detector at focus	1 in	40	InSb, LN ₂ Beam Splitter Si on CaF ₂	NESR ₂ 1 x 10 ⁻¹¹ w/cm ² ster cm ⁻¹ in 100 sec. Res 2 cm ⁻¹ without apodization - Cold Chopper --
*Photometer E-15, 540	0.3907 0.3921 μ m	2°, 5°, 10° (3 units)	1 in	<1	PMT	Same photometers as used on rockets. 2 of 3 channels recorded.
Photometer E-05, 1010	S-20 12 channels, refer to Table I-2	2°	2 in	2 & 24	PMT, cooled	S/N \geq 10 at 10R λ 3914 for 2 sec integrating time
*All-Sky Camera E-13, 430	0.38 - 0.68 μ m	165°	f/1.5	4.3 or 11.4	EK 2475	16 mm standard format. Records IBC I in 11 sec exposure

* From ICECAP 75 -- further data in Appendix.

[†] Also Type V interferometer in side window with view to 20° elevation,
1.2 - 3.1 μ m, 4 cm⁻¹ apodized, 1-1/2° full field, 1 sec scan.

Table I-2. Multifilter Photometer (System E-05)

Entrance Aperture:	5 cm nominal, circular: $A = 20.3 \text{ cm}^2$
Field of View:	Adjustable iris - 2° circular planned: $A \Omega = 0.0194 \text{ cm}^2 \text{ ster}$
Number of Channels:	12^* , geneva motion sequenced
Dwell, Cycle Time:	1-3/4 sec nominal, 24 sec total
Phototube:	S-20 9558A Thermoelectrically cooled to -20° C Dark current 60 electrons/sec
Recording:	Current mode on chart recorder and A/C tape recorder

*Planned filter cycling mode (refer to text) --

Dark Slide
Tritium-activated phosphor for test/calibration

	FWHM	$\int Td\lambda$
4278 N_2^+ First Negative (0,1) band	7.7 Å	2.38 Å
6300 OI	9.2 Å	5.50 Å
5577 OI	7.9 Å	3.45 Å
5525 OI's background near twilight	9.0 Å	4.61 Å
3914 N_2^+ with ND 1 attenuation	44 Å	
6315 OI	43 Å	
5199 NI doublet	8.5 Å	4.50 Å
5312 continuum & dawn	10.0 Å	7.1 Å
4278 N_2^+ First Negative (0,1)	7.0 Å	
3466 NI	22.4 Å	

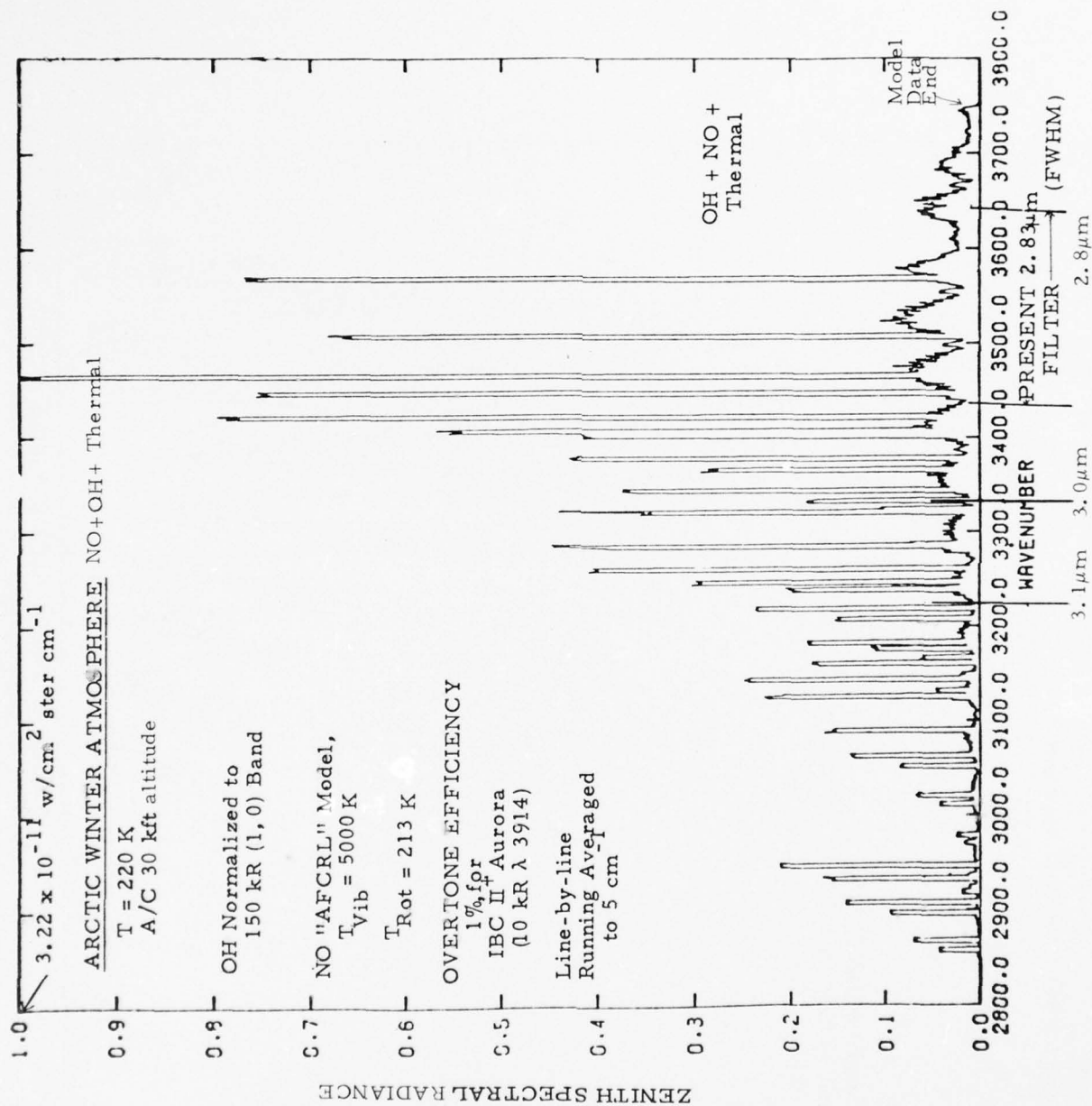
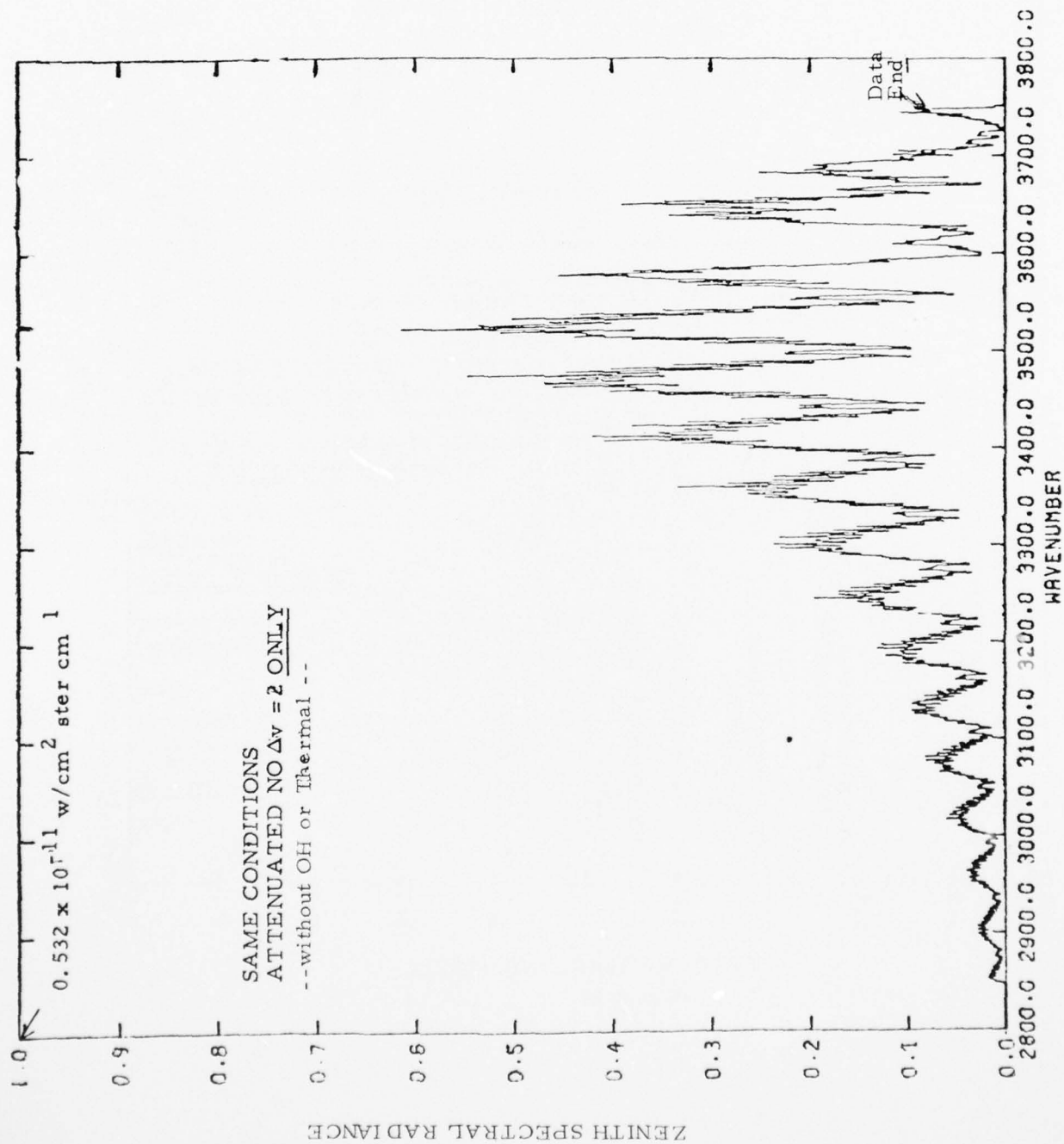


Fig. I-1a



Since the multi-channel photometer is mounted some 600 inches behind the radiometer in the airframe, which twists and flexes in flight, some offset between the two instruments is expected. Thus the single-channel units mounted at A/C Station 490 will be levied for the spatial correlation tests.

Attention is directed to the fact that measuring systems having a limited number of fields may uniquely resolve temporal from spatial signal variations only over a limited frequency band (see, for example, page 158 of A. Omholt's "The Optical Aurora," Springer, 1971). In the case of the single-channel aircraft radiometer, pulsating auroral forms in which the NO vibrational emission lags the fluorescent emission would generally appear to show reduced infrared-visible spatial correlation. On the other hand in pulsating aurora (ibid, p159) spatially uniform over areas large compared to the FOV, the time dependence of the NO signal would provide information about the intermediate processes leading to NO chemiluminescence.

C. Flight Plans and Coordinated Ground Measurements

a) General: The Appendix gives background data on the planned flight program: profiles and checkpoints along the 257°E geomagnetic meridian passing over Poker Flat Research Range (Fig A1 and A3, and Table A1); projections against the rotating auroral oval (Fig A2); and aircraft launch and ground control procedures (pA6). The aircraft arrives Eielson 19 Feb, with first data flight scheduled for 20 Feb LT (moon age 20 da). It will remain on alert status until late Mar, making about 8 maximum 4-5 hours flights. (Some further missions in the March second quarter will be for other projects.) Scattered moonlight does not seriously degrade the aircraft measurements, impacting principally the visible NO precursor and spectral index observations without reducing substantially the precision of $\lambda\lambda 3914$ and 4278 assessments of \geq IBC I+ auroral precipitation. However, supporting ground optical measurements are much more seriously affected.

b) Specific: Table 3 lists the ground support data requested and the flight profiles, which are shown in Tables 4 and 5 and Fig A1. Major requirements are marked *.

A major (indeed, critical) coordination requirement is altitude profiles of energy deposition rate from the Chatanika radar. Further details of the DNA 617 radar's support operation mode are to be finalized in the field. The aircraft instrument fields are well within range of the radar in the "close-in" flight profile of Table I-4 (Fig A2), and remain within range in some of the parallel-arc missions (Table I-5).

Temperature profiles are needed to help assess the thermal emission background from aircraft altitude. Timing of the ASL rocket probes against the aircraft missions will be determined in the field.

The ground radiometry provides secondary calibration for the aircraft's hydroxyl radiometers. (In addition the OH intensity monitors at PKR and Anchorage contribute to the (noninterfering) hydroxyl wave investigations). The array of ground photometers provides more critical backup to the airborne photometers, since their absolute calibration is expected to be more accurate. In addition, the spatial scanning units contribute importantly to characterizing auroral conditions.

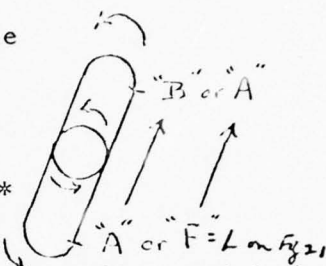
Table I-3. Requested Ground Support Measurements

MISSION FACILITY	1) Altitude Dependence <u>NO</u>	2) Spectral Distribution <u>NO</u>	3) Spatial Structure <u>NO</u>	4) OH Structure
FLIGHT PROFILE	Table I-4	Table I-5	Figure A1→N	Figure A1→ S
DNA 617 Radar [†]	*Altitude Profile of [e]	Altitude Profiles (E-W?)	*Meridian Scans	N/A
SWIR Radiometers	Hydroxyl background fluctuations			
3 Color Photometers	Spectral Index	Spectral Index	*Meridian Scans	Na Correlation?
3 Beam Photometers	E - region drift			λ 5577, 6300 waves
Fixed Photometers	N ² D (P?)			OI?
RAOB's	* Temperature and water vapor profile for each flight mission			
Geophysical Institute	* Standard range network data package			
DMSP Satellite	Copy of record from midnight pass in both * visible and infrared radiometer channel			

* Principal requirement; refer to text.

Table 14. Eielson Local - PFRR Profile

1.05'	{	66°12'N 146°05'W - "B" S of FYU	* Read L on Fig 21 S of E. ckn
		65°08'N 147°29'W - "A" PKR	
		64°03'N 148°47'W - "F"	



(each position is 73.3 nm or 10 min (@ 440kts) from previous position)

Entry point and holding pattern control point - "A", FL 380 to FL 410 as fuel permits.

Exit point - as determined for each sortie ^{E-09} (chopper requires 30 minute warm up prior to descending below FL 250 on let down).

Holding pattern may be shifted between "F" and "A" vice above scheme. ^{Read L*}

Basic Sequence - Entry point - level; + 5 min enter 10 min/15° left bank/circular orbit, roll out arrive "B" + 5 min; reverse course with 5 min/15° left bank/half circle; + 5 min enter 10 min/15° left bank/circular orbit, roll out arrive abeam "A" + 5 min; reverse course with 5 min/15° left bank/half circle. Total elapsed time to control point "A" = 50 min.

Two complete orbits = 1 + 40

Climb + descent = $\frac{1 + 30}{3 + 10}$

Variation - If strong signals are received when aircraft is in bank, Project will immediately notify navigator, for initiation of straight and level chase on (immediate heading - 90°) for 100 nm maximum chase. Reverse course and return to "A". Continue pattern as above. Total time: 3 + 45 (approx.).

-- from J. Reed Test Plan

* of Ref. 2

Table I-5. Eielson Local - Parallel Arc Profile

tear drop reverse course

69°21'N 141°04'W - "E"

68°18'N 142°54'W - "D"

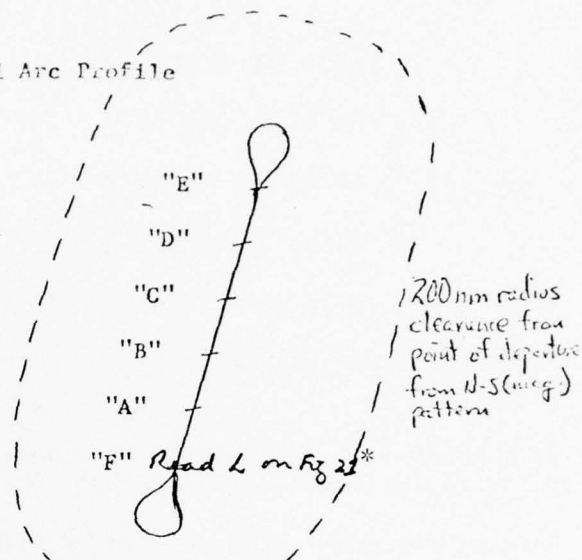
67°16'N 144°32'W - "C"

66°12'N 146°05'W - "B"

65°08'N 147°29'W - "A"

64°03'N 148°47'W - "F"

tear drop reverse course



(each position is 73.3 nm or 10 min (@ 440kts GS) from previous position; plan reverse course so as to arrive at last position 10 minutes later).

Entry point - A (Poker Research Range), FL 350 or above cirrus

Exit point - As determined for each sortie (chopper requires 30 minute warm up prior to descending below FL 250 on let down).

Variation - Upon interception of bright aurora 1 arc or upon ground notification of bright aurora build up East or West of aircraft track, initiate 200nm clearance of current location so as to place aircraft beneath bright arc on heading parallel to direction of arc. Reverse course as necessary. After successful data run, return to original track. Total time: 5 + 00 (approximate).

-- from J. Reed Test Plan

* of Ref. 2

NOTE: Course can be reversed at any lettered position to allow aircraft to follow auroral activity.

D. Ground Coordination

Major J. W. Reed will be AFGL aircraft program director. A. T. Stair, Jr., ICECAP Project Scientist, will serve as ground support and range instrument coordinator. Technical assistance will be provided by I. L. Kofsky, to whom comments on this planning document should be addressed.

The flight crew will be on standby alert at Eielson AFB for aircraft launch from 2100 hours. Headquarters for aircraft direction and ground coordination will be the Geophysical Institute's Telecommunications Center, 6th floor Elvey Building.

Note: The Appendix referred to herein is Section IV of Ref 2.

<u>Appendix</u>	<u>Ref 2</u>
Table A1	Table 4
Fig A1	Fig 21
Fig A2	p. II-7
Table A2	Table 5
Fig A3	Fig 22

APPENDIX II
MEMORANDUM

DATE: 10 May 1976

TO: C.A. Blank, A.T. Stair, Jr./ICECAP

FROM: I.L. Kofsky, PhotoMetrics

SUBJECT: Optical Method for Determining Altitude of Aurora for
Investigations of NO⁺ and Other IR Backgrounds

Introduction, History

Measuring the effective fluorescence yield of NO vibrational quanta as a function of altitude at which energy is deposited in the atmosphere, is a major goal of the HAES program. Toward this end we coordinated the DNA 617 incoherent-scatter radar with the AFGL KC-135 aircraft's radiometer & spectrometer in ICECAP 76. The former instrument measures altitude profile of free electron concentration $[e](h)$ in the auroral ionosphere, from which, with some assumptions we shall note later, the rate of production of ion pairs $+d[e](h)/dt$ can be inferred; and the latter measure surface radiance of the accompanying NO overtone, a quantity more related to $+ \int dh d[e](h)/dt$. The aircraft also carried a coaligned multi-channel optical photometer that measured zenith radiance in appropriately-coordinating auroral spectroscopic features.

It is the purpose of this note to show, with the aid of an example from these IC 76 aircraft data, that

- simple photometry of auroral emission lines and bands can also be applied to infer the altitude profile of volume ionization rate $+d[e](h)/dt$, and
- the optical method is comparatively inexpensive, requiring only an absolutely calibrated photometer; it permits continuous measurement on the air volume that lies in the field of the infrared spectroradiometer, thus providing good statistics in a fully self-contained aircraft experiment; and its systematic uncertainties are now probably no worse (if at all) than those of the radar method, and can be readily reduced still further.

Procedure

The method for remotely sensing the energy spectrum of aurora-producing electrons (J.G.R. 79, 5181 (1974)) was developed by M.H. Rees, quondam scientific advisor for aeronomy at NSF. A related but less sophisticated procedure was earlier published by R.J.R. Judge (Planet. Space Sci. 20, 2081 (1972)) of U Cal San Diego, and further, it is implicit in some DNA auroral codes. To facilitate this presentation, I shall delay until later detailed discussion of it (failings included), suggestions for improvements by applying existing DNA codes, and some comparison to the radar method.

Briefly described, the photometric method quantifies the principle that the altitudes from which various auroral emission bands and lines arise are functions of relative and absolute atmosphere composition, as well as the energy distribution of the primary precipitating electrons (or protons). Thus it is closely related to the well-known diagnostic procedure that determines by ground-based instruments the energy spectrum of thermal x-rays from an exoatmospheric explosion, from ratios of radiance in fluorescence features excited and quenched at different altitudes.

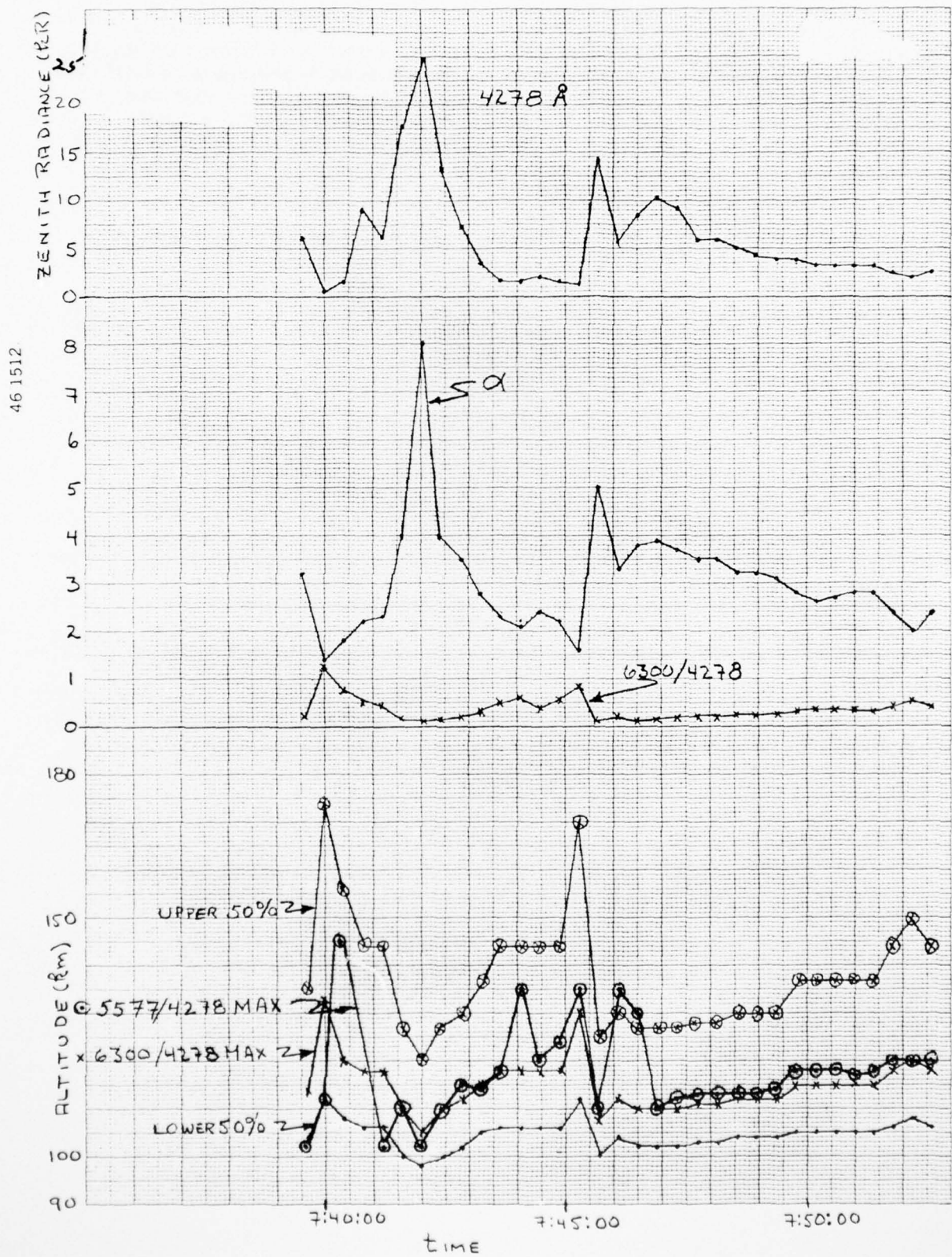
Rees fits the ratio of radiance of a feature originating in the F-region to one coming mainly from the E-region accessible to the harder electrons, as an adjustable parameter of a "reasonable" model differential particle energy distribution function. The spectral form is $E^1 \exp(-E/\alpha)$, and his theory also inputs absolute auroral intensity. From this spectrum an energy deposition-rate profile for a known altitude dependence of atmosphere density can be readily computed. These auroral features are - as expected - the largely-quenched OI $\lambda 6300$ line (of the doublet) and N_2^+ $\lambda 4278$ -band fluorescence. The more intense $\lambda 3914$ band is less favored because of its greater scattering in the lower atmosphere.* In this connection, aircraft measurements give particularly accurate results since they require negligible correction for effective attenuation of the aurora's radiance after passage through an incompletely-specified atmosphere.

The 1974 JGR paper also quantifies the principle for the OI $\lambda 5577/\lambda 4278$ column intensity ratio. Since the model of $\lambda 5577$'s multifarious excitation- and-quenching processes toward the bottom of the E-region does not incorporate EXCEDE's new findings, this radiating pair may at present provide less reliable "absolute" altitudes. On the other hand, however, the $\lambda 5577/\lambda 4278$ ratio does offer advantages in time and 3-D space resolution (refer to discussion in the Addendum).

Illustrative Example

We applied Rees' procedure to a brief segment of PhotoMetrics / OPR's photometer data from the "parallel-arc" aircraft mission ICECAP 10 (08 Mar 76), getting the encouraging results shown in the accompanying graph. The segment of auroral arc intercepted in the generally E-W flight path far N of the ground support facilities at PKR has maximum $\lambda 4278$ zenith brightness 25 kR (IBC II+) and minimum 1/2 kR. The radiance ratio $\lambda 6300/\lambda 4278$ varied between 1.28 and 0.086, giving from Rees' graphs (with the absolute $\lambda 4278$ intensity) characteristic e-folding energy α ranging from 1.4 to 8.0 keV. Altitudes of peak energy deposition rate lie between 105 and 133 km, which differ by a factor 34 in atmosphere number density, with the spread to half-peak deposition as shown (the model of course also allows detailed profiles of $d[e]/dt$ to be calculated). Peak altitude using the ratio $\lambda 5577/\lambda 4278$ shows satisfactory agreement despite the aforementioned uncertainty in the $\lambda 5577$ excitation-deexcitation model adopted; the half-power points are omitted for clarity in the display of results.

*Refer to Section V.



This optical remote sensing principle of course can also support measurements on NO^+ and NO^{++} from ground stations, as well as measurements on all infrared radiators from rockets or balloons (or Space Shuttle). The visible-aurora data from the ICECAP 76 flights are all in hand for application to determining, with the $2.83\mu\text{m}$ radiometer and interferometer data, systematics of the altitude dependence of NO^+ 's excitation efficiency. The great volume of radiometric data that can be taken in aircraft flights has the effect of sharpening up the altitude or number-density "resolution" of auroral simulations, which is desirable because the natural particle energy deposition at any one time is spread over a broad range of altitudes (as the graph on p. II-3 indicates).

Addendum: Brief Review of Rees' Method, Comparison to Radar Option

Fred Rees has been working on this procedure for some time, and it was even applied more than two years before its eventual publication in Dec 74 (by Eather & Mende, and Gattinger & Vallance Jones). Among his earlier precursor-preparation articles is one with Belon & Romick (Planet. Space Sci. 14, 597 (1966)) that gives the altitude profile in a convenient though incomplete form, which we used in the attached graph. OPTIR or ARCTIC or any other of DNA's auroral-deposition codes could readily be applied to improve the altitude profile from the α 's derived from the spectroscopic radiance ratios. Furthermore, some of the codes based on A. E. S. Green's group's earlier work that output zenith radiances in several auroral features (over and above the three prominent ones used by Rees), could be applied — in effect, "inverted" — to fit multi-parameter models of the input particle energy spectra. With validation and calibration from the "air truth" provided by rocket-borne particle-spectrometers such as on ICECAP's A18.219-1, which show a somewhat more complex spectral form in the vicinity of arcs, this optical method would provide more reliable remote sensing of auroral altitude profiles.

Rees' method is implicitly contained in OPTIR and in the ARCTIC code as described in Section 2 of DNA 3297F. It considers, at least in principle, partition of the primary electrons' energy into production of secondary electrons and UV, excitation of a large number of states of ambient and even aurora-excited species (including continuous energy loss to free electrons), and various other sinks; and then follows the energetic secondaries, considers quenching and cascading, and so on. The results may or may not be sensitive to input parameters —: no sensitivity studies, or systematic experimental test of the calculations, have yet been made.

The major identifiable assumptions in the theory are magnetic field-alignment of the measuring spectrophotometer's field of view; steady state excitation-loss of O^1D or S^1S (upper states of $\lambda 6300$ and $\lambda 5577$); and of course the simplified form of the spectrum. The first of these would require that the auroral-particle precipitation be

reasonably uniform over the $\sim 13^\circ$ ($90^\circ - \sim 77^\circ$ dip) typical offset from the magnetic field direction in the auroral oval, plus 2° field, of the aircraft's photometer. This condition isn't usually very well met for lower F-region $\lambda 6300$ in flights along geomagnetic meridians, although it could be achieved readily by tilting the photometer and spectroradiometer field axes. The effective time constant for $\lambda 6300$ emission is about 30 sec (figuring in quenching and some population by electron dissociative recombination), during which time the aircraft moves some 7 km, a distance comparable to the N-S horizontal scale of high-intensity auroral precipitation. These two factors are the reason for our earlier comments about the attractiveness of $\lambda 5577$, which has effective time constant $\sim 1/2$ sec and comes principally from an E-region layer not far offset from N_2^+ fluorescence. Results for flights parallel to the auroral oval, such as in our illustration, would be expected to be somewhat more reliable than those from cross-arc flights (the ICECAP 76 Operating Plan, Appendix I, describes mission profiles).

Additionally, the assumed shape of the particle energy spectrum is a potential source of error: as we noted, the spectra measured in arcs from various ICECAP rockets fit the Rees ("Maxwellian") model rather poorly. As also noted, this fit can be improved by extending the spectroscopic data to include further auroral features, in particular those partially collisionally quenched (such as N_2 Vegard-Kaplan and First Positive, and N_2^+ Meinel bands).

Note also that most of the NO^+ radiation in effect arises from below ~ 135 km. At higher altitudes the time constant for the $e + NO^+$ and $N_2^+D + O_2$ (and other intermediate) reactions becomes longer than ~ 20 sec, which represents a time-space scale over which the infrared emission doesn't "follow" well the prompt auroral fluorescence measured from the moving aircraft. At still somewhat higher altitudes N_2^+D is de-excited principally on O atoms. Calculations of NO^+ excitation efficiency must take this effect into account (as we pointed out in our "precursor" article in AFCRL 72-0114); the correction increases with softening of energy spectrum and increasing rate of change of particle flux, in both time and space.* In any case, the results of the simulation improve with increasing uniformity in space and time of the auroral precipitation (with the high altitude component requiring more uniformity).

Insofar as one man's revelation is another man's heresy, a hasty and incomplete comparison to the incoherent-scatter radar's $+d[e]/dt$ would serve no purpose. I have therefore started to review in detail the two approaches to altitude profiling, with inclusion of a comparison between time-overlapping meridian scans published by Chatanika and made by the Geophysical Institute and LMSC photometers.* Recent comparison of column integrals for determining total energy fluxes by the LMSC photometry-SRI radar groups†, and concentration by SRI on profiling and energy spectra, set the stage for this work.

*See also Section V.

†J.G.R. 80, 4361 (1975)

(Suffice it to say for the time being that the radar's throughput is so low ("normally" it requires ~ 5 sec integrating time per series of points along the beam) that it follows poorly the moving aircraft instruments' field-of-view (against which the dish can't be conveniently tracked anyhow) and, for that matter, much of the natural auroral variation; that deriving $+d[e](h)/dt$ from $[e](h)$ requires the assumptions of equilibrium $[e]$, the value of the effective recombination coefficient at altitude h , and negligible transport of charge in the ionosphere; and that the absolute calibration for $[e]$, the square of which figures in calculating $+d[e]/dt$, may be subject to some fundamental uncertainties and has not yet been systematically tested in intense aurora.) We note that the aforementioned problems of non-coincident excited air volumes are if anything exacerbated when the radar is applied: uniformity is still needed.

While I would not be ready to compare absolute effectiveness, I expect that the cost/effectiveness of the optical method of assessing altitude profiles of auroral excitation rate for aircraft programs is superior, both in terms of the low cost of implementing the measurements and the long time over which useful coordinating data can be taken. Further, the onboard capability permits use of the natural aurora frequently far north of PKR, and in "soft" precipitation regions of the oval. The issue in any case is less one of absolute accuracy of an instantaneous determination of $+d[e](h)/dt$, than one of how apposite the data are to coordinated HAES experiments with aircraft-borne infrared spectroradiometers.

Summary, Recommendations

Spectrophotometric remote sensing of altitude profiles of energy deposition rate in aurora is an inexpensive, convenient, and continuously-operating (high-throughput) method for application to determining dependence on altitude of infrared excitation processes. Good measurement statistics, and full capability of the mobile aircraft station to operate anywhere in the auroral oval and polar cap, are other important advantages. The accuracy of the method appears at least adequate for present HAES needs. It could be improved by pointing the visible- and infrared-sensitive instruments along the magnetic field direction (which poses no real problem in aircraft investigations), and expanding the theoretical model to a base of further altitude-dependent auroral emission lines and bands (applying existing DNA codes).

WEDNESDAY, JUNE 16, 1976
ROOM 2B
Chairman: D.J. McEwen

ATMOSPHERIC AND SPACE PHYSICS

Note in proof: Related recent papers, from APS Bulletin 21, 819 (1976). See also comments on p. 5531, JGR 81 (01 Nov 76).

9:00

EDI

Modelling of Electron Aurora

A.V. JONES, *Herzberg Institute of Astrophysics, N.R.C.*

Methods are discussed of calculating the height distributions and intensities of auroral emission features from an initial primary electron energy distribution. For indirect excitation processes the ion and neutral chemistry and electron temperatures must be considered.

11:40

ED5 Auroral and Airglow Emissions in the Polar Cap
Observed by ISIS-2 Auroral Scanning Photometer.* S.
SMALL and L.L. COGGER, *Univ. of Calgary*.--Diffuse
auroral emissions in the entire polar cap at 5577 and

3914Å were observed by the ISIS-2 Auroral Scanning
Photometer. Regions of soft particle precipitations in
different sectors of the polar cap were determined from
5577/3914Å intensity ratios.

APPENDIX III

MEMORANDUM

DATE: 24 August 1976

TO: A. T. Stair, Jr., OPR-1

FROM: I. L. Kofsky, PhotoMetrics, Inc.

SUBJECT: Pictorial Review of the
Space and Time Variations of the Natural Hydroxyl Airglow

- III-1 Spectrum of $\Delta v = 1$ sequence. PhotoMetrics model spectrum from AFGL's $H + O_3 \rightarrow O_2 + OH^+$ population data and NBS's transition probabilities. Total mean system intensity adapted from A. Vallance Jones, Space Sci. Rev's 15, 355 (1973).
- III-2 List of geophysical factors affecting column intensity. Very little data and theory are available on the variability of the profile of volume emission rate. Changes in the altitude profile from its normal $\sim 85 \pm 7$ km will of course also impact the radiance seen by sidelooking instruments.
- III-3 Time, space, & magnitude scale of each type of variation.
- III-4 Diurnal Variation. One type seen at middle latitudes, from AFGL TR 76-0032, Jan 76. Other types of behavior are almost as frequently observed, as is a fairly strong latitude dependence. The daytime behavior is not known.
- III-5 Seasonal, Solar cycle variation. French ground network data (R. Wiens & G. Weill, Planet. Space Sci. 21, 1011 (1973)), all near midnight to minimize the contribution of diurnal effect.
- III-6 Stratospheric warming increase. Sporadic warmings of the stratosphere are observed by radiometers on Nimbus-type satellites in spring and occasionally winter. Neither their origin or the mechanism(s) by which they "cause" spectacular increases in OH emission at high latitudes are understood. (Data from J.G. Walker & E.I. Reed, NASA X-621-75-6, Jan 75.)
- III-7 Latitude variation. OGO-4 data taken with a 9-3 band down-looking photometer with poor spatial resolution. The readings have some contamination by earth albedo, and some from a stratwarm. These represent essentially the only systematic satellite data on OH available, and they are not considered very accurate. Note the substantial (factor ~ 10) variations. (Same ref as IV-6.)

AD-A047 376

PHOTOMETRICS INC LEXINGTON MASS

F/G 4/1

DATA REDUCTION AND AURORAL CHARACTERIZATIONS FOR ICECAP III. HA--ETC(U)

JAN 77 I L KOFSKY, D P VILLANUCCI, R B SLUDER DNA001-76-C-0161

UNCLASSIFIED

PHM-02-77

DNA-4220F

NL

3 OF 3

ADA047 376



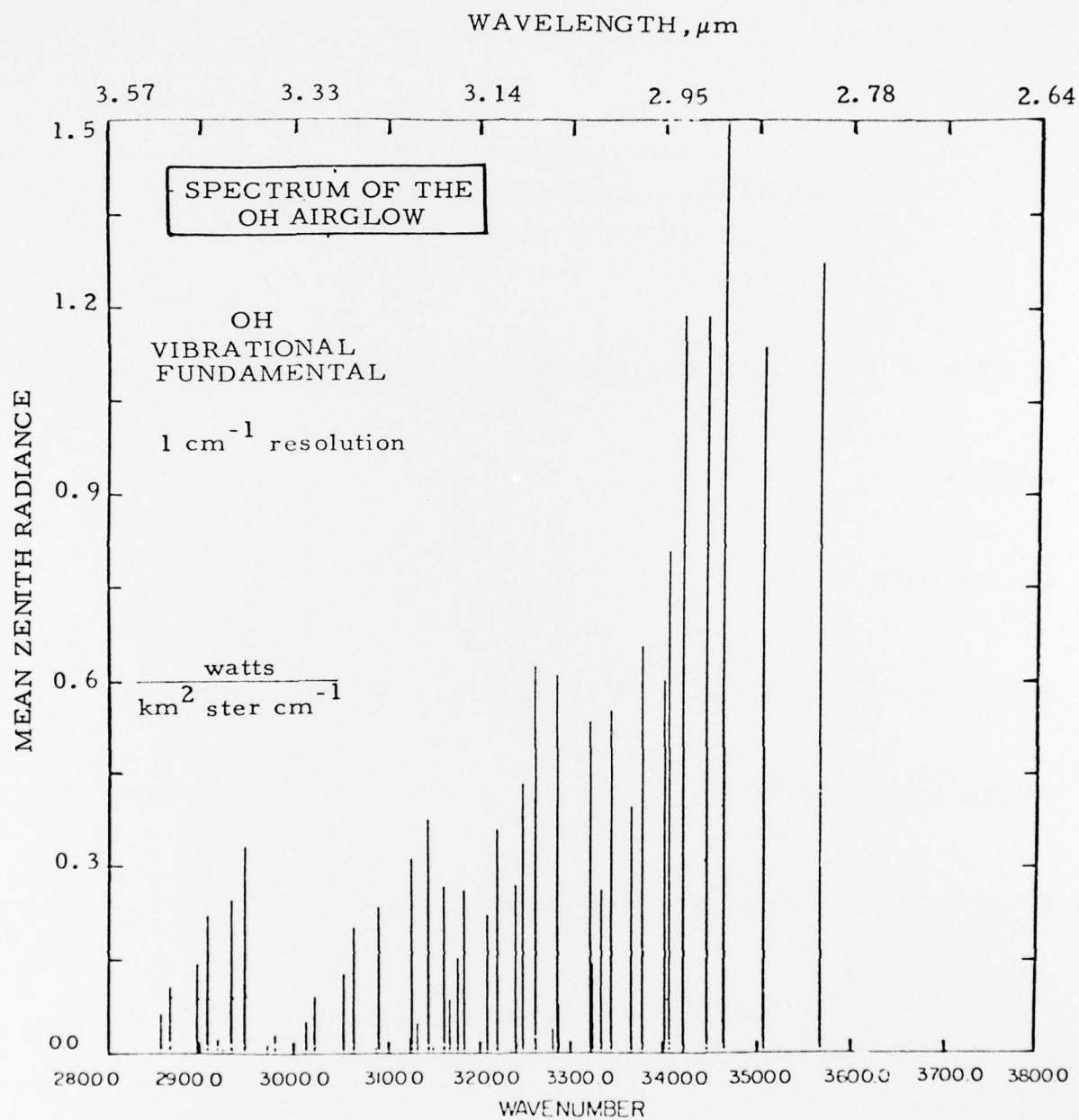
END

DATE
FILMED

1 - 78

DDC

- III-8 Geomagnetic storm variation. High latitude data are missing because the Russians observed only at strongly aurora-contaminated visible and NIR wavelengths (N. Shefov, Planet. Space Sci. 17, 797 (1969)). The results can be interpreted in terms of long-period waves.
- III-9 Geomagnetic activity variation. AFGL OH data from TR-76-0032 on which we have shown the K-sum for the period 12-24 hr before the observations, better illustrates the magnitude of the effect at high latitude.
- III-10 Short-period variations. These Japanese balloon data illustrate the mix of "traveling" fluctuations. The radiometer, sensitive between 1.5 and 2.5 μm , makes an almucantar scan at 30° elevation angle. (T. Sugiyama et al., Nature 246, 57 (1973).)
- III-11 Contours of peak [O]. No such body of systematic data exists for [OH⁺]. These show the strong natural variability of [O], which diffuses downward to drive [O₃] and thus [OH⁺]. (OGO-6 data from T. M. Donahue et al., J.G.R. 79, 1959 (1974).)



ZENITH INTENSITY OF
THE NATURAL AIRGLOW IN THE OH BANDS
IS KNOWN TO VARY WITH:

- TIME OF DAY(SOLAR ZENITH ANGLE, DIURNAL EFFECT)
- SEASON
- LATITUDE
- MAGNETOSPHERIC ACTIVITY (& HISTORY) → SOLAR CYCLE
- STRATOSPHERIC WARMINGS
- (● RATE OF DOWNWARD FLOW OF OXYGEN ATOMS)

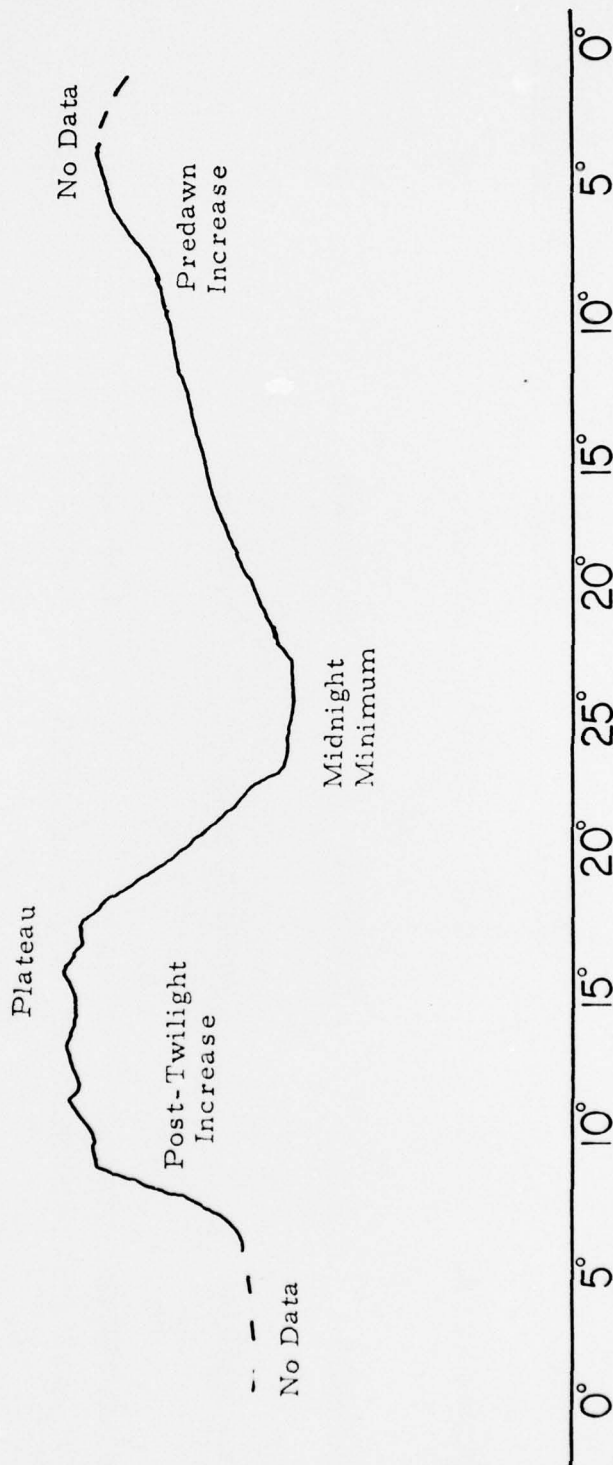
"GENERALIZATIONS ARE DANGEROUS"
SYSTEMATIC SURVEY DATA ARE SPARSE

NATURAL VARIATIONS IN OH INTENSITY

	<u>TIME PERIOD</u>	<u>SPATIAL SCALE</u>	<u>PEAK-TO-PEAK MAGNITUDE*</u>
• SOLAR CYCLE	DECADE, YEARS	GLOBAL	1½
• SEASONAL	MONTHS	10,000 km	3
• STRATWARMS	WEEKS, DAYS	5,000 km	4
• GEOMAGNETIC STORMS	DAYS	5,000 km	5
- WAVE DISTURBANCES	HOURS, MINUTES	2,000 - 20 km	1½
• DIURNAL	HOURS	Latitude - Dependent	2 Night ? Day

* Depends on latitude

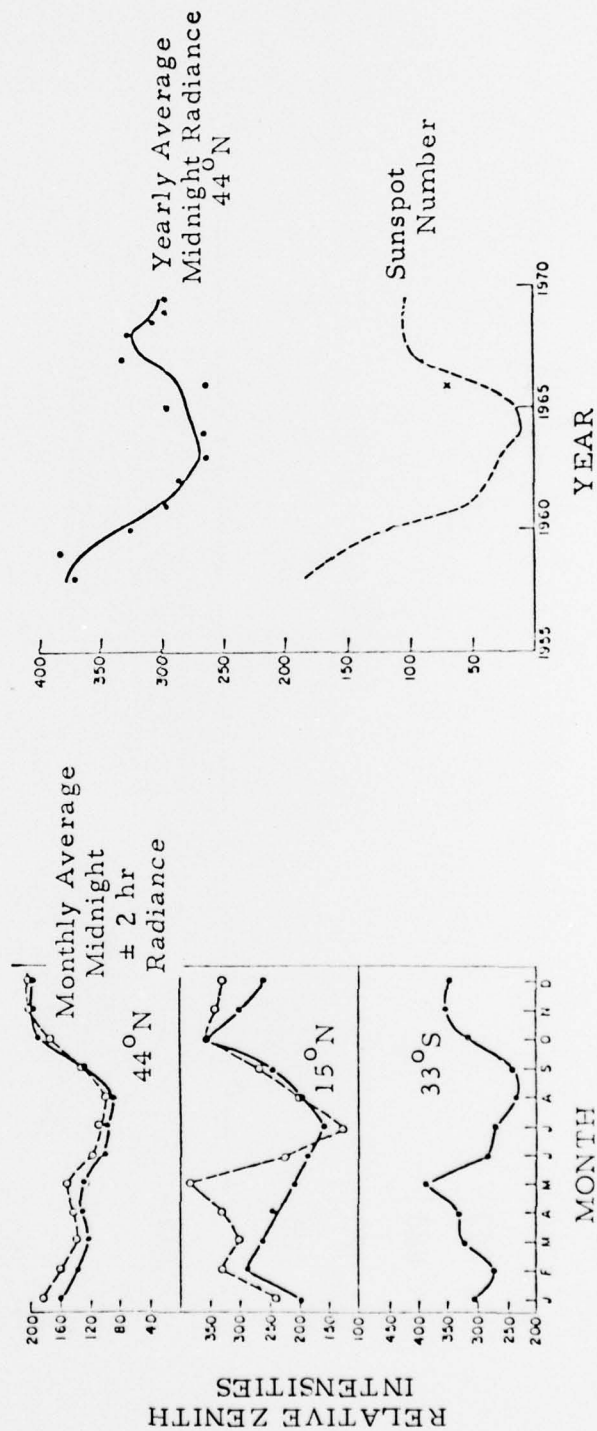
-- DIURNAL VARIATION --
(Fairly Typical of Midlatitude)



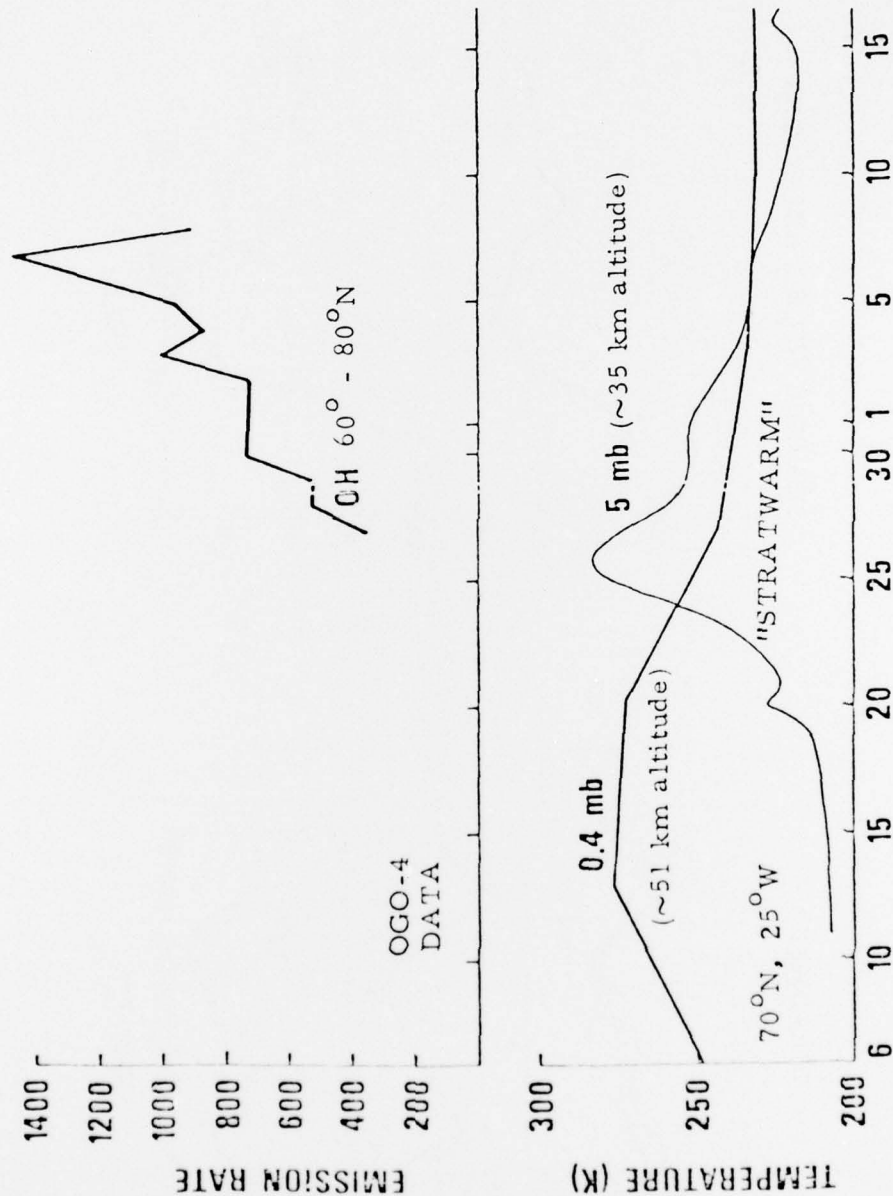
SOLAR DEPRESSION
(FROM 0 KM ALTITUDE)

SOLAR CYCLE VARIATIONS --

- SEASONAL &



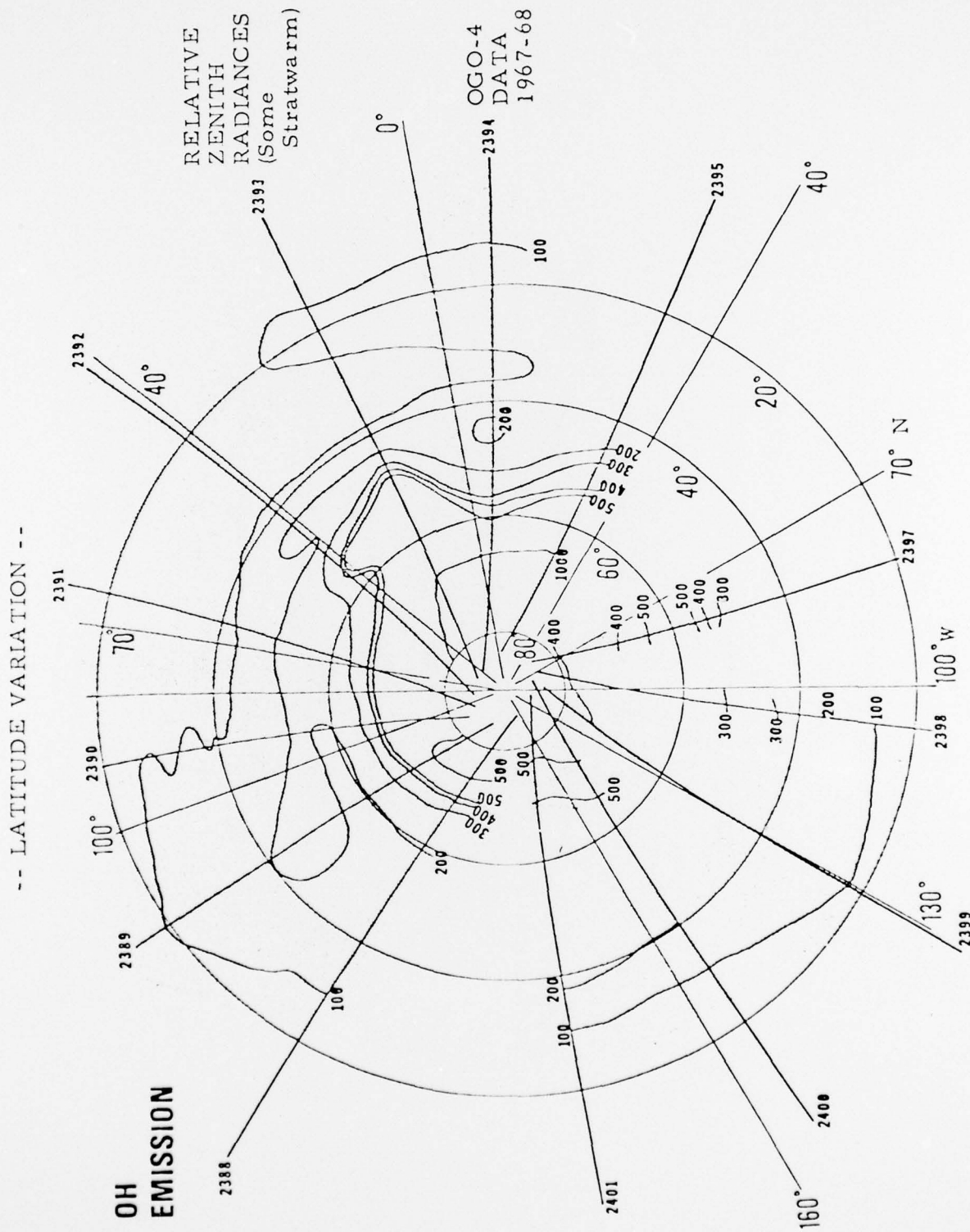
-- STRATOSPHERIC WARMING VARIATION --



JAN. 1968

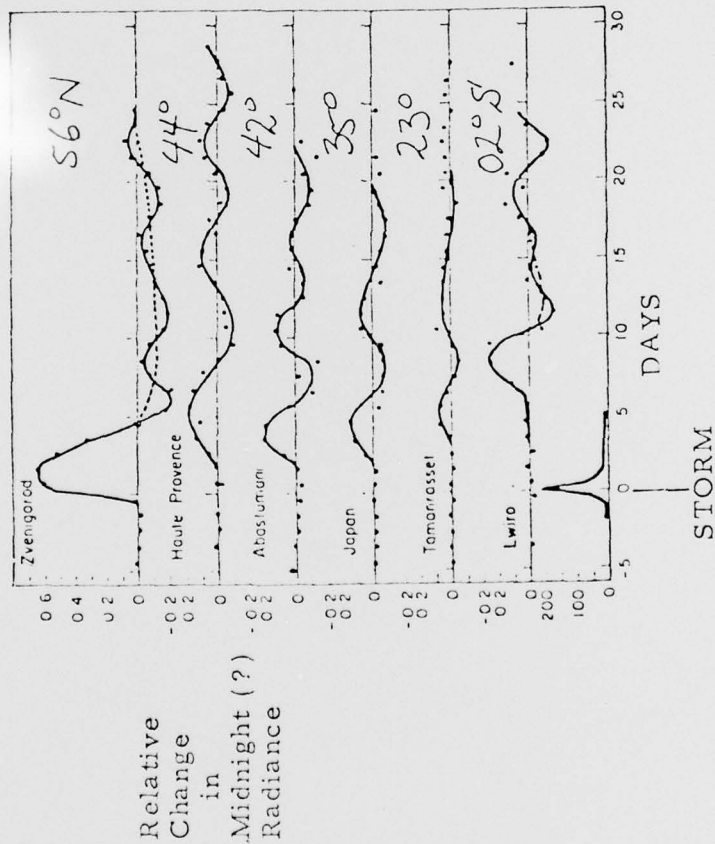
DEC. 1967

III -6



-- GEOMAGNETIC STORM VARIATION --

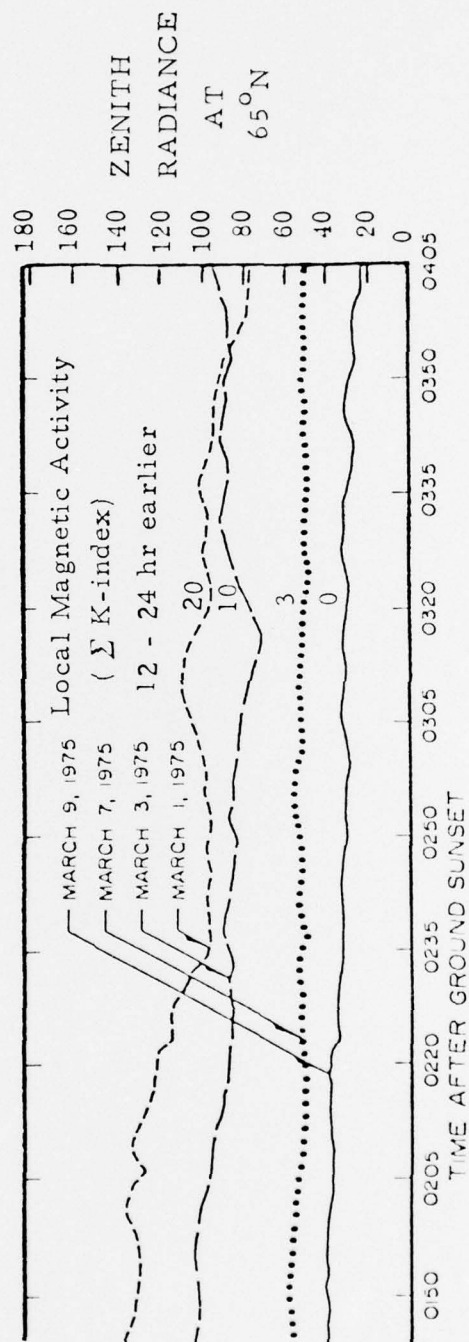
(Data for higher latitudes (g))



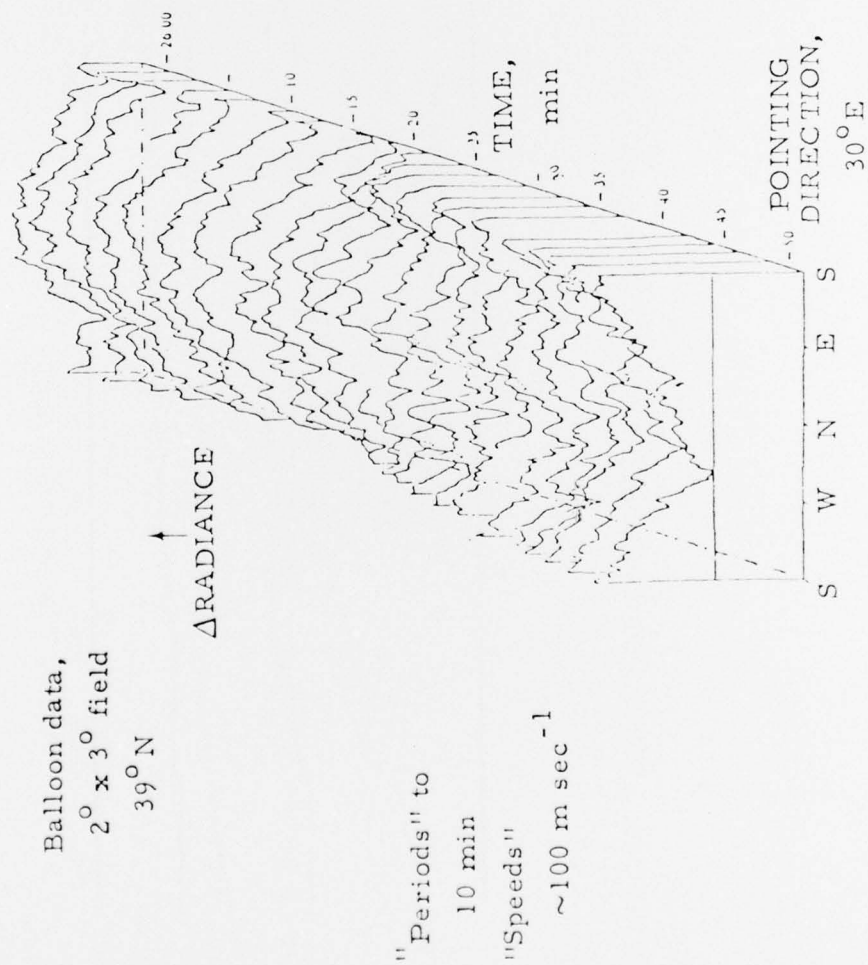
$K_p = 6 \text{ to } 9$

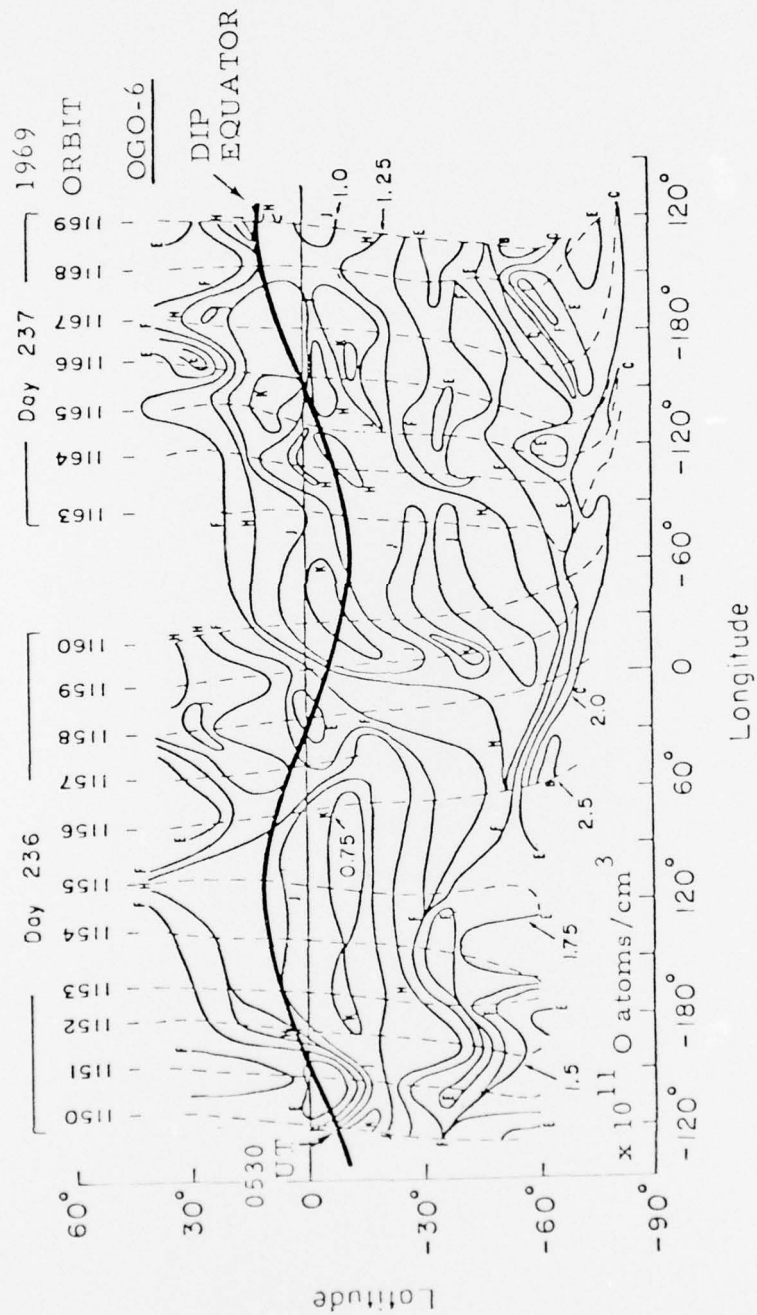
RUSSIAN DATA

TYPICAL EFFECT OF GEOMAGNETIC DISTURBANCE AT HIGH LATITUDE



-- SHORT-PERIOD VARIATIONS --





III-11. CONTOURS OF MAXIMUM DENSITY
OF OXYGEN ATOMS
(all at 97 ± 2 km altitude)

DISTRIBUTION LIST

DEPARTMENT OF DEFENSE

Director
Defense Advanced Research Proj. Agency
ATTN: LTC W. A. Whitaker
ATTN: Strategic Technology Office
ATTN: Nuclear Monitoring Research

Defense Documentation Center
Cameron Station
12 cy ATTN: TC

Director
Defense Nuclear Agency
ATTN: TISI, Archives
3 cy ATTN: TITL, Tech. Library
2 cy ATTN: RAAE, Charles A. Blank
ATTN: RAEV, Harold C. Fitz, Jr.
ATTN: RAAE, Major John Clark
ATTN: RAAE, Major James W. Mayo
ATTN: DDST

Dir. of Defense Research & Engineering
Department of Defense
ATTN: S&SS (OS)

Commander
Field Command
Defense Nuclear Agency
ATTN: FCPR

Chief
Livermore Division, Field Command, DNA
Lawrence Livermore Laboratory
ATTN: FCPRL

DEPARTMENT OF THE ARMY

Commander/Director
Atmospheric Sciences Laboratory
US Army Electronics Command
ATTN: DRSEL-BL-SY-S, F. E. Niles
ATTN: DRSEL-BL-SY-S, D. Snider
ATTN: H. Ballard
ATTN: R. Olsen

Commander
Harry Diamond Laboratories
2 cy ATTN: DRXDO-NP, F. N. Wimenitz

Commander
US Army Nuclear Agency
ATTN: MONA-WE, J. Bereberet

Director
BMD Advanced Tech. Center
Huntsville Office
ATTN: ATC-O, W. Davies
ATTN: ATC-T, Melvin T. Capps

Dep. Chief of Staff for Rsch. Dev. & Acq.
Department of the Army
ATTN: NCB Division
ATTN: DAMA-CSZ-C
ATTN: DAMA-WSZ-C

DEPARTMENT OF THE ARMY (Continued)

Chief of Engineers
Department of the Army
ATTN: Fernand DePercin

Deputy Chief of Staff for Ops. & Plans
Department of the Army
ATTN: DAMO-DDL, Colonel D. W. Einsel
ATTN: Dir. of Chem. & Nuc. Ops.

Director
US Army Ballistic Research Labs.
ATTN: Tech. Lib., E. Baicy
ATTN: John Mester
ATTN: J. Heimerl
ATTN: M. Kregl

Commander
US Army Electronics Command
ATTN: DRSEL-PL-ENV, Hans A. Bomke
ATTN: DRSEL
ATTN: Stanley Kronenberg
ATTN: DRSEL-RD-P
ATTN: DRSEL-TL-IR, E. T. Hunter
ATTN: Inst. for Exploratory Rsch.
ATTN: Weapons Effects Section

Commander
US Army Foreign Science & Tech. Center
ATTN: Robert Jones

Commander
US Army Material Dev. & Rdns. Cmd.
ATTN: DRXCD-TL
ATTN: DRCCDC, J. A. Bender

Commander
US Army Missile Command
ATTN: DRSMI-ABL
ATTN: Chief, Doc. Section
ATTN: DRSMI-XS, Chief, Scientist

Chief
US Army Research Office
ATTN: CRDARD-OCS, Hermann Robl
ATTN: CRDARD-P, Robert Mace

DEPARTMENT OF THE NAVY

Commanding Officer
Naval Intelligence Support Center
ATTN: Document Control
ATTN: Code 40A, E. Blase

Superintendent (Code 1424)
Naval Postgraduate School
ATTN: Code 2124, Tech. Reports Librarian

Commander
Naval Weather Service Command
Naval Weather Service Hqs.
Washington Navy Yard
ATTN: Mr. Martin

DEPARTMENT OF THE NAVY (Continued)

Chief of Naval Research

Navy Department

ATTN: Code 461, Jacob Warner
ATTN: Code 461, R. G. Joiner
ATTN: Code 421, B. R. Junker

Commander

Naval Ocean Systems Center

ATTN: Code 2200, Verne F. Hildebrand
ATTN: Code 2200, Ilan Rothmuller
ATTN: Code 2200, William F. Moler
ATTN: Code 2200, Jurgen Richter
ATTN: Code 2200, Richard Pappert
ATTN: Tech. Lib. for T. J. Keary
ATTN: Code 2200, Herbert Hughes

Director

Naval Research Laboratory

ATTN: Code 7700, Timothy P. Coffey
ATTN: Douglas P. McNutt
ATTN: Code 7750, Darrell F. Strobel
ATTN: Code 7709, Wahab Ali
ATTN: Code 7701, Jack D. Brown
ATTN: Code 2600, Tech. Lib.
ATTN: Code 7127, Charles Y. Johnson
ATTN: Code 7750, Paul Julienne
ATTN: Code 7750, J. Davis
ATTN: Code 7750, Klaus Hein
ATTN: Code 7120, W. Neil Johnson
ATTN: Code 7750, Joel Fedder
ATTN: Code 2027, Tech. Lib.
ATTN: Code 7750, S. L. Ossakow
ATTN: Code 7730, Edgar A. McClean

Officer in Charge

Naval Surface Weapons Center

ATTN: Code WA501, Navy Nuc. Prgms. Off.
ATTN: Code WX21, Tech. Lib.
ATTN: L. Rudlin
ATTN: D. J. Land

DEPARTMENT OF THE AIR FORCE

AF Geophysics Laboratory, AFSC

5 cy ATTN: LKB, Kenneth S. W. Champion
5 cy ATTN: OPR, Alva T. Stair
2 cy ATTN: OPR-I, R. Murphy
5 cy ATTN: OPR, J. C. Ulwick
2 cy ATTN: OPR-I, J. Kennealy

AF Weapons Laboratory, AFSC

5 cy ATTN: SUL
5 cy ATTN: DYT
5 cy ATTN: DYC
ATTN: CA
2 cy ATTN: DYM
ATTN: G. J. Fryer

Commander

ASD

ATTN: ASD-YH-EX, Lt Col Robert Leverette

SAMSO/SZ

ATTN: SZJ, Major Lawrence Doan

AFTAC

5 cy ATTN: TD
2 cy ATTN: Tech. Lib.

DEPARTMENT OF THE AIR FORCE (Continued)

Hq. USAF

ATTN: DLS
ATTN: DLCAW
ATTN: DTL
ATTN: DLXP
ATTN: SDR
ATTN: Tech. Lib.

SAMSO/AW

ATTN: AW

ENERGY RESEARCH & DEVELOPMENT ADMINISTRATION

Division of Military Application

US Energy Research & Dev. Admin.

ATTN: Doc. Con. for Major D. A. Haycock
ATTN: Doc. Con. for Col T. Gross
ATTN: Doc. Con. for Donald I. Gale
ATTN: Doc. Con. for David Slade
ATTN: Doc. Con. for F. A. Ross

Los Alamos Scientific Laboratory

ATTN: Doc. Con. for R. A. Jeffries
ATTN: Doc. Con. for C. R. Mehl
ATTN: Doc. Con. for G. Rood
ATTN: Doc. Con. for H. V. Argo
ATTN: Doc. Con. for D. Steinhaus
ATTN: Doc. Con. for J. Judd
ATTN: Doc. Con. for T. Bieniewski
ATTN: Doc. Con. for D. M. Rohrer
ATTN: Doc. Con. for Martin Tierney
ATTN: Doc. Con. for Marge Johnson
ATTN: Doc. Con. for John S. Malik
ATTN: Doc. Con. for William Maier
ATTN: Doc. Con. for S. Rockwood
ATTN: Doc. Con. for Donald Kerr
ATTN: Doc. Con. for W. D. Barfield
ATTN: Doc. Con. for Reference Library
ATTN: Doc. Con. for W. M. Hughes
ATTN: Doc. Con. for E. W. Jones, Jr.
ATTN: Doc. Con. for John Zinn
ATTN: Doc. Con. for E. A. Bryant

University of California

Lawrence Livermore Laboratory

ATTN: G. R. Haugen
ATTN: A. Kaufman
ATTN: D. J. Wuebbles
ATTN: J. F. Tinney
ATTN: Julius Chang
ATTN: Tech. Info. Dept.
ATTN: W. H. Duewer

Sandia Laboratories

ATTN: Doc. Con. for W. D. Brown
ATTN: Doc. Con. for Org. 9220
ATTN: Doc. Con. for Craig Hudson
ATTN: Doc. Con. for J. C. Eckardt
ATTN: Doc. Con. for C. W. Gwyn
ATTN: Doc. Con. for D. A. Dahlgren
ATTN: Doc. Con. for M. L. Kramm
ATTN: Doc. Con. for T. Wright
ATTN: Doc. Con. for Charles Williams
ATTN: Doc. Con. for Sandia Rpt. Coll.
ATTN: Doc. Con. for Doc. Con. Div.

ENERGY RESEARCH & DEVELOPMENT ADMINISTRATION
(Continued)

Sandia Laboratories
Livermore Laboratory
ATTN: Doc. Con. for Thomas Cook

Argonne National Laboratory
Records Control
ATTN: Doc. Con. for A. C. Wahl
ATTN: Doc. Con. for S. Gabelnick
ATTN: Doc. Con. for J. Berkowitz
ATTN: Doc. Con. for Lib. Service Rpts. Sec.
ATTN: Doc. Con. for Len Liebowitz
ATTN: Doc. Con. for David W. Green
ATTN: Doc. Con. for Gerald T. Reedy

US Energy Research & Dev. Admin.
Div. of Hqs. Services
Library Branch G-043
ATTN: Doc. Con. for D. Kohlsted
ATTN: Doc. Con. for J. D. LaFleur
ATTN: Doc. Con. for Class Tech. Lib.
ATTN: Doc. Con. for George Regosa
ATTN: Doc. Con. for Rpts. Section
ATTN: Doc. Con. for R. Kandel
ATTN: Doc. Con. for H. H. Kurzwiek

DEPARTMENT OF DEFENSE CONTRACTORS

Aero-Chem. Research Laboratories, Inc.
3 cy ATTN: A. Fontijn

AeroDyne Research, Inc.
ATTN: M. Camac
ATTN: F. Bien

Aerospace Corporation
ATTN: Thomas D. Taylor
ATTN: R. D. Rawcliffe
ATTN: Harris Mayer
ATTN: R. Grove
ATTN: R. J. McNeal

University of Denver
Colorado Seminary
Denver Research Institute
ATTN: Sec. Officer for Mr. Van Zyl
ATTN: Sec. Officer for David Murcay

General Electric Company
TEMPO-Center for Advanced Studies
5 cy ATTN: DASIAC, Art Feryok
ATTN: Warren S. Knapp

General Research Corporation
ATTN: John Ise, Jr.

Geophysical Institute
University of Alaska
ATTN: T. N. Davis
3 cy ATTN: Neal Brown

Honeywell Incorporated
Radiation Center
ATTN: W. Williamson

Institute for Defense Analyses
ATTN: Ernest Bauer
ATTN: Hans Wolfhard

DEPARTMENT OF DEFENSE CONTRACTORS (Continued)

Lockheed Missiles & Space Company, Inc.
ATTN: Tom James
ATTN: Billy M. McCormac, Dept. 52-54
ATTN: Martin Walt, Dept. 52-10
ATTN: J. B. Reagan, D/52-12
ATTN: John B. Cladis, Dept. 52-12
ATTN: John Kumer
ATTN: Richard G. Johnson, Dept. 52-12
ATTN: Robert D. Sears, Dept. 52-14

Mission Research Corporation
ATTN: D. Archer
ATTN: P. Fischer

Photometrics, Inc.
ATTN: Irving L. Kofsky
ATTN: D. P. Villanucci
ATTN: R. B. Sluder

Physical Dynamics, Inc.
ATTN: Joseph B. Workman

Physical Sciences, Inc.
ATTN: Kurt Wray

R & D Associates
ATTN: Robert E. LeLevier
ATTN: Forrest Gilmore

R & D Associates
ATTN: Herbert J. Mitchell

The Rand Corporation
ATTN: James Oakley

Science Applications, Inc.
ATTN: Daniel A. Hamlin

Space Data Corporation
ATTN: Edward F. Allen

Stanford Research Institute
ATTN: Walter G. Chestnut
ATTN: M. Baron
ATTN: Ray L. Leadabrand

Stanford Research Institute
ATTN: Warren W. Berning

Technology International Corporation
ATTN: W. P. Boquist

Utah State University
ATTN: Kay Baker
ATTN: Doran Baker
ATTN: D. Burt
ATTN: C. Wyatt

VisiDyne, Inc.
ATTN: Henry J. Smith
ATTN: William Reidy
ATTN: J. W. Carpenter
ATTN: T. C. Degges
ATTN: L. Katz
ATTN: Charles Humphrey

OTHER GOVERNMENT AGENCIES

Department of Commerce
Office of Telecommunications
Institute for Telecom Science
ATTN: William F. Utlaut